Processing particulate organic matter from municipal wastewater into a particle-free short-chain fatty acids stream for bio-based products recovery

Zur Erlangung des akademischen Grades eines

DOKTORS DER INGENIEURWISSENSCHAFTEN (Dr. -Ing.)

von der KIT-Fakultät für Chemieingenieurwesen und Verfahrenstechnik des

Karlsruher Instituts für Technologie (KIT)

genehmigte

DISSERTATION

von

M.Sc. Nikhil Shylaja Prakash

aus Kerala, India

Tag der mündlichen Prüfung: 01.08.2025

Erstgutachter: Prof. Dr. Harald Horn

Zweitgutachter: Prof. Dr.-Ing. Tobias Morck

Declaration in lieu of oath

I hereby declare that this thesis was written only by me and I have used no other sources than those indicated.

Literal or analogous quotations are marked as such.

I hereby agree that the present work can be loaned for scientific purposes, copied, and placed in the library of the Engler-Bunte-Institut, Water Chemistry and Water Technology.

Karlsruhe, 2025

Acknowledgement

First and foremost, I would like to express my deepest gratitude to Prof. Dr. Harald Horn, for the exceptional supervision, unwavering support, and for providing me with the opportunity to work as a PhD student. Your guidance has been instrumental in shaping the direction of this thesis, and I am truly thankful for your trust and encouragement throughout this journey.

A heartfelt thank you to Dr. Andrea Hille-Reichel, whose continuous supervision, support, and positivity have been a source of motivation. Your invaluable advice, kindness and uplifting energy made this process feel so much lighter. I will always appreciate your encouragement to keep pushing forward. I was lucky to have you as my supervisor.

My sincere thanks to Dr. Florencia Saravia for her support in reviewing the manuscript and for her support since my time as a master student. Your insights and kindness have been extremely helpful.

A special thank you to Dr. Abbt-Braun, Ms. Ursula Schäfer and Ms. Sylvia Heck for their incredible administrative support, which has made navigating the complexities of this PhD much smoother.

I would like to extend my deepest gratitude to Ali Sayegh, whose encouragement in pursuing a PhD started this entire journey. I will always be thankful for your guidance.

My heartfelt thanks to Behnam Askari for the fun moments, and for his collaboration. Working alongside you has been an absolute pleasure.

I am grateful to Mr. Peter Maurer for his technical support, and to the Workshop in Buesanu for assisting me in assembling the reactors, an essential part of this work. A special mention to Mr. Volker Preyl, whose provision of essential equipment when I needed it the most has been invaluable. To Axel Heidt, Matthias Weber, Reinhard Sembritzki and Uli Reichert, thank you for your invaluable assistance in measuring all of my samples. Your technical support was key to completing this work.

I would like to express my sincere gratitude to Prof. Dr.-Ing. Tobias Morck from the University of Kassel for serving as the second examiner of this work. His valuable insights, thoughtful feedback, and expert guidance have significantly contributed to the quality and depth of this thesis. I deeply appreciate the time and effort he dedicated to reviewing and supporting this research.

I would also like to thank Prof. Dr.-Ing. habil. Roland Dittmeyer for serving as the chairman of the examination committee. I extend my thanks to Prof. Dr.-Ing. Alexander Grünberger for his role as examiner. His expertise and critical perspective added great value to this work and helped ensure a rigorous and well-rounded assessment.

I would also like to thank Willow Neske for her dedication in operating the pilot-scale bioelectrochemical system for almost a year. I would like to thank my colleagues Andreas Netsch, Max Miehle, Max Rümenapf, Jan Singer, Yair Morales, Nurul Himma, Süheyla Duran, Zhizhao Xiao, Ben Schädlich for being great colleagues. Special thanks to Zhizhao Xiao and Andreas Netsch for their help in processing the OCT images.

Abstract

Around 24 g TOC·capita^{-1}·d^{-1} is generated as sludge in a typical municipal wastewater treatment plant which is 60 % of the influent stream of 40 g TOC·capita^{-1}·d^{-1}. Typical wastewater treatment plants aim at recovering the organic carbon content in sludge as biogas via anaerobic digestion. However, recent interests have shifted more towards a sustainable and circular economy warranting a better utilization of the organic carbon content in sludge. Therefore, more efforts have been directed towards redesigning wastewater treatment plants into wastewater biorefineries for a better valorization of organic carbon. In this study, a potential wastewater biorefinery is evaluated by focusing on the extraction of chemical precursors in the form of a particle-free short-chain fatty acids (SCFAs) substrate from the organic carbon content in primary sludge, which can be then used for bio-based products recovery. The main objectives of this thesis include fermenting SCFAs through dark fermentation and separating these SCFAs from the solids into a particle-free permeate using a combination of chamber filter-press and microfiltration. In addition, a terminal treatment step in the form of microbial electrolysis is also assessed.

Firstly, dark fermentation was tested across lab (2 L), bench (40 L), and pilot (300 L) scales to optimize SCFAs production by assessing parameters such as pH, temperature, and hydraulic retention time (HRT) in both batch and semi-continuous modes. Results indicated that SCFA yields could be enhanced at shorter HRTs of 1.5 to 3 days, a neutral pH of 7 and a mesophilic temperature of 32 °C. Under these conditions, yields reached 222 ± 24 mg$_{SCFAs}$·g$_{VS}^{-1}$ (volatile solids, VS) at an organic loading rate (OLR) of 18 ± 3 g$_{VS}$·L^{-1}·d^{-1}, which could be further improved to 350 ± 55 mg$_{SCFAs}$·g$_{VS}^{-1}$ at an OLR of 11 ± 3 g$_{VS}$·L^{-1}·d^{-1}. Acetic and propionic acids were the primary fermentation products, contributing between 30 and 40 % of the total SCFAs concentration. Methane production remained below 2 NmL·g$_{VS}^{-1}$, resulting in minimal solids reduction in the hydrolyzate compared to primary sludge.

Following dark fermentation, the aim is to produce a particle-free permeate containing predominantly SCFAs. However, the high solids content (2 to 5 %) due to minimal solids reduction limits the direct use of microfiltration as it can severely foul microfiltration membranes and also result in a significant retention of SCFAs. For this reason, the hydrolyzate was first conditioned with a cationic starch-based flocculant, hydroxypropyltrimethyl ammonium starch (HPAS), and subsequently dewatered with a chamber filter-press with a 100 µm-mesh size. This treatment removed up to 60 % of total solids (TS) at a dosage range of 8–25 mg$_{HPAS}$· g$_{TS}^{-1}$, yielding a filtrate with suspended solids between 100 and 1300 mg·L^{-1}, while achieving up to 85 % volume recovery. The filtrate was further processed with a ceramic microfiltration membrane (α-Al$_2$O$_3$) of 0.2 µm pore size, utilizing a filtration area of 0.316 m² in a cross-flow configuration. A method was developed to optimize cross-flow by monitoring changes in total filtration resistance, establishing an optimal cross-flow velocity of at least 2.3 m·s^{-1} for long-term filtration. Despite reduced suspended solids after the filter-press and the high cross-flow velocity employed, significant membrane fouling occurred due to HPAS passing through the filter-press and interacting electrostatically with the membrane. Backwashing every 600 seconds for 20 seconds sustained a permeate flux of about 20 L·m^{-2}·h^{-1} (LMH) for a monitored period of 96 hours, and adjusting pH below the membrane's isoelectric point (to repel cationic HPAS) maintained flux of 70 to 80 LMH for a monitored period of 140 hours. In a semi-continuous cascade involving dark fermentation, filter-press, and microfiltration, the system filtered approximately 900 L per m^2 of membrane area without chemical cleaning, while maintaining flux in the range of 50 to 60 LMH. Chemical cleaning with basic (pH ≈ 12) followed by acidic (pH ≈ 2) solutions removed organic and HPAS-

related fouling, respectively, recovering at least 75 % of permeate flux. The particle-free permeate showed a recovery of around 4 g $TOC_{SCFAs} \cdot capita^{-1} \cdot d^{-1}$ from the solids stream of 24 g $TOC \cdot capita^{-1} \cdot d^{-1}$, achieving purity levels of 0.85 to 0.97 $C_{SCFAs} \cdot DOC^{-1}$ (carbon (C) in SCFAs per dissolved organic carbon (DOC)).

For the final treatment step, a pilot-scale 100-L rotating disk bioelectrochemical reactor (RDBER) was used to convert SCFAs after microfiltration into hydrogen via microbial electrolysis. The RDBER is distinguished by its rotary circular anodes with a high specific anodic area (100 $m_{anode}^2 \cdot m_{reactor}^{-3}$). The RDBER was inoculated with the electroactive bacterial strains *Geobacter sulfurreducens* and *Shewanella oneidensis* and operated for 200 days in batch and continuous modes, testing various physical and chemical parameters. The RDBER was operated for a 200-day period in batch and continuous modes to optimize pH, hydraulic retention time (HRT), conductivity, recirculation rates, rotational speed, and anode potential. The batch phase was operated in the defined dual-species inoculation, and peak current densities of 240 $mA \cdot m_{anode}^{-2}$ at 300 mV vs SHE (standard hydrogen electrode) was achieved when the pH was increased from 6 to 7.7, reaching Coulombic efficiencies (CE) above 70 %. During the batch phase, maximum hydrogen production reached up to 36 L $H_2 \cdot m_{reactor}^{-3} \cdot d^{-1}$. Starting the reactor under the defined dual-species condition successfully prevented methanogenesis, maintaining a CH_4-free gas phase with hydrogen content up to 80 % for 130 days. Among the tested operational parameters, increased recirculation rate of the medium content from 1 to 3 cycles per hour (($m^3 \cdot h^{-1}) \cdot m_{reactor}^{-3}$) improved current density by 100 %. Continuous operation with unsterile hydrolyzate shifted the reactor to biohythane production (9 % H_2, 86 % CH_4, 3 % CO_2). At an HRT of around 3 days, highest stable current density of 170 $mA \cdot m_{anode}^{-2}$ was maintained, achieving CE of 33 % with a productivity of 3 L $H_2 \cdot m_{reactor}^{-3} \cdot d^{-1}$. and 33 L $CH_4 \cdot m_{reactor}^{-3} \cdot d^{-1}$. Biofilm distribution obtained from gravimetric- and image-based analyses showed that the effective surface coverage was 3.3 m^2. Considering the effective biofilm-covered area, the highest possible current density achieved during continuous feeding was 510 $mA \cdot m_{anode}^{-2}$. Low relative velocities between the anode disks in the middle sections of the RDBER likely hindered nutrient, substrate and product transfer, affecting biofilm growth and distribution. Although the rotary motion of the anode can improve substrate uptake and product removal, the associated tangential velocity and the potential distribution supposedly led to an annular distribution of biofilm. In any case, the RDBER merits optimization in terms of reactor architecture as there is great potential that can be leveraged to advance bioelectrochemical systems.

Zusammenfassung

Etwa 24 g TOC·EW^{-1}·d^{-1} werden als Schlamm in einer typischen kommunalen Abwasserbehandlungsanlage erzeugt, was 60 % des Zulaufstroms von 40 g TOC·EW^{-1}·d^{-1} entspricht. Typische Abwasserbehandlungsanlagen zielen darauf ab, den organischen Kohlenstoffgehalt im Schlamm durch anaerobe Vergärung in Biogas umzuwandeln. Allerdings könnte der organische Kohlenstoff im Sinne einer nachhaltigen und zirkulären Wirtschaft besser genutzt werden. So wurde verstärkt daran geforscht, Abwasserbehandlungsanlagen in Abwasser-Bioraffinerien umzuwandeln. In dieser Studie wird eine potenzielle Abwasser-Bioraffinerie bewertet, wobei der Fokus auf der Extraktion chemischer Grundstoffe aus dem organischen Kohlenstoffgehalt des Primärschlamms liegt. Diese werden in Form eines partikelfreien Hydrolysats bereitgestellt, das reich an kurzkettigen Fettsäuren (SCFAs, short-chain fatty acids) ist und das für die Rückgewinnung biobasierter Produkte genutzt werden kann. Die Hauptziele dieser Dissertation umfassen die Fermentation von SCFAs durch Dunkelfermentation und die Trennung dieser SCFAs von den Feststoffen zur Produktion eines partikelfreien Filtrats unter Verwendung einer Kombination aus Kammerfilterpresse und Mikrofiltration. Darüber hinaus wird ein abschließender Behandlungsschritt in Form einer mikrobiellen Elektrolyse untersucht und bewertet.

Zunächst wurde die Dunkelfermentation im Labor (2 L), im Technikumsmaßstab (40 L) und im Pilotmaßstab (300 L) getestet, um die SCFA-Produktion zu optimieren, indem der Einfluss der Parameter pH-Wert, Temperatur und hydraulische Verweilzeit (HRT, hydraulic retention time) in Batch- und halbkontinuierlichem Betrieb bewertet wurden. Die Ergebnisse zeigten, dass SCFA-Ausbeuten bei kürzeren hydraulischen Verweilzeiten von 1,5 bis 3 Tagen, einem neutralen pH-Wert von 7 und einer mesophilen Temperatur von 32 °C gesteigert werden konnten. Unter diesen Bedingungen erreichten die Ausbeuten 222 $\pm$ 24 mg$_{SCFAs}$·g$_{VS}^{-1}$ (VS, volatile solids, Glühverlust) bei einer organischen Beladung von 18 $\pm$ 3 g$_{VS}$·L^{-1}·d^{-1}, und 350 $\pm$ 55 mg$_{SCFAs}$·g$_{VS}^{-1}$ bei einer organischen Beladung von 11 $\pm$ 3 g$_{VS}$·L^{-1}·d^{-1}. Essigsäure und Propionsäure waren die Hauptfermentationsprodukte, die zwischen 30 und 40 % der gesamten SCFA-Konzentration ausmachten. Die Methanproduktion blieb unter 2 NmL·g$_{VS}^{-1}$, was zu einer minimalen Reduktion der Feststoffe im Hydrolysat im Vergleich zum Primärschlamm führte.

Nach der Dunkelfermentation besteht das Ziel darin, ein partikelfreies Filtrat zu erzeugen, das überwiegend SCFAs enthält. Der hohe Feststoffgehalt (2 bis 5 %) aufgrund der minimalen Feststoffreduktion begrenzt jedoch die direkte Verwendung der Mikrofiltration, da er zu einem starken Fouling der Mikrofiltrationsmembranen und auch zu einem erheblichen Rückhalt von SCFAs führen kann. Aus diesem Grund wurde das Hydrolysat zunächst mit einem kationischen stärkehaltigen Flockungsmittel, Hydroxypropyltrimethylammonium-Stärke (HPAS), konditioniert und anschließend mit einer Kammerfilterpresse mit einer Maschenweite von 100 µm entwässert. Diese Behandlung entfernte bis zu 60 % der Gesamtschwebstoffe (TS, total solids) bei einer Dosierung von 8–25 mg$_{HPAS}$·g$_{TS}^{-1}$ und lieferte ein Filtrat mit suspendierten Feststoffen zwischen 100 und 1300 mg·L^{-1}, während eine Volumenrückgewinnung von bis zu 85 % erreicht wurde. Das Filtrat wurde anschließend mit einer keramischen Mikrofiltrationsmembran (α-Al$_2$O$_3$) mit einer Porengröße von 0,2 µm filtriert, wobei eine Filtrationsfläche von 0,316 m² in einer Cross-Flow-Konfiguration verwendet wurde. Eine Methode wurde entwickelt, um den Cross-Flow zu optimieren, indem Änderungen im gesamten Filtrationswiderstand überwacht wurden. Eine optimale Cross-Flow-Geschwindigkeit von mindestens 2,3 m·s^{-1} wurde für eine Langzeitfiltration

festgelegt. Trotz der reduzierten suspendierten Feststoffe nach der Filterpresse und der hohen Cross-Flow-Geschwindigkeit trat ein signifikantes Membranfouling auf, da HPAS die Filterpresse passierte und elektrostatisch mit der Membran interagierte. Durch das Rückspülen alle 600 Sekunden für 20 Sekunden konnte ein Permeatflux von etwa 20 $L \cdot m^{-2} \cdot h^{-1}$ (LMH) für einen überwachten Zeitraum von 96 Stunden aufrecht erhalten werden, und die Anpassung des pH-Werts unterhalb des Isoelektrischen Punktes der Membran (um kationisches HPAS abzustoßen) ermöglichte einen Flux von 70 bis 80 LMH für einen Zeitraum von mindestens 140 Stunden. In einem halbkontinuierlichen Kaskadensystem, das Dunkelfermentation, Filterpresse und Mikrofiltration umfasst, filtrierte das System etwa 900 L pro m² Membranfläche ohne chemische Reinigung, während ein Flux im Bereich von 50 bis 60 LMH aufrechterhalten wurde. Chemische Reinigung mit basischen (pH ≈ 12) gefolgt von sauren (pH ≈ 2) Lösungen entfernte organisches und HPAS-bezogenes Fouling und stellte mindestens 75 % des Permeatfluxes wieder her. Im partikelfreien Filtrat konnte eine Rückgewinnung von etwa 4 g $TOC_{SCFAs} \cdot EW^{-1} \cdot d^{-1}$ aus dem Feststoffstrom von 24 g $TOC \cdot EW^{-1} \cdot d^{-1}$ und erreichte Reinheitsgrade von 0,85 bis 0,97 $C_{SCFAs} \cdot DOC^{-1}$ (Kohlenstoff (C) in SCFAs pro gelöstem organischen Kohlenstoff (DOC)) erreicht werden.

Für den letzten Behandlungsschritt wurde ein bioelektrochemischer Scheibentauchkörperreaktor (RDBER, rotating disk bioelectrochemical reactor) im Pilotmaßstab (100 L) verwendet, um SCFAs nach der Mikrofiltration mittels mikrobieller Elektrolyse in Wasserstoff umzuwandeln. Der RDBER zeichnet sich durch seine rotierenden Anodenronden mit einer hohen spezifischen Anodenfläche (100 $m_{anode}^2 \cdot m_{reaktor}^{-3}$) aus. Der RDBER wurde mit den elektroaktiven Bakterienstämmen *Geobacter sulfurreducens* und *Shewanella oneidensis* inokuliert und 200 Tage lang im Batch- und im kontinuierlichen Modus betrieben, um pH-Wert, hydraulische Verweilzeit (HRT), Leitfähigkeit, Rezirkulationsraten, Rotationsgeschwindigkeit der Anoden und Anodenpotenzial zu optimieren. Im Batch-Betrieb wurden mit der definierten Kultur maximale Stromdichten von 240 $mA \cdot m_{Anode}^{-2}$ bei einem Anodenpotential von 300 mV vs SHE (Standard-Wasserstoffelektrode) erreicht, als der pH-Wert von 6 auf 7,7 erhöht wurde, bei einer Coulombschen Effizienz (CE) von über 70 %. In der Batch-Phase wurde auch die maximale Wasserstoffproduktion bis zu 36 L $H_2 \cdot m_{Reaktor}^{-3} \cdot d^{-1}$ erreicht. Das Starten des Reaktors mit der definierten Zwei-Spezies-Kultur und synthetischem Substrat verhinderte erfolgreich die Methanogenese, sodass über einen Zeitraum von 130 Tagen eine CH_4-freie Gasphase mit einem Wasserstoffanteil von bis zu 80 % produziert werden konnte. Unter den getesteten Betriebsparametern hatte die Erhöhung der Rezirkulationsgeschwindigkeit des Mediums von 1 auf 3 Zyklen pro Stunde (($m^3 \cdot h^{-1}) \cdot m_{Reaktor}^{-3}$) den größten Effekt und führte zu einer Erhöhung der Stromdichte um 100 %. Der kontinuierliche Betrieb mit unsterilem Hydrolysat führte zu einer Verschiebung der Reaktorleistung zur Biohythanproduktion (9 % H_2, 86 % CH_4, 3 % CO_2). Bei einer HRT von etwa 3 Tagen wurde eine stabile Stromdichte von 170 $mA \cdot m_{anode}^{-2}$ aufrechterhalten, was zu einer CE von 33 % bei einer Produktivität von 3 L $H_2 \cdot m_{Reaktor}^{-3} \cdot d^{-1}$ und 33 L $CH_4 \cdot m_{Reaktor}^{-3} \cdot d^{-1}$ führte. Bildbasierte Analysen des Biofilms auf der Anodenfläche des Reaktors ergaben, dass nur 3,3 m² Anodenfläche (von den dargebotenen 10 m²) tatsächlich bewachsen waren. Unter Berücksichtigung dieser tatsächlich bewachsenen Fläche wurde eine maximale Stromdichte von 510 $mA \cdot m_{Anode}^{-2}$ während des kontinuierlichen Betriebs erreicht. Niedrige relative Geschwindigkeiten zwischen den Anodenscheiben in den mittleren Abschnitten des RDBER behinderten wahrscheinlich den Nährstoff-, Substrat- und Produkttransport, was das Biofilmwachstum und die -verteilung beeinträchtigte. Obwohl die Rotation der Anode die Substrataufnahme in den und die Produktentfernung aus dem Biofilm verbessern

kann, führten sowohl die damit verbundene tangentiale Geschwindigkeit als auch die Potentialverteilung vermutlich zu der gefundenen ringförmigen Verteilung des Biofilms auf den Anodenronden. Das Potenzial, das der RDBER im Hinblick auf die Nutzbarmachung bioelektrochemischer Systeme besitzt, kann durch eine Optimierung der Reaktorarchitektur sicherlich signifikant gesteigert werden.

Publications

Shylaja Prakash, N., Maurer, P., Horn, H., Hille-Reichel, A., 2024. Valorization of organic carbon in primary sludge via semi-continuous dark fermentation: First step to establish a wastewater biorefinery. Bioresour. Technol. 397, 130467. https://doi.org/10.1016/j.biortech.2024.130467

Shylaja Prakash, N., Maurer, P., Horn, H., Saravia, F., Hille-Reichel, A., 2025. Separation of Short-Chain Fatty Acids from Primary Sludge into a Particle-Free Permeate by Coupling Chamber Filter-Press and Cross-Flow Microfiltration: Optimization, Semi-Continuous Operation, and Evaluation. Membranes 15, 1–21. https://doi.org/10.3390/membranes15010022

Shylaja Prakash, N., Maurer, P., Horn, H., Saravia, F., Hille-Reichel, A., 2024. Coupling dark fermentation and membrane separation methods to extract organic acids from the solids stream of municipal wastewater at pilot-scale: A sustainable approach towards establishing a biorefinery. Poster at 19th IWA Leading Edge Conference on Water and Wastewater Technologies

Shylaja Prakash, N., Neske, W., Rümenapf, M., Xiao, Z., Netsch, A., Horn, H., Ullmann, J., Reiner, J.E., Hille-Reichel, A., 2025. Evaluation of a novel pilot-scale rotating disk bioelectrochemical reactor for hydrogen production in a wastewater biorefinery. Chemical Engineering Journal (under review)

List of contents

Nomenclature

Abbreviations

AA or HAc	acetic acid
BA or HBu	butyric acid
BA-iso or HBu-iso	iso-butyric acid
BES	bioelectrochemical system
COD	chemical oxygen demand
EtOH	ethanol
f_{DOC}	fraction of dissolved organic carbon as short-chain fatty acids
HRT	hydraulic retention time
HPAS	hydroxypropyl trimethyl ammonium starch
MEC	microbial electrolysis cell
OCT	optical coherence tomography
OLR	organic loading rate
OP	operation phase
PA or HPr	propionic acid
PHA	polyhydroxyalkanoates
POC	particulate organic carbon
PS	primary sludge
RDBER	rotating disk bioelectrochemical reactor
sCOD	soluble chemical oxygen demand
SCFAs	short-chain fatty acids
SHE	standard hydrogen electrode
tSCFAs	total short-chain fatty acids
TKN	total kjeldahl nitrogen
TOC	total organic carbon

TP	total phosphorus
TS	total solids
VA or HVa	valeric acid
VA-iso or HVa-iso	iso-valeric acid
VS	volatile solids
WWBr	wastewater biorefinery
WWTP	wastewater treatment plant

Symbols

AA or HAc	acetic acid ($mg \cdot L^{-1}$)
A_{anode}	area of anode (m^2)
A_{CS}	cross-sectional area (m^2)
$A_{polygon}$	area of polygon (-)
$A_{polygon,tot}$	total area of a polygon (-)
$A_{polygon,uncovered}$	uncovered area of polygon (-)
$A_{specific}$	specific area (m^2)
$A_{uncovered}$	area of uncovered substratum (μm^2)
A_{eff}	effective filtration area of membrane (m^2)
BA_{eff}	effective biofilm area (m^2)
BA or HBu	butyric acid ($mg \cdot L^{-1}$)
BA-iso or HBu-iso	iso-butyric acid ($mg \cdot L^{-1}$)
BV	biovolume ($\mu m^3 \cdot \mu m^{-2}$)
CE	coulombic efficiency (%)
COD	chemical oxygen demand ($mg \cdot L^{-1}$)
D_b	dry biomass (g)
$d_{channel}$	hydraulic diameter of the channel (m)
D_{HPAS}	dosage of hydroxypropyl trimethyl ammonium starch (mg HPAS per g TS)

d_{pore}	diameter of the pores (m)
$\Delta_{R_T}(v_{cf})$	relative change of total resistance (-)
$E_{anode,\,app}$	applied potential at the anode (mV)
EtOH	ethanol (mg·L^{-1})
F	faraday's constant (C·mol^{-1})
f_D	Darcy's friction factor (-)
g	acceleration due to gravity (m·s^{-2})
H	height (m)
H_{outlet}	height at the outlet (m)
H_{inlet}	height at the inlet (m)
HRT	hydraulic retention time (d)
I	current (mA)
J	current density (mA·m^{-2})
J_{CW}	standardized clean water flux (L·m^{-2}·h^{-1} or LMH)
J_{std}	standardized permeate flux (L·m^{-2}·h^{-1} or LMH)
L	length of channel or module (m)
m_N	normalized biomass (g·m^{-2})
N	number of anode disks (-)
n	number of vertices (-)
n_{e^-}	number of electrons (-)
OLR	organic loading rate (g$_{VS}$·L$_{reactor}$$^{-1}$·d^{-1})
μ	dynamic viscosity (N·s·m^{-2})
PA or HPr	propionic acid (mg·L^{-1})
Q_{CF}	cross-flow rate (m^3·h^{-1})
$Q_{permeate}$	permeate flow rate (L·h^{-1})
R_f	fouling resistance (m^{-1})

Re	Reynold's number (-)
R_m	intrinsic membrane resistance (m^{-1})
rpm	rotation per minute (-)
Rec_{SCFAs}	recovery of short-chain fatty acids (%)
R_T	total resistance (m^{-1})
$R_{T,v_{cf,final}}$	total resistance at the highest cross-flow velocity (m^{-1})
$R_{T,v_{cf,max}}$	maximum total resistance at the highest cross-flow velocity (m^{-1})
R_x	retention of a specific parameter (%)
SC	substrate coverage (%)
SC_{eff}	effective surface coverage (%)
sCOD	soluble chemical oxygen demand ($mg·L^{-1}$)
SCFAs	short-chain fatty acids ($mg·L^{-1}$)
ρ	density of water ($kg·m^{-3}$)
TKN	total kjeldahl nitrogen ($mg·L^{-1}$)
TMP	transmembrane pressure (bar or $N·m^{-2}$)
TOC	total organic carbon ($mg·L^{-1}$ or $g·L^{-1}$)
TP	total phosphorus ($mg·L^{-1}$ or $g·L^{-1}$)
TS	total solids ($mg·L^{-1}$ or $g·L^{-1}$)
tSCFAs	total short-chain fatty acids ($mg·L^{-1}$)
VA or HVa	valeric acid ($mg·L^{-1}$)
VA-iso or HVa-iso	iso-valeric acid ($mg·L^{-1}$)
VS	volatile solids ($mg·L^{-1}$ or $g·L^{-1}$)
V_B	biofilm volume (μm^3)
v_{cf}	cross-flow velocity ($m·s^{-1}$)
V_{rec}	volume recovery (%)
V_W	working volume (L)

Y_{SCFAs} yield of short-chain fatty acids ($mg_{SCFAs} \cdot g$)

Y_{VS} yield of short-chain fatty acids with respect to volatile solids ($mg_{SCFAs} \cdot g_{VS}$)

1   Introduction and motivation

The "use and dispose" strategy in a linear economy has led to an excessive consumption of fossil fuels, the primary reason for high pollution levels and climate change. The shift towards a circular economy is seen as a critical path to achieving environmental sustainability in the 21st century, addressing the overuse of non-renewable resources (Atasoy et al., 2018). The transition from a linear to a circular model focuses on turning waste streams into valuable, marketable products through economically viable processes (Moretto et al., 2020). This concept aims to reduce dependency on fossil fuels and other non-renewable feedstocks while minimizing waste and pollution. A circular economy can significantly reduce environmental impact when marketable products from waste are "green", meaning they are sustainable, create less waste, and can potentially replace conventional products produced from non-renewable resources (Andersen et al., 2018). Such innovations not only help mitigate resource depletion but also play a crucial role in lowering overall greenhouse gas emissions (Andersen et al., 2018). Researchers have emphasized the importance of this model (Crutchik et al., 2018; Da Ros et al., 2020), and according to the European Union, shifting from fossil-fuel-based resources to bio-based alternatives could lead to a reduction of up to 2.5 billion tons of CO_2-equivalents annually by 2030 (European Commission, 2015).This underscores the potential for circular economy strategies to make a substantial impact on climate goals.

Wastewater generated from urban areas, i.e. municipal wastewater, is supposedly an untapped waste stream whose potential needs careful consideration within the context of a circular economy. This is due to the fact that municipal wastewater contains valuable organic pollutant loads, and typical wastewater treatment plants (WWTP) aim at removing them and partly recovering them. For instance, organic carbon is partly removed in the main stream via aerobic oxidation in the conventional activated sludge process and partly recovered in the sludge stream via anaerobic digestion in the form of a combustible fuel, i.e. biogas. Indeed, biogas has already been shown to be an effective source for electrical and thermal energy, and can also be used within a WWTP for self-sustainability. However, the possibility to generate value-added products that hold a higher value than biogas in the market, demands a better utilization of organic carbon. In addition, the combustion of biogas releases around 0.1 kg $CO_2 \cdot m^{-3}_{wastewater}$ which contributes to around 25 to 30 % of the total CO_2 emissions from a conventional WWTP (Campos et al., 2016). Hence, recovering value-added products can also reduce CO_2 emissions due to combustion, and since the load of organic carbon processed in anaerobic digestion is reduced as a certain portion is recovered, there is direct reduction in sludge disposal costs as well.

The idea of capitalizing on pollutant loads to generate value-added products from the sludge stream of a WWTP is referred to as a wastewater biorefinery (WWBr). **Figure 1.1** shows two scenarios, one for WWTP and the other for WWBr. Around 60 % of the influent organic carbon load is collected as sludge in a municipal WWTP, which includes both primary sludge and excess sludge (see **Figure 1.1**). Approximately 30 % of influent organic carbon is recovered as biogas which typically comprises of 60 % methane and 40 % carbon dioxide (Wan et al., 2016). Biogas production occurs via anaerobic digestion, during which complex organic substrates are broken down in several steps into methane and carbon dioxide. Short-chain fatty acids (SCFAs) are metabolic intermediates during anaerobic fermentation of organic carbon-enriched-sludge. The possibility to control methanation, while enhancing the accumulation of SCFAs provides a pathway towards valorization. The question of feasibility for a WWBr lies in the fact of how much organic carbon can be recovered as SCFAs in a usable form. In this study, focus is directed at valorizing the organic carbon content in primary sludge.
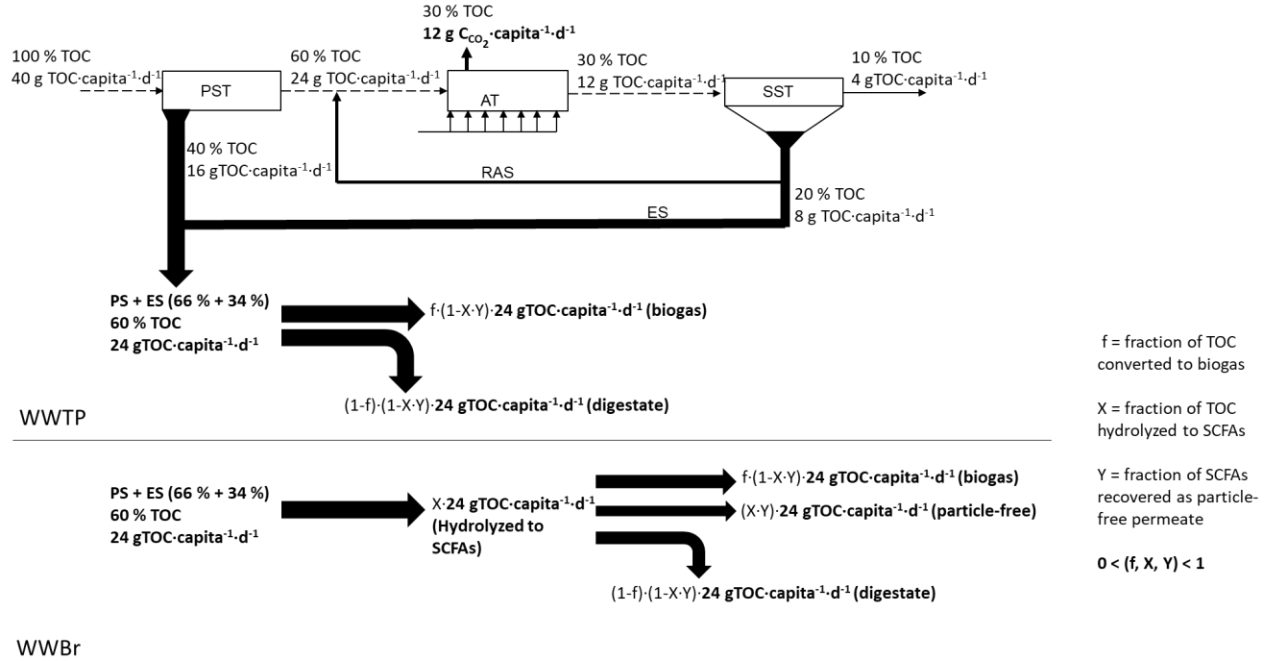
Figure 1.1: Schematic representation of the organic carbon load in a wastewater treatment plant (WWTP) and a wastewater biorefinery (WWBr). The value of f ranges between 0.5 to 0.6 (Wan et al., 2016). X and Y are zero for WWTP. The values of TOC are modified based on Wan et al., 2016. (PST = Primary sedimentation tank, AT = Aeration tank, RAS = Return activated sludge, SST = Secondary sedimentation tank, ES = Excess sludge, TOC = Total organic carbon).

1.1   Dark fermentation – A pathway to ferment short-chain fatty acids

Primary sludge generated via mechanical separation of wastewater after screening and grit chamber in a primary sedimentation tank is rich in organic content due to the presence of faeces, vegetables, fruits, textiles, paper, etc. (Ruiken et al., 2013; Yuan et al., 2006). A significant fraction of these organic carbon compounds in primary sludge is easily degradable (Yuan et al., 2010), and anaerobic digestion offers a simple but effective way to treat such a substrate. The presence of an existing anaerobic microbial consortium along with a high organic carbon concentration in primary sludge makes it a source for both, substrate and inoculum. The process of anaerobic digestion involves several groups of anaerobic microorganisms performing complex reduction-oxidation processes (see **Figure 1.2B**), and is typically described by four steps (Sikora et al., 2017), 1) hydrolysis: breakdown of complex macromolecules into simpler low-molecular-weight compounds, 2) acidogenesis: simpler organic molecules are further broken down into low-molecular-weight fatty acids (i.e., short-chain fatty acids (SCFAs)) along with hydrogen (H_2) and carbon dioxide (CO_2), 3) acetogenesis: further degradation of SCFAs into acetate, H_2 and CO_2, and 4) methanogenesis: acetate is used as substrate in acetoclastic methanogenesis for production of CH_4 and CO_2, whereas H_2 and CO_2 are used as substrates for production of CH_4 via hydrogenotrophic methanogenesis. The final two steps occur due to a syntrophic relationship between the respective microbes, as the process itself is thermodynamically unfavorable (Sikora et al., 2017).

Each step is governed by the growth of different groups of microbes, and advantageously, the growth rate of the microorganisms can be capitalized to optimize anaerobic digestion. It is known that anaerobic digestion is a slow process, requiring about 20 to 30 days for biogas production, due to the slow growth of methanogens. In contrast, hydrolysis and acidogenesis occur at a relatively faster rate. This offers a window

to capture or accumulate SCFAs, before they are used up for methanation. The process of controlling methanation, while accumulating SCFAs is known as dark fermentation. **Figure 1.2A** shows a hypothetical scenario describing the occurrence of each step in a batch mode eventually leading to the production of biogas.

SCFAs generated during the acidogenic phase of primary sludge digestion have chain lengths varying from C2 to C5, with acetic and propionic acid being predominant (Da Ros et al., 2020; Wu et al., 2010, 2009). Linear and branched forms of butyric and valeric acids are also formed during this phase. The fermentation of SCFAs by acidogenic bacteria has been shown to often occur through the pyruvate pathway (see **Figure 1.2B**), but the proportion of individual SCFAs is dependent on factors like substrate and specific microbial population (Nagarajan et al., 2022). The organic substrate or macromolecules in primary sludge can be classified as proteins, carbohydrates and lipids. Although primary sludge is inhabited by a diverse microbial community, a large proportion of the microorganisms have been shown to ferment on macromolecules to produce a mixture of SCFAs (Huang et al., 2021). During acidogenesis, acetic acid is produced the most as it´s formation offers the highest energy yield, while butyric and propionic acids are produced to maintain a low hydrogen partial pressure (Mosey, 1983). There are several factors that require careful consideration to optimize dark fermentation with a few being crucial, 1) hydraulic retention time (HRT), 2) pH-value, 3) temperature, and 4) organic loading rate (OLR). It is important to note that these parameters are interdependent and optimization has to be carried out in a way that enhances SCFAs production while also considering the effect on downstream process steps and economical aspects. **Table 1** shows a comparison of high performing reactors at different conditions.
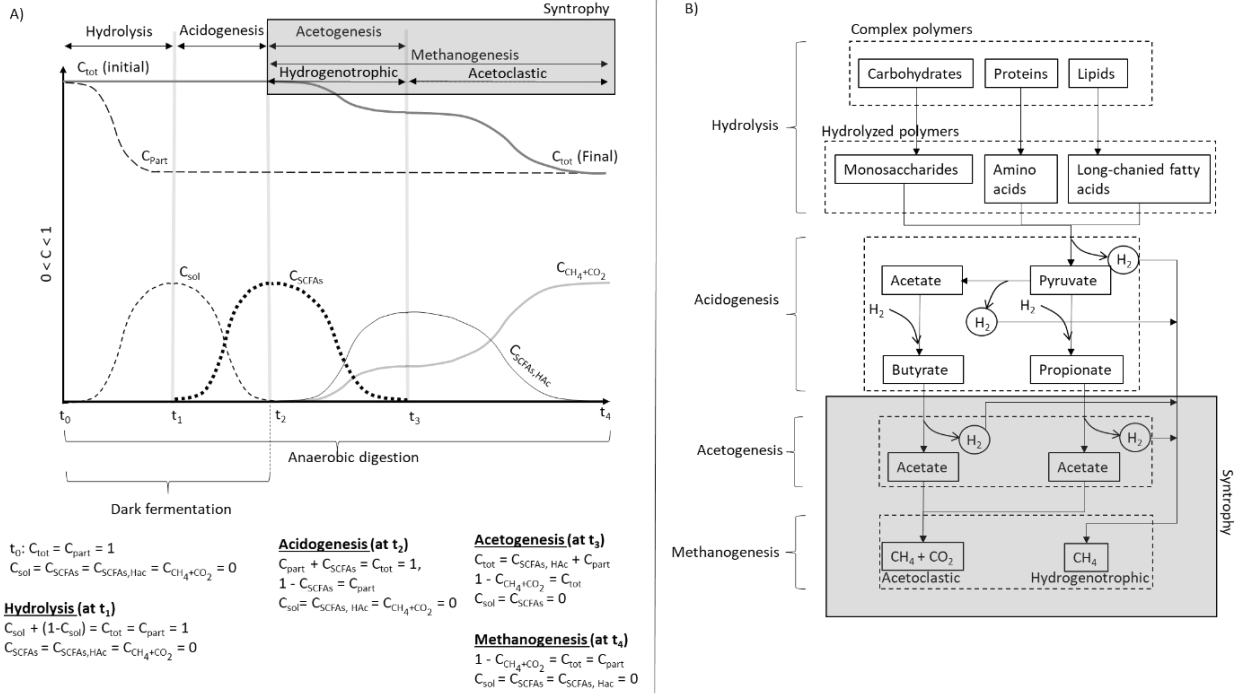
Figure 1.2: A) Hypothetical carbon balance (substrate production and consumption) during different steps in anaerobic digestion (batch mode) adapted from Calise et al., 2020. C_{part} = particulate organic carbon, C_{sol} = dissolved organic carbon, C_{Tot} = total organic carbon, C_{SCFAs} = carbon equivalents of SCFAs (during acidogenesis), $C_{SCFAs,HAc}$= carbon equivalents of acetic acid (HAc) during acetogenesis, and $C_{CH_4+CO_2}$ = carbon content in methane and carbon dioxide.

Note: substrate production and consumption are subject to significant differences under real conditions. B) The four main stages of anaerobic digestion (adapted from Mosey, 1983).

HRT plays a very important role in the performance of dark fermentation of primary sludge, and several studies have shown that HRTs are required in the range of 1 to 6 days to increase yields of SCFAs (Crutchik et al., 2018; Da Ros et al., 2020; Eastman & Ferguson, 1981; Miron et al., 1999; Canziani et al., 1995). The selection criteria for HRT is crucial in enhancing the acidogenic phase while minimizing methanation, but it is also dependent on the pH used at fixed HRTs. Alkaline pH-values are advantageous in solubilizing the particulate organic matter, but there is a requirement of longer adaptation periods, and hence longer HRTs (Wu et al., 2010, 2009). When working in a near-neutral to neutral range, a plateau of maximum production is reached at a much earlier stage, requiring relatively lower HRTs (Eastman & Ferguson, 1981; Miron et al., 1999; Canziani et al., 1995). At lab-scale and an HRT of 1.5 days, Eastman & Ferguson, 1981 achieved higher yields of 377 $mg_{SCFAs, COD} \cdot g_{VS}^{-1}$ at pH 6.7 which was 80 % higher than what Wang et al., 2021 at a similar scale at pH 9.5 and HRT of 5 days (see **Table 1.1**). At a similar scale, Miron et al., 1999 at pH 5, 25 °C and a low range of HRTs had yields close to Pittmann & Steinmetz, 2013 at pH 6 and 30 °C. At pilot-scale (within the surveyed literature), Da Ros et al., 2020 and Ossiansson et al., 2023 realized higher values in comparison to Christensen et al., 2022, and it is suspected that a better mixing due to stirrers or pumps in the former studies may have had a notable impact as there is not a clear description whether a proper mixing was conducted in the latter. Nonetheless, there are considerable advantages when working with shorter HRTs and neutral pH-values in terms of smaller reactor volume and lower chemical costs.

OLR is a vital parameter as dark fermentation employs much higher OLRs in comparison to anaerobic digestion as HRT is much lower in dark fermentation. OLR is a function of both HRT and the substrate concentration. The former is a fixed physical parameter, while the latter is subjected to considerable fluctuations due to seasonal and daily variations. Therefore, there is a risk in terms of extremely high or low sludge loading periods as influent wastewater is susceptible to varying suspended solids load, and this results in a direct effect on concentration of solids (substrate) in primary sludge. Therefore, at fixed HRTs, a high or low solids load could have a direct impact on dark fermentation. Dark fermentation can be enhanced by maintaining an optimum OLR (Pandey et al., 2022; Skalsky and Daigger, 1995), and during periods of low load or high solids load, the inflow rate can be adjusted in such a way that this period of loading can be maintained constant.

Table 1.1: Literature survey of yields of SCFAs on primary sludge carried out in semi-continuous or continuous mode

Reactor volume (L)	OLR ($gv_S \cdot L^{-1} \cdot d^{-1}$)	HRT (d)	pH	T (°C)	Yield of SCFAs ($mg_{SCFAs, COD} \cdot gv_S^{-1}$)	Yield of SCFAs ($mg_{SCFAs} \cdot gv_S^{-1}$)	Yield of SCFAs (%)	Literature
1500	8 ± 1	5	5.2	28*	250*	-	-	Ossiansson et al., 2023
2600	8	6	9[a] to 4.9	37	322 ± 56	-	-	Da Ros et al., 2020
5	-	5	9.5	36 ± 1	209	-	-	Wang et al., 2021
15	-	6	6	30	-	-	22	Pittmann & Steinmetz, 2013
3000	14	3	7	35	-	42	-	Christensen et al., 2022
2.5	18[b]	1.5	6.7	35	377	-	-	Eastman & Ferguson, 1981
5	5 to 2	3 to 8	5	25 ± 1	-	-	18	Miron et al., 1999

* the value is approximate, [a] pH-value was controlled at the start of the process, [b] OLR is in terms of volatile suspended solids

The pH-value used in dark fermentation has a strong impact on the performance of dark fermentation. A main aspect of pH-value is the resulting abundance of specific microbial communities or change in metabolic pathways within the same community which directly affects the fermentation products, i.e., SCFAs (Horiuchi et al., 2002). In addition to the biological effect, alkaline pH ranges can also have a physicochemical effect by aiding the acidogenic process through improved hydrolysis (Wu et al., 2010). For instance, the higher concentration of OH^- ions can breakdown peptide bonds in complex proteins resulting in the formation of free amino acids that can be used up easily by the acidogenic bacteria (Dahiya et al., 2015). However, this comes at a cost of longer adaptation periods as mentioned earlier, requiring longer HRTs. pH-values are also known to affect the redox conditions of the system. A redox environment, driven by the equilibrium between NADH and NAD^+, can determine the production of different SCFAs (Mosey, 1983).

Temperature generally has a notable impact on reaction rates, and it is known that higher temperature increases reaction rates following the van´t Hoff´s rule. Other than this physical effect, temperature has a significant effect on the microbiology. It has been well established that temperature is a decisive factor leading to selective abundance of specific bacteria, which can directly influence the production of fermentation products (Huang et al., 2021; Ossiansson et al., 2023). In case of sludge fermentation, mesophilic temperatures are commonly chosen as there is a decline in acidogenesis at a thermophilic range even though hydrolysis can be improved (Li et al., 2014).

Figure 1.3 shows an example of a complete shift in microbial community composition in hydrolyzed primary sludge in comparison to raw primary sludge at different pH and temperature values. In addition, there is also a significant difference in fraction of SCFAs after hydrolysis in comparison to primary sludge, specifically acetic, propionic and butyric acids (**Figure 1.3B**), while other SCFAs are also detected in

notable concentrations. The spectrum of bacteria detected in primary sludge is narrow, but in case of hydrolyzed primary sludge, there is a wider spectrum, with a significant fraction of them having a relative abundance of less than 2 % (shown as others in **Figure 1.3A**). This clearly shows the importance to control pH and temperature to maintain a specific microbial community that can sustain steady fermentation of SCFAs during dark fermentation.
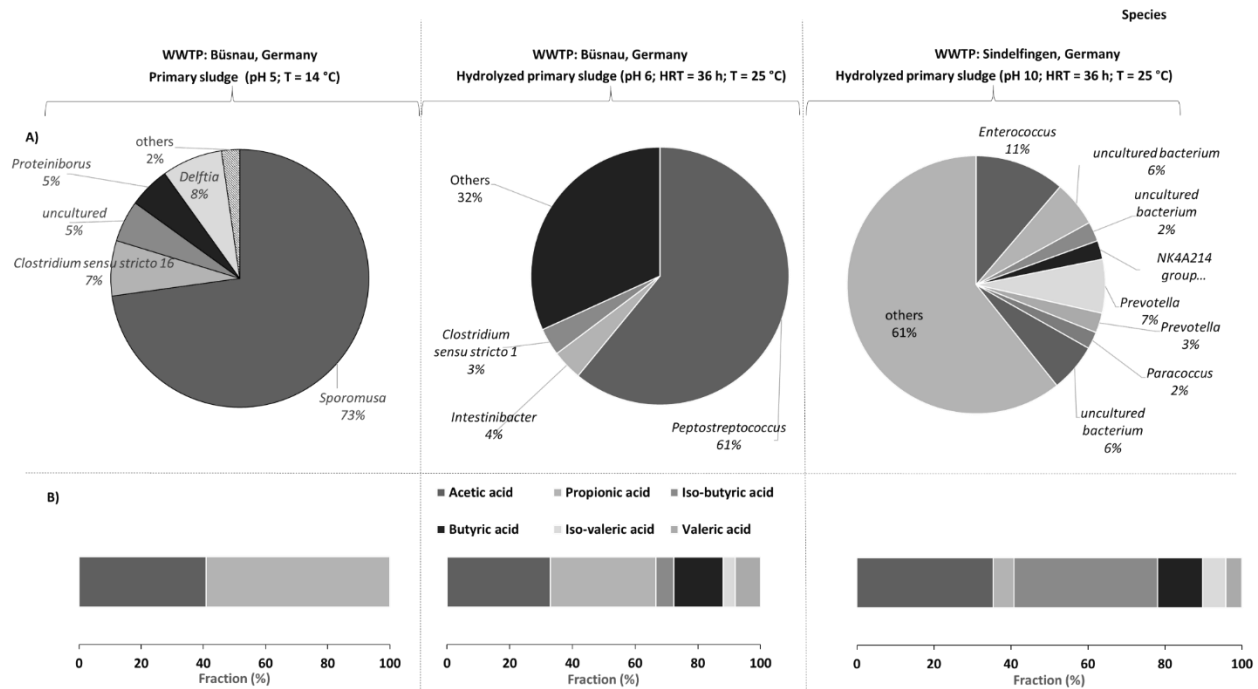
Figure 1.3: A) Relative abundance of genera, B) fraction of SCFAs, and concentration of SCFAs in primary sludge and hydrolyzed primary sludge at different pH-values and temperatures. Note: Relative abundance less than 2 % are classified as "others".

1.2   Solids separation – Production of a particle-free stream

The process of dark fermentation can provide a hydrolyzate with a sizeable concentration of SCFAs. However, this concentration of SCFAs is present along with a very high solids concentration similar to that of the primary sludge itself, as the amount of solids (i.e., volatile solids) removed during dark fermentation is very low. The latter is dependent on the amount of biogas produced, as carbon is only volatilized from the fermentation broth as methane and/or CO_2. Since HRT is kept short, methanogens are washed out (see **Figure 1.2A**) and the production of gas is very low. This means that the concentration of suspended particles present is very high and the hydrolyzate cannot be directly processed in biotechnological applications. It is also important to consider the diverse microbial community present in hydrolyzed sludge (Huang et al., 2017), which can interfere with downstream recovery processes. In their pilot-scale study on polyhydroxyalkanoates (PHA) accumulation using mixed cultures from industrial wastewater, Tamis et al. (2014) clearly outlined the importance of having a suspended solids-free substrate for better PHA yields. The authors also highlighted the reduction on PHA yields caused by organisms that are incapable of storing PHAs which can limit susbtrate availability for PHA accumulating organisms. Similarly, another pilot-scale study described that higher PHA yields could be achieved with a particle-free wastewater (Ntaikou et al., 2014). In case of biohydrogen production using microbial electrolysis cells, growth of methanogens has shown to compromise the overall hydrogen recovery process (Cusick et al., 2011; Rivera et al., 2015). The

interferences caused by particles or microorganisms in sludge can be tackled by implementing membrane technology.

Particle separation can be achieved using low-pressure filtration techniques like microfiltration and ultrafiltration, which offer significant energy savings. These processes typically require pressures in the range of 1 to 5 bars (Obotey Ezugbe and Rathilal, 2020). Microfiltration is particularly advantageous, as it enables the separation of low-molecular-weight compounds from particulate waste streams via a size-sieving mechanism (Cho et al., 2012). Microfiltration can be operated in two main modes: dead-end and cross-flow. In dead-end filtration, the entire feedwater volume passes through the membrane, with particles larger than the membrane pores being retained on or within the membrane (Roorda, 2004). The flow is perpendicular to the membrane, causing particle accumulation and forming a cake layer that increases flow resistance (see R_f in **Figure 1.4A**), leading to a gradual decline in permeate flux (as shown by $J_{permeate}$ in **Figure 1.4A**). Frequent backwashing and chemical cleaning are required to mitigate fouling and restore system performance (Kennedy et al., 2001). In cross-flow filtration, only part of the feed passes through the membrane, while the rest flows parallel to the membrane surface (**Figure 1.4A**). The tangential flow creates shear forces that prevent a steady buildup of the cake layer by detaching particles from the membrane surface, thus, this mode offers the advantage of higher permeate flux due to reduced fouling. An equilibrium is established between particle deposition and removal, resulting in a relatively stable permeate flow (Aspelund, 2010; Song and Elimelech, 1995).
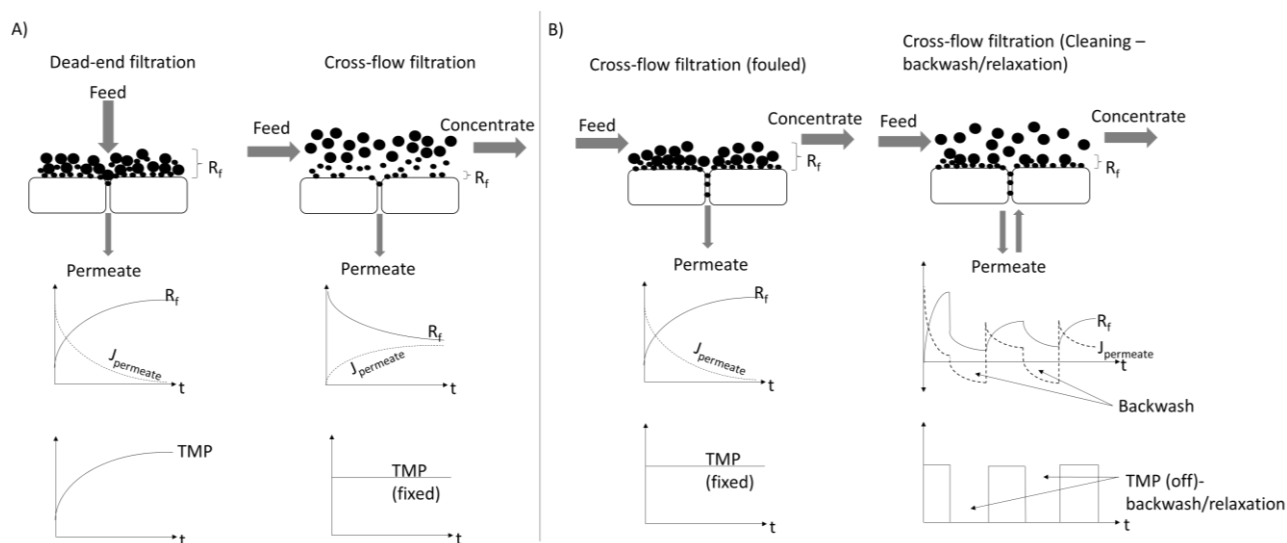
Figure 1.4: A) Two basic modes of microfiltration, dead-end mode and cross-flow mode and B) Physical cleaning methods, backwashing and relaxation after fouling to recover flux. Note: TMP = transmembrane pressure, R_f = fouling resistance, $J_{permeate}$ = permeate flux.

The choice of membrane material is critical and depends on the type of wastewater being treated. Membrane materials are broadly classified as organic or inorganic. Common commercial organic membranes are made from polymers such as polyethersulfone (PES), polyvinylidene fluoride (PVDF), polyacrylonitrile (PAN), polysulfone (PS), and polyvinyl chloride (PVC) (G. Fan et al., 2016). Polymeric membranes are generally less expensive and more compact than inorganic ones (Sutton-Sharp et al., 2018). In contrast, inorganic membranes, typically ceramic, include materials like alumina (Al_2O_3), zirconia (ZrO_2), and titania (TiO_2) (Issaoui and Limousy, 2018). Ceramic membranes offer several advantages over polymeric ones, such as a

narrower pore size distribution, higher porosity, better mechanical and chemical stability, and increased hydrophilicity, leading to higher fluxes at low pressures and reduced fouling (Hofs et al., 2011).

In membrane-based water treatment, two major challenges arise: ensuring water quality by effectively rejecting targeted solutes and managing membrane fouling, which otherwise dramatically reduces the efficiency of filtration (Fan et al., 2002). Fouling, characterized by a decline in permeate flux or an increase in transmembrane pressure (TMP) over time, can be either reversible or irreversible (Bick et al., 2007). The irreversible fouling, which cannot be fully undone by hydraulic cleaning, poses the greatest long-term problem (Jones and O'Melia, 2000). Membrane fouling can occur due to various factors, including the deposition of aggregated particles, adsorption, biofouling, and the precipitation of small particles within membrane pores (Jones and O'Melia, 2000). Larger particulate matter typically forms a cake on the membrane surface, while smaller dissolved matter can penetrate and clog pores, contributing to fouling by reducing pore size or complete pore blocking (Howe & Clark, 2002). Guo et al. (2012) categorized membrane foulants into four groups:

1) Particulates: Fouling by particulates or colloids begins with pore blocking, followed by cake formation. Colloids near the size of the membrane pores block the pores, while larger particles form a cake on top of the membrane surface that can be more easily removed (Huang et al., 2008; Lim & Bai, 2003).

2) Organic fouling: This type of fouling is caused by natural organic matter (NOM), proteins, and polysaccharides. These substances can adsorb onto the membrane surface, block pores, or form a gel or cake layer, leading to a decline in flux (Costa et al., 2006; Zhang et al., 2015).

3) Inorganic fouling: Inorganic compounds cause fouling when they precipitate on the membrane, a process known as scaling. Low-solubility compounds like calcium carbonate, barium sulfate, silica, and calcium phosphate are commonly responsible for inorganic fouling (Van De Lisdonk et al., 2000).

4) Biofouling: Biofilms form when bacteria adhere to the membrane surface, secreting extracellular polymeric substances (EPS) in which they become embedded. These biofilms are difficult to remove and significantly contribute to membrane fouling (Chamberland et al., 2017; Flemming, 1997).

Fouling can be minimized by employing appropriate physical and chemical cleaning methods. Common physical cleaning methods include relaxation and backwashing. These methods are valid for cross-flow microfiltration, as dead-end filtration requires cleaning-out-off-place techniques for flux recovery. Nevertheless, cross-flow filtration works under an applied pressure, and during relaxation, the pressure is released for a certain duration, during which the cross-flow is able to scour off foulants that are loosely attached to the cake layer (see **Figure 1.4B**). In backwashing, the flow of the permeate is reversed through the pores of the membrane (Gul et al., 2021). Detachable foulants in the pores and in the cake layer are briefly transported to the bulk phase, where the cross-flow velocity can transport them away as concentrate (**Figure 1.4B**). It is important to remember that these methods may be effective against reversible fouling, but in case of irreversible fouling, appropriate chemical cleaning is necessary. Chemical cleaning is dependent on the type of foulant present, and for a substrate like wastewater (characterized by proteins, carbohydrates and lipids), organic and biological fouling is predominant. Therefore, alkaline agents like

sodium hydroxide and sodium hypochlorite, and strong oxidizing agents like hydrogen peroxide have been shown to be effective for hydrolysis and oxidation of organic compounds (Holman and Ohlinger, 2007).

Other than fouling and its control, the selection of pore size is also a crucial factor as it is important to allow only the dissolved compounds to pass through. Typically, the size range of microfiltration membranes can vary between 0.1 and 10 µm (Samanta et al., 2022). Tuczinski et al., 2018 showed an optimum membrane cut-off of 0.2 µm, as the particles can be separated from SCFAs. Nevertheless, the authors demonstrated that microfiltration membranes can reject up to 15 % of SCFAs (within a cut-off range of 0.1 to 0.8 µm) due to their adsorption to particles. Similarly, Samanta et al. (2022) also observed that dissolved organic compounds could be retained by a 0.2 µm ceramic membrane up to 20 % due to the presence of high concentrations of suspended solids. Therefore, a similar filtration method, but with a larger pore size is necessary as pre-treatment to sieve off larger particles (see **Figure 1.5**) and reduce the suspended solids load on microfiltration, and eventually reduce the loss of valuable dissolved organic compounds.
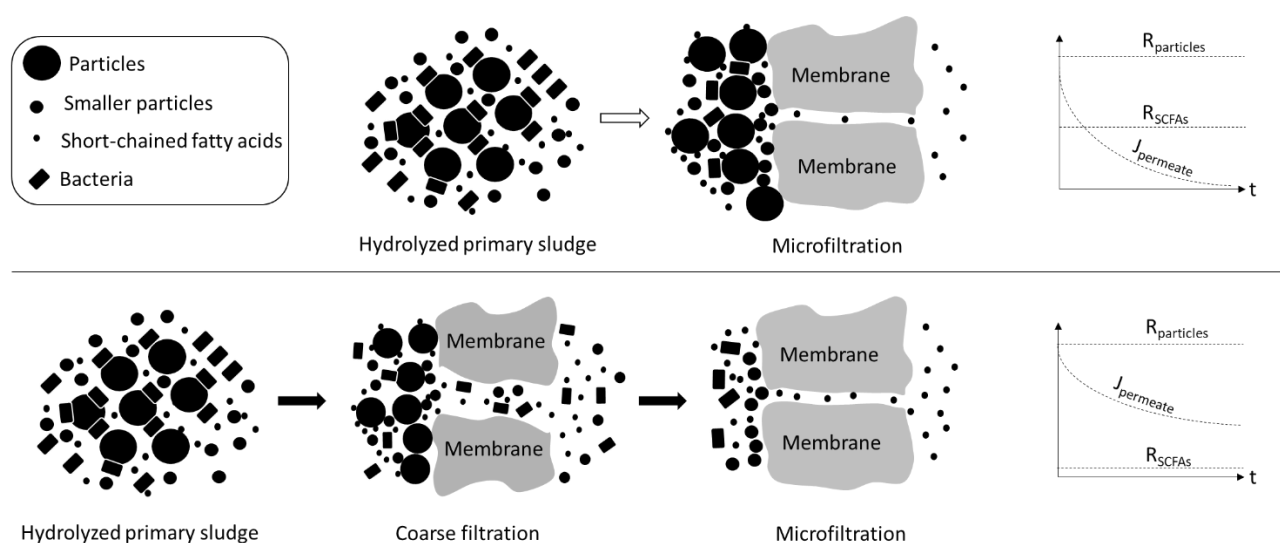
Figure 1.5: Treatment of hydrolyzed primary sludge. The upper figure indicates direct treatment with a microfiltration membrane which results in rapid fouling, flux decline and retention of SCFAs. The lower figure indicates the use of a pre-treatment step with a larger pore size to sieve off larger particles resulting in a reduced load of particles on the final microfiltration step. This results in a low retention of SCFAs along with a higher flux. Note: R denotes retention, $J_{permeate}$ denotes flux.

1.3 Terminal treatment step – Waste to chemical energy carrier

The particle-free stream containing SCFAs after membrane filtration can serve as a valuable precursor for recovery of value-added products. Biofuels, platform chemicals and bioplastics are some bio-based products that can be generated from SCFAs-streams. It is well known that biogas is produced during anaerobic digestion of sludge in a WWTP. However, the possibility of generating a biofuel like hydrogen is more interesting, specifically due to its green nature (Wong et al., 2014).

Bioelectrochemical systems (BES), more specifically microbial electrolysis cells (MEC) pave the way to efficiently harvest biohydrogen from waste streams containing SCFAs. MECs are characterized by two electrodes, an anode and a cathode, separated by an electrolyte. Electroactive microorganisms are able to form a biofilm on the surface of the anode that can convert chemical energy in the organic compounds into electrical energy (Fudge et al., 2021). In other words, electroactive microorganisms can oxidize SCFAs to

generate electrons which are released to the anode, whereas protons and CO_2 are released into the aqueous electrolyte (**Figure 1.6**). The electrons migrate through a conductive material to the cathode, where protons are reduced (by the electrons) after passing through the aqueous electrolyte to the cathode, producing biohydrogen (Kehrein et al., 2020).
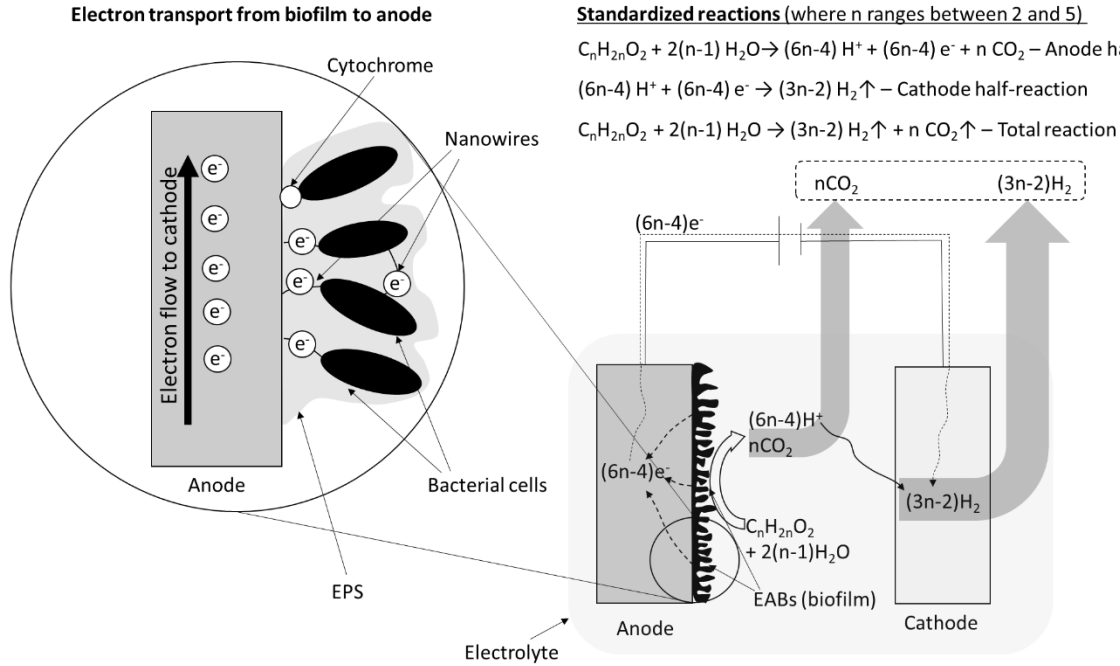
Figure 1.6: Mechanism of hydrogen production using electroactive microorganisms in a microbial electrolysis cell. The mechanism of electron transfer was adapted from Hazzan et al., 2023; Hu et al., 2022. **Note:** EPS indicates extracellular polymeric substances, EAB indicates electroactive bacteria. $C_nH_{2n}O_2$ represents the general formula for SCFAs, where n ranges between 2 and 5 (SCFAs have chain lengths varying from C2 to C5).

Electroactive microorganisms, for instance, Geobacter sp. can utilize solid electrodes (in the absence of soluble electron acceptors) poised at an oxidative potential to transfer electrons via extracellular electron transfer from an easily degradable carbon source, like SCFAs (see **Figure 1.6**), to generate an anodic current (Kitching et al., 2017). The working principle of an MEC is comparable to water electrolysis, but MECs offer the advantage of requiring significantly less external energy input. For example, the anode potential produced from the oxidation of a degradable carbon source like acetate is approximately -300 mV (versus the standard hydrogen electrode, SHE), while the reversible potential of the H^+/H_2 redox couple is around -414 mV. This results in a minimum theoretical voltage of 114 mV necessary for hydrogen evolution at the cathode—substantially lower than the 1.6–2 V typically needed for conventional water electrolysis (Villano et al., 2011).

$C_2H_4O_2 + 2\ H_2O \rightarrow 8\ H^+ + 8\ e^- + 2\ CO_2\ (E^0 = -0.28\ V\ vs\ SHE)$ – Anode half-reaction   1.1

$8\ H^+ + 8\ e^- \rightarrow 4\ H_2{\uparrow}\ (E^0 = -0.42\ V\ vs\ SHE)$ – Cathode half-reaction   1.2

$C_2H_4O_2 + 2\ H_2O \rightarrow 4\ H_2{\uparrow} + 2\ CO_2{\uparrow}(E^0 = -0.114\ V\ vs\ SHE)$ – Total reaction   1.3
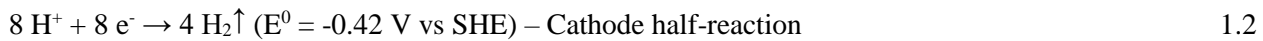
1.4   Thesis Structure

This dissertation deals with the treatment of primary sludge as a potential source to recover value-added products. The dissertation can be classified into four major chapters.

Chapter 2: Optimization of dark fermentation of primary sludge at lab-scale, bench-scale, and pilot-scale to evaluate the yields of short-chain fatty acids. Parameters tested include pH, temperature, and hydraulic retention time in batch and semi-continuous modes.

Chapter 3: Evaluating the effect of pressure loss in tubular cross-flow microfiltration. Determining a method to optimize cross-flow velocity for microfiltration of dewatered hydrolyzed primary sludge under the influence of pressure loss.

Chapter 4: The optimized conditions from **chapter 2** were used to run a pilot-scale dark fermentation reactor to produce short-chain fatty acids which are separated using a combination of chamber filter-press and microfiltration to produce a particle-free substrate. The study focuses on determining optimum dosage of flocculants for efficient dewatering, and the subsequent solids removal efficiencies. Additionally, the mechanism of fouling of microfiltration and the appropriate cleaning method to maintain stable filtration through long-term experimentation is extensively discussed.

Chapter 5: A novel 100-L rotating disk bioelectrochemical reactor as a potential terminal treatment step for recovering hydrogen out of the particle-free short-chain fatty acids stream obtained in **chapter 4**. Monoseptic conditions and unsterile conditions were experimented, and operating conditions such as anode disk rotation speed, electrical conductivity, and applied anode potential are discussed. Additionally, the distribution of biofilm on the anode disks and along the reactor length is evaluated

2 Valorization of organic carbon in primary sludge via semi-continuous dark fermentation: First step to establish a wastewater biorefinery

Graphical abstract
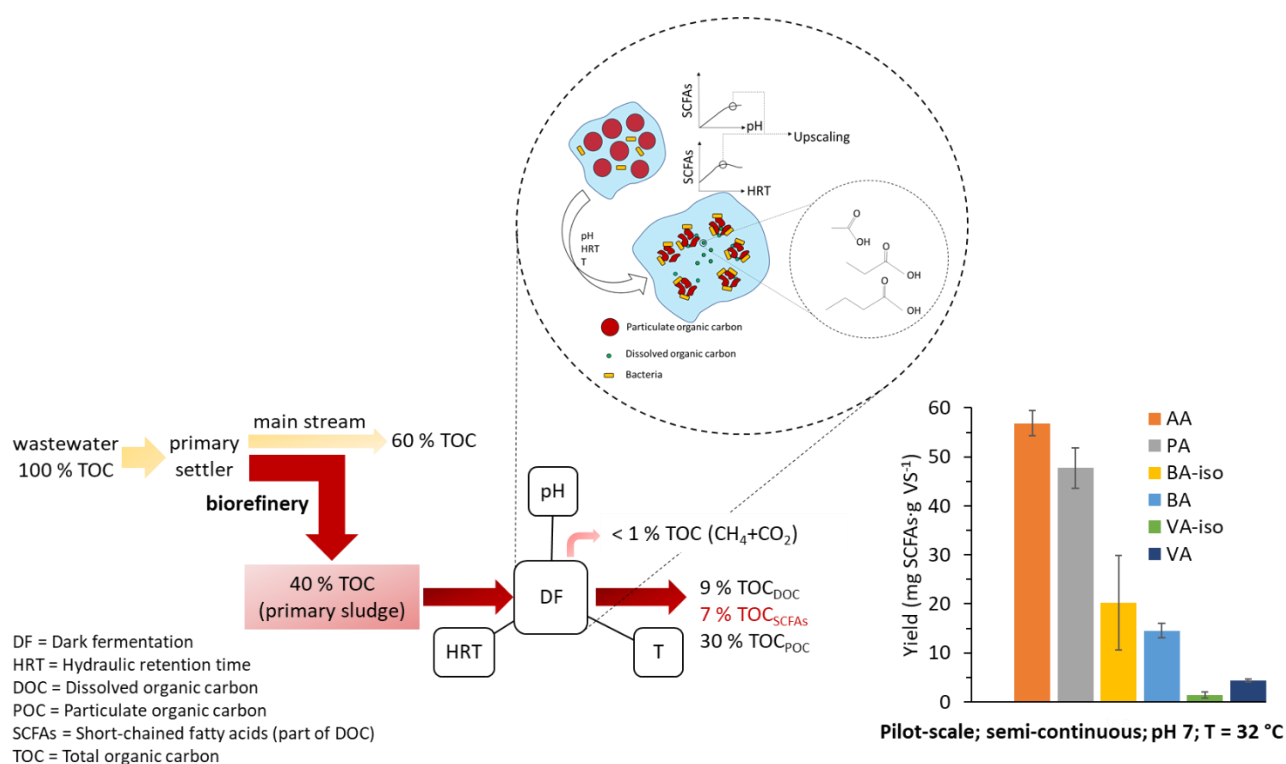
Abstract

In this study, lab-scale, bench-scale, and pilot-scale experiments were carried out to optimize short-chain fatty acids production from primary sludge. Batch tests showed the requirement of short retention times and semi-continuous operation mode showed a plateau of maximum daily productivity at 36-hours hydraulic retention time with minimal methanation. Optimization from pH 5 to pH 10 at 36 h-hydraulic retention time under long-term semi-continuous operating mode revealed that production of short-chain fatty acids was pH dependent and highest yields could be achieved at pH 7 by establishing optimum redox conditions for fermentation. Pilot-scale experiments at 32 °C showed that daily productivity ($3.1 \ \text{g} \cdot \text{L}_{reactor}^{-1} \cdot \text{d}_{HRT}^{-1}$) and yields ($150 \ \text{mg} \cdot \text{g}_{VS}^{-1}$; OLR = $21 \ \text{g}_{VS} \cdot \text{L}_{reactor}^{-1} \cdot \text{d}_{HRT}^{-1}$; pH 7) of short-chain fatty acids could be significantly improved, specifically for acetic and propionic acids. From these results, a robust dark fermentation step for recovery of valuable products from the solids treatment step in a biorefinery can be achieved.

Highlights

o   Higher accumulation of fatty acids at retention times of less than 48 hours

o   Both pH and temperature had an effect on the selective production of fatty acids

- o Neutral to slightly alkaline pH conditions led to highest yields of individual fatty acids

- o Upscaling of dark fermentation showed a steady-state yield of 150 mg VFAs·gVS^{-1}

- o Significant improvement of acetic and propionic acid yields at 32 °C

Keywords

Acidogenesis, Long-term stability, Acetic acid, Upscaling

2.1 Introduction

Lately, resource recovery from wastewater has gained increasing interest in research prompted by the depletion of non-renewable resources (Kehrein et al., 2020; Kleerebezem et al., 2015). Municipal wastewater treatment plants (WWTPs) have been traditionally developed to remove pollutant loads like carbon (C), nitrogen (N), and phosphorus (P) to prevent surface water pollution. However, the need for sustainable development has made municipal wastewater an untapped source for resource recovery (Parchami et al., 2020). Redesigning WWTPs to wastewater biorefineries (WWBrs) would realize such a necessity and directly address the environmental challenges associated with WWTPs by shifting from a linear to a circular economy (Sarkar et al., 2020).

To realize the idea of WWBrs, organic carbon needs to be valorized effectively as it can contribute directly to the production of value-added products. Organic carbon collected as sludge in a WWTP is typically converted to biogas (CH_4 and CO_2) during anaerobic digestion. In a conventional WWTP, around 30 % of influent chemical oxygen demand (COD) is converted to CO_2 in the biological treatment step, and approximately 33 % is converted to biogas (60 % CH_4 and 40 % CO_2) (Wan et al., 2016). Although biogas production via anaerobic digestion is a state-of-the-art process that provides a pathway for energy recovery, the metabolic intermediates during anaerobic fermentation (i.e., short-chain fatty acids (SCFAs)) have attracted increasing attention due to their higher value compared to biogas (Wainaina et al., 2019). SCFAs can be used as a carbon and/or energy source in many applications, for example, biological denitrification, production of biodiesel, current production in microbial fuel cells (MFCs), hydrogen production in microbial electrolysis cells (MECs), and synthesis of polyhydroxyalkanoates (PHAs). Dark fermentation has shown to be a highly effective biological approach due to its environmental friendliness and cost-effectiveness in producing SCFAs under anaerobic conditions. These SCFAs can serve as precursors to facilitate valuable products' recovery (Ramos-Suarez et al., 2021).

During fermentation, hydrolysis and acidogenesis occur in series with the former involving the breakdown of complex macromolecules like proteins, carbohydrates, and fats into simpler molecules, making them available for growth metabolism (Eastman and Ferguson, 1981). The considerable faster growth rate of acidogenic bacteria in comparison to methanogenic archaea provide a pathway towards SCFAs accumulation by controlling parameters like hydraulic retention time (HRT), pH, and temperature. For HRT, there are quite a few factors that need to be considered to enhance SCFAs production by acidogenic bacteria such as 1) providing adequate time for hydrolytic bacteria to breakdown particulate organic carbon (POC) and make it available to acidogenic bacteria for consumption; 2) preventing washout of acidogenic bacteria before SCFAs are produced or reach a plateau of maximum production; and 3) mitigating the growth of methanogens to not lose SCFA to methane production. In the case of pH, alkaline conditions can also serve as a pre-treatment similar to thermal, chemical, ultrasonic, and thermochemical pre-treatments to enhance the faster breakdown of POC and promote dark fermentation (Li et al., 2014). In addition, pH has shown to be highly influential in establishing favorable conditions for microbial communities and instigating changes

in metabolic pathways leading to different fractions of SCFAs (Feng et al., 2018; Feng et al., 2009). Also, changes in temperature can also cause significant shift in microflora and can selectively increase concentrations of SCFAs (Huang et al., 2021).

Primary sludge (PS) generated via mechanical separation of wastewater after screening and grit chamber in a primary sedimentation tank is rich in organic content due to the presence of faeces, vegetables, fruits, textiles, paper, etc. (Yuan et al., 2006). Around 70 % of the sludge production in a WWTP arises from PS making its valorization an essential step in establishing a WWBr. Within the scope of this project, focus is directed towards establishing dark fermentation as a promising and stable process to treat PS in a semi-continuous operation. Since wastewater can undergo significant changes on a daily basis, the composition of PS will inevitably change. The impact of such variable conditions on dark fermentation has to be tested as it is a crucial step in the long-term functioning of a WWBr. Studies conducted on PS have shown that alkaline pH-values improve the solubilization of macromolecules and promote acidogenesis (Wu et al., 2010, 2009). For alkaline fermentation (pH 10), the need of longer HRTs have been reported (5 days) whereas, Wang et al., 2021 showed that at pH 9.5, high productivity could be achieved in 2 days. Other studies have shown that mildly acidic conditions with long HRTs can also provide favorable conditions for acidogenesis (Bouzas et al., 2002; Yuan et al., 2010). Concerning temperature, in sludge fermentation, higher temperatures (from mesophilic to thermophilic) can enhance yields of SCFAs (Huang et al., 2021) but a contrary finding was observed by Crutchik et al., 2018, wherein the yields of SCFAs declined above the mesophilic range. Such discrepancies in key parameters need to be addressed by careful optimization.

Integration of crucial parameters such as pH, HRT, temperature, and operational stability over long-term changing PS conditions in a real WWTP and their effect on SCFAs productivity and yields have not been reported in literature so far. However, knowledge of the corresponding process stability is of great importance for assessing the possible recovery of commercial products (like H_2 and PHA) from SCFAs. In this study, experiments were done systematically from lab-scale to bench-scale to pilot-scale to achieve maximum daily productivities and yields of total and individual SCFAs. Batch-scale experiments were performed to observe changes in SCFAs during long HRTs. Bench-scale experiments were carried out to optimize HRT and pH while also comparing PS from two different WWTPs. The pilot-scale process ran under optimized conditions and was tested for the influence of temperature.

2.2   Materials and methods
2.2.1   Experimental setup

In this study, experiments were performed using three different reactor setups and distinguished into different operation phases (OP). The information on the different OPs is listed in **Table 2.1**. The initial optimization experiments (OP I) were carried out using six stirred lab-scale batch reactors with a working volume (V_w) of 1.8 L each (V_{tot} = 2 L), the description of which can be found elsewhere (Ali et al., 2021). Further experiments in semi-continuous mode were performed using a bench-scale reactor with a total volume (V_{tot}) of 40 L (OPs II, III, IV). V_w was set at 35 L for phase II, and 30 L for OPs III and IV. The reduced V_w was to cope with the shortage of PS during OPs III and IV. A screw pump (Netzsch, Germany) with a flow rate (Q_{pump}) of 400 L·h^{-1} (11 to 13 recirculations per hour) was used for the homogenization of the PS as well as to harvest and feed the primary sludge at regular intervals to maintain specific HRTs. The optimized results from the lab-scale and bench-scale setups were then transferred to a stainless-steel pilot-scale reactor insulated by polyurethane with V_{tot} of 300 L and V_w of 200 L (OP V). For the pilot-scale reactor, V_w was fixed based on the load of the PS generated under a constant influent flow rate of wastewater into the WWBr (1 m^3·h^{-1}). **Figure 2.1** shows a schematic representation of the pilot-scale reactor setup.

Table 2.1: Conditions for different OPs performed in batch (I-A to I-C) and semi-continuous modes (II-A to V-B)) (*temperature was controlled). V_R: reactor volume; HRT: hydraulic retention time; OP: Operation phase

OP	V_R (L)	Mode	HRT (h)	pH	T (°C)	Sludge
I-A	2	Batch	168	5.40 ± 0.11	30.0	Buesnau
I-B	2	Batch	168	5.81 ± 0.18	30.0	Buesnau
I-C	2	Batch	168	6.77 ± 0.30	30.0	Buesnau
II-A	40	Semi-continuous	12	5.94 ± 0.01	23.2 ± 1.4	Buesnau
II-B	40	Semi-continuous	18	5.94 ± 0.01	23.2 ± 1.4	Buesnau
II-C	40	Semi-continuous	24	5.96 ± 0.01	24.1 ± 0.9	Buesnau
II-D	40	Semi-continuous	36	5.96 ± 0.01	24.1 ± 0.9	Buesnau
II-E	40	Semi-continuous	48	5.96 ± 0.01	24.1 ± 0.9	Buesnau
III-A	40	Semi-continuous	36	5.21 ± 0.01	$22.2 \pm 0.8*$	Buesnau
III-B	40	Semi-continuous	36	6.11 ± 0.27	$23.6 \pm 1.6*$	Buesnau
III-C	40	Semi-continuous	36	7.11 ± 0.26	$24.6 \pm 1.4*$	Buesnau
III-D	40	Semi-continuous	36	8.13 ± 0.13	$24.8 \pm 0.4*$	Buesnau
III-E	40	Semi-continuous	36	8.97 ± 0.06	$22.6 \pm 1.5*$	Buesnau
III-F	40	Semi-continuous	36	9.91 ± 0.09	$24.0 \pm 0.6*$	Buesnau
IV-A	40	Semi-continuous	36	5.87 ± 0.10	$23.1 \pm 0.8*$	Sindelfingen
IV-B	40	Semi-continuous	36	8.01 ± 0.15	$23.1 \pm 0.8*$	Sindelfingen
IV-C	40	Semi-continuous	36	9.98 ± 0.22	$23.1 \pm 0.8*$	Sindelfingen
V-A	300	Semi-continuous	36	7.11 ± 0.15	25.2 ± 1.9	Buesnau
V-B	300	Semi-continuous	36	6.89 ± 0.01	32.4 ± 0.4	Buesnau

For the pilot-scale setup, Q_{pump} of the screw pump was set to 2300 L·h^{-1} (12 recirculations per hour) and 4300 L·h^{-1} (22 recirculations per hour) for phases V-A and V-B, respectively. At pilot-scale, a primary sedimentation tank was directly coupled with the dark fermentation reactor. Primary sludge generated in the primary sedimentation tank was fed using the screw pump and the same was used to harvest the hydrolyzate to maintain specific HRTs (see **Figure 2.1**). Two dosage pumps, P1 and P2 (Prominent, Germany), were implemented in the recirculation line of the setup to control the pH-value. The pH was adjusted using 5 M HCl and NaOH solutions. A pH meter (Greisinger, Germany) was also installed in the recirculation line, and the data was monitored using a data acquisition software (Volker Preyl, Germany). The flow rate of the gas produced was recorded using a drum-type gas meter (Ritter, Germany). Gas samples were collected regularly from the headspace of the reactor, and the composition of the gases was analyzed using a gas chromatograph coupled with a helium ionization detector (HP 6890 series, USA). The temperature in the reactor was controlled using a thermostat (Julabo GmbH, Germany) connected to a coil within the reactor vessel (for the pilot-scale, temperature control was carried out by varying the flow rate of the pump (see *section 2.3.4*)).
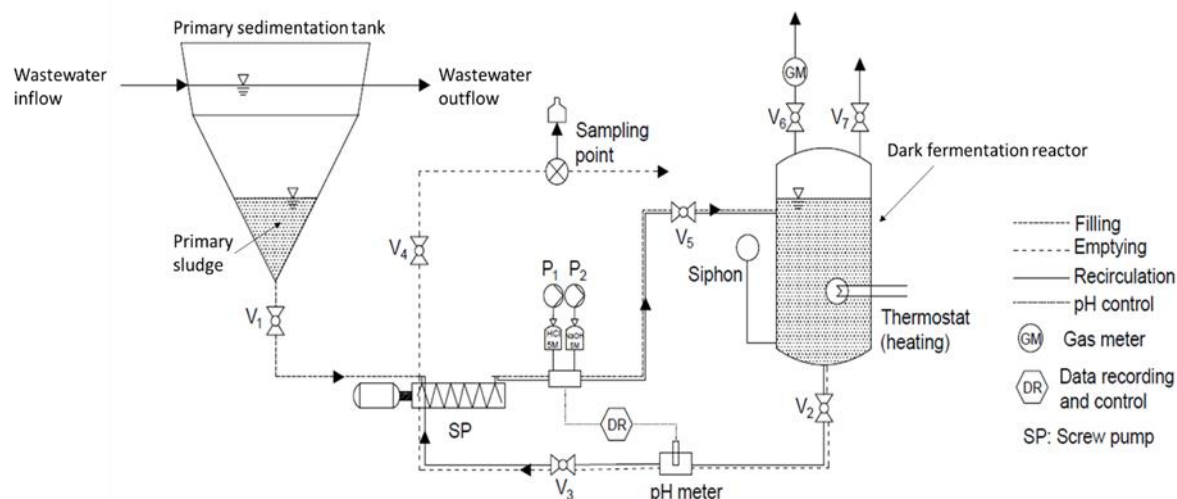
Figure 2.1: Schematic representation of pilot-scale dark fermentation reactor coupled with primary sedimentation tank.

2.2.2 Analytical methods

Due to temporary availability constraints during the study, two sources of PS were used for the experiments. For phases I, II, III, and V, the PS was obtained from Buesnau WWTP (Germany), meanwhile for phase IV, the PS was taken from Sindelfingen WWTP (Germany). Parameters in the sludge and hydrolyzate were classified into total and dissolved parameters, determined from raw or filtered samples, respectively. To measure the dissolved parameters, samples were first centrifuged at 4000 rpm. Then, the supernatant was filtered off using a glass fiber membrane with a pore size of 1 µm, followed by a regenerated cellulose (RC) membrane with a pore size of 0.45 µm. Total organic carbon (TOC), total Kjeldahl Nitrogen (TKN) and total phosphorus (TP) were measured according to DIN EN 13137, DIN EN 16169, and DIN EN ISO 17294-2, respectively. Total solids (TS) and volatile solids (VS) were measured using standard methods (DIN 38414). Dissolved parameters such as dissolved organic nitrogen (DOC) and ammonium nitrogen (NH_4^+-N) were measured in accordance with DIN EN 1484 and DIN 38406-5-2, respectively. All parameters mentioned above have been measured twice. For batch tests, duplicate experiments were carried out and for semi-continuous experiments, two to five values were used for reproducibility (see ***section 2.2.3***).

In addition, lactic acid (LA) and SCFAs from the filtered samples were detected using ion chromatography (IC) systems 881 Compact Pro (Metrohm, Switzerland). LA had a high instability in production and was found only in very low concentrations, less than 80 mg·L^{-1}. For this reason, LA was not included in any calculations defined by equations in ***section 2.2.4***. Methanol and ethanol were occasionally measured using a gas chromatograph coupled with a flame ionization detector (Agilent 7890B, USA) and concentrations were always less than the detection limit of 100 mg/L. A portable multimeter (WTW Multi 350i, Xylem, USA) was used to corroborate the pH-value. Dissolved oxygen (Greisinger, Germany) and oxidation reduction potential (WTW, Multi 350i, Xylem, USA) were measured occasionally in the semi-continuous operation mode to ensure anaerobic conditions since the reactor underwent regular feeding. DO was approximately 0 mg·L^{-1} and ORP was between minus 350 mV and minus 390 mV.

2.2.3 Experimental conditions

The batch experiments were performed in duplicates to test reproducibility. For the semi-continuous operation mode, a certain steady-state phase was established for the production of SCFAs to assure process stability. To establish reproducibility of each phase, an OP was carried out for a period of at least two times the chosen HRT. The steady-state (arbitrary steady state, SS_{ar}) itself was established arbitrarily and defined as the spot where the coefficient of variation (CV) for total short-chain fatty acids (tSCFAs) productivity was equal to or below 10 %. It is to be noted that when calculating yield values for individual short-chain fatty acids (SCFAs), the values were chosen when SS_{ar} was met for tSCFAs. However, there was one instance for phase IV-A where SS_{ar} was not completely met ($SS_{ar} = 16$ %). The combination of the two conditions, HRT and CV, are represented in the following equation,

$$SS_{ar} = \{OP \geq HRT\,(h) \times 2 \,\nabla\, CV(d[tSCFAs] \leq 10\,\%\} \qquad\qquad 2.1$$

The OPs performed in this study are listed in **Table 2.1**. OPs I and II were done to optimize the HRT. OPs III and IV were performed to optimize pH. The temperature was not controlled for OP I as the experiments were performed during warm weather conditions. For OP II and III, the temperature was controlled due to cold weather conditions in order to provide comparability. The OP V-A was conducted under optimum HRT and pH, while the OP V-B was carried out to test the effect of temperature.

2.2.4 Data interpretation

The study mainly focuses on daily productivity, and the yields of SCFAs, CH_4, and H_2.

2.2.5 Daily productivity

For batch experiments, the apparent daily productivity, P_X, was calculated using the following equation,

$$P_X\,[mg \cdot L^{-1} \cdot d^{-1}] = r_X\,[mg \cdot L^{-1} \cdot d^{-1}] \times \frac{V_W\,[L]}{V_{f/h}\,[L]} = \frac{c_{X,t_i}[mg \cdot L^{-1}] - c_{X,t_o}[mg \cdot L^{-1}]}{t_i\,[d] - t_o\,[d]} \qquad\qquad 2.2$$

i (d) = 1,2,3…n

where, r_x is the reaction rate, the subscript X refers to the dissolved parameters whose daily productivity was calculated, V_W is the working volume and $V_{f/H}$ is the volume fed or harvested (for batch systems, there is no feeding, hence $V_W = V_{f/H}$), c_{X,t_i} and c_{X,t_o} represent the mass concentrations of SCFAs or tSCFAs at the time (t_i) and initial time (t_0). tSCFAs is the sum of mass concentrations of individual SCFAs such as acetic acid (AA), propionic acid (PA), iso-butyric acid (BA-iso), butyric acid (BA), iso-valeric acid (VA-iso), and valeric acid (VA).

For semi-continuous operation, the daily productivity, P_X, was estimated using the following equation,

$$P_X\,[mg \cdot L^{-1} \cdot d^{-1}] = r_X\,[mg \cdot L^{-1} \cdot d^{-1}] \times \frac{V_W\,[L]}{V_{f/h}\,[L]} = \frac{c_{X,out}\,[mg \cdot L^{-1}] - c_{X,in}\,[mg \cdot L^{-1}]}{dt\,[d]} \qquad\qquad 2.3$$

where $c_{X,out}$ and $c_{X,in}$ represent the mass concentrations of SCFAs or tSCFAs in the effluent and influent of the reactor, respectively, and dt is the duration of each cycle, which is approximately one day.

Yield

The yield, $Y_{X/VS}$, was calculated using the following equation,

$$Y_{X/VS} \ [mg \cdot g^{-1}] = \frac{r_X \ [mg \cdot L^{-1} \cdot d^{-1}]}{OLR \ [g_{vs} \cdot L^{-1} \cdot d^{-1}]} \qquad\qquad 2.4$$

where OLR is the organic loading rate, expressed as g of volatile solids fed per liter and day.

The average gas yield for CH_4 and H_2 was estimated using the following equations,

$$Y_{CH_4,H_2,avg/VS} \ [NmL \cdot g^{-1}] = \frac{Q_{CH_4,H_2} \ [NmL \cdot d^{-1}]}{OLR \ [g_{vs} \cdot L^{-1} \cdot d^{-1}] \times V_W \ [L]} \qquad\qquad 2.5$$

To estimate the acidification fraction, f_{DOC} was used to show the overall contribution of SCFAs to DOC in the hydrolyzate, expressed as a ratio between SCFAs as carbon equivalents to DOC.

$$f_{DOC} [\%] = \frac{C_{SCFAs,out} \ [mg \cdot L^{-1}]}{DOC,out \ [mg \cdot L^{-1}]} \times 100 \qquad\qquad 2.6$$

where $C_{SCFAs,out}$ and $C_{DOC,out}$ represent the mass concentrations of SCFAs as carbon equivalents and DOC in the outflow, respectively. The results for f_{DOC} can be found in the supplementary data (**Appendix A4**).

2.3   Results and discussions

2.3.1   Characteristics of primary sludge and process stability during semi-continuous operation

In general, PS underwent notable changes as experiments were performed over longer periods of time and at different times during the year. As experiments were performed over a long-time span, **Table 2.2** shows the feeding characteristics of PS which are essentially the influent concentrations for different OPs. For experiments performed with PS obtained from Buesnau, sludge was taken from the primary sedimentation tank on a daily basis. On the other hand, for experiments performed with PS sourced from Sindelfingen, the PS was stored in a storage tank. The latter PS underwent changes during storage, and the parameters in the influent were measured every day to obtain the actual values of P_X and $Y_{X/VS}$ (see **Appendix A3** for the parameters in the influent for different OPs).

Table 2.2: Characteristics of the PS at different OPs. σ denotes standard deviations determined throughout the respective OPs. PS: Primary sludge; OP: Operation phase; TS: Total solids; VS: Volatile solids; TOC: Total organic carbon; TKN: Total Kjeldahl nitrogen; TP: Total phosphorus; OLR = Organic loading rate

OP	$g \cdot L^{-1}$			$mg \cdot L^{-1}$		C:N	OLR	OLR
	TS	VS	TOC	TKN	TP	$(g_{TOC} \cdot g_{TKN}^{-1})$	$(g_{VS} \cdot L^{-1} \cdot d^{-1})$	$(g_{TOC} \cdot L^{-1} \cdot d^{-1})$
I-A, B, C	37 ± 2	33 ± 2	19 ± 1	-	-	-	-	-
II-A	29 ± 6	26 ± 6	13 ± 3	1012 ± 245	248 ± 64	13 ± 1	52 ± 12	26 ± 5
II-B	40 ± 4	34 ± 3	16 ± 1	1072 ± 225	348 ± 37	16 ± 5	45 ± 3	22 ± 2
II-C							31 ± 2	15 ± 1
II-D	35 ± 3	31 ± 2	15 ± 1	1286 ± 70	288 ± 14	12 ± 1	21 ± 1	10 ± 1
II-E							16 ± 1	8 ± 1
III-A	37	37	18	991 ± 133	27 ± 2	18 ± 3	25	12
III-B	37 ± 6	35 ± 5	17 ± 2	985 ± 155	43 ± 7	17	24 ± 3	11 ± 2
III-C	22 ± 6	20 ± 5	10 ± 3	642 ± 146	158 ± 31	16 ± 1	14 ± 4	7 ± 2
III-D, E, F	32 ± 7	27 ± 6	13 ± 3	775 ± 115	160 ± 72	17 ± 2	18 ± 4	9 ± 2
IV-A	30 ± 4	25 ± 4	11 ± 1	1060 ± 154	453 ± 50	10	17 ± 2	7 ± 1
IV-B	35 ± 2	29 ± 2	13 ± 1	1246 ± 66	512 ± 18	10 ± 1	19 ± 1	8
IV-C	48 ± 6	40 ± 5	17 ± 2	1725 ± 198	661 ± 66	10 ± 1	27 ± 4	11 ± 1
V-A, B	38 ± 5	32 ± 4	16 ± 2	831 ± 114	167 ± 107	19 ± 1	21 ± 3	10 ± 1

Since terminal treatment steps, say hydrogen and bioplastic production, require stable production of tSCFAs and, more importantly individual SCFAs, it was essential to evaluate process stability to observe if SCFAs underwent significant changes in coefficient of variation (CV). In all OPs at semi-continuous feeding mode, the dominant SCFAs produced were AA, PA, BA, and BA-iso, with VA and VA-iso having mass fractions less than 10 %. In most cases during the SS_{ar}, CV for individual SCFAs (dominant fractions) was less than 15 %, with some exceptions (see **Appendix A2).** Maintaining ideal conditions by appropriately controlling parameters like HRT, pH and temperature can ensure long-term functioning of dark fermentation with low CVs.

2.3.2   Evaluation of hydraulic retention time at batch and semi-continuous operation modes

OP-I was performed in a batch mode to observe the trend of SCFAs and methane productivity (see **Figure 2.2**) in dependency on the pH-value (5.4 ± 0.1 (OP I-A), 5.8 ± 0.2 (OP I-B), and 6.8 ± 0.3 (OP I-C)). Production of C2 to C5 fatty acids was observed in all cases with branched SCFA, BA-iso being more predominant at I-C at 18 h. The SCFAs were generally produced from the solubilization of macromolecules, proteins, carbohydrates, and lipids, which were then quickly fermented to pyruvate via glycolysis and then to SCFAs (Fang et al., 2020; Yu et al., 2003). The fraction of AA:PA:BA was close to 90 % for I-A and I-B. This fraction was reduced to approximately 80 % in I-C due to higher production of BA-iso. After 24 h, the trend from I-A to I-C exhibited similar patterns except for PA and BA-iso in I-C (**Figure 2.2**). PA was more dominant in I-A and I-B, while in I-C, AA was relatively higher. BA was the third most prevalent SCFA from I-A to I-C (see **Figures 2.2A, 2.2B and 2.2C**). The dominance of BA-iso at pH above 6 was also shown in batch tests performed with sludge obtained from Bruchsal WWTP (Data for batch tests on Bruchsal PS can be found in **Appendix A1**) and in some of the semi-continuous operation phases (OP III-C to III-E, IV-B, IV-C, and V). In this study, it could be deduced that accumulation of BA-iso appears to be prompted at pH-values above 6. The accumulation of BA-iso could be caused by its poor biodegradability compared to other SCFAs (Wu et al., 2010). However, BA-iso decreased significantly after 18 h implying its degradation (**Figure 2.2C**). In a defined triculture anaerobic environment, Carola Matthies & Bernhard

Schink, 1992 observed isomerization of BA-iso to BA and the subsequent degradation of BA to AA and CH_4. These reactions were also noted to be an important first step in methanogenesis for the degradation of this branched SCFA. A study conducted by Chiu-Yue Lin, 1993 on sludge acclimatized with butyric and iso-butyric acid had also reported such a pathway for BA-iso degradation to AA. There appears to be a rise in P_{CH_4} and P_{AA} at around 70 h after a significant decrease in P_{BA-iso} at 40 h (**Figure 2.2C**). However, the 30-h offset between degradation and production does not necessarily offer validation for such a pathway.

Higher P_{AA} in OP I-C could also be related with lower P_{CH_4} during the initial batch phase. For methanation, there are several pathways and among them, hydrogen and AA consumption have been known to be predominant in AD (Calise et al., 2020; Harirchi et al., 2022). Hydrogen ($4 H_2 + CO_2 \rightarrow CH_4 + 2 H_2O$) and AA ($CH_3COOH \rightarrow CH_4 + CO_2$) are substrates to methane production via hydrogenotrophic and acetoclastic methanogenesis, respectively. In OP I, P_{H_2} was relatively low and was between 3 to 10.5 $NmL \cdot d^{-1}$. This would indicate the H_2 partial pressure was very low due to interspecies hydrogen transfer between obligatory producing and consuming bacteria (Boušková et al., 2005). The relatively lower productivities of AA in I-A and I-B would be a result of AA consumption during acetoclastic methanogenesis (**Figures 2.2A and 2.2B**). However, with rising P_{CH_4} at 70 h in I-C, a decrease in P_{AA} should be expected but the contrary was observed (**Figure 2.2C**). At this particular time (70 h), H_2 was absent from the headspace of the reactor and could be used as a substrate for both homoacetogens ($4H_2 + 2CO_2 \rightarrow 2CH_3COOH$) and hydrogenotrophic methanogenesis (Supriya et al., 2022).

Nevertheless, daily productivity did not change notably for I-A and I-B over the course of the batch. But there was an accumulation of SCFAs (specifically BA-iso and AA) in the first day of the batch at pH 6.8 ± 0.3 (I-C) ($P_{tSCFAs} = 2901 ± 284$ mg·$L^{-1} \cdot d^{-1}$). Such a trend could also be observed with PS obtained from Bruchsal at pH 6 ($P_{tSCFAs} = 995 ± 38$ mg·$L^{-1} \cdot d^{-1}$ at 20 °C after 24 h) and pH 6.5 ($P_{tSCFAs} = 1773 ± 202$ mg·$L^{-1} \cdot d^{-1}$ at 20 °C after 24 h). For Bruchsal PS, there was an increase for C2 to C5 fatty acids after 24 h. At pH-values above 6, in both batch tests, higher SCFAs productivity along with higher methanation was observed. Although at pH-range 5 – 5.5, methanation is low, there is a drawback in terms of lower productivity. Therefore, pH 6 was chosen to maintain low methanation as well as relatively higher productivity for semi-continuous experiments to determine HRT in OP II.
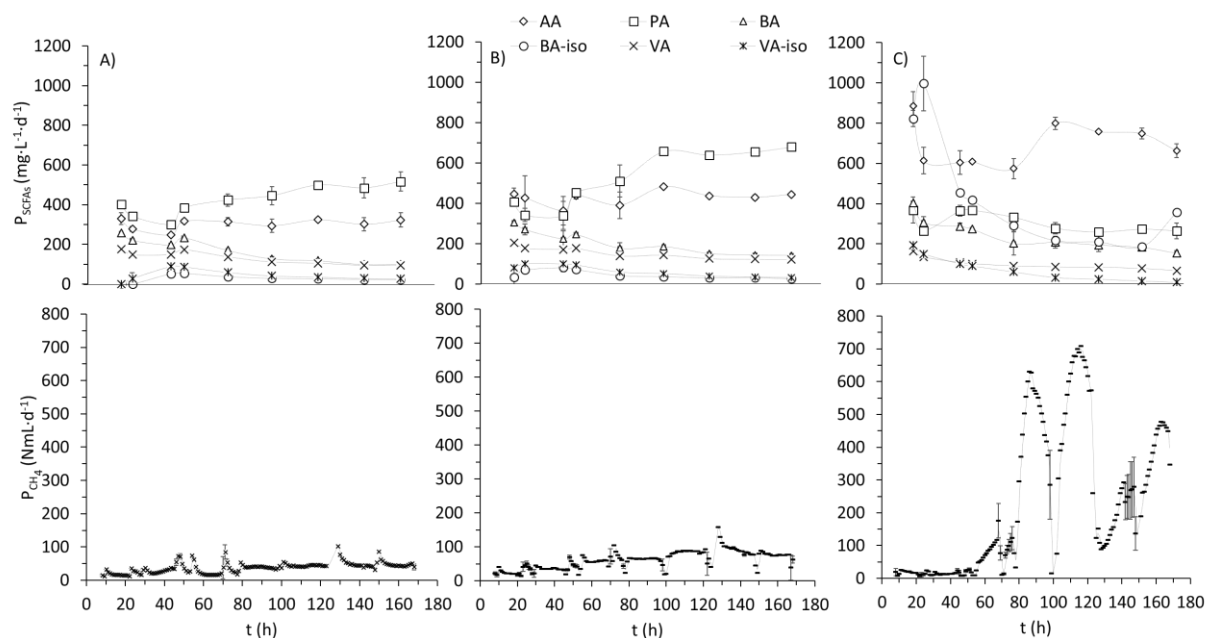
Figure 2.2: Daily productivities of individual short-chain fatty acids (SCFAs) (P$_{SCFAs}$) and CH$_4$ (P$_{CH_4}$) for different pH-values, A) 5.4 ± 0.1 (operation phase (OP) I-A), B) 5.8 ± 0.2 (OP I-B), and C) 6.8 ± 0.3 (OP I-C) (refer **Table 2.1** for detailed parameters).

Similar to the results from the batch operation phases, C2 to C5 fatty acids, linear, and branched SCFAs were produced with AA, PA, and BA having the highest concentrations from 12 h to 48 h and mass fractions (in sum) of more than 85 % in all cases. **Figures 2.3A and 2.3C** show a linear increase in P$_{tSCFAs}$ and P$_{SCFAs}$ from 12 h to 36 h HRT (OP II-A to II-D) after which no significant difference was observed at 48 h. Interestingly, AA dominated until HRT of 18 h after which productivities of AA and PA were similar until 48 h HRT. This equivalence in productivity could be construed as a reduction of AA productivity which coincides with rising methanogenic activity, P$_{CH_4}$ (see **Figures 2.3B and 2.3C**) from HRT of 24 h. Similarly, Canziani et al., 1995 had reported a significant reduction of soluble COD (sCOD) concentrations at HRTs above 48 h due to increasing rates of methanation. At the steady state conditions SS$_{ar}$, P$_{tSCFAs}$ reached maximum values of 4705 ± 384 mg·L^{-1}·d^{-1} and 5407 ± 305 mg·L^{-1}·d^{-1} at 36 h and 48 h HRT, respectively. In general, having low HRTs can be beneficial to extract the maximum productivity of SCFAs. Yehuda Miron et al., 1999 reported that to maintain acidogenesis, HRT less than 192 h was still appropriate. Furthermore, the minor increase in P$_{tSCFAs}$ at 48 h compared to 36 h does not justify the higher OLR that could be processed at HRT 36 h. For this reason, HRT of 36 h was chosen to optimize pH.
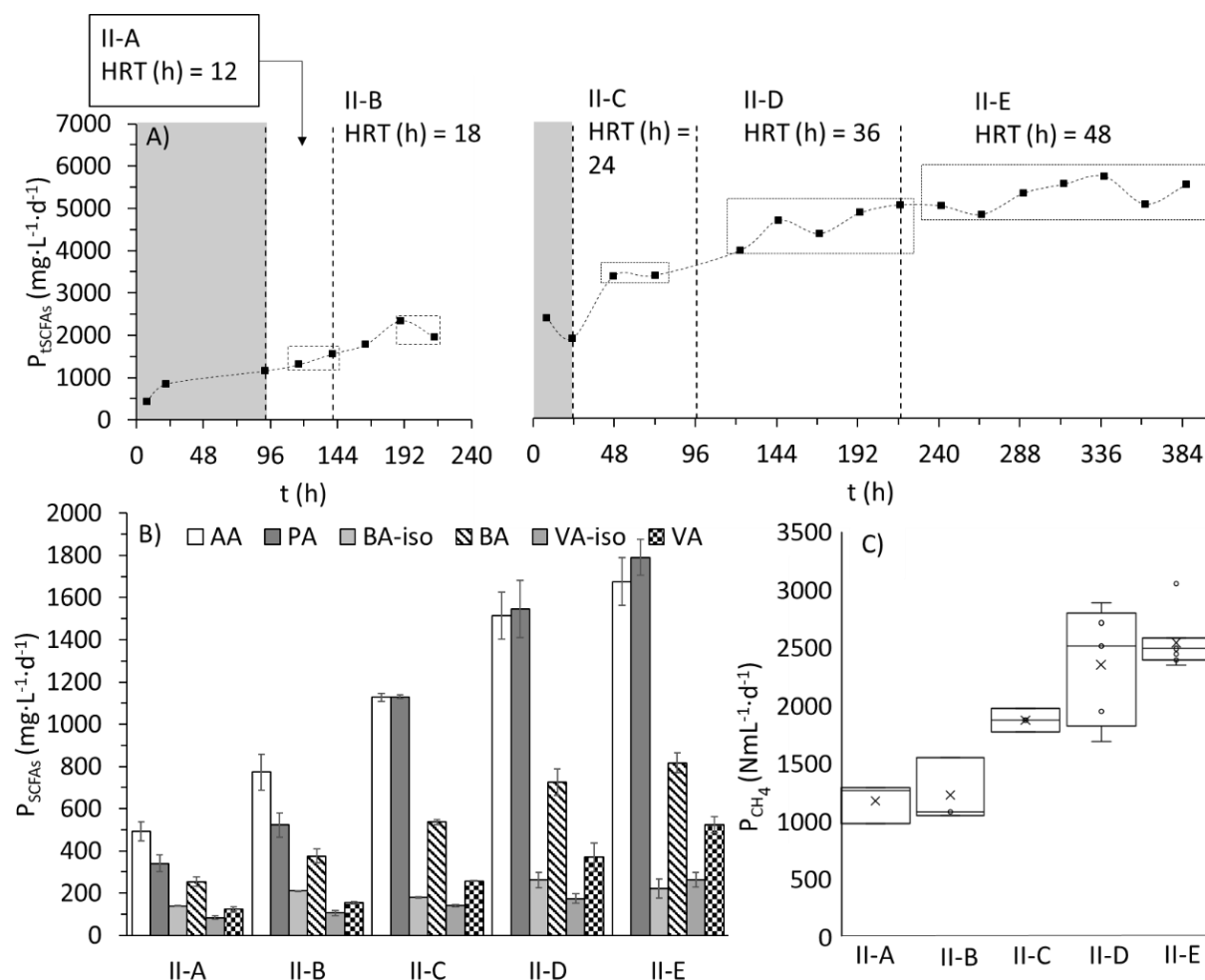
Figure 2.3: Daily productivities of A) total short-chain fatty acids (tSCFAs) (P_{tSCFAs}), B) individual SCFAs (P_{SCFAs}) and C) CH_4 (P_{CH_4}) for hydraulic retention times from 12 h to 48 h at pH 6 (operation phase (OP)-II) (refer **Table 2.1** for detailed parameters). The boxes indicate arbitrary steady-state and the shaded area shows the start-up batch phase.

2.3.3 Effect of pH on short-chain fatty acids production and composition at semi-continuous operating mode

For determination of the effect of pH on SCFAs production, the optimized HRT of 36 h (OP II-D) was chosen. In these experiments, pH values ranging from 5.2 to 10 were tested in OP III and IV. The results depicted in **Figure 2.4A** show a notable increase of P_{tSCFAs} from pH 5.2 to pH 6.1 (III-A to III-B) by a factor of approx. 2.5, while the increase from 5.2 to neutral/slightly alkaline conditions of 7.1 (III-C) was even by a factor of 3.5 to 4, reaching the maximum productivity of almost 4 g· L^{-1}·d^{-1} even at low OLRs (OLR was different during the OPs and it was even lower at OP III-C, see **Table 2.2**). At moderately alkaline conditions with pH-values between 8.1 and 9 (OP III-D to III-E, and IV-B), a slightly lower P_{tSCFAs} was mostly maintained, showing no significant difference within this range except for variations among individual SCFAs. At pH 9.9/10 (OP III-F and IV-C), this productivity notably declined. Although pH-range 5 to 7 could be very well be optimum (based on batch and semi-continuous tests) at this HRT, it could be claimed that optimum HRT could be different at an alkaline pH-range. Wang et al., 2021 were able to achieve very high productivity at pH 9.5 within 48 h of fermentation for PS while Dahiya et al., 2015 could

23

also observe high productivities at pH 10 within 10 h (until 48 h) of fermentation using food waste (inoculated with digested sludge). In this study, the decline at pH 9.9/10 (OP III-F and IV-C) shows the requirement of extended adaptation periods for acidogenesis. Wu et al., 2010 showed that at 5 days the highest yields of tSCFAs could be achieved at pH 10. The authors noted that, alkaline redox conditions favored faster breakdown of proteins to amino acids which were utilized by acidogenic bacteria. Similar results were also shown with excess sludge and waste activated sludge (Chen et al., 2006; Yuan et al., 2006). However, it is important to consider, that long retention times (between 5 and 8 days depending on the substrate) are required to achieve physicochemically aided biological effect. In this study, the decline at pH 9.9 (OP III-F)/pH 10 (OP IV-C) stated in **Figures 2.4A and 2.4B** clearly arose mainly from the reduction in productivities of specifically PA and also from AA and BA. Such a trend was also observable from both kinds of PS as shown in OP-III and IV (compare OPs III and IV in **Figure 2.4B**). Since several consortia of microorganisms are responsible for producing the individual SCFAs, the significant reduction in PA productivities could result from unfavorable conditions for the propionic bacterium, whose optimal range for growth could be between pH 6 and 8 (Horiuchi et al., 2002). Nevertheless, there was a general trend of higher P_{tSCFAs} at alkaline conditions compared to pH 5.2 and pH 6.1.

When considering the spectrum of SCFAs produced, mainly C2 to C5-acids were determined (**Figure 2.4B**). However, the composition of SCFAs showed a notable change in the pH-range from pH 7.1 to 9.9 (OPs III-C to III-F) and pH-values of 8.1 and 10 (OPs IV-B and IV-C). AA, PA, BA-iso and BA production were significantly improved at pH 7.1 (**Figure 2.4C**) above which the productivity declined. AA, PA, BA-iso, and BA are directly fermented from proteins, carbohydrates, and fats. However, VA and VA-iso are the results of protein degradation via reductive deamination or Stickland reaction (Chen et al., 2006). The higher productivities of these SCFAs at alkaline pHs compared to acidic ranges could be caused by higher solubilization of non-proteinaceous macromolecules (protein degradation appears to be low at OPs III and IV (see *section 3.5*) at higher pHs as VA and VA-iso show no significant changes in productivity.

Inhibition of hydrogenotrophic methanogenesis prevented complete consumption of H_2 at alkaline conditions at OP III-E, III-F and IV-C (**Figures 2.4C and 2.4D**). Cessation of methanogenesis at pH-values close to 10 also led to the accumulation of low concentrations of FA, which is another substrate for methanogenic archaea ($4HCOOH \rightarrow CH_4 + 3CO_2 + 2H_2O$) and could be seen in OPs III-F and IV-C (**Figure 2.4B**). In this study, it is more or less clear that the major substrates for methane production are FA, H_2 and AA. Although alkaline pH-ranges (from pH 9 to pH 10) may hinder methanation, which should see a significant increase in SCFAs, there is a reduction or lack of increase in SCFAs production indicating that at short HRTs, alkaline pHs could hinder fermentation due to the requirement of extended adaptation periods and to see a considerable impact, HRT should be increased. However, providing optimum redox conditions for fermentation can significantly improve the productivity and yields. In conclusion, as neutral/slightly alkaline conditions showed the highest productivity of SCFAs in OP III-C with moderate methane production rates compared to acidic and alkaline conditions, pH in the neutral range was implemented for the pilot-scale setup.
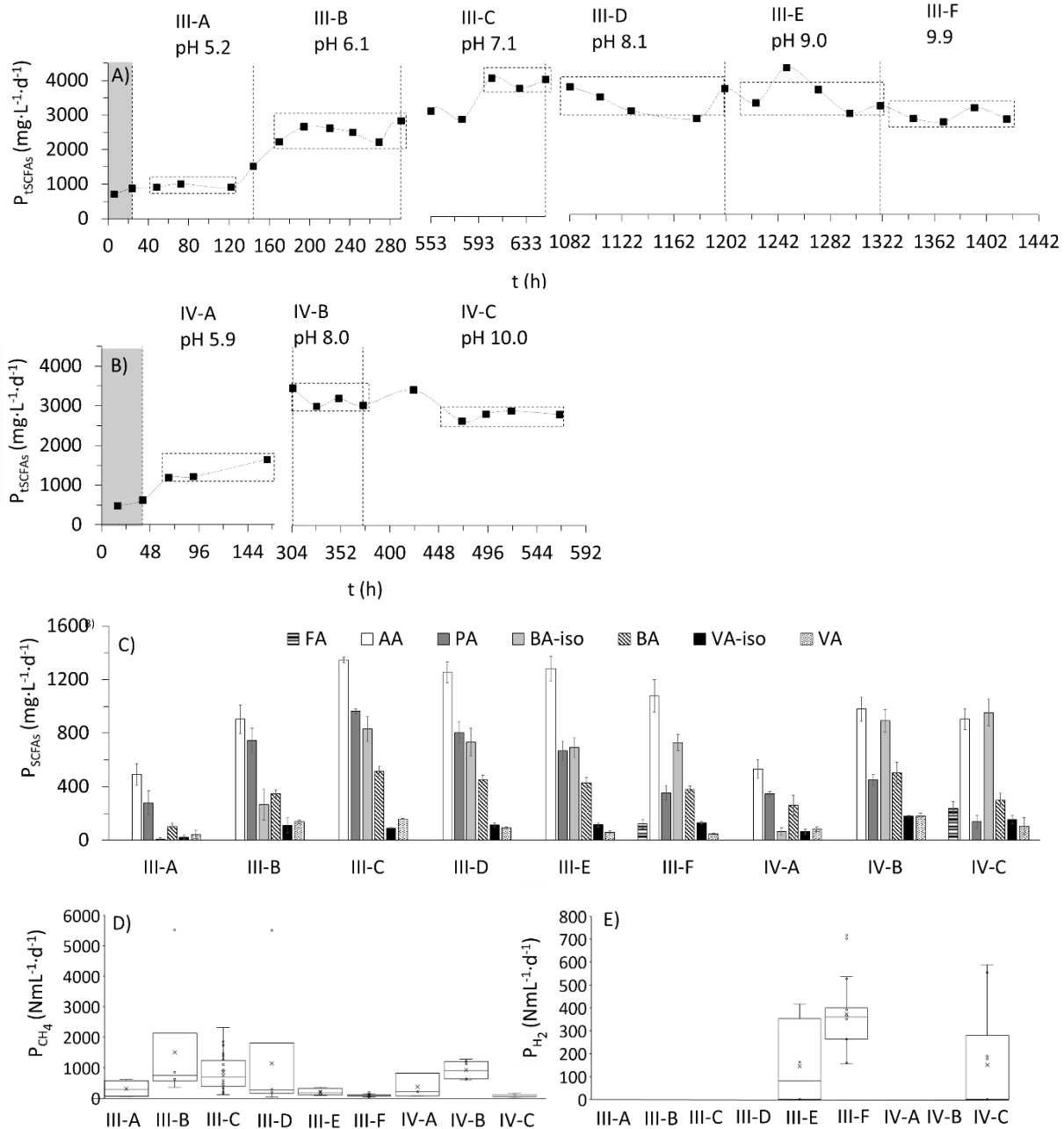
Figure 2.4: Daily productivities of A) total short-chain fatty acids (tSCFAs) (P_{tSCFAs}) for Buesnau primary sludge (PS) (operation phase (OP)-III), B) tSCFAs (P_{tSCFAs}) for Sindelfingen PS (OP-IV), C) individual SCFAs (P_{SCFAs}), D) CH_4 (P_{CH_4}) and, E) H_2 (P_{H_2}) for different pH-values (OP-III; pH 5.2 to 9.9 and OP-IV; pH 5.9 to 10.0) at hydraulic retention time of 36 h (refer **Table 2.1** for detailed parameters). The boxes indicate arbitrary steady-state and the shaded area shows the start-up batch phase.

2.3.4 Upscaling to a 300 l-reactor under optimum conditions and effect of temperature

During the upscaling experiment from 40 L to 300 L, temperature influence played a significant role due to the heat generated by the screw pump. The temperature was, thus, not controlled with an external thermostat, but rather the flow rate of the pump was raised to increase the temperature. Such an effect occurred because

of energy loss due to frictional losses in the pump which was transformed into heat. This heat was prevented from dissipation by a polyurethane insulation of the reactor vessel leading to temperature containment in the reactor.

As expected, higher temperatures lead to increased reaction rates and higher production of SCFAs. It was also shown that temperature has a selective impact on SCFAs production. Depending on temperature requirements of the single microbial species of the consortium, biocoenosis composition will likely change with changing temperatures leading to an increase or decrease in production rates (Komemoto et al., 2009; Wainaina et al., 2019). In this study, raising the temperature by approximately 7 °C did not simply improve P_{tSCFAs} (**Figure 2.5A**). While BA-iso, BA, VA-iso, and VA productivities were unaffected by the temperature increase, AA and PA productivities increased significantly by a factor of approx. 1.6 and 2.1, respectively (**Figure 2.5B**). This probably shows that AA and PA-producing organisms were highly active around 32 °C. Research conducted on shifts in microflora in sludge at a genus level showed an increase in microbial communities that promoted production of individual SCFAs (including AA and PA) at 35 °C during sludge fermentation (Huang et al., 2021). Experiments performed by Christensen et al., 2022 on PS showed a similar increase in the production of tSCFAs when the temperature rose from 30°C to 35 °C. The authors showed an increase of 1.5 and 1.2 at pH-values of 5 and 7, respectively. In addition to acidogenesis, methanogenesis was also notably enhanced (**Figure 2.5C**).

As explained above, the temperature increase was a result of a higher flow rate of the pump. Thus, with this increase in recirculation rate of the liquid, also the mixing intensity in the reactor was higher (see ***section 2.2.1***). It is uncertain whether the increased recirculation rates did not positively affect reaction rates by affecting mass transfer in general or through sludge particle destruction due to increased shear stresses, or negatively by increasing mechanical damage of microorganisms through turbulence and shear forces. However, Ong et al., 2002 showed that there was no notable difference in SCFAs and biogas production between continuous and intermittent mixing at different impeller speeds. Similar experiments were also conducted to test the effect of recirculation duration/frequencies on biogas production from dairy manure with minimal effect of different recirculation frequencies (Rico et al., 2011). These findings, plus the fact that the observed overall increase in SCFAs production corresponds to the expected increase following the van´t Hoff-Arrhenius theory it is assumed, that the positive effect of temperature on production rates shown in this work are mainly attributed to temperature.
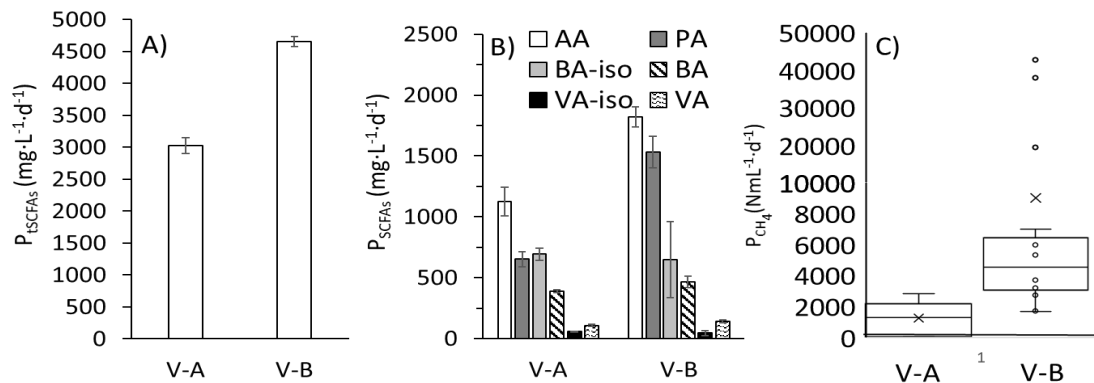
Figure 2.5: Daily productivities of A) total short-chain fatty acids (tSCFAs) (P_{tSCFAs}), B) individual SCFAs (P_{SCFAs}) C) CH_4 (P_{CH_4}) for different temperatures (operation phase (OP) V-A; T = 25.2 °C and V-B; T = 32.4 °C) at hydraulic retention time of 36 h during 3-day arbitrary steady-state (refer **Table 2.1** for detailed parameters).

2.3.5   Yields for bench-scale and pilot-scale setups at semi-continuous operating mode

The yields calculated for all OPs are depicted in **Figure 2.6A**. Maximum yields achieved for HRT optimization (OP -II) were at 36 h and 48 h as shown in **Figure 2.6A** (36 h was chosen for reasons mentioned in *section 2.3.2*). At bench-scale (OP III-C), the highest yield of around 200 $mg_{SCFAs} \cdot g_{VS}^{-1}$ was achieved at pH 7.1. In the upscaled reactor system under optimum conditions (HRT of 36 h, a neutral pH value and a temperature of 32 °C (OP V-B), a stable yield of around 150 $mg_{tSCFAs} \cdot g_{VS}^{-1}$ (f_{DOC} = 84 %) at a 3-day SS_{ar} can be achieved. The gas yields of CH_4 and H_2 were less than 5 $NmL_{CH_4} \cdot g_{VS}^{-1}$ and 1 $NmL_{H_2} \cdot g_{VS}^{-1}$ (see **Table 2.3**).
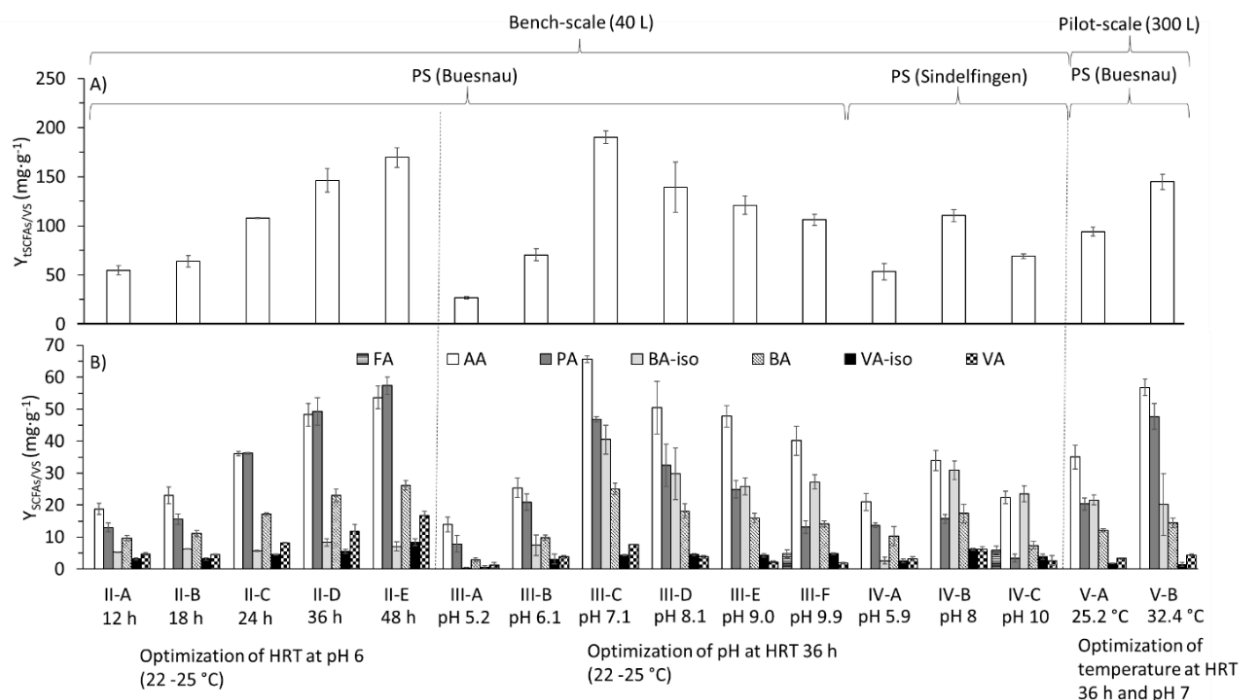
Figure 2.6: Yield of A) total short-chain fatty acids (tSCFAs) (Y_{tSCFAs}) and B) individual SCFAs (Y_{SCFAs}) for optimization of hydraulic retention time (HRT) at pH 6 (operation phase (OP)-II), optimization of pH at HRT of 36h for two different primary sludge (OP-III and IV) and, optimization of temperature at HRT 36 h and pH 7 (OP-V) (refer **Table 2.1** for detailed parameters).

When comparing modes with similar conditions, specifically OP II-D and III-B, certain discrepancies in yields were obvious. There appears to be an overall decrease in Y_{tSCFAs}, Y_{SCFAs} and Y_{CH4} for III-B compared to II-D (see **Figures 2.6A, 2.6B** and **Table 2.3**). In addition, overall gas production appears to have decreased compared to OP II. OLR was notably different and could not be maintained constant during the course of different OPs. It is known that, for biogas production in anaerobic digestion, significant increase in OLR leads to reactor failure due to SCFAs accumulation causing hyper acidification. A study conducted by Bouzas et al. on PS in a continuous system showed increasing yields of tSCFAs with increasing OLRs at HRT of 6 and 10 days. However, at 8 and 10 days, the yields were more or less stable (Bouzas et al., 2002). In this study, yields of tSCFAs were stable in the range of 12 to 22 $g_{VS} \cdot L^{-1} \cdot d^{-1}$ (results are not shown). OLR does not appear to have a major influence in this study at least within the tested range. Also, from the results of Wu et al., 2009 and Wu et al., 2010 done in a batch mode, wherein PS was obtained from the same location, the yields for tSCFAs and SCFAs remained constant for PS (at similar pH and temperature conditions) despite the significant difference in the concentration of initial VSS added (which deviated by 60 %).

Interestingly, yields of ammonium were notably higher at II-D compared to III-B (see **Table 2.3**). The higher $Y_{NH4+/VS}$ shows that proteins were degraded more in OP II-D compared to III-B. When comparing sludge from Buesnau (OPs II, III and V), C/N ratio was low in OP-II indicating the higher nitrogen content (in the form of proteins). C/N ratio is crucial in influencing metabolic pathways and producing different SCFAs (Rughoonundun et al., 2012). The authors noted that higher molecular weight-SCFAs such as VA and VA-iso were shown to decrease at higher C/N ratios due to a lack of proteinaceous substances. On the

28

contrary, OP IV (PS from Sindelfingen) also had low C/N ratio but $Y_{NH4+/VS}$ was lower. The yields of SCFAs at OP IV (PS from Sindelfingen) were moderately lower but followed a similar trend as OP III. The composition and yields of SCFAs was also quite similar but there was a notable difference in yields of PA especially at the alkaline range (AA was also quite low). Such differences in SCFAs production between sludge types was also noted by Yuan et al., 2010.

Table 2.3: Average yield of CH_4 and H_2 ($Y_{CH4, H2, avg/VS}$), yield of NH_4^+ ($Y_{NH4+/VS}$) for optimization of HRT at pH 6 (OP-II), optimization of pH at HRT 36 h for two different PS (OP-III and IV) and, optimization of temperature at HRT 36 h and pH 7 (OP-V) (refer **Table 2.1** for detailed parameters). HRT: hydraulic retention time; OP: Operation phase

OP	$Y_{NH_4^+/VS}$ (mg·g^{-1})	$Y_{CH_4, avg/VS}$ (NmL·g^{-1})	$Y_{H_2, avg/VS}$ (NmL·g^{-1})
II-A	4 ± 1	0.6	-
II-B	7 ± 1	0.8	-
II-C	13 ± 1	1.7	-
II-D	23 ± 3	3.2	-
II-E	20 ± 4	4.7	-
III-A	3 ± 0	0.4	-
III-B	9 ± 1	1.8	-
III-C	13 ± 2	2.1	-
III-D	8 ± 4	2.8	-
III-E	12 ± 1	0.4	0.3
III-F	10 ±	0.2	0.7
IV-A	9 ± 1	0.7	-
IV-B	16 ± 2	1.6	-
IV-C	8 ± 1	0.1	0.2
V-A	8 ± 1	0.3	-
V-B	7 ± 2	2.1	-

The distribution of macromolecules (among proteins, carbohydrates and fats) in PS are critical in producing SCFAs and require further investigations, since higher fractions of fats (specifically long-chain fatty acids (LCFAs)) have been shown to negatively impact the process of acidification (Miron et al., 1999; Vidal et al., 2000). Higher yields of VA and VA-iso along with a higher yield of NH_4^+ could hint that the fraction of lipids (LCFAs) is lower in OP II compared to OPs III, IV, and V. However, it is necessary to investigate the composition of PS (distribution of carbohydrates, proteins and fats) and the changes it can undergo during various seasons as it can increase or decrease the yield. Da Ros et al., 2020 and Crutchik et al., 2018 showed that PS enriched with cellulose (cellullosic PS) is able to hydrolyze more efficiently into SCFAs (especially AA and PA). Indeed, the composition of PS has a major influence on the overall yields that can be achieved as there was notable difference in the distribution of SCFAs. Also, shifts in fermentation parameters like pH, temperature, and nutrient ratios can lead to the selective growth of different organisms, and, thus, cause a significant shift in biocoenosis that produces different metabolites (Chen & Chang, 2017; Huang et al., 2021; Lin et al., 2018; Wang et al., 2021). Some of these studies could show certain commonalities in phyla

that could dominate at defined conditions like pH and temperature in a complex substrate like sludge. Although biocoenosis composition has not been investigated in this study, the stability and ratio of SCFAs production achieved at different conditions with low CVs could potentially hint at the prevalence of specific phyla. In that case, significant changes in phyla may not occur during optimized pH and temperature conditions and could maintain a stable yield over long-term functioning of dark fermentation.

In any case, dark fermentation has to be adapted to the changing conditions of PS. The highest yield that was achieved at bench-scale was approximately 280 $mg_{tSCFAS, COD} \cdot g_{VS}^{-1}$ at 3-day SS_{ar} (pH 7.1, T = 25 °C, HRT = 36 h; OP III-C). AA and PA had the highest yields of 68 $mg_{tSCFAS, COD} \cdot g_{VS}^{-1}$ and 69 $mg_{tSCFAS, COD} \cdot g_{VS}^{-1}$, respectively. Yields achieved with PS at lab-scale at pH 10 was between 190 and 300 $mg_{tSCFAS, COD} \cdot g_{VS}^{-1}$ (J. Wang et al., 2021; Wu et al., 2010, 2009). At pilot-scale, at SS_{ar}, the yield was found to be around 207 $mg_{tSCFAS, COD} \cdot g_{VS}^{-1}$ (at pH 6.9, T = 32 °C, HRT = 36 h; OP V-B). The yields for AA and PA were 61 $mg_{COD} \cdot g_{VS}^{-1}$ and 72 $mg_{COD} \cdot g_{VS}^{-1}$. Similar conditions (pH 7, T = 35 °C) were also tested by Christensen et al., 2022 at HRT of 72 h at pilot-scale (3 m^3) and the yield was 80 % lower compared to this study.

Performance of the reactor was rather stable but it is unclear how extremely low sludge loading periods (high dilution) could impact the overall stability. Although alkaline pH-ranges may enhance yields at longer HRTs, there are practical disadvantages which can be addressed with the optimized conditions in this study such as, smaller reactor size (due to short HRTs) which provides an advantage in terms of operability and low chemical requirement (neutral pH conditions) to maintain a stable pH-value. Also, when run at stable alkaline pH conditions, a post-acidification step might be necessary if downstream commercial product recovery steps, like bioelectrochemical H_2-production, demand a near neutral pH-range (Liu et al., 2012). With the yields achieved in this study, the process itself is a practical option for H_2 production after subsequent membrane separation. For instance, using an MEC, Liu et al., 2012 were able to achieve a yield of 1.2 $mL_{H_2} \cdot mg_{COD}^{-1}$ at tSCFAs concentration of 6042 $mg_{tSCFAS, COD} \cdot L^{-1}$ with AA (2544 $mg_{AA, COD} \cdot L^{-1}$) and PA (1143 $mg_{PA, COD} \cdot L^{-1}$) as the dominant SCFAs. At OP V-B, 1943 $mg_{AA, COD} \cdot L^{-1}$ and 2315 $mg_{PA, COD} \cdot L^{-1}$ could be achieved, making such a process very plausible. In both cases, the distribution among SCFAs were quite similar. In case of PHA, it is necessary to have a higher PA/AA ratio to enhance polymer production with enhanced physical and mechanical properties (Jiang and Chen, 2009). Frison et al., 2015 was able to achieve a consistent distribution among 3-hydroxybutyrate, 3-hydroxyvalerate and 3-hydroxyhexanoate (56 %:42 %:2 %) at PA/AA ratio of 1.1 $g_{COD, PA} \cdot g_{COD, AA}^{-1}$. In this study, PA/AA ratio of 1.2 $g_{COD, PA} \cdot g_{COD, AA}^{-1}$ (OP V-B) can be achieved at optimized conditions and could also be well suitable for PHA recovery. Also, SCFAs which are easily degradable can be used as carbon source for biological nutrients removal, specifically denitrification.

2.4   Conclusions

Dark fermentation can be a viable preliminary approach for valorizing organic carbon in the solids treatment step in a WWBr. The requirement of HRT less than 48 hours, pH 7 and a temperature of 32 °C makes this process a feasible pre-treatment step from an economic standpoint. Maximum yields achieved at pilot-scale amounted to around 150 $mg_{SCFAs} \cdot g_{VS}^{-1}$ with yields of AA and PA reaching up to 57 and 48 $mg \cdot g_{VS}^{-1}$, respectively. The highest productivity of AA and PA at pilot-scale were 1.2 and 1 $g \cdot L_{reactor}^{-1} \cdot d_{HRT}^{-1}$ and could make commercial products recovery a potential option in the solids stream.

3   Optimizing cross-flow velocity under pressure loss conditions in pilot-scale tubular microfiltration of dewatered primary sludge

3.1   Introduction

Microfiltration (MF) has shown to be an efficient filtration process for separation of valuable dissolved organic and inorganic compounds from complex particulate waste streams. In general, MF can be operated in a dead-end, cross-flow or submerged filtration mode, depending on the type of waste stream to be treated. In principle, cross-flow filtration has a significant advantage in terms of higher achievable permeate fluxes as the flow is parallel to the membrane which minimizes the build-up of fouling layer. After this restrained formation of a cake layer, there is an equilibrium established between the convectional deposition of particles, and removal due to hydrodynamically-assisted diffusion, resulting in a relatively constant permeate flow (Song and Elimelech, 1995).

Despite this operation-based advantage, cross-flow MF is anyway susceptible to fouling due to the nature of the particles present, and the interaction they can have with the membrane (Al-Malack and Anderson, 1997; Lim and Bai, 2003). Optimizing operational parameters in cross-flow MF is crucial to ensure long-term stable filtration, and to minimize the frequency of in situ or ex situ chemical cleaning (Gul et al., 2021). Typically, cross-flow MF can be optimized in two ways, 1) fixing transmembrane pressure (TMP), and varying cross-flow velocities, and observing how the fouling resistance develops at each cross-flow velocity (Choi et al., 2005), or 2) fixing the cross-flow velocity, and varying TMP to the point at which permeate flux stabilizes, reduces or ceases (Sayegh et al., 2022).

Above methods are critical to ensure long-term filtration, and although there is a limitation when scalability is brought into the picture, they have been well established due to their easy application. Permeate flux is a function of TMP, but in this study it was found that cross-flow velocity presumably affects TMP by influencing the pressure loss in the channels, and permeate flux becomes a function of cross-flow velocity. Therefore, a method needs to be established for optimization of cross-flow under the influence of pressure loss. In addition, cross-flow velocities have been shown to decline during long-term filtration (Samanta et al., 2022), but the impact on TMP and permeate flux is little known and has to be understood.

Within the scope of a wastewater biorefinery, fermenting short-chain fatty acids from the solids stream of municipal wastewater (Shylaja Prakash et al., 2024), and their subsequent recovery using a combination of chamber-filter press and ceramic cross-flow tubular microfiltration serves as the main source for producing a particle-free short-chain fatty acids stream. The particle-free stream can then be conveniently used for recovery of valuable products in biotechnological applications (Atasoy et al., 2018). This clearly outlines the reason why cross-flow microfiltration has to provide a stable performance, and with an optimized cross-flow velocity, at least the initial rapid build-up of fouling layer can be prevented. In this study, declining cross-flow velocities could increase transmembrane pressure by affecting the pressure drop across the filtration module. Therefore, selection of cross-flow velocity has to be done in such a way that its decline over the course of filtration does not increase transmembrane pressure to the point of complete fouling. This further signifies the importance of a method for optimizing cross-flow velocities.

The aim of this study mainly focuses on 1) calculating the pressure loss in a pilot-scale ceramic cross-flow tubular microfiltration membrane, 2) developing a simple and new approach to optimize cross-flow

velocities, and 3) understanding the impact of cross-flow velocity decline on permeation flux in a long-term experiment.

3.2   Materials and Methods
3.2.1   Feed solution

The feed solution used here is obtained from hydrolyzed primary sludge, i.e, hydrolyzate, after filtration with a chamber-filter press (mesh size = 100 µm). To improve the filtration performance of the chamber-filter press, the hydrolyzate was preconditioned with a cationic starch-based flocculant. The starch-based flocculant (potato-based) was comprised of approx. 20 % amylose and 70 % amylopectin (Gadhave et al., 2017). The flocculant was grafted with 2,3-epoxypropyltrimethylammonium chloride. The end product was hydroxypropyltrimethyl ammonium starch (HPAS) (HKF CleanTech AG, Germany). Details on the starch-based flocculant and the grafting procedure can be found elsewhere (Hermann-Josef Melcher and Jan Berg, 2013). The hydrolysate was conditioned with 1000 mg HPAS per kg of hydrolyzate, corresponding to 25 to 30 mg HPAS per g of total solids in hydrolyzate (TS in hydrolysate was between 33 and 40 g total solids per kg hydrolyzate) The filtrate obtained from the filter-press was further treated with a microfiltration membrane. The composition of the filtrate used for optimization and long-term experimentation of microfiltration can be found in **Table 3.1** and **Table 3.2**, respectively.

3.2.2   Tubular ceramic cross-flow microfiltration

In this research, a fully loaded cross-flow filtration system (Atec, Ulm, Germany) incorporated with pumps and sensors was used (see **Figure 3.1**). Two ceramic membranes (α-Al_2O_3 (Inopor, Germany); pore size = 0.2 µm; length = 1.2 m; number of channels = 7 (axially arranged), number of modules = 2, channel diameter = 6 mm; effective filtration area (A_{eff} = 0.316 m^2)) were incorporated into the cross-flow filtration unit. A pre-filter (Atec, Ulm, Germany) with a pore size of 60 µm was utilized prior to cross-flow microfiltration to prevent larger particles from entering the membrane module. A manometer (P_{in}) was installed at the inlet section to measure the inlet pressure. A flowmeter was used to measure the cross-flow rate (Q_{CF}) and on the permeate side (Q_P). A thermometer (T) measured the temperature in the modules. A thermostat was used to heat the modules during the cleaning procedure. Separate external tanks were used for tap water (i.e., clean water (CW)), or cleaning solutions (not shown in Figure).
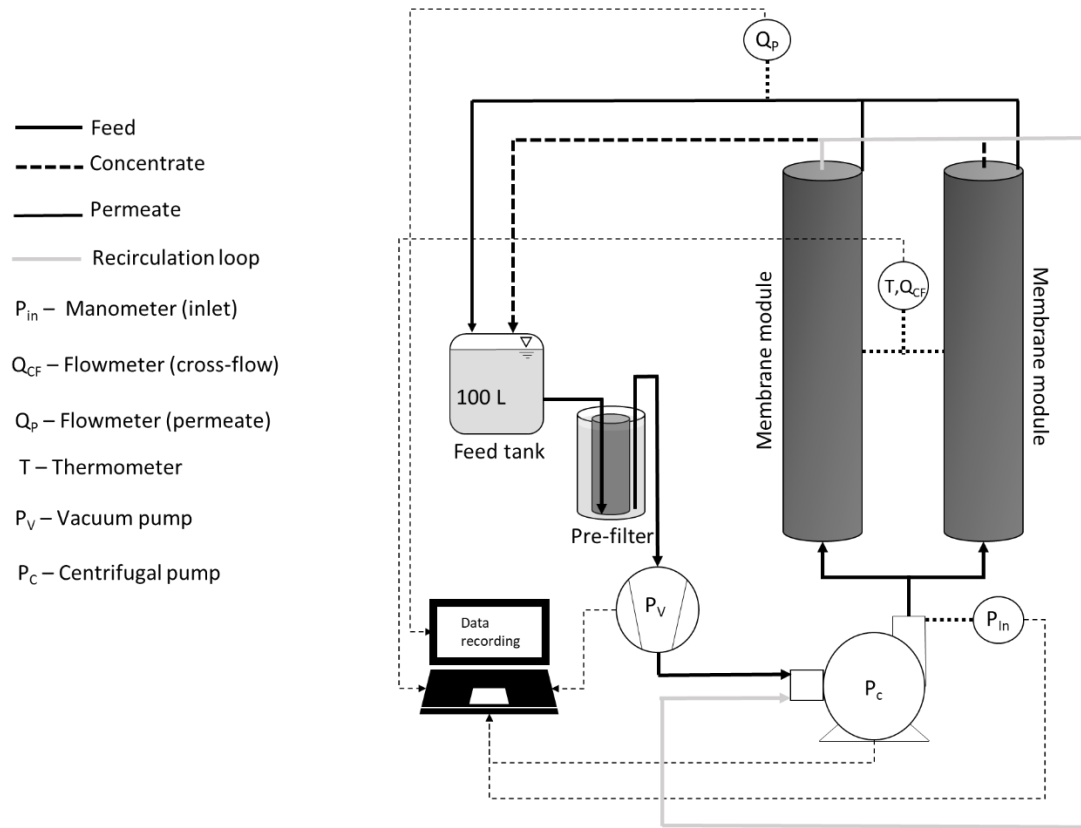
Figure 3.1: Schematic representation of cross-flow microfiltration with tubular ceramic membranes.

3.2.3 Membrane filtration

There are two types of MF experiments in this study, 1) cross-flow velocity optimization, and 2) long-term experimentation at optimum cross-flow velocity. In both cases, the concentrate and the permeate were recycled back into the feed tank to maintain consistent feed composition as shown in **Figure 3.1**. The feed volume used for filtration was 100 L. During filtration, a vacuum pump (P_V) sucked the feed liquid into the system, while a centrifugal pump (P_C) generated the required cross-flow velocity in a recirculation loop (see **Figure 3.1**). The pressure at the inlet was maintained at 2.2 bars. The pump efficiency of the centrifugal pump (P_C) was changed between 5 and 80 % to achieve the required cross-flow velocites between 0.2 and 3.6 m·s^{-1}. The relationship between pump efficiency and cross-flow velocity can be seen in **Figure A4**. After filtration, cleaning was performed according to the procedure described in ***section 3.2.4***.

Experiment description for cross-flow optimization

To determine the optimum cross-flow velocity (as described in ***section 3.3.1***), change in total resistance was monitored. Cross-flow velocity was varied (by changing the pump efficiency) from the highest to the lowest in a step-wise manner, and from each step, cross-flow velocity was again reverted back to the highest. The order in which the cross-flow velocity was varied is shown by the brackets (next to cross-flow velocity values) in **Figure 3.2**. For instance, the starting point would be 7 m·s^{-1} (1), and then reduced to the next lowest (i.e., 6 m·s^{-1} (2)), after which it would be increased back again to 7 m·s^{-1} (3). Then, cross-flow velocity would be reduced to the next lowest (5 m·s^{-1} (4)), and then increased again to 6 m·s^{-1} (5) and then 7 m·s^{-1}

(6). By doing so, the pattern of how resistance develops at each cross-flow velocity was plotted. The reason for the descending order for evaluating cross-flow velocity can be explained by the immediate fouling that can occur when starting at a very low cross-flow velocity and the actual total resistance at the higher cross-flow velocities may never be achieved. Each step of cross-flow velocity was evaluated for approximately 3 to 5 minutes. This time step was chosen, as a similar experiment was performed with a 20 minute-time step and the variation in total resistance was rather alike (see **Figure A3**). However, only one point of the cross-flow velocity was reverted (0.5 m·s^{-1}) to the highest cross-flow velocity (see **Figure A3**). To improve this experiment, multiple cross-flow velocities were evaluated in this study, and the time step was reduced. **Figure 3.2** shows four different hypothetical scenarios for development of resistance as a function of cross-flow velocity.

1) Scenario 1 – Irreversible fouling: **Figure 3.2A** shows how resistance between the cross-flow velocity to be evaluated (for instance, 4 m·s^{-1} (7)) is unchanged in comparison to the highest cross-flow velocity (7 m·s^{-1} (10)). This indicates that fouling cannot be reversed at higher cross-flow velocities.
2) Scenario 2 – Reversible fouling: In this scenario reverting cross-flow velocity from any low cross-flow velocity reduces the resistance to the initial resistance at 7 m·s^{-1}, indicating that the fouling formed is completely reversible (**Figure 3.2B**).
3) Scenario 3 – Irreversible and reversible fouling: The order in which cross-flow velocity was changed is similar to scenarios 1 and 2, but as can be seen from **Figure 3.2C**, the resistance can be reduced to a certain extent by increasing the cross-flow. For instance, from 3 m·s^{-1} (11) to 7 m·s^{-1} (15), resistance can be reduced significantly, but from 6 m·s^{-1} (2) to 7 m·s^{-1} (3), a slight reduction in resistance is observed. This indicates that fouling formed at low cross-flow velocities is reversible.
4) Scenario 4 - No fouling: Resistance would be unchanged at any cross-flow velocity as there is no fouling (**Figure 3.2D**). This condition is applicable only for CW.
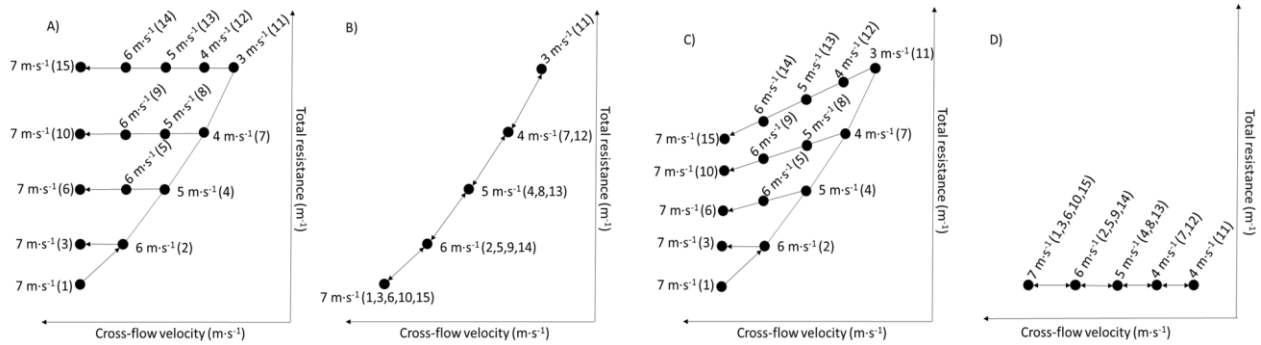
Figure 3.2: Hypothetical scenarios (a) irreversible fouling, (b) reversible fouling, (c) irreversible and reversible fouling, and (d) no fouling. **Note:** The numbers in the brackets represent the chronological order in which the cross-flow velocity was changed. The values used for cross-flow velocity are hypothetical.

3.2.4   Chemical cleaning to recover permeate flux

HPAS can interact with the membrane and cause significant fouling due to charge interaction. A detailed description can be found in *section 4.3.2* and **Figure 4.2**. Therefore, a specific protocol for chemical cleaning was established. Membrane cleaning to recover the flux after filtration with the filtrate was done as follows,

1) Filtration with CW at 40 °C for 1 hour at 3 m·s^{-1}

2) Filtration with an alkaline solution (Atec, Ulm, Germany; Product no.: Atec 2610) at pH 12 at 40 °C for 1 hour at 3 m·s^{-1}

3) Filtration with CW at 40 °C for 0.5 hours at 3 m·s^{-1}

4) Filtration with an acidic solution (Atec, Ulm, Germany; Product no.: Atec 3027) at pH 2 at 40 °C for 1 hour at 3 m·s^{-1}

5) Filtration with CW at 40 °C for 0.5 hours at 3 m·s^{-1}

3.2.5 Analytical methods

Parameters in this study were classified into total and dissolved components. Total parameters such as total organic carbon (TOC) and total solids (TS) were measured according to (Characterization of waste - Determination of total organic carbon (TOC) in waste, sludges and sediments, 2001) and (German standard methods for the examination of water, waste water and sludge; sludge and sediments (group S); determination of water content, of dry residue and of solids content (S 2), 1985), respectively. Total suspended solids (TSS) and volatile suspended solids (VSS) were determined according to (Rice et al., 2017). To measure dissolved organic carbon (DOC), samples were first centrifuged at 4000 rpm. Then, the supernatant was filtered off using a glass fiber membrane with a pore size of 1 µm, followed by a regenerated cellulose (RC) membrane with a pore size of 0.45 µm. DOC was measured in accordance with ("Water analysis - Guidelines for the determination of total organic carbon (TOC) and dissolved organic carbon (DOC)," 2019).

3.2.6 Data interpretation

Permeate flux (J_{std}) was standardized to 25°C, and calculated using the following equation,

$$J_{std} \left[L \cdot m_{eff}^{-2} \cdot h^{-1}; LMH \right] = \frac{Q_{permeate}}{A_{eff} \times f_T} \qquad \qquad 3.1$$

where $Q_{permeate}$ (L·h^{-1}) is the permeate flow rate, A_{eff} (m^2) is the effective filtration area of the membrane, and f_T is the temperature correction factor. During operation of microfiltration, the heating up of the systems due to the pumps led to an increase in the temperature of the feed solution during filtration. This affected the viscosity of the liquid, and to normalize the values of $Q_{permeate}$, a separate experiment was performed to obtain a correlation between $Q_{permeate}$ and temperature. Using this calibration, f_T was calculated and used in **equation 3.1** to normalize the flux (J). The calibration curve between the two parameters can be found in **Figure A5**. Flux for CW (J_{CW}) was also standardized to 25°C.

Cross-flow velocity (v_{cf}) was calculated according to the equation given below,

$$v_{cf} \left[m \cdot s^{-1} \right] = \frac{Q_{CF}}{A_{CS}} \qquad \qquad 3.2$$

where Q_{CF} is the volumetric flow rate (m^3·s^{-1}) in the membrane channels, and A_{CS} (m^2) is the cross-sectional area of the membrane channels.

Optimum v_{cf} was obtained based on the experiment description in *section 3.2.3*. To determine the optimum v_{cf}, firstly, the relative change of total resistance ($\Delta_{R_T}(v_{cf})$) for each v_{cf} is estimated.

$$\Delta_{R_T}(v_{cf}) = = \frac{R_T(v_{cf,final})}{R_T(v_{cf,initial})} \qquad 3.3$$

Basically, this is the ratio of final total resistance that can be achieved at the highest v_{cf} when reverted from a particular v_{cf} ($R_T(v_{cf,final})$) to the intial total resistance at the highest cross-flow velocity ($R_T(v_{cf,initial})$) at the start of the experiment. For instance, if a cross-flow velocity of 3 m·s^{-1} is to be evaluated ($\Delta_{R_T}(3\,m \cdot s^{-1})$), the total final resistance ($R_T(7\,m \cdot s^{-1})$) is the value obtained by reverting the cross-flow from 3 m·s^{-1} to 7 m·s^{-1} (see **Figure 3.2A** to **3.2D**, i.e., from point 11 to point 15). The intial resistance ($R_T(7\,m \cdot s^{-1})$) is the value of the highest cross-flow velocity obtained at the start of the experiment (see point 1 in **Figure 3.2A** to **3.2D**). The values of $\Delta_{R_T}(v_{cf})$ are plotted against v_{cf}, and the slope is monitored to determine the optimum cross-flow velocity (explained in *section 3.2.3*).

3.3   Results and discussions
3.3.1   Cross-flow-flux hysteresis in microfiltration of clean water

Before an optimum cross-flow velocity was determined for wastewater, clean water flux (J_{CW}) was evaluated for the ceramic membrane at different cross-flow velocities (v_{cf}) at a fixed inlet pressure (p_{inlet}) of 2.2 bars. To do this, the pump efficiency of the centrifugal pump was changed between 10 % and 80 % (5 %-interval), generating v_{cf} between 0.2 and 3.6 m·s^{-1}. This interval of 5 % was chosen arbitrarily to generate a high frequency of steps between each cross-flow velocity, which is around 0.5 m·s^{-1}. Interestingly, a rather peculiar relationship was observed between between J_{CW} and v_{cf} (see **Figure 3.3A**). Typically, the solvent flux (here clean water) is proportional to the pressure difference or, the so-called transmembrane pressure (TMP) across the membrane, which can be modelled according to Darcy's law (Lim and Bai, 2003) as shown below,

$$Q = \frac{A_{eff} \cdot TMP}{\mu \cdot [R_m + R_f]}; \text{ where } R_m + R_f = R_T \qquad 3.4$$

where, Q is the solvent flow rate, μ is the dynamic viscosity (8.9×10^{-4} N·s·m^{-2}; at 25 °C), R_m is the intrinsic membrane resistance, R_f is the resistance due to fouling, and R_T is the total resistance. **Equation 3.4** can be further rewritten as follows,

$$J = \frac{TMP}{\mu \cdot [R_m + R_f]} \qquad 3.5$$

For CW, R_f is zero, and solvent flux is directly proportional to TMP,

$$J \,\alpha\, TMP \text{ or } J = k \cdot TMP; where\; k = \frac{1}{\mu \cdot R_m} \qquad 3.6$$

However, based on this equation, the cross-flow velocity (v_{cf}) should not affect the clean water flux J_{CW}. However, it appears to influence the flux, potentially hinting at the influence of pressure loss in the filtration module (see **Figure 3.3**A). To calculate the pressure loss, it is necessary to find out the TMP at different v_{cf}. **Equation 3.7** (after rearranging **equation 3.5**) was used to determine TMP at different v_{cf}. Since both

TMP and the intrinsic membrane resistance R_m are unknown, R_m must first be calculated. The relative change of J_{CW} at 0.2 m·s^{-1} with respect to J_{CW} at 2.5 m·s^{-1} (from **Figure 3.3**A) is around 5 %, which indicates that the pressure loss is quite low at low v_{cf}. Therefore, it can be assumed that P_{inlet} is similar to TMP between 0.2 and 2.5 m·s^{-1}. From this, R_m (at 0.3 m·s^{-1}) was found to be 3.3×10^{12} m^{-1}.

$$TMP = J \cdot \mu \cdot R_m \tag{3.7}$$

It is clear that the filtration undergoes pressure loss at high cross-flow velocities, but it is not possible to estimate the exact losses in the module as there is no pressure sensor at the outlet. However, to establish a relationship between pressure loss and TMP, an inexplicit assumption was made wherein the pressure measured at the inlet must be transformed to TMP all through the membrane module. Therefore, in case of no pressure loss, P_{inlet} should be equal to TMP and can be presumably expressed as follows,

$$p_{inlet} - TMP = 0 \; (p_{inlet} = TMP) \tag{3.8}$$

Whereas, in case of pressure loss in the filtration module, the empirical pressure loss ($P_{loss,E}$) is represented as,

$$p_{loss,E} = p_{inlet} - TMP \tag{3.9}$$

It can be seen that there was a significant loss of pressure of 60 % at high cross-flows (v_{cf} = 3.6 m·s^{-1}; see **Figure 3.3A**). For instance, p_{inlet} at 3.6 m·s^{-1} is 2.2 bars, and TMP at 3.6 m·s^{-1} is 0.92 bars (according to **equation 3.7**), which results in a $p_{loss,E}$ or discrepancy of 1.3 bars (**Figure 3.3B**).
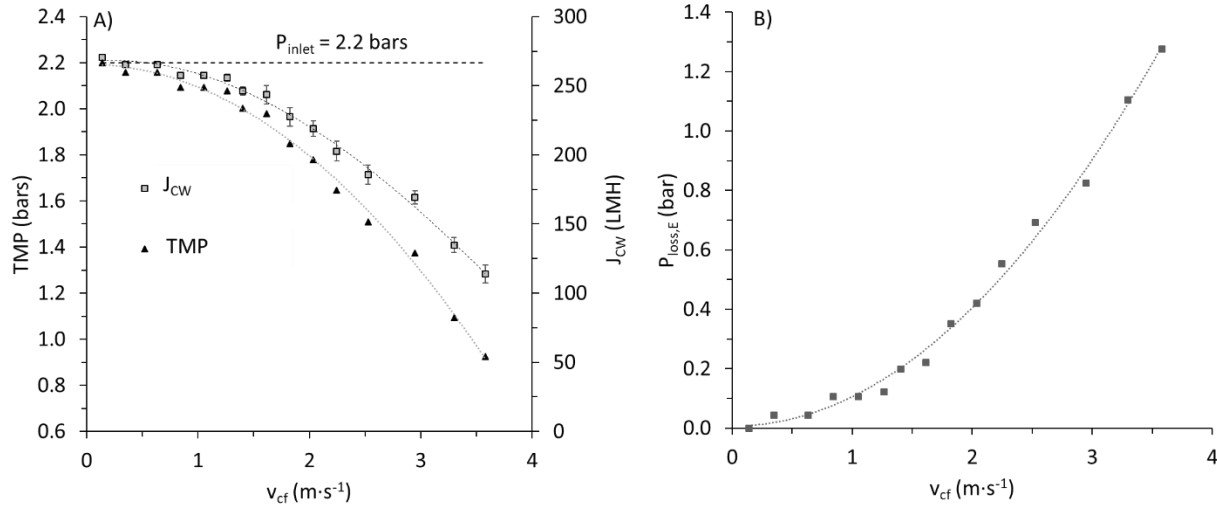
Figure 3.3: A) Clean water flux (J_{CW}) and transmembrane pressure (TMP) in dependence of cross-flow velocity (v_{cf}) and empirical pressure loss ($P_{loss,E}$) calculated from **equation 3.9**.

It is well known that frictional losses can cause a significant pressure loss in a filtration module. Darcy-Weisbach equation (Valiantzas, 2008) was used to evaluate frictional loss ($p_{loss,friction}$) as follows,

$$p_{loss,friction} = f_D \cdot \frac{\rho}{2} \cdot \frac{(v_{cf})^2}{d_{channel}} \cdot L \tag{3.10}$$

Where, f_D is the Darcy friction factor, $d_{channel}$ is the hydraulic diameter of the channel, and L is the length of the channel. f_D is dependent on the Reynolds number (Re) and surface roughness (ϵ) to channel diameter ratio. Re was calculated using the following equation as shown by Moody, 1944),

$$Re = \frac{\rho \cdot v_{cf} \cdot d_{channel}}{\mu}$$

3.11

The relationship between v_{cf} and Re can be found in **Figure A6**. In most cases, the flow regime is turbulent. For the calculation, a surface roughness (ϵ) to channel diameter ratio of 10^{-6} (ϵ/d) is used, which reflects a rather smooth surface (Darcovich et al., 1999).

Friction factor (f_D) was calculated according to the following equation obtained from (Avci and Karagoz, 2009) which can be used for a turbulent regime (which is mostly the case),

$$f_D = \frac{6.4}{\left[(ln(Re) - ln\left(1 + 0.01 \cdot Re \cdot \epsilon \cdot (1 + 10 \cdot \sqrt{\epsilon})\right)\right]^{2.4}}$$

3.12

For a laminar flow regime, the following equation is used as described by (Cumming et al., 1999),

$$f_D = 64 \cdot Re^{-1}$$

3.13

In any case, it can be seen that frictional loss alone shows a notable discrepancy and does not account for a significant part of the pressure loss (see **Figure 3.4**). It is suspected that the cross-flow loop used in this system has a pressure profile created by the centrifugal pump at the pumping and suction side in addition to the frictional loss (see **Figure 3.1**). It is posited that the pressure at the inlet which is fixed at 2.2 bars reduces gradually along the length of the module due the suction created at the end of the recirculation line. However, to validate such a theory, a pressure sensor is required at the outlet of the module. In any case, it is important to consider the change in TMP at different cross-flow velocities, and how it can impact the membrane filtration performance. Therefore, the major focus in this chapter is on the optimization of cross-flow velocity under the influence of pressure loss (see *section 3.3.2*) and how it can effect long-term filtration (*section 3.3.3*).
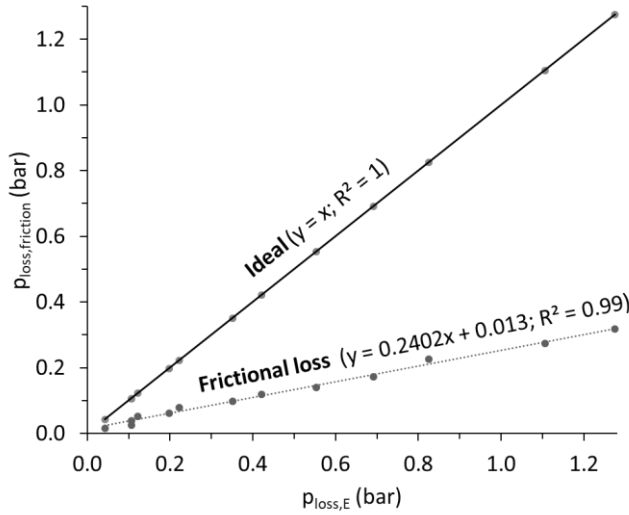
Figure 3.4: Depiction of frictional pressure loss as a fuction of empirical pressure loss ($P_{loss,E}$).

3.3.2 Optimization of cross-flow velocity to filtrate obtained from chamber filter-press

Nonetheless, based on **equation 3.9**, there is a pressure loss at higher cross-flow velocities, and subsequently, there is also decrease in transmembrane pressure (TMP) at higher cross-flow velocities (v_{cf}) as seen with clean water flux (**Figure 3.3A**). As the cross-flow itself can reduce a part of fouling resistance by shearing, it was important to evaluate how different cross-flow velocities, and the resulting pressure drops could relate to the filtration of the filtrate from chamber-filter press. The composition of the filtrate used for optimization can be found in **Table 3.1**.

Table 3.1: Composition of filtrate obtained from chamber-filter press.

Parameters	Unit	Measured values
pH	-	8.3
TS	mg·L⁻¹	2864 ± 352
TSS	mg·L⁻¹	224 ± 24
TOC	mg·L⁻¹	928
DOC	mg·L⁻¹	849

Since there are two variables, TMP and flux (J), at different v_{cf}, total resistance (R_T) was evaluated by rearranging **equation 3.4** as it incorporates both the variables (see **equation 3.14**).

$$R_T = R_f + R_m = \frac{TMP}{\mu \cdot J}$$

3.14

To determine the optimum v_{CF} which can be fixed for long-term filtration, R_T was evaluated at different cross-flow velocities as described in **section 3.2.3**. v_{cf} was varied from the highest to the lowest (by changing the pump efficiency), because starting from the lowest v_{cf} was expected to cause immediate fouling, and the actual flux at higher v_{CF} would never be achieved (as explained in **section 3.2.3**). As the

cross-flow velocity was reduced step-wise, cross-flow velocity was again reverted back step-wise to the highest v_{CF} (see **section 3.2.3** for detailed description). This was done mainly to see how reverting the cross-flow could lower R_f (caused by reversible fouling) by shearing along with the loosening of the foulants (because of the overall pressure reduction due to the pressure loss) across the membrane. When evaluating R_T, it can be seen that, despite maintaining a high v_{cf}, R_T builds up consistently with decreasing v_{cf} (see **Figure 3.5A**). However, below 2 m·s^{-1}, R_T could be decreased with increasing v_{CF}. This could indicate that reversible fouling can develop at low v_{cf}. However, the initial build-up of R_T hints at the initial interaction of specific foulants in the pores. It is important to consider that HPAS used for sludge conditioning is cationic, and this notable build-up of initial resistance can probably be attributed to either unbound HPAS and/or flocs (with bound HPAS) that pass through the coarse pores (100 µm) of the filter-press and foul the microfiltration membrane due to charge interaction (S. Wang, Li, and Li 2011). The resistance due to this interaction is unavoidable and is not affected by high cross-flow velocities. Nevertheless, it is important to prevent the development of resistance due to reversible fouling, as it can contribute greatly to the overall fouling resistance, and can also eventually transform into irreversible fouling over time *(Choi et al., 2005)*.

Figure 3.5B shows that a minimum of around 2.2 m·s^{-1} (based on the change in slope) is required for continuous filtration, as maintaining v_{cf} below this value would increase the probability of development of reversible and/or irreversible fouling over time causing a higher resistance, and the eventual flux decline. It is important to note that v_{cf} optimized in this experiment could differ based on the feed composition used. For instance, poor flocculation may lead to higher suspended solids concentration in the filtrate, and the formation of a dense fouling layer could be unaffected by high cross-flow velocities. Therefore, similar experiments need to be conducted at different solids concentration to monitor how the trend of fouling development woud differ. When comparing with literatures, it is rather obvious that optimum cross-flow velocity is dependent on the type of waste stream used. For instance, for microfiltration of activated sludge with a polymeric membrane, v_{cf} of around 3 m·s^{-1} was needed. For secondary effluent from wastewater treatment, around 1 to 2 m·s^{-1} was required to maintain a stable flux (membrane material used was polymeric) (Al-Malack and Anderson, 1997). For a similar feed composition using inorganic membrane (ZrO$_2$), v_{cf} in the range of 1 to 3 m·s^{-1} showed stable results (Vera et al., 1997). In comparison to these studies, the optimum v_{cf} is within a comparable range. However, a greater understanding of the particle size distribution in the filtrate is required to gain a deeper insight into the specific forms of resistances.
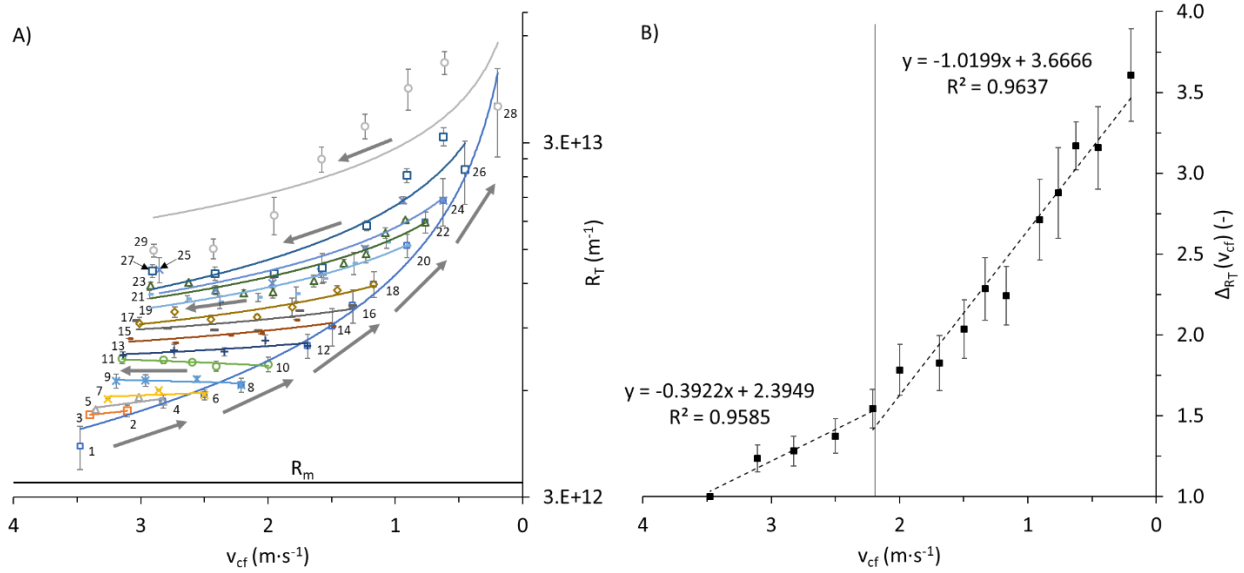
Figure 3.5: (a) Total resistance (R_T) as a function of v_{cf} for different cycles of v_{cf}, and (b) relative change of total resistance (d_{R_T}) as function of v_{cf}. **Note:** The numbers in **Figure 3.5A** represent the order in which v_{cf} was changed and reverted. Intermediate points are not marked with numbers in **Figure 3.5A** as only the end point is used to calculate $\Delta_{R_T}(v_{cf})$ in **Figure 3.5B**. The shaded arrows in **Figure 3.5A** indicate the direction in which the cross-flow velocity was changed. The shaded vertical line in **Figure 3.5B** indicates the requirement of a minimum v_{cf}, which could prevent rapid fouling. Note: Total resistance (R_T) is the sum of intrinsic membrane resistance (R_m), and fouling resistance (R_f).

3.3.3 Effect of cross-flow velocity on permeate flux at long-term operation

Since the context of this research focuses on the effect of cross-flow velocity (v_{cf}) on permeate flux (J), the optimization of microfiltration is not focused here. Nevertheless, cationic HPAS was suspected to have caused major fouling, and this could be corroborated by the experiments done on chemical and physical cleaning to sustain flux (see ***section 4.3.2***). In any case, two optimum methods (discussed in ***section 4.3.2***) were identified for long-term filtration (see **Table 3.2**), 1) Experiment A: Increased backwashing frequency (every 600 s for 20 s), or 2) Experiment B: Increased backwashing frequency (every 600 s for 20 s) along with reducing pH of the feed solution below the iso-electric point (IEP) of the ceramic membrane (IEP of **α**-Al_2O_3 is between 8 and 9 (Chen et al., 2021a)).

The former can mitigate pore narrowing and membrane fouling (Sayegh et al., 2021), while the latter along with the reduction of pore narrowing and membrane fouling, is suspected to have induced a change in charge of the ceramic membrane to more positive or neutral, and reduce interaction of cationic HPAS. Both experiments were performed well above the minimum v_{cf} of 2.2 m·s⁻¹ (see **Table 3.2**). The pump efficiency of P_C was fixed at 75 % for both experiments, but the repeated use of the membrane module without ex-situ cleaning may have affected the efficiency of the pump in maintaining similar flow rates for all experiments, and hence the discrepancy in the initial v_{cf} (see **Table 3.2**). Nevertheless, evaluating the change in v_{cf} and its effect on flux is crucial because TMP was established as a function of v_{CF} in ***section 3.3.1***. Additionally, as v_{CF} is reduced, the shear stress scouring the fouling layer declines, leading to more foulant deposition on the membrane surface and increasing the overall fouling resistance (R_f). In addition, decreasing v_{cf} reduces pressure loss, and TMP approaches p_{inlet} which contributes more towards fouling.

Table 3.2: Description of experiments performed with cross-flow ceramic tubular microfiltration (VSS ≈ TSS).

Experiment	Cleaning	Conditions	Frequency of physical cleaning	Duration of physical cleaning	Initial pH	TS (mg·L⁻¹)	TSS (mg·L⁻¹)	TOC (mg·L⁻¹)	DOC (mg·L⁻¹)	Initial v_{cf} (m·s⁻¹)
A	Physical	Backwashing			8.1					3.3
			600 seconds	20 seconds		6262 ± 619	430 ± 94	2326 ± 255	1508 ± 304	
B	Physical/ chemical	Backwashing			5.4					2.9

For experiment A, the dependence between v_{cf} and flux was evident. As shown in **Figure 3.6A**, the trends of decline and stability in flux and v_{CF} appear to be very similar. This indicates a potential correlation where the decline in v_{cf} is mirrored by a decline in flux, suggesting that reductions in v_{CF} may directly influence flux by altering the pressure conditions within the membrane module. For experiment B, there was further insight into the relationship between v_{cf} and flux. Notably, during the period from 70 to 108 hours, there was an increase in flux by approximately 20 % (from 66 to 79 LMH), while v_{cf} decreased from around 2.5 m·s⁻¹ to 1.5 m·s⁻¹ (see **Figure 3.6B**). This inverse relationship, where flux increased as v_{cf} decreased, implies a complex interaction between pressure drop and crossflow velocity. As v_{cf} decreases, the associated pressure drop decreases (TMP increases), allowing more permeate to pass through the membrane at lower v_{CF}.

To evaluate the effect of v_{cf} on flux, the parameters are plotted against each other, and the slope (m) is analyzed, and expressed as L·h⁻¹·m⁻²·bar⁻¹ (see values of m in **Figure 3.6C and 3.6D**). As shown in **Figure 3.6B**, beyond a certain pressure threshold, flux increases significantly. This trend is particularly notable in experiment B, evidenced by the positive slope value (m(IV)) in **Figure 3.6D**. This slope indicates a strong positive correlation between TMP and flux, possibly supporting the hypothesis that higher TMPs (due to declining cross-flow velocities) enhance permeate flux. A similar trend was observed in experiment A, as indicated by the slope value (m (IV)) in **Figure 3.6C**. Based on the results obtained in this study, maintaining cross-flow velocities below optimum conditions can affect membrane filtration in two ways, 1) low shearing rates, which leads to rapid fouling, and 2) quick decline in cross-flow velocity, which causes subsequent increase in TMP, leading to more fouling. In conclusion, working with an optimum cross-flow velocity is highly important, especially due to the indirect relationship with TMP. The pressure loss at high cross-flow velocities can be an advantage in terms of maintaining long-term filtration. In addition, it could be seen that declining cross-flow velocities could enhance permeate flux.
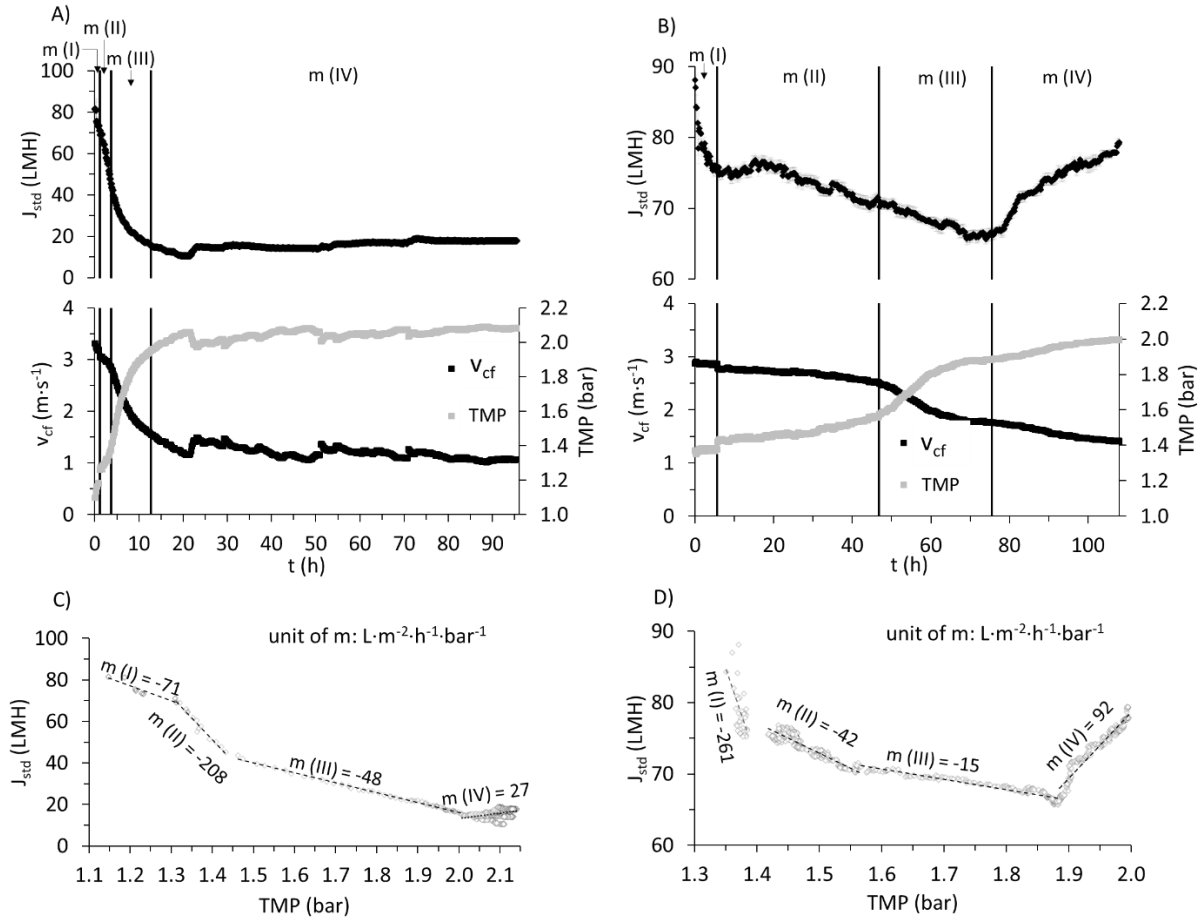
Figure 3.6: Variation of standardized permeate flux (J_{std}), transmembrane pressure (TMP), and cross-flow velocity (v_{cf}) for (a) filtration with backwashing cycles every 600 s for 20s (experiment A), (b) filtration with backwashing cycles every 600 s for 20 s with pH reduced to 5.4 in the feed at the start of the filtration (experiment B). Correlation between standardized permeate flux (J_{std}), and empirical transmembrane pressure (TMP) for (c) experiment A, and (d) experiment B. The correlation is expressed as slope values (m) and the unit of m is $L·h^{-1}·m^{-2}·bar^{-1}$.

3.4   Conclusions

Understanding the relationship between cross-flow velocity, transmembrane pressure, and permeate flux is critical for optimizing cross-flow tubular microfiltration and achieving stable long-term membrane performance. However, there is a lack of understanding about the exact reasons for pressure loss in this study as frictional loss did not account for a significant part of the overall pressure loss. It is suspected that the centrifugal pump plays a predominant role in influencing the pressure profile within the module. In any case, pressure drops due to cross-flow velocity can reduce transmembrane pressure and eventually the permeate flux. High cross-flow velocities can mitigate reversible fouling by reducing transmembrane pressure (due to pressure drops), and by improving shearing rates. Long-term experiments showed that declining cross-flow velocities can affect permeate flux by aggravating fouling due to increasing transmembrane pressure (declining pressure drop).

4 Separation of short-chain fatty acids from primary sludge into a particle-free permeate by coupling chamber filter-press and cross-flow microfiltration: Optimization, semi-continuous operation and evalua-tion

Graphical abstract
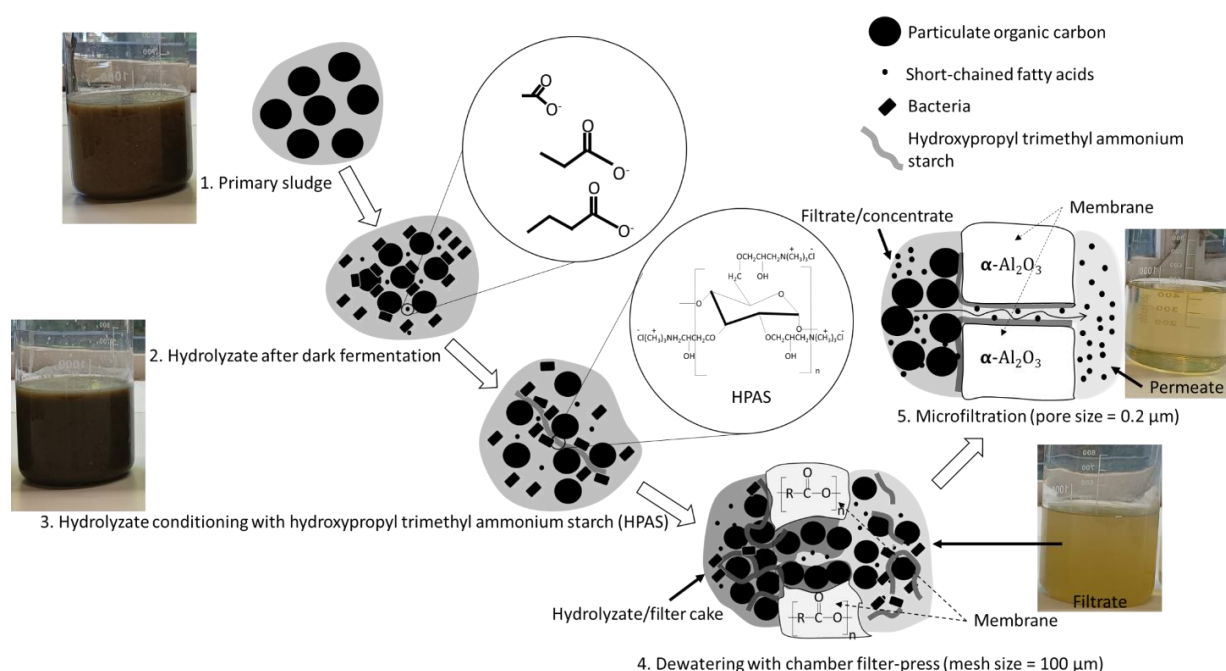
Abstract

Short-chain fatty acids (SCFAs) are valuable metabolic intermediates that are produced during dark fermentation of sludge, which when capitalized on, can be used as chemical precursors for biotechnological applications. However, high concentrations of solids with SCFAs in hydrolyzed sludge can be highly detrimental to downstream recovery processes. This pilot-scale study addresses this limitation and explores the recovery of SCFAs from primary sludge into a particle-free permeate through a combination of chamber filter-press (material: polyester, mesh size: 100 µm) and cross-flow microfiltration (material: α-Al$_2$O$_3$, pore size: 0.2 µm, cross-flow velocity: 3 m·s^{-1}, pressure = 2.2 bars). Firstly, primary sludge underwent dark fermentation yielding a hydrolyzate with a significant concentration of SCFAs along with total solids (TS) concentration in the range of 20 to 30 g·L^{-1}. The hydrolyzate was conditioned with hydroxypropyl trimethyl ammonium starch (HPAS), and then dewatered using a filter-press reducing TS by at least 60%, resulting in a filtrate with suspended solids concentration ranging from 100 to 1300 mg·L^{-1}. Despite the lower suspended solids concentration, the microfiltration membrane underwent severe fouling due to HPAS' electrostatic interaction. Two methods were optimized for microfiltration, 1) increased backwashing frequency can sustain permeate flux of 20 L·m^{-2}·h^{-1} (LMH), and 2) surface charge modification can maintain flux between 70 and 80

LMH. With backwashing, microfiltration can filter around 900 $L \cdot m_{eff}^{-2}$ (without chemical cleaning) with flux between 50 and 60 LMH under semi-continuous operation. Evaluating the particle-free permeate obtained from the treatment chain, around 4 $gC_{SCFAs} \cdot capita^{-1} \cdot d^{-1}$ can be recovered from primary sludge with a purity of 0.85 to 0.97 $C_{SCFAs} \cdot DOC^{-1}$.

Highlights

- 60 %-solids removal with filter-press after starch-based flocculation

- Cationic starch-based flocculant can severely foul microfiltration membrane

- Backwashing or surface charge modification can mitigate fouling

- Around 4 $gC_{SCFAs} \cdot capita^{-1} \cdot d^{-1}$ can be recovered from the solids stream

- SCFAs (as carbon equivalents) to DOC averages around 90 % in the permeate

Keywords

Primary sludge, dark fermentation, short-chain fatty acids, flocculation, microfiltration, biorefinery

4.1   Introduction

Out of the influent load of 40 $g_{TOC} \cdot capita^{-1} \cdot d^{-1}$, a sludge load of 24 $g_{TOC} \cdot capita^{-1} \cdot d^{-1}$ is produced in a conventional municipal wastewater treatment plant (WWTP) (Wan et al., 2016). Although sludge produced serves as an excellent source for biogas production, within the context of a wastewater biorefinery (WWBr), organic carbon in sludge can be tapped more efficiently to produce bio-based products that have more value in the economy in comparison to biogas (Da Ros et al., 2020). Some of the bio-based products that have gained increasing interests in recent years include bioplastics (Pittmann and Steinmetz, 2016) and biohydrogen (Wong et al., 2014), typically due to their green nature. Therefore, research in the last decades has focused more towards fermentation of short-chain fatty acids (SCFAs) from waste streams as they can serve as valuable precursors for biotechnological applications (Atasoy et al., 2018).

To operate an economically viable WWBr, fermentation of SCFAs from the solids stream needs to be optimized, and dark fermentation is an effective method to produce SCFAs (Shylaja Prakash et al., 2024). However, the amount of total solids converted to gas is very low during dark fermentation, and the solids are still mostly present in the suspended and dissolved phase. Hence, the total solids concentration between sludge and hydrolyzed primary sludge or hydrolyzate is similar. This means that the concentration of particles present in the hydrolyzate is very high and cannot be directly processed in biotechnological applications. It is also important to consider the diverse microflora present in sludge (M. Huang et al., 2017), which can interfere with downstream recovery processes. For instance, in their pilot-scale study on polyhydroxyalkanoates (PHA) accumulation using mixed cultures from industrial wastewater (Tamis et al., 2014), the authors clearly outlined the importance of having a suspended solids-free substrate for better PHA yields. The authors also highlighted the impedance on PHA yields caused by organisms that are incapable of storing PHAs. Similarly, another pilot-scale study described that higher PHA yields could be achieved with a particle-free wastewater (Ntaikou et al., 2014). In case of biohydrogen production using microbial electrolysis cells, growth of methanogens has shown to compromise the overall hydrogen recovery process (Cusick et al., 2011; Rivera et al., 2015). These drawbacks due to particles or microorganisms in sludge can be tackled by implementing membrane technology to produce a particle-free permeate for biotechnological use.

Separation of short-chain fatty acids from primary sludge into a particle-free permeate by coupling chamber filter-press and cross-flow microfiltration: Optimization, semi-continuous operation and evaluation

Microfiltration can offer an economical and technical advantage, as low-molecular-weight compounds can be separated from the particulate waste stream through size sieving mechanism (Cho et al., 2012). Ceramic membranes in particular have attracted increasing interest because of their narrow pore size distribution, robustness, wide range of pH tolerance, high porosity, and hydrophilicity which leads to higher permeate fluxes and reduced fouling in comparison to polymeric membranes (Chen et al., 2021b; Hofs et al., 2011). Indeed, the pore size is a crucial factor as it is important to allow only the dissolved compounds to pass through. Typically, the size range of microfiltration membranes can vary between 0.1 and 10 µm (Samanta et al., 2022). A membrane cut-off of 0.2 µm was found to be optimum (Tuczinski et al. 2018), as the particles can be separated from SCFAs. Nevertheless, the authors demonstrated that microfiltration membrane can reject up to 15 % of SCFAs (within a cut-off range of 0.1 to 0.8 µm) due to adsorption on particles. Similarly, it was reported that, dissolved organic compounds could be retained by a 0.2 µm ceramic membrane up to 20 % due to the presence of high suspended solids concentrations (Samanta et al., 2022). Therefore, in this study, a chamber-filter press was introduced as a pre-treatment stage to sieve off larger particles and reduce the suspended solids load on microfiltration.

In this study, experiments were carried out at pilot-scale to treat primary sludge in a real WWTP. Dark fermentation was subjected to long-term experimentation under different organic loading rates which could produce hydrolyzate with varying total solids concentration. The hydrolyzate was conditioned with a cationic flocculant, and then dewatered using a chamber filter-press, which would then undergo cross-flow microfiltration. For this research, starch-based flocculant was used due its economic viability, environmental friendliness and biodegradability in comparison to its synthetic counterpart which poses a hazardous nature (Razali and Ariffin, 2015). In general, SCFAs produced in dark fermentation can generate a higher revenue than biogas, when used for bio-based products recovery (like PHAs) (Da Ros et al., 2020). However, the yields calculated for such bio-based products solely based on the performance of dark fermentation may not be practical, as the presence of particles can significantly impede the functioning of downstream processes. Hence, the novel treatment chain presented here at pilot-scale to produce a particle-free SCFAs permeate via membrane technology offers a practical solution to the aforementioned issues due to particles, and could be a potential concept to sustain a functional WWBr. To the best of our knowledge, a combination of solids separation and dark fermentation to produce a substrate free of particles containing predominantly SCFAs has not been reported in literatures so far. The main objectives of this research were 1) sludge conditioning using biodegradable cationic starch-based flocculant to produce low suspended solids filtrate for microfiltration, 2) identifying fouling and providing suitable remedies for long-term cross-flow microfiltration, and 3) evaluating the overall treatment chain in a semi-continuous mode for SCFAs recovery at pilot-scale in terms of load and revenue generated.

4.2   Materials and Methods
4.2.1   Experimental setup
In this study, experiments were carried out at pilot-scale in a wastewater research facility (Buesnau, Germany). Based on the influent flowrate (24 $m^3 \cdot d^{-1}$) into the primary sedimentation tank, and total suspended solids concentration (TSS) in the range of 50 to 500 $mg \cdot L^{-1}$ in the inflow to this WWTP (Lasaki et al., 2024), around 100 to 150 L of primary sludge was produced per day. There are three major steps in this study, 1) dark fermentation of primary sludge to produce SCFAs, 2) conditioning of primary sludge after dark fermentation (i.e., hydrolyzate) with a starch-based flocculant followed by dewatering using a chamber-filter press to reduce solids concentration, and 3) cross-flow microfiltration to recover

Separation of short-chain fatty acids from primary sludge into a particle-free permeate by coupling chamber filter-press and cross-flow microfiltration: Optimization, semi-continuous operation and evaluation

SCFAs in a particle-free permeate. The three steps were optimized separately, and then were combined together and evaluated as a treatment chain. The descriptions of the experimental setup can be found in the sub-sections below. The schematic representation of the cascade can be found in **Figure 4.1**.

Primary sedimentation tank coupled to a dark fermentation reactor

A primary sedimentation tank with a volume of 3 m^3 was coupled to a dark fermentation reactor (made of stainless-steel insulated with polyurethane) with a total volume of 0.3 m^3. The working volume of the reactor was kept at 0.2 m^3 (130 L of primary sludge was produced on an average per day) to maintain a hydraulic retention time (HRT) of 1.5 d (changes in HRT are described in *section 4.3.3*). A screw pump (Netzsch, Germany) with a flow rate of 4300 L·h^{-1} (22 recirculations per hour), was used for homogenization as well as to harvest the hydrolyzate and feed the primary sludge. The screw pump at this flowrate experienced energy losses, which was transformed to heat. The polyurethane insulation of the reactor vessel may have prevented this heat from dissipating, resulting in temperature containment within the reactor and an eventual temperature rise, thus, a temperature of 32 °C could be maintained without using an external thermostat. Two dosage pumps (Prominent, Germany), were implemented in the recirculation line of the setup to control the pH-value. The pH-value was adjusted using 5 M-HCl and-NaOH solutions. A pH electrode (Greisinger, Germany) was also installed in the recirculation line, and the data was monitored using a data acquisition software (Volker Preyl, Germany). The flow rate of the gas produced was recorded using a drum-type gas meter (Ritter, Germany). Gas samples were collected regularly from the headspace of the reactor, and the composition of the gases was analyzed using a gas chromatograph coupled with a helium ionization detector (HP 6890 series, USA).

Lab-scale-and pilot-scale-sludge conditioning and pilot-scale dewatering

Firstly, the hydrolyzate that was harvested from dark fermentation underwent lab-scale flocculation experiments to determine optimum dosages of flocculant which could then be used for the pilot-scale filter-press. Flocculation was performed using 0.4 L-beakers which were agitated using stainless-steel stirrers. For lab-scale (*section 4.3.1*), and pilot-scale (*section 4.3.2*) tests, potato-based starch (Emsland KCG 750, Emsland group, Germany) was used. The starch-based flocculant was grafted with 2,3-epoxypropyltrimethylammonium chloride. The end product was hydroxypropyl trimethyl ammonium starch (HPAS). Details to the starch-based flocculants can be found elsewhere (Hermann-Josef Melcher and Jan Berg, 2013). Following the dosage of HPAS at lab-scale, the hydrolyzate underwent rapid stirring at 150 rpm (rotations per minute) for 10 minutes (for colloidal destabilization) followed by slow stirring at 80 rpm for 10 minutes to ensure floc formation. The hydrolyzate was then poured on to the sieves, which were subjected to gravity-driven filtration. These filtrations were carried out using a polyester-based sieve (mesh size: 630 µm; RAI-TILLIERES SAS, France), and stainless-steel sieves (mesh size: 100 µm).

For pilot-scale experiments (experimented as a cascade in *section 4.3.4*), pea-based starch (HKF CleanTech AG, Germany) was utilized. The change in the type of HPAS from the lab-scale was due to the discontinued supply of the previous starch-based flocculant. In any case, using a similar grafting procedure as described previously, HPAS was generated as the end product. A stainless-steel stirrer was used for rapid-stirring to destabilize the colloids. A screw pump was used for slow mixing to promote floc formation. The total duration of mixing (rapid and slow) was between 15 and 20 minutes. Based on the average volume of the daily-harvested hydrolyzate (around 130 L), 4 chambers are required per dewatering experiment. The chambers were lined with polyester-based sieves (mesh size: 100 µm), and

clamped at a pressure of 400 bars using a hydraulic lever. Once the chambers were filled completely, the pressure in the chambers could be increased up to 15 bars. Filtration was stopped when the flow rate was very low, after which chambers were opened to remove the highly concentrated filter cake. A submersible pump was used to transfer the filtrate to a feed tank prior to microfiltration.

4.2.2 Pilot-scale microfiltration

A preconfigured cross-flow filtration setup incorporated with pumps and sensors obtained from Atec, Ulm, Germany was used to treat the filtrate generated from the chamber-filter press. In this research, two tubular ceramic microfiltration membranes (Inopor, Germany) were integrated into the filtration setup. The following are the details to the ceramic microfiltration membranes, material: $\boldsymbol{\alpha}$-Al_2O_3, pore size = 0.2 µm, length = 1.2 m, number of channels = 7, channel diameter = 6 mm, effective filtration area = 0.316 m^2. A pre-filter (Atec, Ulm, Germany) with a pore size of 60 µm was utilized prior to cross-flow microfiltration to prevent larger particles from entering the membrane module. Manometer, permeate flow sensor, cross-flow sensor and temperature sensor were part of the filtration setup as shown in **Figure 4.1**. A vacuum pump sucked the feed liquid into the system, while a centrifugal pump generated the required cross-flow. Inlet pressure was fixed at 2.2 bars. Separate external tanks depending on the feed, clean water, or cleaning solutions (acid or base) were used for microfiltration (see **Figure 4.1**). Microfiltration was either experimented in recirculation condition or concentrating condition. In the recirculation condition, the concentrate and permeate are directed to the feed tank to maintain a constant feed composition, while in concentrating condition, only the concentrate is recirculated back into the feed tank whereas the permeate is collected separately. The former is done to optimize the microfiltration process, while the latter is done to replicate a realistic condition. Flux determined with clean water for the ceramic membrane or clean water flux (J_{CW}) was found to be 135 $L \cdot m_{eff}^{-2} \cdot h^{-1}$ or LMH. To recover the flux, membrane cleaning after filtration with the filtrate was done as follows,

1) Filtration with clean water at 40 °C for 1 hour at 3 m·s^{-1}
2) Filtration with an alkaline solution (Atec, Ulm, Germany; Product no.: Atec 2610) at pH 12 at 40 °C for 1 hour at 3 m·s^{-1}
3) Filtration with clean water at 40 °C for 0.5 hours at 3 m·s^{-1}
4) Filtration with an acidic solution (Atec, Ulm, Germany; Product no.: Atec 3027) at pH 2 at 40 °C for 1 hour at 3 m·s^{-1}
5) Filtration with clean water at 40 °C for 0.5 hours at 3 m·s^{-1}
6) Chemical cleaning is exclusive to this study due to the type of wastewater used, and a detailed description can be found in ***section 4.3.2***.

Separation of short-chain fatty acids from primary sludge into a particle-free permeate by coupling chamber filter-press and cross-flow microfiltration: Optimization, semi-continuous operation and evaluation
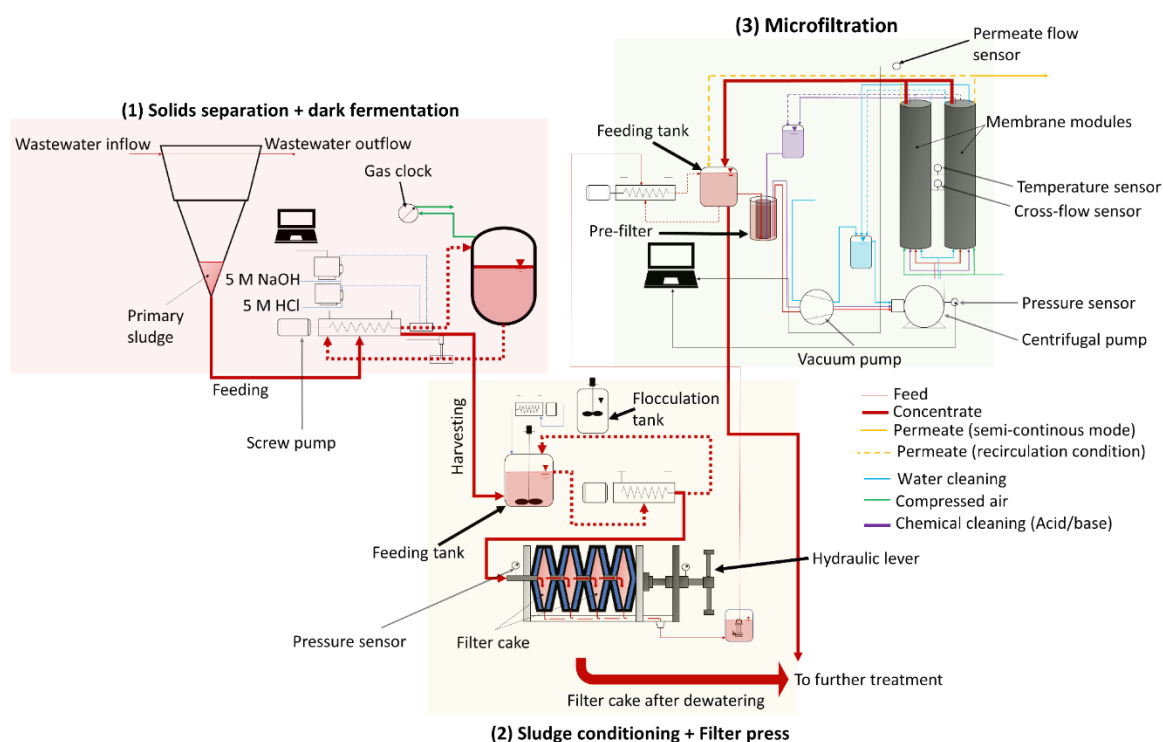
Figure 4.1: Schematic representation of the cascade comprising of 1) solids separation and dark fermentation, 2) sludge conditioning and dewatering using a chamber filter-press, and 3) microfiltration.

4.2.3 Analytical methods

Total organic carbon (TOC) was measured according to DIN EN 13137 (Characterization of waste - Determination of total organic carbon (TOC) in waste, sludges and sediments, 2001). Total solids (TS) and volatile solids (VS) were measured using standard methods (DIN 38414) (German standard methods for the examination of water, waste water and sludge; sludge and sediments (group S); determination of water content, of dry residue and of solids content (S 2), 1985). Total suspended solids (TSS) and volatile suspended solids (VSS) were determined according to (Rice et al., 2017). To measure the dissolved parameters, samples were first centrifuged at 4000 rpm. Then, the supernatant was filtered off using a glass fiber membrane with a pore size of 1 µm, followed by a regenerated cellulose membrane with a pore size of 0.45 µm. Dissolved organic carbon (DOC) was measured in accordance with DIN EN 1484 (Water analysis - Guidelines for the determination of total organic carbon (TOC) and dissolved organic carbon (DOC), 2019). In addition, lactic acid and SCFAs (acetic acid (HAc), propionic acid (HPr), iso-butyric acid (Hbu-iso), butyric acid (Hbu), and iso-valeric and valeric acid (HVa-iso and HVA) from the filtered samples were detected using ion chromatography (IC) (881 Compact Pro (Metrohm, Switzerland)). Lactic acid had a high instability in production and was found only in very low concentrations. Therefore, lactic acid was not included in calculations. All the above-mentioned parameters were measured in duplicates. SCFAs were measured on a daily basis for pilot-scale dark fermentation. In case of dewatering (lab- and pilot-scale), samples were measured in the feed (at the start), concentrate and filtrate (at the end of the run). In case of optimization of microfiltration, parameters were measured on a daily basis. For semi-continuous microfiltration, parameters were measured once in the feed (at the start of filtration) and twice in the concentrate and permeate, once when half the volume recovery was reached, and finally at the end of the filtration run. Dissolved oxygen

concentration (GMH 5630, Greisinger, Germany) and oxidation reduction potential (WTW, Multi 350i, Xylem, USA) were measured occasionally in the dark fermentation reactor to ensure anaerobic conditions, as the reactor underwent regular feeding. Dissolved oxygen concentration was approximately 0 mg·L^{-1}, and ORP was between minus 350 mV and minus 390 mV.

4.2.4 Data interpretation

Since this research focuses on two key steps, dark fermentation and membrane filtration, the equations are classified below in separate sections.

Fermentation

The yields of SCFAs in dark fermentation, Y_{SCFAS}, was calculated using the following equation,

$$Y_{SCFAs} \ [\%] = \left\{ \frac{c_{SCFAs,out} \ [g_C \cdot L^{-1}] \times \frac{V_{f/h}[L]}{V_W \ [L] \times dt \ (d)}}{OLR \ [g_{TOC} \cdot L^{-1} \cdot d^{-1}]} \right\} \times 100 \qquad 4.1$$

where $c_{SCFAs,out}$ represents the mass concentrations of SCFAs (as carbon equivalents) in the effluent of the dark fermentation reactor. V_W is the working volume and $V_{f/h}$ is the volume fed or harvested per day. OLR is the organic loading rate, expressed as g of total organic carbon (TOC) fed per liter and day. Primary sludge is hydrolysed when it enters the dark fermentation reactor, but this is not implemented in the equation. Since hydrolysis in the sedimentation zone is inevitable, yields were evaluated in the hydrolysate.

Filtration

Permeate flux (J_{std}) for microfiltration was standardized to 25°C, and calculated using the following equation,

$$J_{std} \left[L \cdot m_{eff}^{-2} \cdot h^{-1}; \ LMH \right] = \frac{Q_{permeate} \left[\frac{L}{h} \right]}{A_{eff} \ [m^2] \times f_T} \qquad 4.2$$

where $Q_{permeate}$ is the permeate flow rate, A_{eff} is the effective filtration area of the membrane (0.316 m^2), and f_T is the temperature correction factor. f_T was calculated using a calibration curve between clean water flux and temperature (see **Appendix A7**).

Cross-flow velocity (v_{CF}) was calculated according to the equation given below,

$$v_{CF} \ [m \cdot s^{-1}] = \frac{Q_{CF} \left[\frac{m^3}{s} \right]}{A_{CS} \ [m^2]} \qquad 4.3$$

where Q_{CF} is the volumetric flow rate in the tubular membrane channels, and A_{CS} is the cross-sectional area of the membrane channels.

The dosage of HPAS (D_{HPAS}) in the hydrolyzate was calculated as follows,

$$D_{HPAS} [mg_{HPAS} \cdot g_{TS}^{-1}] = \frac{m_{HPAS} [mg]}{V_{hyd} \ [L] \times TS \left[\frac{g}{L} \right]} \qquad 4.4$$

where m_{HPAS} is the amount of HPAS dosed, V_{hyd} is the volume of hydrolyzate, and TS is the total solids concentration in the hydrolyzate.

The volume recovery (V_{rec}) after microfiltration or filter-press was calculated as follows,

$$V_{rec} \ (\%) = \frac{V_{p,f} \ [L]}{V_{f \ [L]}} \times 100 \qquad\qquad 4.5$$

where $V_{p,f}$ is final volume in the permeate (for microfiltration)/filtrate (filter-press) after filtration and V_f is the initial volume in the feed prior to start of filtration.

Retention (R_x) of a certain parameter (represented as x) was calculated according to the follow equation,

$$R_x \ (\%) = \left\{ \frac{C_{in,x} - C_{out,x} \ [mg \cdot L^{-1}]}{C_{in,x} \ [mg \cdot L^{-1}]} \right\} \times 100 \qquad\qquad 4.6$$

where $C_{in,x}$ and $C_{out,x}$ is the concentration of a certain parameter x in the influent and effluent of the corresponding membrane process (chamber filter-press or microfiltration), respectively.

Recovery of SCFAs: dark fermentation-filter-press-microfiltration cascade

To calculate recovery of SCFAs (Rec_{SCFAs}) after filtration, **equation 4.1** is modified as shown below to include V_{rec} after subsequent filtration steps,

$$Rec_{SCFAs} \ [\%] = \left\{ \frac{c_{SCFAs,f/p}[g_C \cdot L^{-1}] \times V_{p,f} \ (L)}{OLR \ [g_{TOC} \cdot L^{-1} \cdot d^{-1}] \times HRT \ (d) \times V_{f/h}[L]} \right\} \times 100 \qquad\qquad 4.7$$

Where, $c_{SCFAs,f/p}$ represents the mass concentrations of SCFAs (as carbon equivalents) in the filtrate or permeate. HRT is the hydraulic retention time.

Permeate quality after microfiltration (f_{DOC}) was assessed based on ratio of SCFAs (as carbon equivalents) to DOC,

$$f_{DOC} \ [\%] = \left\{ \frac{c_{SCFAs,p}[g_C \cdot L^{-1}]}{DOC_p \ [g \cdot L^{-1}]} \right\} \times 100 \qquad\qquad 4.8$$

Where, $c_{SCFAs,p}$ represents the mass concentrations of SCFAs (as carbon equivalents) in the permeate, and DOC_p is the concentration of dissolved organic carbon (DOC) in the permeate.

4.3   Results and discussions

In this study, there are three major parts, 1) optimization of flocculation at lab-scale to produce a low-solids filtrate (discussed in *section 4.3.1*), and optimization of microfiltration at pilot-scale to determine an optimum method to ensure long-term filtration (discussed in *section 4.3.2*), 2) semi-continuous operation of treatment chain comprising of pilot-scale dark fermentation (*section 4.3.3*), chamber filter-press (*section 4.3.4*) and microfiltration (*section 4.3.4* and *section 4.3.5*) under optimized conditions, and 3) evaluation of SCFAs recovery out of the treatment chain (*section 4.3.6*).

4.3.1   Lab-scale flocculation experiments to test dewaterability of hydrolyzed primary sludge Semi-continuous mode

Initially, a lab-scale study was conducted on hydrolyzed primary sludge or hydrolyzate with total solids (TS) content in the range of approximately 30 to 50 g·L^{-1} to test the flocculation efficiency of the starch-

based flocculant. Experiments were performed to test the dosage requirement, and its influence on retention of TS, and the attainable effluent quality. Potato-based hydroxypropyl trimethyl ammonium starch (HPAS) was used for the batch tests as described in ***section 4.2.1***. Initially, three batch experiments were carried out with a 630 µm sieve (pH 6 to 6.3), and the trend in retained TS on the sieves was monitored. In the first two batch tests (see **Table 4.1**), there was a rise in retained TS, which was followed by a breakpoint. The increase in TS suggests the destabilization of the negatively charged colloids, while further addition of HPAS led to a decline in retained TS due to the excess positive charge from HPAS causing repulsion and the eventual restabilization (M. Huang et al., 2017). In the first two batch tests, the highest value of retained TS was at a similar HPAS-dosage (D_{HPAS}) of 33 $mg_{HPAS} \cdot g_{TS}^{-1}$, after which a breakpoint was observed. The third batch showed no breakpoint, and the TS retained on the sieve increased until D_{HPAS} of 45 $mg_{HPAS} \cdot g_{TS}^{-1}$. This effect is suspected to have been caused by the contents of the hydrolyzate, which is evaluated further in the 100 µm batch tests.
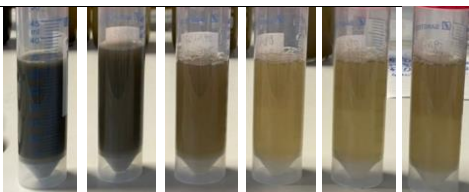
In the 100 µm batch tests (fourth and fifth batch; pH 8.97), there appears to be delayed response in breakpoint in the fourth batch in comparison to the fifth batch (see **Table 4.1**). In the fourth batch, the highest retained TS (79 $g \cdot kg^{-1}$) was achieved at D_{HPAS} of 39 $mg_{HPAS} \cdot g_{TS}^{-1}$, and this dosage is significantly higher than the fifth batch (25 $mg_{HPAS} \cdot g_{TS}^{-1}$). Interestingly, the concentration of SCFAs and DOC was higher in the fourth batch (3210 $mg_{DOC} \cdot L^{-1}$; 5119 $mg_{SCFAs, HAc} \cdot L^{-1}$) than in the fifth (2220 $mg_{DOC} \cdot L^{-1}$; 4188 $mg_{SCFAs, HAc} \cdot L^{-1}$). During dark fermentation, complex organic compounds are broken down into simpler molecules which are then fermented into SCFAs. A large part of the dissolved organic fraction can be in the form of molecules that contain carboxylic acid groups, which can be deprotonated at higher pH-values. In addition to the dissolved components, it is also important to consider the negative charges on microbes [7,17], and a more hydrolyzed sludge can contain more biomass. Overall, this increases the negative charge in the hydrolyzate, and the amount of HPAS required to neutralize the negative charge in the hydrolyzate increases. Therefore, the lack of breakpoint in the third batch could be that the sludge obtained was hydrolyzed more, requiring a higher dosage of HPAS.

Looking into the effect of pH, the flocculation efficiency was compared between the two sieves. TS retained on the sieve was normalized to TS in the hydrolyzate (i.e., ratio of TS retained on the sieve to the TS in hydrolyzate; see **Table 4.1**). The average values of ratio of TS retained on the sieve normalized to the TS in hydrolyzate was 2.2 ± 0.3 for the 630 µm batch tests (pH 6 to 6.3), while it was 2.1 ± 0.2 for the 100 µm batch tests (pH 8.97). It appears as though an alkaline pH does not have a significant effect on flocculation efficiency (within the tested range) as the filtrate in the fifth batch (pH 8.97) also showed a low total suspended solids (TSS) concentration of 330 $mg \cdot L^{-1}$ (see photograph of filtrate in **Table 4.1** for fifth batch at D_{HPAS} of 30 $mg_{HPAS} \cdot g_{TS}^{-1}$). In line with this finding, it was shown that a positive charge density for cellulose-based flocculant could be held relatively stable between pH 7 and 9, while a significant decline was observed only when the pH-value was increased to 10 (Suopajärvi et al., 2017).

Evaluating the filtrate in the fourth and fifth batch tests (100 µm), sludge conditioning is of absolute necessity as R_{TS} is very low without conditioning. In both batch tests (100 µm) without conditioning, R_{TS} is less than 60 %, while optimum dosages can remove more than 75 % of TS. It is necessary to maintain a D_{HPAS} within an optimum range to avoid having high TSS concentration in the filtrate which can significantly increase cake layer formation on the microfiltration membrane (Choi et al., 2005), and lead to higher retention of SCFAs due to adsorption on particles. Since dry matter content in hydrolyzate can change on a daily basis, optimum dosage cannot be always maintained as it takes at least 48 h to determine the dry matter content. However, based on the range of total solids in the hydrolyzate in this study, filtrate with a low TSS can be achieved within the tested range of flocculant dosage.

Table 4.1: Gravity driven batch tests with different sieve sizes to test flocculation efficiency. The photographs are representative of the filtrate from the fifth batch test with 100 µm sieve.

Sieve Size	pH	TS in Hydrolyzate	Batch Number							
	pH 6.3	38 g·L⁻¹	First batch	D_{HPAS} (mg$_{HPAS}$·g$_{TS}$⁻¹)	0	13	20	25	33	38
				TS retained on sieve (g·kg⁻¹)	-	77	83	87	91	90
				$\frac{\text{TS retained on sieve (g·kg}^{-1})}{\text{TS in hydrolyzate (g·kg}^{-1})}$ (−)	-	2	2.2	2.3	2.4	2.4
600 µm		45 g·L⁻¹	Second batch	D_{HPAS} (mg$_{HPAS}$·g$_{TS}$⁻¹)	0	20	22	25	27	30
				TS retained on sieve (g·kg⁻¹)	-	79	86	88	82	82
	pH 6			$\frac{\text{TS retained on sieve (g·kg}^{-1})}{\text{TS in hydrolyzate (g·kg}^{-1})}$ (−)	-	1.8	1.9	2	1.8	1.8
		36 g·L⁻¹	Third batch	D_{HPAS} (mg$_{HPAS}$·g$_{TS}$⁻¹)	0	13	20	27	34	39
				TS retained on sieve (g·kg⁻¹)	79	82	82	89	89	92
				$\frac{\text{TS retained on sieve (g·kg}^{-1})}{\text{TS in hydrolyzate (g·kg}^{-1})}$ (−)	2.2	2.3	2.3	2.5	2.5	2.6
		33 g·L⁻¹	Fourth batch	D_{HPAS} (mg$_{HPAS}$·g$_{TS}$⁻¹)	0	18	27	30	39	41
				TS retained on sieve (g·kg⁻¹)	63	65	67	70	79	78
				$\frac{\text{TS retained on sieve (g·kg}^{-1})}{\text{TS in hydrolyzate (g·kg}^{-1})}$ (−)	1.9	2	2	2.1	2.4	2.4
				TS in the filtrate (mg·L⁻¹)	14197	9519	9439	8329	8075	8378
				R_{TS} (%)	57	71	72	75	76	75
100 µm	pH 8.7			D_{HPAS} (mg$_{HPAS}$·g$_{TS}$⁻¹)	0	18	25	30	36	39
				TS retained on sieve (g·kg⁻¹)	65	73	77	72	65	66
				$\frac{\text{TS retained on sieve (g·kg}^{-1})}{\text{TS in hydrolyzate (g·kg}^{-1})}$ (−)	1.9	2.1	2.2	2.1	1.9	1.9
				TS in the filtrate (mg·L⁻¹)	14754	10,372	8929	8288	7982	8086
				R_{TS} (%)	58	71	75	76	77	77
				TSS in the filtrate (mg·L⁻¹)	-	-	630	330	630	750
		35 g·L⁻¹	Fifth batch	$\frac{\text{TSS in the filtrate (mg·L}^{-1})}{\text{TS in hydrolyzate (g·L}^{-1})}$ (mg·g⁻¹)	-	-	18	9	18	21

Visual observation of filtrate

4.3.2 Evaluating membrane performance at pilot-scale to physical and chemical cleaning methods

Following the optimum dosage that was determined at lab-scale, dewatering was done using a pilot-scale chamber filter-press at a dosage of 28 mg$_{HPAS}$·g$_{TS}$⁻¹ to produce a filtrate which could be then used for optimizing microfiltration. The dewatering procedure produced a filtrate with low TS and TSS concentrations as shown in **Table 4.2**. Since the aim was to optimize microfiltration based on the produced filtrate, this particular pilot-scale dewatering experiment was not assessed in detail. However, the analysis of retention parameters for the filter-press is performed in detail during the semi-continuous operation in *section 4.3.4*. In any case, the objective was to optimize microfiltration with the filtrate to ensure long-term operation without fouling which could then be used for semi-continuous filtration. Concentrate and permeate were recycled back into the feed solution (recirculation condition as shown in **Figure 4.1**) to maintain consistent feed composition. All experiments were performed at cross-flow velocity averaging at 3 ± 0.2 m·s⁻¹. The details to the experiment and composition of the filtrate can be found in **Table 4.2**,

Separation of short-chain fatty acids from primary sludge into a particle-free permeate by coupling chamber filter-press and cross-flow microfiltration: Optimization, semi-continuous operation and evaluation

Table 4.2: Description of experiments performed with cross-flow ceramic tubular microfiltration (VSS ≈ TSS).

Exp	Cleaning	Conditions	Frequency of physical cleaning	Duration of physical cleaning	pH[b]	TS (mg·L^{-1})	TSS (mg·L^{-1})	TOC (mg·L^{-1})	DOC (mg·L^{-1})
1	Physical	Relaxation	300 seconds	10 seconds	7.8				
2	Physical/ chemical	Relaxation	600 seconds		8				
3	Physical	Backwashing	1800 seconds	20 seconds	8.3	6262 ± 619	430 ± 94	2326 ± 255	1508 ± 304
4	Physical	Backwashing			8.1				
5	Physical/c hemical	Backwashing	600 seconds		5.4[a]				

[a]the pH-value was reduced from 8 to 5.4 with HCl, [b]the pH-value at the start of the experiment

Experiment 1 was performed with relaxation cycles wherein the pressure would be released every 300 s for 10 s, allowing the cross-flow to scour the membrane surface. Interestingly, loss of standardized flux (i.e., J_{std}) occurred in the first 6 hours (see **Figure 4.2A)** of filtration despite the low total suspended solids (TSS) concentration and the high cross-flow velocity used. It is important to consider the nature of the foulants, and not only the concentration. Hydroxypropyl trimethyl ammonium starch (HPAS) can foul the membrane via electrostatic interaction, as ceramic membranes have an iso-electric point (IEP). For **α**-Al_2O_3, IEP was found to be in the range of 8 to 9 (Chen et al., 2021a). Since pH-value is in the range of IEP (pH 7.8), unbound cationic HPAS or particles bound to HPAS (referred to as HPAS-flocs) is hypothesized to have caused this rapid fouling via electrostatic attraction (with negatively charged **α**-Al_2O_3). Such a phenomenon was also reported for polymeric membranes (Sen Wang et al., 2011), and the authors identified that pore blocking was the major mechanism by organic flocculants.

This phenomenon can be further supported by a cleaning procedure employed after complete fouling in experiment 1 (see **Figure** 4.**2C**). Initially, chemical cleaning was performed with an alkaline solution which partially restored clean water flux J_{CW} (40 to 50 % compared to actual J_{CW}; see **Figure** 4.**2C**). However, with acid cleaning, around 80 to 90 % of J_{CW} could be recovered. The drained solution (after acid cleaning) showed visible flocs, resembling flocs formed during flocculation before dewatering (as shown in the photograph in **Figure 4.2C**). Acid cleaning is generally performed to remove inorganic fouling via solubilization. Organic fouling is more predominant in microfiltration with wastewater (Gupta and Chellam, 2022), and therefore, the hydroxide ions along with chelating agents should have completely removed such

a fouling either via saponification, chelation, hydrolysis, and/or solubilization. But the higher recovery of J_{CW} with acid cleaning implies a drastic shift towards a more positively charged membrane which should have repelled HPAS back to the bulk solution.

It should be noted that the cleaning solutions usually contain other compounds that contribute towards chelation or emulsification, but information on the exact composition of such solutions is not known. To differentiate the effect of membrane's surface charge (due to the acid solution's contact with the membrane) from possible chemical agents that could have desorbed HPAS, experiment 2 was performed at similar physical cleaning conditions (as experiment 1 with minor variations, see **Table 4.2**), and similar to experiment 1, the membrane was susceptible to immediate fouling. Decline in J_{std} occurred in the first 12 hours. At around 25 h, pH in the feed solution was reduced from pH 8 to pH 6.5 with HCl. The sudden reduction in pH and the coincidental increase in J_{std} (see **Figure 4.2B**) support the idea that charge interaction plays a significant role in the attraction/repulsion of unbound HPAS or HPAS-flocs. Also, when the pH-value reached 8.4, there was a decrease in J_{std} (as shown in **Figure 4.2B**), supposedly indicating how a more negatively charged **α**-Al_2O_3 could facilitate more attraction of unbound HPAS or HPAS-flocs.

Chemical cleaning was again performed with respect to the procedure described in **Figure 4.2C** to recover J_{CW}. To improve upon optimization, backwash cycles were introduced as an alternative cleaning procedure in experiment 3 (see **Table 4.2**). During backwashing, the permeate flow would be reversed to remove any fouling in the pores, and the membrane surface (Sayegh et al., 2021). In experiment 3, backwashing was performed every 1800 s for 20 s. Such a frequency did not have any effect on the stability of J_{std}, as it saw a rapid decline at around 10 h (**Figure 4.2A**). However, when frequency of backwashing was increased to every 600 s for 20 s (Exp 4; **Figure 4.2B**), a rather stable J_{std} of around 20 LMH was observed after an initial decline in J_{std}. This hints at how an inevitable interaction of HPAS with the membrane can severely cause fouling despite the low TSS concentration. In any case, initial interaction of HPAS is unavoidable, but with a higher frequency, fouling and pore blocking could be reduced allowing for long-term filtration. In comparison, using the same membrane ($v_{cf} = 3$ m·s^{-1}, pressure = 2.2 bars, without physical cleaning) to treat swine manure, a steady state flux of 20 LMH for a 3-day period was attained under recirculation condition (Samanta et al., 2022). However, the TSS concentration in the study was around 5 g·L^{-1}, and was found to have contributed majorly towards membrane fouling. A similar range of flux was achieved with polymeric microfiltration membrane (pore size = 0.3 µm) for filtering activated sludge with TSS of 5800 mg·L^{-1} (Choi et al., 2005). The presence of particles was found to be the major cause of fouling resistance in their study. Nevertheless, to further support the phenomenon of HPAS-fouling and improve up on J_{std}, experiment 5 was performed with filtrate at a rather low pH (pH 5.4) with the optimized backwashing conditions from experiment 4 (see **Table 4.2** for experimental conditions). The experiment was carried out for 168 h, and maintained around 70 to 80 LMH, and demonstrated no signs of decline in J_{std}. This clearly shows that HPAS is the major cause for fouling, and the rapid decline in J_{std} at the start of filtration is caused by HPAS or HPAS-flocs. With a low pH, initial electrostatic interaction of HPAS with the membrane could be significantly reduced, allowing for a high J_{std} to be maintained over long-term. In addition, the increased backwashing frequency could significantly prevent pore blocking. This option could still be considered for continuous filtration as the amount of volume that can be filtered is significantly higher. After a filtration duration of 96 h, approximately 6840 L per m^2 of effective membrane area can be filtered with conditions from experiment 5, which is around 3.9 times higher than with experiment 4 (1770 L·m$_{eff}^{-2}$) with backwashing.
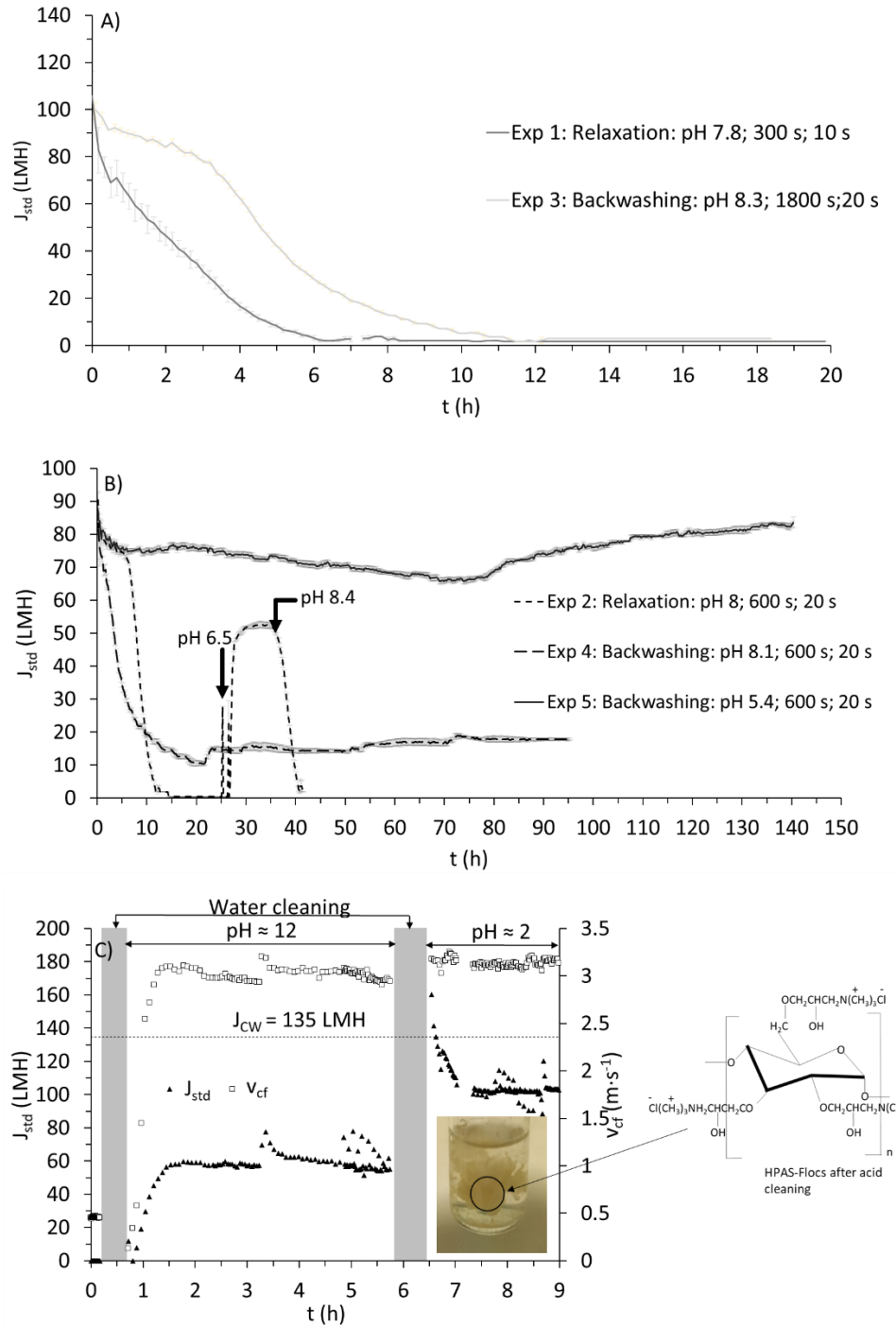
Figure 4.2: Variation of standardized permeate flux (J_{std}) with time for A) experiment 1 (relaxation) and 3 (backwashing), B) experiments 2 (relaxation), 4 (backwashing) and 5 (backwashing), and C) chemical cleaning (the dashed line indicates clean water flux (J_{CW})). The photograph shows the desorbed flocs of hydroxypropyl trimethyl ammonium starch after removing the waste stream from the microfiltration system. Note: the data for flux is obtained every 5 seconds. Average and standard deviation are made at a 10-minute interval.

4.3.3 Dark fermentation at different organic loading rates

Following the optimization of microfiltration, a cascade experiment was performed to evaluate SCFAs recovery from the solids stream. Firstly, dark fermentation was done for around 30 days, and during this period, SCFAs production varied significantly due to changes in OLR. As key parameters like pH (pH 6.9 $\pm$ 0.1), temperature (T = 32 °C), and HRT (36 h) were already optimized according to (Shylaja Prakash et al., 2024), the changes in SCFAs concentration could be monitored to variations in OLR. Several days (shown as phases I to VIII in **Figure 4.3A**) were chosen to evaluate the effect of OLR on yields of SCFAs (Y_{SCFAS}). All phases were carried out at optimized conditions excluding phase VI which had an HRT of 72 h (other parameters like pH and temperature were similar). The change in HRT was due to shortage of required sludge volume to maintain 1.5-day HRT.

Irrespective of the different OLRs, percentage of individual SCFAs accounting for total SCFAs was slightly similar (see **Figure 4.3C**). However, when evaluating Y_{SCFAS}, a stability over a wide range (between 7 and 12 $g_{TOC} \cdot L^{-1} \cdot d^{-1}$) was observed (see **Figure 4.3B**) but increased below 7 $g_{TOC} \cdot L^{-1} \cdot d^{-1}$. The highest yields were observed at phases IV (6.4 $g_{TOC} \cdot L^{-1} \cdot d^{-1}$), VI (2.7 $g_{TOC} \cdot L^{-1} \cdot d^{-1}$), and VII (5.1 $g_{TOC} \cdot L^{-1} \cdot d^{-1}$) (see **Figure 4.3B**). At lower OLRs, Y_{SCFAS} could be improved by around 15 to 50 %. OLR is a function of both HRT and concentration of the substrate (here TOC). As mentioned earlier, HRT at phase VI was 72 h, and the higher Y_{SCFAS} at this phase VI could be attributed to longer residence times, but it is important to mention that a plateau of Y_{SCFAS} was achieved at around HRT of 48 h in the previous study (Shylaja Prakash et al., 2024), and Y_{SCFAS} (here in phase VI) is also lower than or close to the yields observed at phases IV and VII (both of which had HRT of 36 h). Therefore, the effect of lower OLR is suspected to have caused this increase at phase VI.

In phases IV, VI and VII, sludge was relatively diluted with TOC concentration being at least 25 % lower compared to other phases. Although, higher OLRs can enhance fermentation, it appears as though maintaining a relatively low/optimum OLR can increase the overall yields of SCFAs (Pandey et al., 2022). (Skalsky and Daigger, 1995)also showed that a slightly diluted substrate or low sludge loading periods improved SCFAs production significantly which could mainly be attributed to reduced inhibitory effect of the concentrated substrate (i.e organic carbon) on the biomass, as well better mixing and uptake of the substrate by the biomass during low sludge loading periods. Similar results were also reported by (Banister and Pretorius, 1998), where the authors showed an optimum dilution for maximizing SCFAs yields beyond which a decrease was observed, and the reason was attributed to reduced inhibitory effects at optimum concentrations.
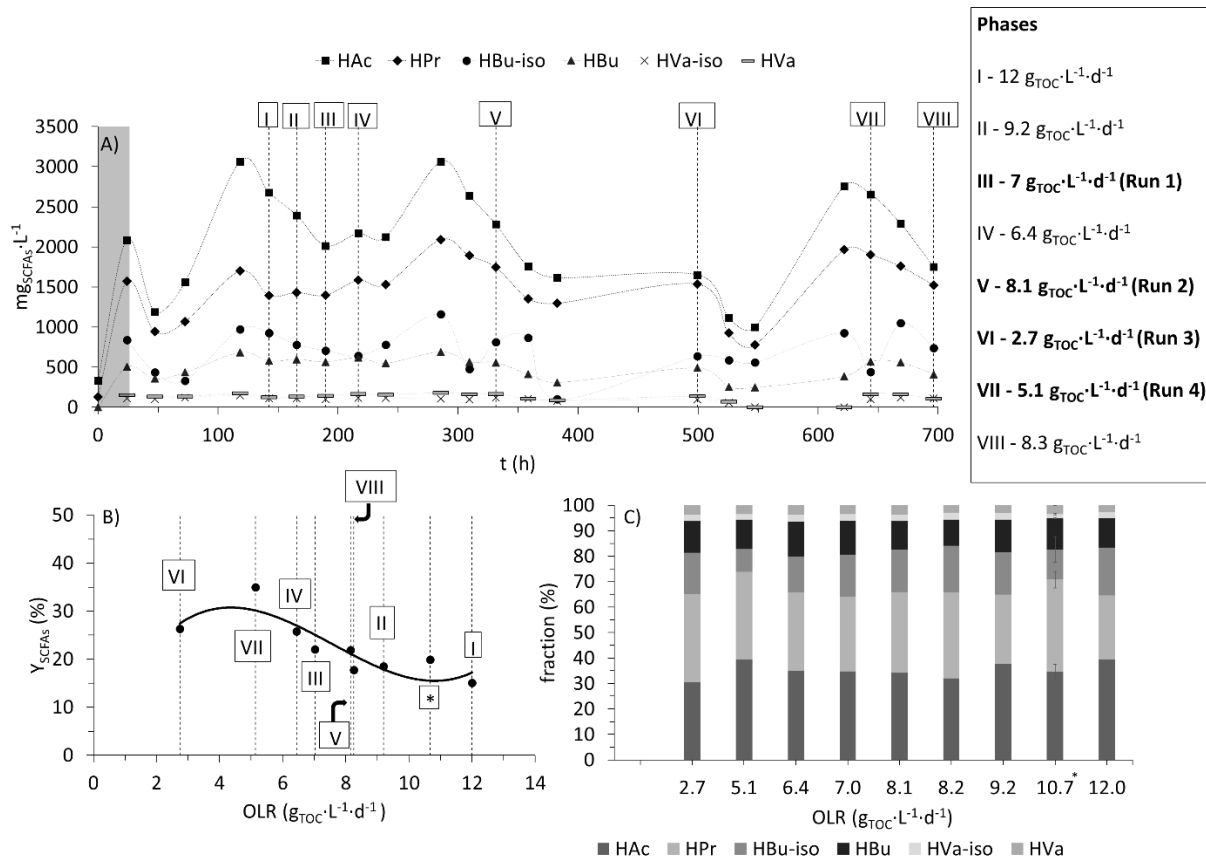
Figure 4.3: A) Variation in concentration of short-chain fatty acids (SCFAs) in the hydrolyzate with time. The roman numerals marked in **Figure 3A** denote the different phases. Arbitrary days (denoted as runs) were chosen for membrane separation (marked in bold in the text box in **Figure 4.3A**). B) yields (Y_{SCFAs}) for SCFAs based on the organic loading rate (OLR). C) fraction (%) shows the percentage of individual SCFAs accounting for the total SCFAs. The point marked as asterisk in **Figure 4.3B** and **4.3C** is not shown in this research, and the data is from a previous study (Shylaja Prakash et al., 2024).

4.3.4 Pilot-scale dewatering and microfiltration: Evaluation of retention

The hydrolyzate obtained after dark fermentation (from the four runs that are marked in **Figure 4.3A**) was then treated using a chamber-filter-press to reduce the solids load on microfiltration. A total of four dewatering runs were carried out. Pea-based hydroxypropyl trimethyl ammonium starch (HPAS) was used here, and dosage (D_{HPAS}) was increased from run 1 to run 4 to monitor the effects of solids removal.

Despite lower D_{HPAS} in comparison to batch tests, a high total solids retention (R_{TS}) was observed (**Table 4.3**). This can be explained by HPAS used for pilot-scale dewatering, which was pea-based (as mentioned in *section 4.2.1*). The pea-based flocculant had a higher degree of substitution (DS) meaning that the number of OH groups replaced in starch by a quaternary ammonium salt was significantly higher compared to potato-based HPAS (used for lab-scale). The latter had a DS-value less than 1.6 (DS < 55 %; exact value is unknown) while that of the former was 3 (theoretically 100 %). A higher DS can reduce the dosage requirements, and it was also found that flocculation efficiency of starch-based flocculants with a higher DS-value was higher (M. Huang et al., 2017). However, the authors also noted that there is an increased risk of faster stabilization due to the higher charge density, which is suspected to have occurred in run 4 as there

58

was breakpoint in retention. R_{TS} could reach an average of 67 until run 3, past which there was a significant reduction of R_{TS} to 55 %. In addition, ratio of concentration of total suspended solids (TSS) in the filtrate to the concentration of TS in the hydrolyzate (expressed as mg·g^{-1}; see **Table 4.3**) could be kept minimum in the filtrate (6 mg·g^{-1}) at a D_{HPAS} of 19 mg$_{HPAS}$·g$_{TS}$$^{-1}$, after which there was an increase. In retrospect, to obtain such a low value (9 mg·g^{-1}), D_{HPAS} of 30 mg$_{HPAS}$·g$_{TS}$$^{-1}$ was necessary for the fifth batch (100 µm) in *section 4.3.1*. Using the filter-press, a volume recovery (V_{rec}) of 85 % can be achieved.

The filtrate of the chamber filter-press from the four runs was then treated with ceramic microfiltration to achieve a particle-free-SCFAs-permeate. Using microfiltration, complete TSS removal (particle-free, see photograph of permeate in **Figure 4.5B**) could be achieved (R_{TSS} = 100 %), and a V_{rec}-value (after microfiltration) of 70 % could be reached. R_{TS} for microfiltration was in the range of 20 % for runs 1, 2 and 4, while it was less than 10 % in run 3 (see **Table 4.3**). In contrast, a retention by around 80 % after 3 days of filtration was found in a study (Samanta et al., 2022), and authors assumed a significant portion of dissolved organic compounds adsorbed to the suspended solids contributed to such high retention values. This further signifies the importance of having a filter-press to reduce the suspended solids load on microfiltration, and eventually prevent loss of SCFAs. The removal of particles after microfiltration also leads to a high permeate quality as evidenced by the high ratio of SCFAs (as carbon equivalents) to DOC (represented by f_{DOC} in **Table 4.3**), and the average values of f_{DOC} from the four runs is around 89 %.

In any case, dewatering and microfiltration operate under the mechanism of size sieving, and the retention of low molecular-weight molecules, like SCFAs, should be negligible. However, retention of SCFAs (R_{SCFAs}) has shown to occur in the presence of high concentrations of suspended solids. Co-retention of SCFAs along with TSS has been reported by other researchers for ceramic (0.2 µm) and polymeric membranes (0.1 to 8 µm), and have found to be in the range of 15 to 20 % [15,16]. Similarly, large macromolecules like proteins, and polysaccharides were reported to be retained by more than 30 % by a 0.1 µm ceramic membrane (Zhang et al., 2013). Also, narrowing of pores due to adsorption of foulants and cake layer formation are phenomena that lead to notable rejection of dissolved compounds (in the range of 20 %) in the presence of high concentrations of TSS (Choi et al., 2005). The filter-press lined with polyester membrane showed an R_{SCFAs}-value in the range of 1 to 8 % (**Figure A7** and **Table 4.3**) despite the relatively larger mesh size of 100 µm. The SCFAs produced during dark fermentation have pKa-values in the range of 4.7 and 4.9 (at 25 °C), and exist predominantly in the dissociated or deprotonated forms at a pH-value of 7 (which was used in dark fermentation). It is important to consider the electrostatic interaction between the cationic HPAS and the carboxylate ion (after dissociation) in SCFAs which would have led to this retention, and it was observed that retention of SCFAs increases with increasing dosage of HPAS (see **Figure A7A**). In addition to HPAS' electrostatic interaction, there is a significant concentration of TS in the hydrolyzate, and adsorption to the solids is also suspected to have been a factor that could have contributed to this low retention. However, there is no discernible pattern that can support the theory of adsorption to solids (see **Table 4.3**). In this study, R_{SCFAs} was found to be relatively low for the ceramic microfiltration membrane (0.2 µm). Average R_{SCFAs} was around 5 % for short- and long-term experiments conducted in *section 4.3.2* and also in the four runs in semi-continuous microfiltration (see **Figure A7B** and **Table 4.3**). Based on observations from the studies mentioned above, the low TSS concentration in the filtrate (i.e., feed for microfiltration) could be a major factor preventing significant retention of SCFAs.

Table 4.3: Parameters in the inflow and outflow of chamber-filter press and microfiltration.

Runs	Hydrolyzate obtained from dark fermentation		Dosage (D_{HPAS})	Filtrate after dewatering of hydrolyzae using chamber-filter press				Permeate after microfiltration of filtrate		
	TS	SCFAs		TSS	$\dfrac{\text{TSS in filtrate (mg} \cdot \text{L}^{-1})}{\text{TS in hydrolyzate (g} \cdot \text{L}^{-1})}$	R_{TS}	R_{SCFAs}	R_{TS}	R_{SCFAs}	f_{DOC}
	$g \cdot L^{-1}$	$mg \cdot L^{-1}$	$mg_{HPAS} \cdot g_{TS}^{-1}$	$mg \cdot L^{-1}$	$mg_{TSS} \cdot g_{TS}^{-1}$	%		%		
1	26	4926	6	1300	50	65	1	21	4 ± 2	87
2	30	5686	10	1281	43	68	6	21	4 ± 3	88
3	21	4551	19	115	6	67	4	6	6[a]	85
4	19	5831	25	348	18	55	8	21	3 ± 1	97

[a]the standard deviation was not included as the coefficient of variation was very low (less than 2 %) note: total solids (TS) and short-chain fatty acids (SCFAs) shown in **Table 4.3** were measured in duplicates in the hydrolyzate before dewatering and in the filtrate after dewatering for calculation of retention parameters. For microfiltration, TS was measured in duplicates in the feed before filtration and at the end of the filtration for retention calculation. For calculation of SCFAs retention in microfiltration, SCFAs was once measured in duplicates in the feed, once in permeate (duplicates) when half the volume recovery was achieved, and once again in the permeate (duplicates) when the filtration was done where a maximum volume recovery could be achieved. The measurements were then averaged.

4.3.5 Performance of microfiltration membrane during semi-continuous operation

Semi-continuous microfiltration was performed with backwashes every 600 s for 20 s based on the stable results obtained from recirculation condition in *section 4.3.2*. Average cross-flow velocity during the four runs was 3 ± 0.3 m·s⁻¹. It is important to remember that, similar to the filter-press, semi-continuous filtration was performed, but no interim chemical cleaning was performed between the four runs. The membrane underwent only cleaning with clean water between each run. The duration of microfiltration was between 3 and 4 hours for all four runs. In all four runs, after a steep decline in standardized flux (J_{std}), there is a stable phase that is represented by the upper and lower limits of J_{std} during the filtration period of each run (see the shaded region in **Figure 4.4**). In runs 1,2, and 3, stability of J_{std} is maintained during the course of

filtration, while in run 4 there is a notable deviation which could very well indicate the onset of irreversible fouling (around 40 LMH is reached which is below the lower limit of the shaded region). Further examination into the trend of J_{std} during short-term filtration shows that J_{std} is much higher for the experimented duration compared to the long-term experiment performed at similar physical cleaning conditions (experiment 4 in *section 4.3.2*; see **Figure 4.2B**). In experiment 4, the range of 50 to 60 LMH could only be maintained for a period of 3 hours which is almost close to duration of filtration of one run. One reason could be attributed to the reduced dosage of hydroxypropyl trimethyl ammonium starch while another possible explanation would be the inclusion of short intermittent cleaning with clean water, which can potentially sustain J_{std} for longer durations. Nevertheless, by the end of run 4, a total of around 900 $L \cdot m_{eff, area}^{-2}$ of filtrate was treated, thus, this is the amount of filtrate after which chemical cleaning must be performed to restore the flux in accordance with the procedure described in *section 4.3.2* and **Figure 4.2C**.
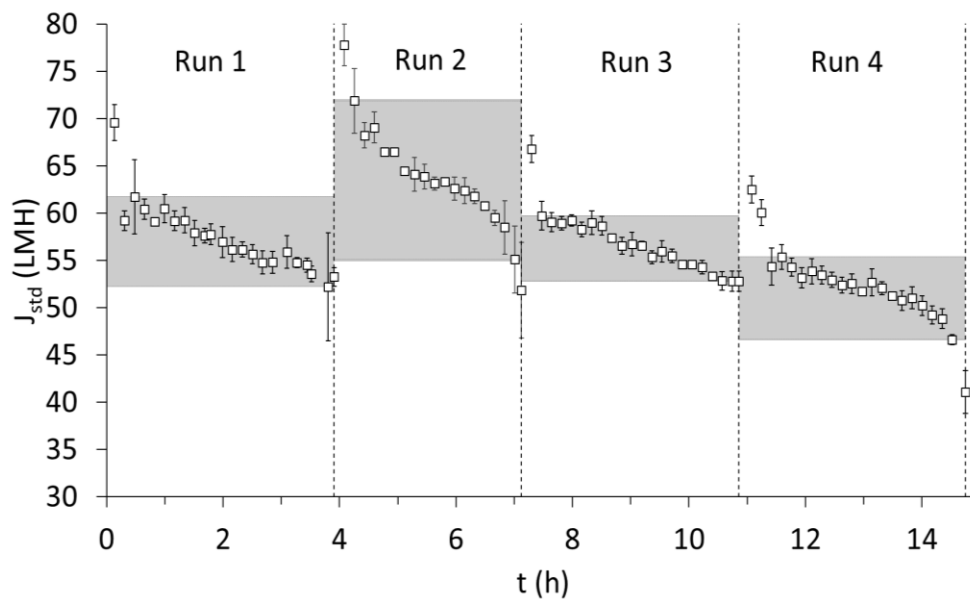
Figure 4.4: Standardized flux (J_{std}) for the 4-runs. Hydrolyzate from the 4-days mentioned in **Figure 3** after pre-treatment with filter-press was used for microfiltration. Conditions: pH 7, see **Table 4.3** for parameters in the feed solution (filtrate). Note: the data for flux is obtained every 5 seconds. Average and standard deviation are made at a 10-minute interval.

4.3.6   Evaluation of the SCFAs-load in the cascade

Although with microfiltration, a particle-free permeate can be produced with permeate quality (f_{DOC}) of 85 to 97 %, there is a drawback in terms of the decline in overall recovery of SCFAs (Rec_{SCFAs}) which can be attributed to volume recovery (V_{rec}) (see **Figure 4.5A**). It is important to mention that the 70 %-V_{rec} achieved with microfiltration is a system limitation and recovery of SCFAs (Rec_{SCFAs}) could be increased by having a higher V_{rec} provided there is not a high significant retention of SCFAs. Nevertheless, the overall value of Rec_{SCFAs} after microfiltration is around 15 %. However, with the observed increase in yields at low OLRs in dark fermentation, the Rec_{SCFAs} could be potentially increased by at least 20 %. From both primary and excess sludge, around 24 $g_{TOC} \cdot capita^{-1} \cdot d^{-1}$ is generated. Based on the yields observed in this study after microfiltration (with primary sludge), around 4 $gC_{SCFAs} \cdot capita^{-1} \cdot d^{-1}$ can be recovered from the solids stream (primary and excess sludge) of municipal WWTP (see **Figure 4.5B**).

(a)

(b)
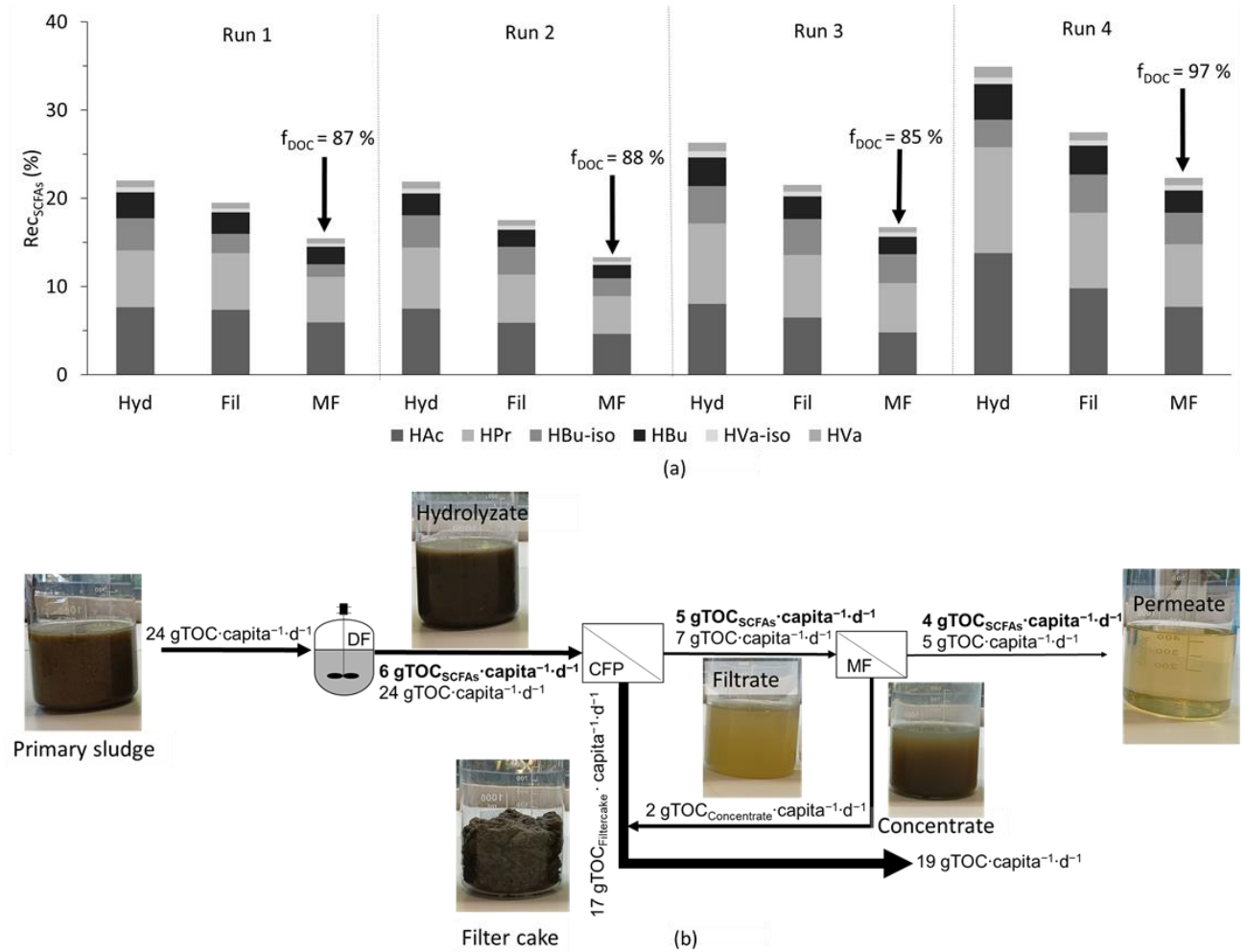
Figure 4.5: A) Recovery of SCFAs (Rec_{SCFAs}) after each step including volume recovery of filtration, and B) Organic carbon load in a biorefinery expressed as TOC. Excess sludge was included in the load, and for the calculation, the yield from the treatment chain with primary sludge was used.

To understand the feasibility of the particle-free permeate and its significance in a wastewater biorefinery (WWBr), a simple revenue-expenditure analysis was performed in terms of per capita and annum (a) based on two cases (**Figure 4.6**). In case 1, a typical wastewater treatment plant (WWTP) was assessed with biogas as the major source of revenue, while in case 2, PHA recovery with SCFAs obtained as particle-free permeate after microfiltration in a WWBr was evaluated.

The organic carbon load is 24 $g_{TOC}\cdot capita^{-1}\cdot d^{-1}$ produced as primary and excess sludge. For case 1, the revenue generated is based on conversion of organic carbon to biogas. The amount of revenue generated based on the electrical energy obtained (from methane) through combined heat and power is 0.36 $€\cdot kg_{TOC}^{-1}$ (Da Ros et al., 2020). Therefore, based on TOC load (24 $g_{TOC}\cdot capita^{-1}\cdot d^{-1}$), this is equivalent to a revenue of 3.15 $€\cdot capita^{-1}\cdot a^{-1}$, while the cost associated with sludge disposal is around 100 € per ton of TS (Amann et al., 2021). Based on the solids load generated, the sludge disposal costs amount to 0.68 $€\cdot capita^{-1}\cdot a^{-1}$.

For case 2, the revenue generated from biogas is reduced as a sizeable portion of the organic carbon is diverted to recovery of SCFAs (as shown in this study). Firstly, for WWBr, two scenarios can be considered for biogas production. For scenario 1 in case 2 (case 2: WWBr (1)), both the filter-cake (from the chamber-filter press) and the concentrate of microfiltration which amounts to a load of 19 $g_{TOC}\cdot capita^{-1}\cdot d^{-1}$ was used for biogas production generating a revenue of 2.5 $€\cdot capita^{-1}\cdot a^{-1}$ (0.36 $€\cdot kg_{TOC}^{-1}$ (Da Ros et al., 2020)). This revenue reduces to 2.2 $€\cdot capita^{-1}\cdot a^{-1}$ when only the filter-cake is used (17 $g_{TOC}\cdot capita^{-1}\cdot d^{-1}$), while the concentrate of microfiltration is used for process optimization (case 2: WWBr (2)). The concentrate of microfiltration has a notable load of SCFAs (around 2 $g_{TOC}\cdot capita^{-1}\cdot d^{-1}$; see **Figure 4.5B**) which can be used for biological nutrient removal. Interestingly, SCFAs mixture obtained from hydrolyzed primary sludge (after centrifugation) improved rates of denitrification in comparison to HAc (Christensen et al., 2022). In case of pre-anoxic treatment in a municipal WWTP, there would be periods of low organic carbon load in the influent, and this can be met with the SCFAs load in the concentrate of microfiltration, which can reduce the cost of external HAc (0.63 $€\cdot kg_{HAc}^{-1}$ Business Analytik (2024)). For PHA calculation in case 2, an average yield of 0.33 g C_{PHA}/gC_{SCFAs} was chosen (Morgan-Sagastume et al., 2015) and an overall revenue of 3.5 $€\cdot capita^{-1}\cdot a^{-1}$ could be generated (at an average selling price of 4 $€\cdot kg_{PHA}^{-1}$ (Gholami et al., 2016)). However, around 50 % of the revenue generated by PHAs is offset by the extraction and purification costs (Da Ros et al., 2020). Other major costs include the dosage requirements of NaOH and starch for dewatering, which were 0.14 $g_{NaOH}\cdot g_{TOC}^{-1}$ (0.22 $€\cdot kg^{-1}$; from Business Analytik (2024)) and 0.02 $g_{HPAS}\cdot g_{TOC}^{-1}$ (1.6 $€\cdot kg_{HPAS}^{-1}$; HKF CleanTech AG, Germany), respectively, which accounted for 0.55 $€\cdot capita^{-1}\cdot a^{-1}$. The energy demand for microfiltration is low, and does not have a notable effect on the cost and is not included). In conclusion, the revenue generated in a WWBr can be increased by an average of 50 % based on case 2 (see **Figure 4.6**).
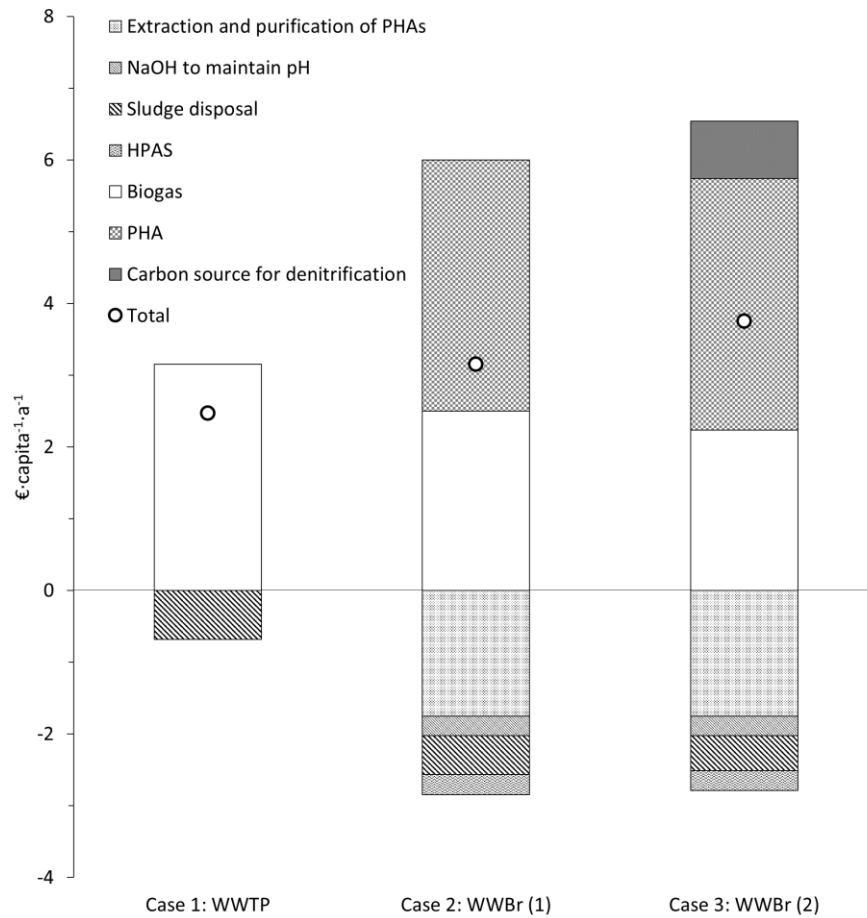
Figure 4.6: Revenue-expenditure analysis for wastewater treatment plant and wastewater biorefinery.

4.4   Conclusions

Implementing dark fermentation in combination with filter-press and microfiltration is a viable option to produce a particle-free-short-chain fatty acids (SCFAs) permeate from the solids stream of municipal wastewater.

1) Dark fermentation stands as a crucial step and the yields of SCFAs can be potentially enhanced by at least 20 % by maintaining lower organic loading rates ($2 - 5$ $g_{TOC} \cdot L^{-1} \cdot d^{-1}$).

2) Filter-press (mesh size: 100 µm) coupled with hydroxypropyl trimethyl ammonium starch (HPAS) is an effective pre-treatment stage and can remove more than 60 % of the solids and produce a filtrate with low suspended solids concentration.

3) HPAS contributes significantly to fouling of microfiltration but fouling can be mitigated by increased backwashing frequency, and also by reducing solution's pH below membrane's iso-electric point.

4) Approximately 4 $g_{CSCFAs} \cdot capita^{-1} \cdot d^{-1}$ can be recovered in a particle-free permeate from the sludge stream of a wastewater biorefinery.

5 Evaluation of a novel pilot-scale rotating disk bioelectrochemical reactor for hydrogen production in a wastewater biorefinery

Graphical abstract:

Abstract:

A novel custom-made 100-L rotating disk bioelectrochemical reactor (RDBER) was evaluated as a H_2-producing terminal treatment step in a wastewater biorefinery concept. The RDBER is distinguished by its rotatory circular anodes with a high specific anodic area ($100\ m_{anode}^2 \cdot m_{reactor}^{-3}$). The RDBER was inoculated with *Shewanella oneidensis* and *Geobacter sulfurreducens*, with the latter as the primary exoelectrogens for substrate oxidation. The RDBER was operated for a 200-day period in batch and continuous modes to optimize pH, hydraulic retention time (HRT), electrical conductivity, recirculation, rotational speed, and anode potential. The batch mode was operated with the defined dual-species culture in a sterilized medium, whereas in the continuous mode, unsterilized hydrolyzate with short-chain fatty acids was utilized. In the

batch phase with the defined culture, a high H_2:CO_2 fraction (80 %:20 %) could be maintained for a 130-day period with the highest steady-state current density of 240 mA·m_{anode}^{-2} (CE $\approx$ 70 %) harvesting a maximum of 36 L H_2·$m_{reactor}^{-3}$·d^{-1}. Among the parameters, increased recirculation rate of reactor medium from 1 to 3 (m^3·h^{-1})·$m_{reactor}^{-3}$ improved current density by 100 %. In continuous feeding the reactor transitioned towards biohythane production (9 % H_2:86 % CH_4). Current density of 170 mA·m_{anode}^{-2} (CE = 33 %) could be maintained, while harvesting 3 L H_2·$m_{reactor}^{-3}$·d^{-1} and 33 L CH_4·$m_{reactor}^{-3}$·d^{-1}. Gravimetric- and image-based biomass analyses revealed an annular-shaped biofilm distribution on the anodes with the biofilm coverage amounting to 3.3 m^2. Further optimization of the architecture and hydrodynamics of the RDBER shows great potential as a promising bioelectrochemical system.

Highlights

o   100-L upscaling of a novel custom-made rotating disk bioelectrochemical reactor

o   Methane-free gas phase in defined dual-species cultivation for a 130-day period

o   Highest current density of 240 $\pm$ 34 mA·m_{anode}^{-2} in a defined dual-species start up

o   Increasing recirculation from 1 to 3 (m^3·h^{-1})·$m_{reactor}^{-3}$ increased current by 100 %

o   Annular distribution of biofilm accounted for 1/3rd of the total anodic area

o   Average effective current density amounted to 520 mA·m_{anode}^{-2}

Keywords

Rotating disk bioelectrochemical reactor, biohydrogen, biohythane, biorefinery, microbial electrolysis

5.1   Introduction

Wastewater generated from urban areas, is an explorable waste stream whose potential needs careful consideration within the context of a circular economy. Biogas is the typical biofuel generated from municipal wastewater treatment plants (WWTPs) during the anaerobic digestion of sewage sludge. However, the possibility to generate value-added products that hold a higher value than biogas in the market, demands a better utilization of organic carbon generated as sludge in a WWTP. The idea of producing bio-based fuels from a waste stream like municipal wastewater has gained increasing interest as a part of closing-the-loop approach (Kitching et al., 2017). Biofuels, specifically hydrogen (H_2) is an emerging interest due its clean nature in comparison to methane (Wong et al., 2014). Bioelectrochemical systems (BES), more specifically microbial electrolysis cells (MEC) have been shown to be an effective reactor concept to harvest biohydrogen from waste streams containing easily degradable carbon sources (Rivera et al., 2015). Previous studies have shown that sewage sludge, both primary and excess sludge obtained from municipal WWTPs, are an excellent source of easily degradable carbon source, i.e., short-chain fatty acids (SCFAs), after dark fermentation (Chen et al., 2006; Da Ros et al., 2020; Shylaja Prakash et al., 2024).

MECs operate on the principle, where electroactive microorganisms, for instance, *Geobacter sp.* can utilize solid electrodes as terminal electron acceptors for their respiratory energy gain. In nature, the bacteria would use, e.g. iron minerals as electron acceptors, whereas in technical applications, they transfer electrons from

the oxidation of easily degradable carbon sources like SCFAs to an electrode poised at an oxidative potential via extracellular electron transfer and thus generate an anodic current (Kitching et al., 2017). The principle of an MEC is similar to that of water electrolysis, but the advantage lies in the fact that the external energy required for MEC is relatively low. The anode potential generated from the oxidation of an easily degradable carbon source like acetate is around -300 mV (vs standard hydrogen electrode (SHE)), and the reversible potential of H^+/H_2 is around -414 mV, which means that a minimum theoretical voltage of 114 mV is required for H_2 evolution at the cathode which is significantly lower than the theoretical voltage of 1.23 V required for water electrolysis (Anantharaj et al., 2019; Gunaseelan et al., 2023).

Reactor design is of paramount importance when operating an MEC, and the simplest classification for reactor design in MECs is between a single- and a dual-chamber system. While dual-chamber systems with a semi-permeable membrane are typically required for water electrolysis to separate hydrogen and oxygen from the respective electrode chambers, this configuration can also be used in MECs to ensure high H_2 recoveries (Call and Logan, 2008). However, semi-permeable membranes can cause proton accumulation in the anode chamber leading to unfavorable pH conditions for electroactivity (H. Wang et al., 2021), develop additional internal resistances (resulting in ohmic losses), and undergo fouling (Logan, 2010). Moreover, per- and polyfluoroalkyl substances (PFAS)-based proton exchange membranes are commonly used in MECs due to their high proton conductivity (Von Tettau et al., 2025). The risk of PFAS leakage and the potential risks and toxicity it poses to the environment is a major aspect that requires consideration during a full-scale implementation (Von Tettau et al., 2025). These limitations make scale-ups of dual-chamber MECs rather challenging. Even though there is a risk of reduced H_2 recoveries in a single-chamber MEC due to H_2 scavenging and/or reoxidation, the simple design when scaling up is a major consideration that can compensate for H_2 losses, especially if a significant volume of H_2 can be harvested (Call and Logan, 2008; Sasaki et al., 2012). A great deal of research has been conducted on MECs at lab-scale (Liu et al., 2012; Lu et al., 2012), however, scaling up MECs to treat a sizeable wastewater load to harvest H_2 or any other biofuel requires a proper reactor architecture.

Evaluating the typical reactor modules for BESs, tubular and flat-sheet, which may or may not need a semi-permeable separator to spatially separate the anode and the cathode (Janicek et al., 2014), this study demonstrates the use of a novel 100-L pilot-scale rotating disk bioelectrochemical reactor (RDBER) developed by Max Hackbarth as a reactor concept based on a 10-L bench-scale RDBER (Hackbarth et al., 2023). The RDBER is characterized by the lack of a membrane separator between the electrodes, high anode surface area to reactor volume ratio ($100 \ m^2 \cdot m^{-3}$), as well as using rotatory anodes to improve substrate uptake (Hackbarth et al., 2023).To the best of our knowledge, research on pilot-scale setups are scarce (Cotterill et al., 2017; Cusick et al., 2011; Heidrich et al., 2013), and a compartmentalized or numbering-up approach may not be suitable for treating high wastewater loads when a large anode surface area is required. Increasing the number of small-sized electrode modules poses disadvantages in terms of larger footprints and huge costs for operating individual modules (Cotterill et al., 2017; Fornero et al., 2010).

The proof of concept of the 100-L RDBER as a terminal treatment step in a wastewater biorefinery (WWBr) is studied in a defined dual-species batch mode with a sterile medium, and in a continuous mode fed with unsterile substrate for an operation period of 200 days. Crucial parameters like rotational speed of the anode, recirculation rates of the reactor medium, electrical conductivity, applied anodic potential, pH, and hydraulic retention time and their effect on the rate of hydrogen evolution and current density are evaluated in this

study. In addition, the reactor was assessed for potential limitations and improvements in design considerations by analyzing the pattern of biofilm development on the rotary anodes via image and gravimetric analyses. A second RDBER that was operated under unsterile conditions at a real WWTP was also evaluated and compared.

5.2   Materials and Methods
5.2.1   Experimental setup

In this study, two 100-L RDBERs were operated. The presented research mainly focuses on the RDBER that was operated under a sterile start-up phase with defined cultures, after which, during experimentation, unsterilized substrates were introduced to test realistic conditions. For general performance comparison, a second RDBER was operated in a completely unsterile condition at a WWTP.

The cross-sectional scheme and photographical representations of the 100 L-RDBER (working volume = 90 L) can be found in **Figure 5.1**. The specific anodic area was 100 m^2 anode area per m^3 of reactor volume or 111 m^2 anode area per m^3 of working volume. The corpus of the reactor including the gas trap were made out of polypropylene. A threaded titanium shaft, placed centrally, along the length of the reactor frame supported the anodes and also acted as an current collector. The circular anode disks (working electrode) were stacked on the shaft separated by titanium nuts. A total of 65 anode disks (material: graphite polymer composite material, thickness: 3 mm, diameter = 33 cm, Whitecell Eisenhuth GmbH & Co. KG, Osterode, Germany) spaced 1.2 cm apart, amounted to a total effective area of 10 m^2 including the front and the back sides. The anode disks each had three holes that were axially distributed to improve advective liquid transport along the reactor length (see **Figure 5.1A** and **Figure A8B** for specifications). The anodes mounted on the titanium rod were connected to a high-resolution stepping motor (Lexium Mdrive Motion Control, Schneider Electric), with which the rotational speed of the anode can be controlled. The counter electrodes, i.e., the perforated stainless steel cathode, shaped as a half cylinder with supports on either side, was placed over the anodes (see **Figure 5.1A** and **Figure 5.1B**). This cathodic configuration mimics that of a lab-scale RDBER that was modified from another lab-scale RDBER that used a set of semi-circular cathode disks arranged closely between the anodes (Hackbarth et al., 2023; Xiao et al., 2025). Such a design change was carried out to reduce reoxidation of hydrogen at the cathode and improve recovery of the same. The cathode area was approximately 0.99 m^2. An Ag/AgCl reference electrode (SE23I, Meinsberg Sensortechnik) was placed at the midpoint of the reactor submerged in the reactor medium (**Figure 5.1A**). A potentiostat (Interface 5000P, Gamry Instruments, USA) was used to control the anodic potential. A gear pump (Masterflex, Ismatec, Germany) was used to mix the reactor medium by creating a flow via recirculation of the liquid phase. A peristaltic pump (Rotarus®, Hirschmann Laborgeräte GmbH & Co. KG, Eberstadt, Germany) was used to feed the reactor during continuous operation. The significance of the direction of flow depicted in **Figure 5.1A** is described in *section 5.3.5*. The volumetric flow rate of the gas leaving the headspace of the gas trap was measured using a drum type gas flow meter (Ritter Apparatebau GmbH, Germany). An electrical silicone heating mat (LCS IsoTherm GmbH & Co. KG, Frankfurt am Main, Germany) was used to insulate the reactor and maintain a constant temperature range over the course of the experiment (see *section 5.3.1* for exact temperature values).
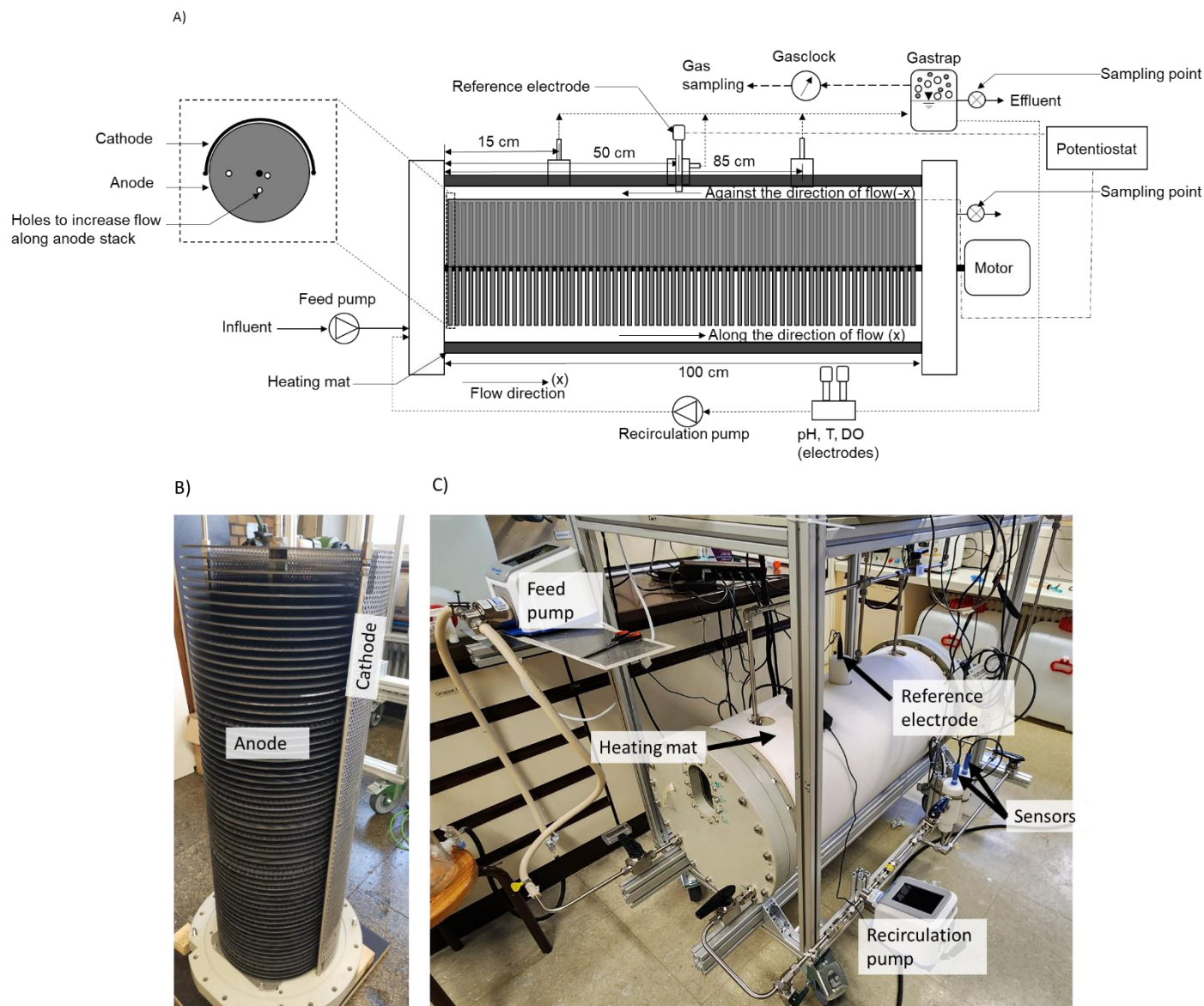
Figure 5.1: A) Cross-sectional scheme of the 100-L RDBER, B) Photograph showing the anodes stacked on the titanium shaft. The perforated cathode shaped as a half-cylinder extends over the length of the stack of anode disks. C) Photograph of the 100-L RDBER. Note: DO represents dissolved oxygen.

5.2.2   Preculture and inoculation

Preculture and inoculation was done according to Hackbarth et al., 2023. During operation, a mixed culture of *Shewanella oneidensis* MR-1 (Venkateswaran et al., 1999) and *Geobacter sulfurreducens* PCA (Caccavo et al., 1994) as the biocatalysts was used in the RDBER, *S. oneidensis*, was aerobically precultured in Luria-Bertani medium (Lennox), while *G. sulfurreducens* was anaerobically grown in a BES medium according to Weiler et al., 2024. *S. oneidensis* and *G. sulfurreducens* were then inoculated in the reactor at a ratio of 9:1 (initial optical density (OD$_{600}$) = 0.1). Separately, *Desulfuromonas acetexigens* 2873 (DSMZ 1397) was also anaerobically grown in the BES medium and introduced at a later stage of the experiment (reinoculation

discussed in *section 5.3.1*). A detailed description of the BES medium composition and inoculation procedure can be found in **Appendix A10.** It is important to mention that the procedure described in **Appendix A10** was also followed for the RDBER operated at the WWTP under unsterile conditions, but was not inoculated with *D. acetexigens* at any point.

5.2.3   Sterilized start-up and reactor anaerobization

Prior to the introduction of the inoculated medium, the RDBER underwent two steps of chemical sterilization with hydrogen peroxide (H_2O_2) and ethanol (EtOH) to prevent the introduction or growth of an unintended microbial community that could hinder the reactor performance, and also to ensure the dominance of the specific strains in the biofilm matrix. Hydrophobic polytetrafluoroethylene (PTFE) membranes with a pore size of 0.2 µm were used at all open-to-atmosphere exit points during the defined dual-species operational period. Details to the sterilization can be found in **Appendix A11**. Following the two-step sterilization, 90 L of anaerobized inoculated BES medium with 25 mM acetate and 25 mM lactate as carbon sources was pumped into the reactor. Due to incomplete drainage of, a notable concentration of EtOH along with acetate and lactate was present as an additional carbon source. In comparison, the RDBER operated at the WWTP did not undergo any form of sterilization prior to the start-up.

5.2.4   Hydrolyzate preparation

The RDBER is intended to be used as a terminal treatment step in a wastewater biorefinery to valorize SCFAs into hydrogen. SCFAs are obtained from the anaerobic fermentation of primary sludge, which are then recovered via a two-step membrane separation method (Shylaja Prakash et al., 2025). The first filtration step is a chamber filter-press characterized by a mesh size of 100 µm, whose filtration efficiency was aided by a cationic starch-based flocculant (hydroxypropyl trimethyl ammonium starch, HPAS, HKF CleanTech AG, Switzerland). The second filtration step is microfiltration (Atec, Ulm, Germany) with a ceramic membrane having pore size of 0.2 µm (Inopor, Germany), and hence the final product is a particle-free permeate containing predominantly SCFAs. It is important to mention that the hydrolyzate obtained after microfiltration underwent long-term storage which resulted in the formation of flocs. For the batch phase (described in *section 5.3.2*), the microfiltered hydrolyzate was again microfiltered (0.2 µm) with a vacuum filtration setup to render it particle-free. The two-time microfiltered hydrolyzate was then autoclaved and used in the batch phase. For the continuous phase (described in *section 5.3.3*), the hydrolyzate obtained after the ceramic microfiltration was directly fed along with particles. The detailed composition of the permeate can be found in **Table A5**. For the RDBER operated at the WWTP, the description of the hydrolyzate used under unsterile conditions can be found in **Figure A18.**

5.2.5   Analytical methods

Dissolved oxygen (DO) and pH sensors (Endress and Hauser, Germany) were installed in the recirculation line. The electrodes were integrated with a temperature sensor. Electric conductivity was measured offline with a portable multimeter (WTW Multi 350i, Xylem, USA). Liquid samples were collected from the sampling points (see **Figure 5.1A**) during batch and continuous modes to quantify SCFAs (mainly acetic (HAc), propionic (HPr), butyric (HBu), iso-butyric (HBu-iso), valeric (HVa), iso-valeric (HVa-iso) acids) and lactic acid (HLa)) after filtration with a 0.45 µm polyether sulfone filter (Sterlitech Corporation, USA) using Metrohm 881 Compact Pro Ion Exchange Chromatograph with a Metrosep Organic Acids 250/7.8 column (Metrohm, Switzerland). The liquid samples, again after filtration, were also tested for soluble

chemical oxygen demand (sCOD) using quick tests (LCK 514, Hach Lange, Germany). HAc and HLa are supposedly expected to be the main carbon sources in the reactor, however, leftover EtOH after sterilization (as described in *section 5.2.3*) was present as an additional carbon source. Only the initial sample was quantified for EtOH using a gas chromatograph coupled with a flame ionization detector (Agilent 7890B, USA). Following samples were quantified by subtracting the COD equivalence of SCFAs from the total sCOD, and expressed in terms of molarity (expressed as $sCOD_{rest}$). This type of quantification was done only until the point of introduction of the hydrolyzate into the reactor. Gas samples were collected at the outlet of the gas clock and the gas composition was measured using a Micro GC (490 Micro GC, Agilent Technologies, Germany).

Illumina sequencing was used to analyze the microbial community composition in the reactor, and samples were taken from the planktonic phase, anodic and cathodic biofilm. Samples were analyzed at private Institute for Molecular Analytics Karlsruhe GmbH (IMA, Germany). Brief explanation to the sequencing can be found in **Appendix A12**. Samples to analyze microbial community in the planktonic phase were taken between day 97 and 105, day 116 and day 200 (after termination of the experiment). Samples from the anodic and cathodic biofilms were taken on day 200 (after termination of the experiment). Microbial community analysis was not carried out for the RDBER operated at the WWTP.

The performance of the RDBER was evaluated by analyzing the biofilm distribution on the anodes. After deconstruction of the RDBER the anodic biofilm distribution was assessed from selected anode disks. Gravimetric analysis revealed the normalized biomass (m_N), while image analysis by means of optical coherence tomography was used to determine the mean biovolume ($\overline{BV}$) and substratum coverage (SC) (Wagner and Horn (2017)), and the effective substratum coverage (SC_{eff}) was calculated from digital images. A detailed explanatory and pictorial description of the methods can be found in **Appendix A13**.

5.2.6   Data interpretation

Current density (j) was calculated using the following equation,

$$j \left(\frac{mA}{m^2}\right) = \frac{I}{A_{anode,tot}} \qquad\qquad 5.1$$

Where, I (mA) is the current produced and $A_{anode,tot}$ (m^2) is the total area of the anodes.

The Coulombic efficiency (CE) was evaluated accordingly,

$$CE\ (\%) = \left[\frac{\left(\int_0^t I.dt\right)}{n_{e^-}\cdot\Delta c\cdot V_W\cdot F}\right] \times 100 \qquad\qquad 5.2$$

Where, I (mA) is the current produced over a specific period (t), and n_{e^-} is the number of electrons released from the consumption of 1 mole of a specific carbon source. For HAc, HPr, HBu-iso, HBu, HVa-iso and HVa, the number of electrons per mole is 8, 14, 20 and 26 moles of electrons (**Table A7**), respectively. If CE is calculated based on COD, then the number of moles of electrons released per gram of COD consumed is 0.125 (**Table A7**). Δc (M) is the actual change in molar concentration (due to consumption) of a specific carbon source or COD and V_W (L) is the working volume. F is the Faraday constant (96,485 C·mol^{-1}).

Hydrogen production ($H_{2,\ produced}$) is calculated based on the current produced,

$$H_{2,produced} \left(\frac{L}{d}\right) = \left(\int_0^t I.dt\right) \cdot (F \cdot y_{e^-})^{-1} \cdot p^{-1} \cdot R \cdot T \qquad 5.3$$

Where, y_{e^-} is the yield of electrons (2 moles of electrons per mole of H_2), p the atmospheric pressure (1 atm), R universal gas constant (0.082 atm·L·mol^{-1}·K^{-1}) and T the temperature (273 K) , respectively.

The volume of gas harvested from the reactor ($H_{2, harv}$ or $CH_{4, harv}$) was calculated from the volumetric flow rate of the gas (obtained from the gas clock) and the corresponding gas fraction, determined by Micro GC. All values of gas are nominalized to standard temperature and pressure.

5.3   Results and discussions
5.3.1   Experimental conditions and overview of the RDBER's operation

An overview of the operational conditions during the different phases is summarized in **Table 5.1**. The development of the experimental parameters are shown as phases (depicted as Roman numerals) in **SI Figure 2.** Phase I through V (batch mode) were operated in a sterile medium, whereas phases I and II were experimented under the defined dual-species inoculation in a sterilized reactor medium. Phases VI and VII were operated under unsterile conditions. The parameters tested were 1) pH and electrical conductivity (phase I), 2) applied anodic potential ($E_{anode, app}$) before and after dilution with anaerobized sterile deminerilized water (phase II), 3) batch feeding of sterilized (autoclaved-microfiltered) hydrolyzate (phase III), 4) effect of rotational speed of the anode and recirculation rate ((i.e., recirculation rate (m^3·h^{-1})/reactor volume (m^3) or simply h^{-1}) (phase IV) , 5) effect of electrical conductivity (phase V), 6) continuous feeding of particle-free unsterilized synthetic hydrolyzate (phase VI), and 7) continuous feeding of unsterilized microfiltered hydrolyzate (not particle-free) (phase VII). In phase VII, though the hydrolyzate was microfiltered, long-term storage led to the formation of agglomerated particles, and hence the hydrolyzate was not particle-free. The temperature was maintained within a constant range between days 3 and around 130 (**Table 5.1**). However, starting from day 130, the seasonal variation in temperature led to significant temperature shifts between the day and night cycle (see **Figure A9A** and **Table 5.1** for difference in temperature). pH was maintained in a relatively stable range between phase II and phase V from day 30 to day 130 (see **Figure A9B**). Notable changes in pH were in phases I, VI and VII (explained in subsequent sections). The system underwent three inoculations, 1) at the beginning of the cultivation with the dual-species (*G. sulfurreducens* and *S. oneidensis*), 2) during the start-up batch (phase I) once the current densities peaked (around day 20), where only *G. sulfurreducens* was reintroduced into the system, and 3) at the end of phase V, with *Desulfuromonas acetexigens*.

Table 5.1: Specific description of phases during the operation of the RDBER (recirculation rate is presented as h^{-1} (i.e., recirculation rate (L·h^{-1})/reactor volume (L).

	Phases	Period (d)	Mode	HRT (d)	pH	T (°C)	Rotational speed of anode (rpm)	Recirculation rate (h^{-1})	$E_{anode, app}$ (mV vs SHE)	Notes
I	Start-up	12 to 30[a]			7.2 ± 0.2	29.8 ± 0.2	1	0.9	300	
II	Effect of applied anode potential and dilution	31 to 38			6.9	29.8 ± 0.2	1	0.9	200	Before dilution
		38 to 41					1	0.9	100	
		41 to 47			7.5 ± 0.1	29.9 ± 0.8	1	0.9	100	The medium was diluted by 50 % on day 41
		47 to 52					1	0.9	0	
		52 to 60					1	0.9	300	
III	44 % RDBER medium replaced with real sterilized hydrolyzate between days 60 and 72; testing applied anodic potential between days 73 and 82	60 to 72	Batch	-	7 ± 0.1	29.7 ± 0.1	1	0.9	300	Hydrolyzate was particle-free
		73 to 74					1	0.9	300	
		74 to 76					1	0.9	400	
		76 to 80					1	0.9	500	
		80 to 82					1	0.9	600	
IV	Influence of anode rotational speed and recirculation rate	82 to 84			7.3 ± 0.1	30.5 ± 0.5	1.2	0.9	600	-
		84 to 87					1.4	0.9	600	
		87 to 90					1.4	1.9	600	
		90 to 91					1.4	2.8	600	
		91 to 96					1.4	3	600	
V	Effect of ionic conductivity	96 to 103			7.5 ± 0.1	30.4 ± 0.5	1.4	3	600	
		103 to 110					1.4	3	600	
VI	Synthetic hydrolyzate	149 to 159	Cont.	3.4 ± 0.3	8.4 ± 0.3	31.2 ± 0.7	3	3	300	The synthetic hydrolyzate was particle-free
VII (A)	Unsterilized real hydrolyzate	169 to 200		6.7 ± 2.8	7.9 ± 0.1	32.2 ± 1.2	3	3	300	Presence of visible particles
VII (B)		169 to 200		8.6 ± 2.5	8.6 ± 0.1		3	3	300	

[a]representation of the steady-steady period after the current peaked and stabilized

5.3.2   Batch phases I to V with dual species-inoculation in a sterilized liquid medium

Phase I was performed at an anode disk rotation of 1 rpm, pH 7 (at the start), and recirculation rate of the reactor content of 0.9 h^{-1} (((i.e., recirculation rate (m^3·h^{-1})/reactor volume (m^3)). During the start-up phase, the applied anode potential (E$_{anode, app}$) was maintained at 0 mV vs SHE for around 0.3 h, after which it was increased to 300 mV vs SHE. At this time (until 0.3 h), there was notable oxygen production and dissolved oxygen (DO) concentration reached as high as 18.4 mg·L^{-1} (see **Figure A11** for DO values) even at 0 mV vs SHE, and continued to increase (at 300 mV vs SHE) to 22.5 mg·L^{-1} for a few minutes, and the stabilized in the range of 19.2 ± 1.8 mg·L^{-1} for around 15 h. The initial production of oxygen is not exactly understood, and could be attributed to water electrolysis. Thereafter, there was complete depletion of DO after 1.5 d due to oxygen reduction to water at the anode (now cathode), as the polarity is reversed. This was characterized by the negative current densities at the start, and after DO depletion current values became less negative from -11.8 mA to -9.4 mA (**Figure 5.2A** and **Figure A10A**). This was followed by a slow increase in current until around day 12 up to around 200 mA (**Figure 5.2A** and **Figure A10A**).

The pH-value, as mentioned earlier, started at 7, but over time decreased to around 6 on day 12. To restore initial conditions, pH-value was increased from 6 to 7.7 which coincidentally led to the highest peak in current which stabilized until day 30 (end of phase I; see **Figure 5.2A** and **Figure A10A**). The addition of a highly conductive solution to raise the pH (0.2 L of 2.5 M NaOH) can have two potential effects, 1) an optimum pH for electroactivity of *G. sulfurreducens* within the electroactive biofilm (EAB) since the pH within the EAB is relatively lower in comparison to pH in the bulk solution (Patil et al., 2011), and 2) reduced electrolyte resistance and the associated internal resistance (Merrill and Logan, 2009). This effect is also further discussed in phase V (effect of electrical conductivity). During this peak (phase 1) of the highest current, there was a coincidental production of H$_2$ reaching up to 3.2 L·d^{-1} (equivalent to 36 L·m$_{reactor}^{-3}$·d^{-1}; see **Table 5.2**). Also, a steady-state current density of 240 ± 34 mA·m$_{anode}^{-2}$ was achieved in phase I for an 18-day period (**Figure 5.2B**). To improve upon the current density during phase I, and also since there was considerable concentration of DO in the beginning which could have impeded the growth of these strict anaerobes (Lin et al., 2004), reinoculation was performed with *G. sulfurreducens*, but this did not have any notable effect on current densities (between days 20 to 30). It is suspected that limited mixing or dead zones as well as uneven potential distribution in the reactor led to a patterned biofilm distribution on the anodes and an irregular biofilm coverage along the reactor axis. Limited mixing could have limited the nutrient or substrate transport to the biofilm as well as the transport of products from the biofilm resulting in limitations of biofilm growth. The potential distribution would be a result of varying resistance between the circumference of the anode and the center. These two explanations could be a reason why reinoculation did not show any considerable effect (this effect of biofilm distribution is further discussed in *section 3.5*).

Interestingly, during the peak and stabilization in current after the pH increase in phase I, there was a simultaneous consumption of notable concentration of EtOH and HPr, and also the highest production rate of HAc. Following the initial spike of current, further consumption of EtOH but at a relatively lower rate, and the subsequent slow production rates of HAc until the end of phase I was observed (see **Figure A10B**). This potentially hints at the use of EtOH as a carbon source, however, a direct use of EtOH as a carbon source has not been reported to be a part of the metabolism of *G. sulfurreducens* (Viulu et al., 2013). However, a significant abundance of homoacetogens (*Sporomusa sphaeroides DSM 2875*) was detected in the planktonic phase, albeit much later, since samples for microbial community analysis were taken between days 97 and 105 and on day 116 (see **Figure A13**) as well as at the end of the cultivation (see **Figure A14**).

S. sphaeroides were also detected in the cathodic biofilm (after termination of the experiment in which the abundance was 62 %; see **Figure A14**). A potential syntrophy existing between *S. sphaeroides* and *G. sulfurreducens* is postulated to have led to the overall current (Rümenapf, 2024). A detailed description of the metabolic pathway and the corresponding stoichiometric calculation can be found in **Appendix A23**. CE-values calculated based on the syntrophy between the two strains as well as based on sCOD-values aligned well at a little over 70 % (see **Table A3**).

In phase II, the batch continued, and in this phase the effect of applied potential at the anode ($E_{anode, app}$) was tested to analyze the limiting potential and the subsequent response in current. There are two parts in this phase, one before and one after dilution. Dilution was performed on day 41 as the concentration of HAc reached around 55 mM (see **Figure A10B**), and along with HPr, SCFAs concentration was at around 65 mM. Härrer et al., 2023 studied the synergistic effect of SCFAs mixture, and observed inhibition of *G. sulfurreducens* at concentrations of higher than 50 mM of SCFAs. For this reason, the medium was diluted to approximately 50 % by removing 45 L of the reactor medium while having the outlet of the gas trap connect to an N_2 source and replacing the same volume with anaerobized sterile deionized water to lower the concentration. $E_{anode, app}$ was changed before and after dilution between 0 and 300 mV vs SHE (**Figure 5.2A**), and current density was averaged at different $E_{anode, app}$. Nevertheless, it can be clearly seen that post dilution, the effect of $E_{anode, app}$ showed a relatively smaller slope value (0.26 mA·m^{-2}·mV^{-1}) in comparison to the slope of 0.48 mA·m^{-2}·mV^{-1} before dilution (see **Figure 5.2B**). The reason for the reduced slope value after dilution can be attributed to the following, 1) sloughing of certain part of biofilm as the medium was pumped out and/or 2) reduction in the electrolyte conductivity due to dilution, and the corresponding increase in internal resistance. In any case, an increase in current density by more than 100 % was observed before and after dilution at 300 mV vs SHE in comparison to 0 mV vs SHE. Similar to phase I, calculations were performed on CE-values (see **Table A6**) and it can be seen that after dilution, CE-values changed notably (see **Figure A16**). Nevertheless, it appears as though CE-values showed a downward trend before dilution with increasing $E_{anode, app}$, and the opposite after dilution (**Figure A16**). Higher CE-values after dilution could possibly suggest a better substrate uptake by the EAB, due to the reduced inhibition as a consequence of lower concentrations of SCFAs mixture as shown by Härrer et al., 2023.

In phase III, sterilized anaerobized hydrolyzate was introduced on specific days to monitor the change in current and the response to the hydrolyzate. 11 % of the reactor medium was replaced by sterilized anaerobized hydrolyzate on specific days (60, 68, 69 and 73) and then run as a batch. Following the four hydrolyzate dilutions a range of applied potentials ($E_{anode, app}$) were tested between 300 and 600 mV vs SHE to see whether the positive correlation between potential and achieved current density extends to potentials above 300 mV vs SHE. **Figure 5.2C** shows that the current remains fairly stable until the third dilution, when current starts to drop by on average 17 %, until after the fourth dilution, when there is a significant reduction to around 50 % current in comparison to the starting point. Sloughing off of biofilm is not necessarily a factor here, as there should have been reduction in current after each dilution step. Since the reduction is strongest after the fourth dilution, the effect can beY Um attributed to the hydrolyzate used itself. For the first three dilutions, the composition of the hydrolyzate was rather similar with a higher SCFAs fraction (averaging at 91 % with respect to sCOD), while in the fourth dilution, the ratio of SCFAs (as COD equivalents) to sCOD is only 66 % (see **Table A5**), meaning a large fraction is unclassified dissolved organic carbon that could be presumably not-easily degradable. The lack of increase in current at higher applied potentials than 400 mV vs SHE might also be attributed to the oxidative stress on EABs which can lead to

cell impairment and inhibition, subsequently lowering the substrate uptake, and hence lower current (Ding et al., 2016; Ndayisenga et al., 2023) or the applied potential until 400 mV vs SHE has made the energy barrier low enough for the highest substrate oxidation or electroactivity, and an increase in $E_{anode,\ app}$ above 400 mV vs SHE is not limiting (**Figure 5.2D**).
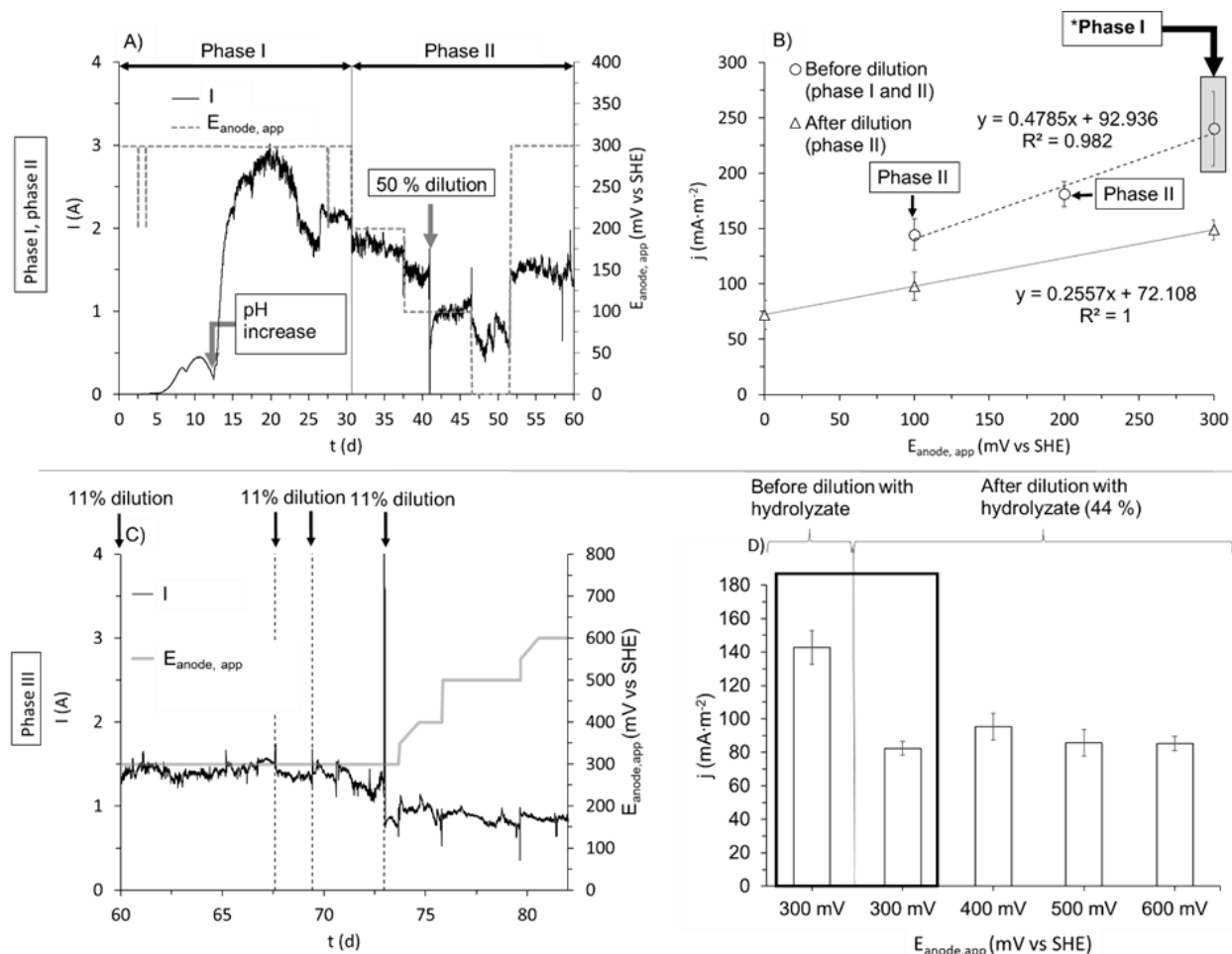
Figure 5.2: Start-up phase (phase I) and effect of applied potential ($E_{anode,\ app}$) before and after dilution (phase II) with anaerobized sterile deionized water on A) current (I) and B) current density (j). Conditions: Anode disk rotation of 1 rpm, temperature of around 30 ± 1 °C, pH 7.3 ± 0.3, and recirculation rate of 0.9 h^{-1}. **Note:** The shaded rectangle in **Figure 5.2B** shows averaged values of steady-state current density in phase I (values were averaged after pH increase until the end of the phase). Effect of different applied potentials ($E_{anode,\ app}$) on C) current (I) and D) current density (j) after dilution with hydrolyzate in phase III. Conditions: Anode disk rotation of 1 rpm, temperature of around 30 ± 1 °C, pH 7.3 ± 0.3, and recirculation rate of 0.9 h^{-1} ((i.e., recirculation rate (m^3·h^{-1})/reactor volume (m^3)).

Hydrodynamic limitations were suspected to cause insufficient mass transfer in the system and limit the current. Subsequently, in phase IV, the anodic rotation speed and the medium recirculation rate were incrementally increased. The anode rotation speed was increased in two steps from 1 to 1.2 rpm (day 82) and 1.4 rpm (day 84), however no noticeable impact on current was visible. In contrast, stepwise increasing the recirculation rate from 0.9 to 3 h^{-1} ((i.e., recirculation rate (m^3·h-1)/reactor volume (m^3)) until day 96 had a pronounced effect on current (see **Figure 5.3A**). The current density could be enhanced by around

100 % (around 160 mA·m^{-2}; **Figure 5.3B**) in comparison to 0.9 h^{-1}. This increment could also be observed by the substrate uptake as evidenced by the higher CE-values (see **Table A6**). A higher substrate transport to the biofilm as well as improved proton transport from the biofilm into the bulk phase and subsequently to the cathode would have led to the higher H$_2$ production. It is postulated that a part of H$_2$ may be redissolved into the system due to the higher recirculation rates, as CE-values were very high, reaching over 200 % (see **Table A6**).

In phase V, from day 96 to day 110, E$_{anode, app}$ was maintained at 600 mV vs SHE, and the influence of electrical conductivity was examined. Conductivity was measured in phase IV, and was found to be 2.6 mS·cm^{-1} (measured on day 90). Between days 96 and 104, the medium in the reactor was spiked twice with a 3.4 M KCl-salt solution to increase the electrical conductivity. Following the second spike, it can be seen that the conductivity reached around 16 mS·cm^{-1}. In any event, there was a strong increase in current at both spikes (maximum of 3.5 A and 2.8 A at the first and second spike, respectively), but was followed by a steady decline, and stabilizing to a level that was achieved in phase IV (around 1.6 A) (see **Figure 5.3C**). The average current densities achieved in phase V after the two spikes were more than 230 mA·m^{-2} (see **Figure 5.3D**). The 1.4-fold increase in current densities can be explained by the decreased internal resistances due to the electrolyte (decreased ohmic losses) (Nam et al., 2010; Rousseau et al., 2020). Although there is a decrease in the internal resistance at the point when the salt solution is added, it is not accompanied by a higher substrate consumption, and hence the current returns to the original state.
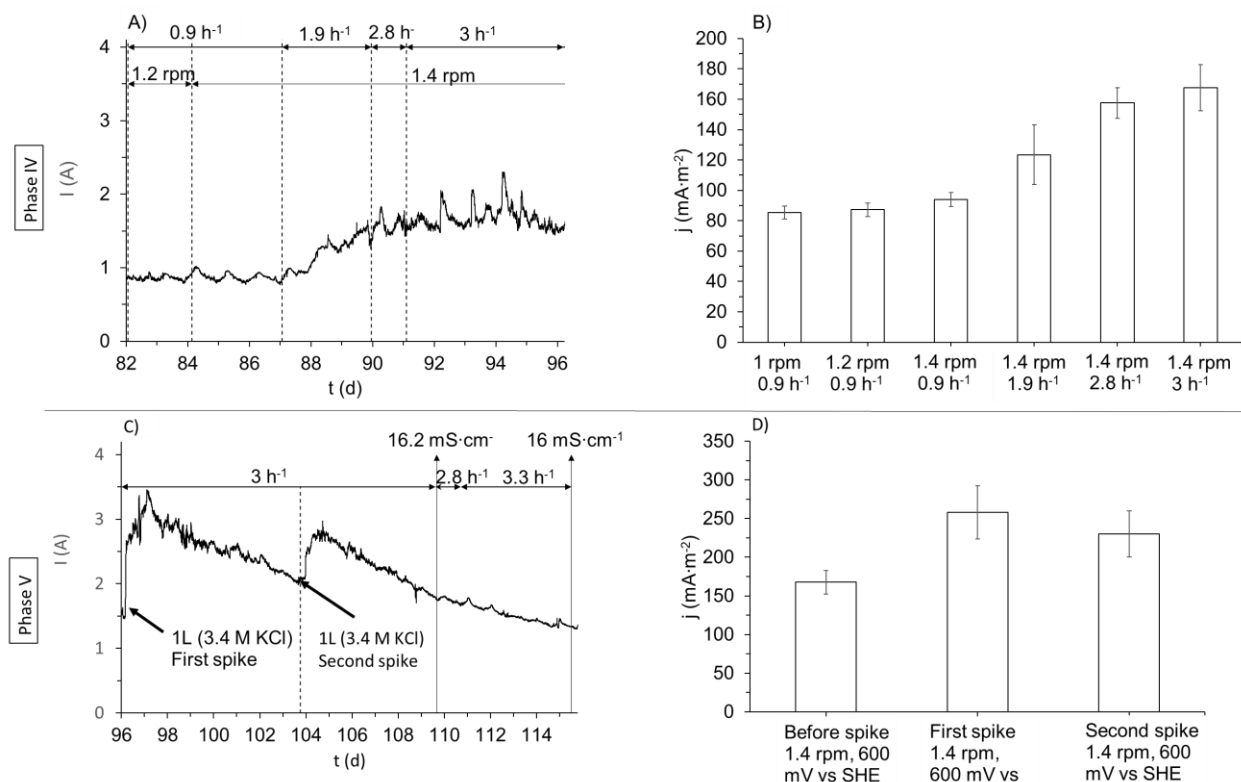
Figure 5.3: Influence of disk rotation speed and reactor content recirculation rate (i.e., recirculation rate ($m^3 \cdot h^{-1}$)/reactor volume (m^3) or h^{-1}) on A) current (I) and B) current density (j) in phase IV. Conditions: Temperature of around 30 ± 1 °C, pH 7.3 ± 0.3, applied potential = 600 mV vs SHE and recirculation rate of 0.9 h^{-1}. Effect of ionic conductivity in phase V on C) current (I) and D) current density (j). Conditions: Temperature of around 30 ± 1 °C, pH 7.3 ± 0.3, applied potential = 600 mV vs SHE, and rotational speed of 1.4 rpm.

The disparity between theoretical hydrogen production and harvested hydrogen yield (**Table 5.2**) was suggested to be caused by the reoxidization of the hydrogen by *G. sulfurreducens.* At the end of batch phase V, the RDBER underwent a second inoculation on day 115 with *Desulfuromonas acetexigens* (**Figure 5.4A**). Both *G. sulfurreducens* and *D. acetexigens* have been found to be enriched in electroactive biofilms inoculated with sludge and wastewater (Katuri et al., 2020; Ketep et al., 2013). However, *D. acetexigens* have been shown to produce higher current densities in comparison to its counterpart (Sapireddy et al., 2021). Also, *G. sulfurreducens* has the ability to use H_2 as an electron donor (Sapireddy et al., 2021), and this can have an overall impact on the volumetric yield of hydrogen (i.e, $H_{2, harvested}$), a setback that can be avoided with *D. acetexigens* (Speers and Reguera, 2012). After inoculation, the system was monitored for changes in current at an $E_{anode, app}$ of 600 mV vs SHE for around 6 days. As no notable improvement was observed, $E_{anode, app}$ was reduced to 300 mV vs SHE, as it was established earlier that there was no significant difference in current between 300 and 600 mV vs SHE (see **Figure 5.2D**), and also the oxidative stress could be avoided; the rotation of the anode was increased to 3 rpm after a certain period to improve substrate convection, but this showed no notable difference. Despite a long start-up phase following the second inoculation (around 20 days), there was no significant change in current (**Figure 5.4A**). Interestingly, the microbiome analysis of the anodic biofilm at the end of the experiment and 85 days after inoculation

revealed that there was no detectable abundance of *D. acetexigens*, which means that the cells did not become established in the RDBER.

5.3.3 Continuous feeding phases VI and VII with unsterile hydrolyzate

On days 135 and 136, 10 L of medium in the RDBER was replaced with unsterilized hydrolysate to test for the system´s behavior under real conditions. The days that followed the second replacement of the hydrolyzate (on day 136) were monitored in a batch mode. Between days 146 and 149, due to the faster degradation of HAc via methanation, the reactor was spiked twice with sodium acetate (not shown) to avoid complete carbon source depletion before continuous feeding started on day 149. Phase VI and phase VII were operated with synthetic hydrolyzate, and hydrolyzate spiked with SCFAs, respectively, averaging at 4037 $mg_{sCOD} \cdot L^{-1}$, 1905 $mg_{sCOD, HAc} \cdot L^{-1}$, 1524 $mg_{sCOD, HPr} \cdot L^{-1}$ and 412 $mg_{sCOD, HBu} \cdot L^{-1}$ (see **Table A5** for complete composition). Phase VI was operated at an average HRT of 3.4 days, while phases VII A and B averaged at HRTs of 7.9 and 8.6 days, respectively. Temperature was in a similar range in the three phases, and the pH-values were mildly alkaline. Other parameters like recirculation rate and anode rotation were maintained constant. In any case, feeding with a synthetic substrate (phase VI) led to higher current (see **Figure 5.4A**) in comparison to phases VII A and VII B, where hydrolyzate was used. One reason could be that the presence of particles in the hydrolyzate (used for phases VII A and VII B), which may have adhered to the anodic biofilm and acted as an interference by inhibiting substrate diffusion to the anode. Comparing VII A and VII B, it is rather clear that alkaline pH-values can slightly mitigate methanation, but this also has a negative effect on the current (see **Figure 5.4A**). The reduced methanation can be seen from the improved gas quality (**Table 5.2)** and also the higher CE-values (**Figure 5.4B**), meaning that the electrons produced from sCOD removal were utilized more towards current generation, and less towards methane production. Nevertheless, the sCOD removal was low in general and extremely low in case of VII B (**Figure A19**). Interestingly, in phase VI, HAc and HPr were consumed (**Figure A19**) and there was production of HBu in the effluent, while in phases VII A and B, HAc and HBu were consumed, and HPr was detected in the effluent. It is unclear as to whether there was a shift in the microflora when the hydrolyzate was fed in phases VII A and B. HBu was removed as high as 50 % in phase VII A and B. In the continuously operated phases, the highest current density was achieved in phase VI (166 ± 42 mA·m^{-2}), and this value reduced to 95 ± 28 and 71 ± 18 mA·m^{-2} in phases VII A and B, respectively (**Figure 5.4B**).
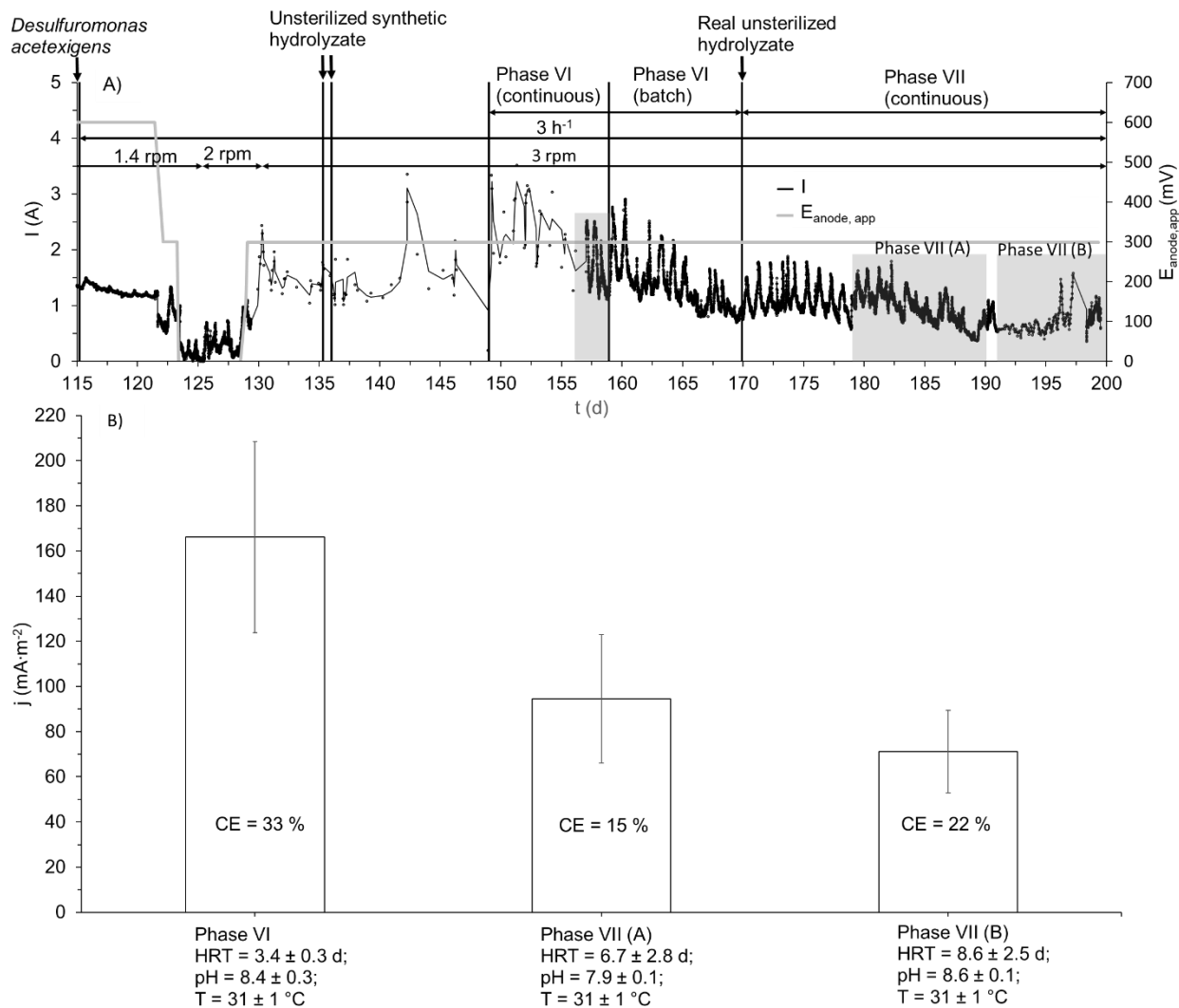
Figure 5.4: A) Current (I) and applied potential ($E_{anode, app}$) and B) pH and gas fraction as a function of time, and C) current density (j) at different phases (VI, VII (A) and VII (B)). **Note:** CE = Coulombic efficiency; The coefficient of variation (CV) of current density was 28 ± 1 % for phases VI and VII. The higher CV in these phases is due to notable temperature shifts during the day and night cycle; The grey area in **Figure 5.4A** indicates the time range during which liquid samples were taken and the values were averaged for current density (j).

5.3.4 Gas production and quality

In general, gas production rates were inconsistent during the phases I, II and III (in batch mode). The volume of H_2 that was harvested in comparison to the volume theoretically produced is around 1 % (i.e., cathodic recovery; see **Table A4**). The low recovery is presumably due to the consumption of H_2 by *S. sphaeroides* growing on the cathode. It is also important to consider the reoxidation of H_2 by *G. sulfurreducens* (Sapireddy et al., 2021) which was evident from the high CE-values in the batch phases. In their study on a lab-scale RDBER, (Xiao et al., 2025) clearly highlighted the reoxidation of H_2 at the cathode with CE-values reaching as high as 353 %, although it is important to mention that the cathodic configuration was different

as mentioned in *section 5.2.1*. With the modified cathodic configuration as like as in this study, reoxidation was still prevalent but lower.

In phase IV, the higher recirculation rates led to a higher and stable hydrogen production (see **Table 5.2**). Other than the higher substrate uptake mentioned before, It is also posited that a higher recirculation rate may have caused some of the trapped H_2-bubbles on the cathode to be sheared off (see **Figure A12**). The evolution of H_2 was also consistent in phase V, where a high recirculation rate was maintained. Evaluating the gas composition, it is important to note that a rather high gas purity (**Table 5.2**) could be maintained with H_2-fraction averaging at around 80 % during phases I to V. This can be attributed to the careful initial two-step chemical sterilization that was carried out before start-up. The lack of methanation can also be confirmed by the complete absence of methanogenic archaea based on samples before the unsterilized hydrolyzate was introduced (see **Figure A13**).

During the preceding sterile operational phases, gas fraction of more than 80 %-H_2 could be maintained over 130 days. However, within a few days after the unsterilized hydrolyzate was fed there was a rise in methane fraction to more than 80 % despite a long and defined dual-species start-up with a sterilized medium. The introduction of real hydrolyzate clearly introduced methanogens in the system, and archaeal analysis at the end of the experiment revealed the presence of methanogens in the anodic biofilm and planktonic phase though none in the cathodic biofilm (see **Figure A15**). However, looking into the pattern of methanation, the rise in CH_4 fraction was concomitant with a decrease in H_2 and CO_2 fraction hinting at hydrogenotrophic methanation (Kokko et al., 2018) by utilizing the redissolved H_2. In contrast, the faster degradation rate of acetate (days 142 and 146 – not shown) indicates the occurrence of acetoclastic methanogenesis.

As mentinoned earlier, phases VI and VII were operated in a continuous mode with unsterilized hydrolyzate. **Table 5.2** clearly shows a complete shift in gas fraction towards a mixture of H_2, CH_4 and CO_2 in phases VI and VII when the unsterilized hydrolyzate was fed. The shift in gas composition clearly shows that an MEC implemented at a WWTP should always account for a large CH_4-fraction. Alkaline pH was maintained in phases VI and VII mainly to reduce methanation, as methanogens are more active in a neutral range (pH 6 to 7) (Wu et al., 2010). Although methanogens can exhibit considerable activity in the alkaline range used in this study (pH 8 to 8.5) (Wu et al., 2010), it is also important to maintain electroactivity as extreme pH conditions can be detrimental (Sun et al., 2019). Nevertheless, a slight suppression of methanogenesis was observed when pH was increased to around 8.5 in phase VII B (see **Table 5.2**). Interestingly, the second RDBER which was operated under unsterile conditions showed no H_2, and the gas fraction comprised of only CH_4 and CO_2 (averaging at 80 % to 20 %; see **Figure A18**). An inference from the comparison of the two RDBERs is the fact that a sterilized start-up phase with defined cultures could maintain a notable concentration of H_2 in the gas phase along with CH_4 (**Table 5.2**). Such a gas mixture can be referred to as biohythane, wherein the typical concentration is 5 to 25 % H_2 (Ghimire et al., 2017).

Table 5.2: Theoretical H_2 production ($H_{2, th}$) based on current values, and average and maximum harvesting rates of H_2 ($H_{2, harv}$) and CH_4 ($CH_{4, harv}$), and average gas composition.

Phase	pH	$H_{2, th}$ $(L \cdot m_{reactor}^{-3} \cdot d^{-1})$		$H_{2, harv}$ $(L \cdot m_{reactor}^{-3} \cdot d^{-1})$			$CH_{4, harv}$ $(L \cdot m_{reactor}^{-3} \cdot d^{-1})$			H_2 (%)		CO_2 (%)		CH_4 (%)	
		μ	σ	μ	σ	Max	μ	σ	Max	μ	σ	μ	σ	μ	σ
I	6.9	268	37	3.4	8.7	35.5	ND	ND	ND	87	13	13	13	ND	-
II	7.5 ± 0.1	149	46	0.7	2	9.4	ND	ND	ND	85	5	15	4	ND	-
III	7 ± 0.1	142	32	0.4	1	3.5	ND	ND	ND	78	3	22	3	ND	-
IV	7.3 ± 0.1	144	42	1.6	1.3	3.9	ND	ND	ND	76	-	24	-	ND	-
V	7.5 ± 0.1	287	39	2.7	2.2	6	ND	ND	ND	77	-	23	-	ND	-
VI	8.4 ± 0.3	185	33	3.2	1	4.9	32.8	12.9	50	8	1	4	2	88	2
VII A	7.9 ± 0.1	105	32	0.2	0.2	0.34	2.1	1.4	3.1	8	-	5	-	87	-
VII B	8.6 ± 0.1	87	21	0.6	0.7	1.9	3.8	4.6	12	12	1	4	-	84	1

μ - Average, σ – Standard deviation, ND - Not detected; "-" negligible standard deviation (low coefficient of variation). The double line indicates the phase (VI) in which unsterilized hydrolyzate was fed

5.3.5   Biomass distribution analysis to evaluate reactor performance

In order to understand the factors limiting the performance of the RDBER, the reactor was dismantled after the 200-day run and evaluated for the distribution of biofilm on the anode disks. The three analysis methods for biofilm characterization are listed below and described in detail in the **SI** *section 1.5.*:

1) digital photographs to determine effective surface coverage (SC_{eff}) (all disks)
2) OCT images to determine mean biovolume ($\overline{BV}$), and substratum coverage (SC) (selected disks)
3) gravimetric analysis to determine normalized biomass (selected disks)

Figure 5.5A to 5.5D shows the difference in biofilm distribution along the reactor length, and both reactor length and radius (**Figures 5.6A to 5.6D**) along the flow directions, x (front side of disk) and -x (back side of the disk). Examining SC_{eff}, the pattern of distribution is rather similar in both directions of flow. The average SC_{eff} -values from 1-20 cm, 20- 50 cm, 50 – 70 cm, and 70 to 100 cm are 37 ± 21 %, 31 ± 16 %, 10 ± 14 % and 41 ± 17 %, respectively.On the anode disks between 50-70 cm very little biofilm accumulation was visible. The results of SC_{eff} was corroborated by the normalized biomass (m_N). The lowest values of m_N were seen on the disk at a distance of around 63 cm from the inlet, and m_N was around 0.1 $g \cdot m^{-2}$ and 0.01 $g \cdot m^{-2}$ for x and -x, respectively. Despite relatively scarce data for m_N, correlating m_N and SC_{eff} showed a rather decent fit of around 76 % and 83 % along x and -x, respectively (see **Figure 5.5C** and 5.**5D**). Closer inspection of the individual disks for biofilm distribution along the disk radius, led to the observation of an obvious pattern visible from the parameters mean biovolume $\overline{BV}$ and substratum coverage SC obtained from OCT-images, wherein the development of biofilm is more pronounced at a longer radii (see **Figure A8C** for instance) resembling the shape of an annulus. At radii of 7 and 11 cm along x, average $\overline{BV}$-values are 1.8 ± 2.3 $\mu m^3 \cdot \mu m^{-2}$ and 3.8 ± 5.8 $\mu m^3 \cdot \mu m^{-2}$, respectively, and this parameter is at a similar range along -x, 0.7 ± 0.3 $\mu m^3 \cdot \mu m^{-2}$ and 1.7 ± 1.9 $\mu m^3 \cdot \mu m^{-2}$, respectively. Substratum coverage (SC) shows an obvious pattern as like that as $\overline{BV}$ at 7 and 11 cm along x and -x, averaging at 8 and 27 %, respectively. $\overline{BV}$ and SC are at least 100 % to 200 % higher at a radius of 15 cm in comparison to the lower radius of 11 cm, and it can be as high as 400 % to 1200 % with respect to the lowest radius of 7 cm (see **Figures 5.6A to 5.6D**).

Based on these data, there are three major observations, 1) the flow direction, x or -x did not have a notable effect (except for the first and last disk) on the front or the back side of the disks for any of the image-based or gravimetric analysis results (see **Table A8** for consolidated results and also **Figure A20** showing the mean values of each parameter), 2) concerning the distribution of biofilm along the reactor length), SC_{eff} was higher and similar in the first half of the reactor, and the last 20 % of the reactor's length, with little to no growth observed between 50 and 70 cm, accounting for around 20 % of the reactor's length and of the anode area, and 3) biofilm growth (based on $\overline{BV}$, SC and the visual observation) was more pronounced along longer radii until the disks' circumference, thus showed an annular shaped distribution.
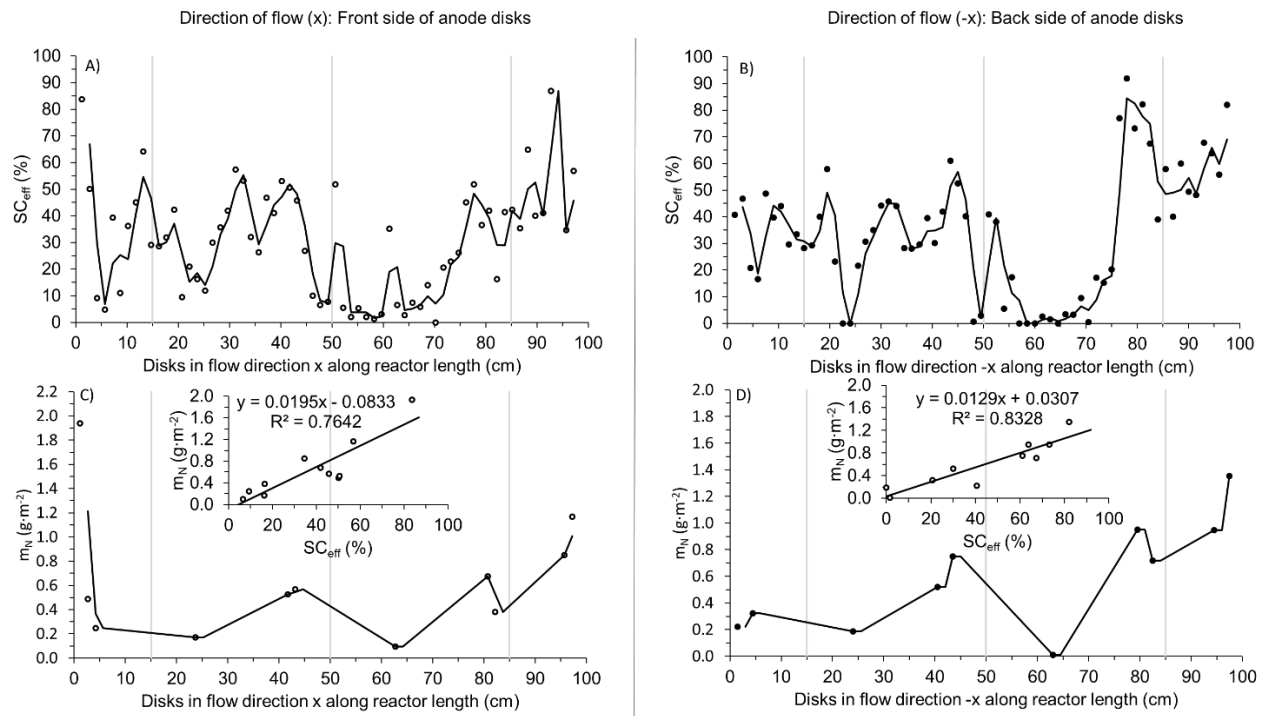
Figure 5.5: Effective surface coverage (SC_{eff}) along A) flow direction (x) and B) flow direction (-x). Normalized biomass (m_N) along A) flow direction (x) and B) flow direction (-x). The figures in C and D show the correlation between m_N and SC_{eff}. **Note:** For disk number 65 (along -x, back side), SC_{eff} was calculated based on a relationship between SC_{eff} and the normalized biomass m_N ($R^2 = 0.83$ $m_N = 0.0129 \cdot SC + 0.0307$; see **Figures 5.5C** and **5.5D** for the relationship between the two parameters). The grey lines in A, B, C and D show the 3 outflow openings at the top of the reactor.

The accumulation of an optimal biofilm thickness is a crucial factor affecting electrogenesis in an electroactive biofilm, as a correlation between higher current and biofilm thickness of EABs is shown by several recent publications. For higher current, optimum biofilm thickness is required as overgrown or thicker biofilms can limit electron transfer within the biofilm (Bonanni et al., 2013). Franks et al. (2012) reported a biofilm thickness of 50 µm for *G. sulfurreducens* reaching a current density of 3500 mA·m^{-2}, while for the same species, Sun et al., 2016 observed a maximum current density of around 4000 mA·m^{-2} at a thickness of 20 µm followed by a reduction until 45 µm. While optimum biofilm thickness is different across several literatures ranging between 20 to 40 µm (Bonanni et al., 2013), the observed $\overline{BV}$-values in this study averages at around 5 µm³·µm^{-2} (mean value of $\overline{BV}$ was 5.0 ± 8.5 µm³·µm^{-2} (see **Table A8**))

possibly hinting at underdeveloped biofilms on the anode which could explain the relatively low current. More so, *Geobacter sp*. contributed to only around 20 % of the anodic biofilm (see **Figure A14**).

From these observations, a synergistic effect of both the flow velocity profile and potential distribution is suspected to be a major factor impeding reactor performance by causing low current production. Firstly, evaluating the entire anode stack, the medium convection to inner sections of the reactor is low due to limited recirculation rate which can be seen from the low values of SC_{eff} in **Figure 5.5A** and **Figure** 5.**5B**. Also, it is important to note that the values of m_N are highest on the first disk along the direction x (front side) and on the last disk along the direction of -x (back side). The higher values could be explained by the presence of a stationary boundary (the reactor itself) and the rotating anode which can potentially improve mass transfer and hence a better biofilm development. Other than the above-mentioned disks, the bulk phase between the anode disks, despite the rotatory movement, is susceptible to lower relative fluid velocities between bulk liquid and anode surface and hence reduced mass transfer due to the small distances between the equally rotating disks. The stagnant bulk phase due to the low relative motion between the anode disks could also explain why an increased rotational speed from 1 to 3 rpm did not have any profound effect, excluding the first and the last disk.

Examining individual anode disks which showed an annular shaped biofilm distribution, the tangential velocity and also the potential distribution are presumable causes for such a specific pattern. Tangential velocity of the rotating disk is a function of radius, and a better substrate uptake occurs along the extended radii favoring more cell attachment and proliferation. However, it is suspected that the tangential velocity predominantly affects the first disk along the direction x (front side) and on the last disk along the direction of -x (back side) due to the stationary boundary formed by the reactor wall. Also, biofilm attachment and development at the outer radius of the disk may have been supported by a lower local internal resistance. The internal resistance (Ohmic loss) increases with distance between anode and cathode, and hence the inner parts of the anode towards the center have a higher local resistance. Therefore, the outer parts or the extended radii of the anode are susceptible to higher current which then decreases towards the center of the anode due to the increased spatial distance from the cathode (Hernández-García, 2020).
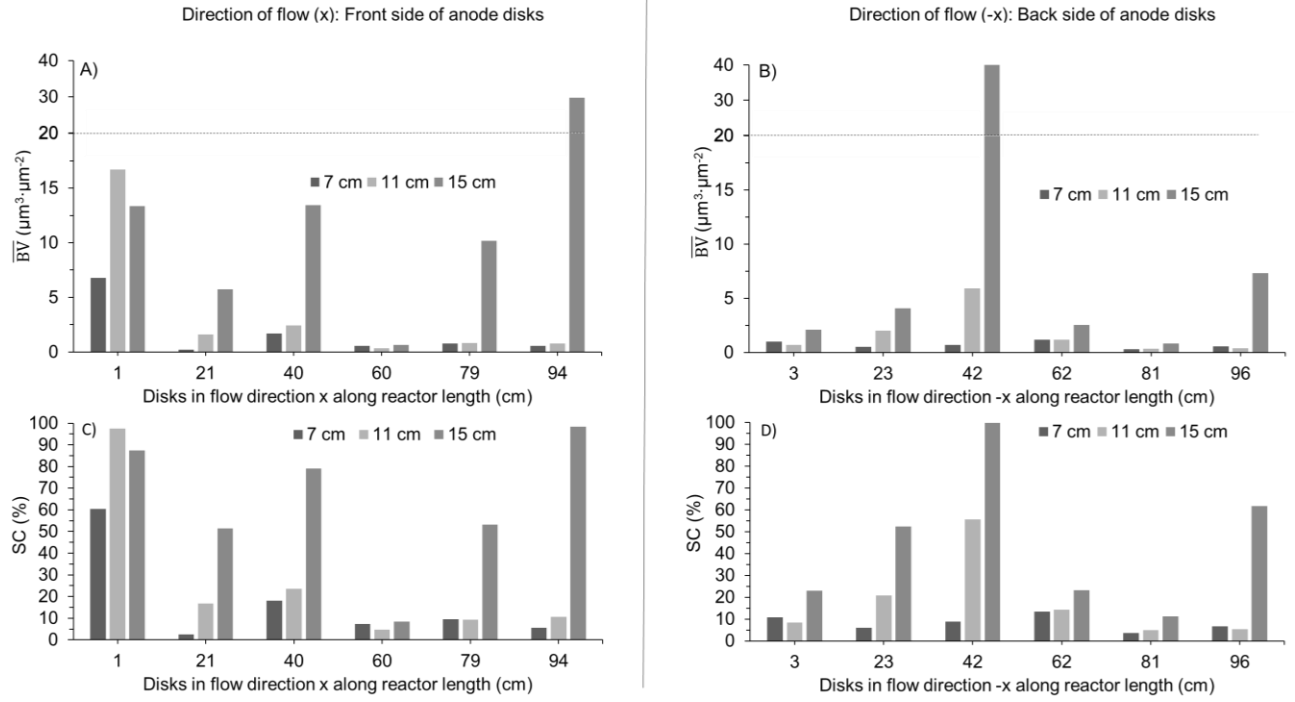
Figure 5.6: A) and B) biovolume ($\overline{BV}$); C) and D) substratum coverage (SC) along the radius for the front (flow direction: x) and back sides (flow direction: -x) of the anode disks.

5.3.6 Reactor performance, limitations and improvements

Firstly, considering the results of effective surface coverage (SC_{eff}) of the anode, the question lies in the fact how the RDBER can be improved. It is obvious that mixing and the subsequent hydrodynamics are a limiting factor. A CFD simulation could provide further insight into the velocity profile and flow distribution. Clearly, recirculation rates increased the current density and the subsequent substrate consumption, therefore, a significant increase in recirculation rates is a proposed parameter that requires further investigation. Increasing the rotational speed of the anode disks from 1 to 3 rpm showed no effect, hinting that this speed is not a limiting factor. In summary, reduced substrate convection and product removal due to low flow velocities in the middle sections of the RDBER is a possible reason that could have affected biofilm distribution.

Nevertheless, the anode area of 10 m^2 is only partially utilized, with the highest value of effective effective biofilm area (BA$_{eff}$, see **equation A5** for calculation) being only 3.27 m^2. Considering the effective biofilm coverage, current density amounted to 508 ± 128 mA·m$_{anode}^{-2}$. Since the high anode area to reactor volume (100 m$_{anode}^2$·m$_{reactor}^{-3}$) is one of the underlining features of the RDBER (with the current effective ratio being 33 m$_{anode}^2$·m$_{reactor}^{-3}$), reducing the number of anode disks may seem contradictory. However, based on the annular shape of the biofilm, a pattern that cannot be necessarily avoided, it would seemingly be more practical to have annular shaped anode disks supported by spokes as the biofilm distribution appears to be governed by the tangential velocity. Such a design could still maintain a relatively high anode area to reactor volume ratio, while also having large areas of openings (due to the annular shaped anode disks) along the reactor axis that will increase convective transport of the fluid, and the subsequent nutrient and substrate transfer to formerly inaccessible areas of the reactor as well as improved product removal. This value of 33

$m_{anode}^2 \cdot m_{reactor}^{-3}$ is still comparatively high and to the best of our knowledge, the highest ratio realized so far at pilot-scale (reactor volume = 175 L) for a MEC was 34 $m_{anode}^2 \cdot m_{reactor}^{-3}$ (Cotterill et al., 2017). Secondly, regarding the cathodic recovery, the amount of H_2 harvested is low as seen from the experiments. The RDBER that was operated at bench scale (10 L) had a different cathodic configuration (Hackbarth et al., 2023). The cathode was a set of semi-circular disks that were arranged between the circular anode disks close to the lower half. It was posited that such a design would result in significant H_2 consumption as the hydrogen that evolved at the cathode would have to bubble over the anode, where potential H_2 scavengers or even *G. sulfurreducens* itself could utilize H_2 as an electron donor. Although the half cylindrical perforated cathode used here was supposedly an upgraded design to enhance H_2 recovery, the contradictory observed here through low recoveries, possibly indicates that the shear forces created during the anodic rotation in the bench-scale reactor may have aided better H_2 recovery. Utilizing a similar configuration as the bench-scale reactor but with the semi-circular cathode disks close to the upper half of the anode disks is hypothesized to improve H_2 recovery and reduce H_2 scavenging.

At any rate, the RDBER has to be compared with existing MEC reactors for posterity. Phase VI in this study is chosen for comparison with the surveyed pilot-scale MEC reactors in the hundred-liter range (**Table 5.3**). Phase VI (pH 8.4 ± 0.3, T = 31 ± 1°C, HRT = 3.4 ± 0.3 d) had the highest current density values, H_2 and CH_4 production, and the highest CE-values during unsterile continuous feeding (see *section 5.3.3* and **Figure 5.3**). The 100-L RDBER is also compared with the 10-L RDBER (Hackbarth et al., 2023) under a defined dual-species start-up conditions to assess the impact of upscaling. A second 100-L RDBER was also operated for a long-term period only under unsterile conditions at a wastewater treatment plant (see **Appendix A26** for results). It appears that a sterile start-up phase can prevent complete dominance of methanation, as H_2 production (along with CH_4) can still be maintained to a certain extent along with higher current densities and CE-values (see **Table 5.3**). The production of biohythane from the RDBER, as mentioned earlier, hints at the opportunity to valorize this gas mixture into an enhanced combustible source for higher energy recovery in comparison to the typical biomethane obtained via anaerobic digestion (Z. Huang et al., 2017). At any rate, the volume of H_2 harvested is in the range of other pilot-scale MECs (compare values in **Table 5.3**). Considering these points, the scalability, rotary motion of the anodes, and adjustable surface area-to-volume ratio are indispensable components of the RDBER that merit a thorough optimization.

Table 5.3: Literature comparison of pilot-scale MEC reactors.

V (L)	Anode area (m²)	Specific anode area ($m_{anode}^2 \cdot m_{reactor}^{-3}$)	Substrate	Mode	pH	T (°C)	HRT (d)	V (mV)	Average stable j ($mA \cdot m_{anode}^{-2}$)	Average stable j ($mA \cdot m_{reactor}^{-3}$)	$H_{2,th}$ ($L\ H_2 \cdot m_{reactor}^{-3} \cdot d^{-1}$)	$H_{2,harv}$ ($L\ H_2 \cdot m_{reactor}^{-3} \cdot d^{-1}$)	CE (%)	$CH_{4,harv}$ ($L\ CH_4 \cdot m_{reactor}^{-3} \cdot d^{-1}$)	Gas fraction	Ref
10	1	100	20 mM HAc, 20 mM HLa	Batch, sterile	7.4	30	--	0[d]	800 to 1300[c]	80000 to 130000	NR	430	NR		88 % H_2	Hackbarth et al., 2023
90	10	111	25 mM HAc, 25 mM HLa, 176 mM etOH	Batch-start up (**phase I**), sterile	7.2 ± 0.2	29	-	300[d]	240 ± 34	26667 ± 3778	268 ± 37	3.4 ± 8.7	74	ND	87 % H_2	
90s	10	111	Synthetic hydrolyzate	Continuous, unsterile (**phase VI**)	8.4 ± 0.3	31 ± 1	3.4 ± 0.3	300[d]	166 ± 42	18444 ± 4666	185 ± 33	3.2 ± 1	33	33 ± 13	8 % H_2/ 88 % CH_4	This study
	3.27	36						300[d]	508 ± 128[a]							
90w	10	111	25 mM HAc, 25 mM HLa	Batch-start up, unsterile	7.1 ± 0.2	29 ± 4	-	0[d]	30 ± 8	3333 ± 889	ND	ND	6	6	85 % CH_4	
	10	111	100 mM HAc, 91 mM HPr, 6 mM HBu	Batch (50 % hydrolyzate), unsterile				900[e]	19 ± 12	2111 ± 1333	ND	ND	1	40	75 % CH_4	
120	2	16.4	Domestic wastewater		6 to 7	17 ± 1	1	1100[e]	270	NR	NR	15	55	ND	100 % H_2	Heidrich et al., 2013
175	6	34		Continuous, unsterile	7 to 8.5	8 to 16	0.2	900[e]	294 ± 185	10080 ± 6343	NR	1 to 5	10 to 30[b]	ND	60 to 93 % H_2	Cotterill et al., 2017
1100	-	-	Winery wastewater		6.4 ± 0.3	31 ± 1	1	900[e]	NR	6000 to 8000[b]	60 to 80	ND	NR	150 to 250	85 % CH_4	Cusick et al., 2011

[a]-calculated based on effective biofilm-covered area (BA$_{eff}$), [b] the values are approximate (note: 7200 mA·m$_{reactor}^{-3}$ was the peak value reported), [c] approximate values (1300 mA·m$_{anode}^{-2}$ is the highest recorded value), [d] applied anode potential vs. SHE, [e] applied voltage. NR- not reported, ND – Not detected, [w]- RDBER operated on-site of a wastewater treatment plant, [s]-RDBER operated with sterile start-up, [f]-volumetric current density based on reactor volume

5.4   Conclusion

The 100-L rotating disk bioelectrochemical reactor (RDBER) was evaluated as a terminal treatment step for H_2-production in a wastewater biorefinery. Current densities in the dual-species sterile start-up phase averaged at 240 mA·m^{-2} with a Coulombic efficiency (CE) of around 70 %. Sterile start-up prevented methanogenesis for a 130-day period, with H_2-fraction averaging at approximately 80 %. During continuous feeding with unsterile hydrolyzate, current density amounted to 170 mA·m$_{anode}^{-2}$ (CE = 33 %) along with the production of biohythane (9 % H_2:86 % CH_4). Image and gravimetric analyses showed an annular-shaped biofilm coverage on the anode disks covering 1/3rd of the area owing to the tangential velocity and the potential distribution profile. The RDBER can compete with other pilot-scale reactors in terms of current density and H_2 harvested, and along with further design upgrades in electrode configuration, the RDBER poses a great potential as a promising bioelectrochemical system.

6 Conclusions and outlook

In this study, evaluation of a potential wastewater biorefinery was carried out by valorizing the organic carbon content in primary sludge. The primary objectives of this study were to ferment short-chain fatty acids (SCFAs) via dark fermentation and subsequently extract the same in a particle-free permeate through a combination of chamber filter-press and microfiltration.

Dark fermentation was evaluated at lab- (2 L), bench- (40 L) and pilot-scale (300 L) to optimize fermentation of SCFAs by assessing crucial parameters like pH, temperature and hydraulic retention time (HRT) in batch and semi-continuous operating modes. The results showed that yields of SCFAs can be enhanced at short HRTs of 1.5 to 3 days, neutral pH of 7 and mesophilic temperature of 32 °C. Yields of SCFAs amounted to 222 ± 24 mg$_{SCFAs}$·g$_{VS}^{-1}$ at organic loading rates of 18 ± 3 g$_{VS}$·L^{-1}·d^{-1}, while yields could be improved to around 350 ± 55 mg$_{SCFAs}$·g$_{VS}^{-1}$ at 11 ± 3 g$_{VS}$·L^{-1}·d^{-1}. In all cases, acetic and propionic acids are the predominant fermentation products contributing to 30 to 40 % of the total concentration, respectively. The amount of methane produced during dark fermentation is less than 2 NmL·g$_{VS}^{-1}$, and hence the concentration of solids removed is negligible in the hydrolyzate in comparison to primary sludge. Therefore, the dry matter content in the hydrolyzate is around 2 to 5 %, which is similar to that of primary sludge.

The hydrolyzate was then conditioned with a starch-based cationic flocculating agent, hydroxypropyltrimethyl ammonium starch (HPAS). The HPAS-conditioned hydrolyzate was then dewatered using a chamber filter-press with a 100 µm-mesh size. A significant concentration of total solids up to 60 % can be removed at a dosage range of $8 - 25$ mg$_{HPAS}$·g$_{TS}^{-1}$, resulting in a filtrate with suspended solids ranging from 100 to 1300 mg·L^{-1}. A maximum volume recovery of 85 % can be achieved with the filter-press. The filtrate was further processed through a ceramic microfiltration membrane (**α**-Al$_2$O$_3$) with a 0.2 µm pore size and a filtration area of 0.316 m^2. The mode of filtration used was cross-flow, and firstly a method was established for cross-flow optimization by analyzing the total filtration resistance. By monitoring the slope of change in total resistance, an optimum cross-flow velocity (at least 2.3 m·s^{-1}) was determined which could be used for long-term filtration. Despite the lower suspended solids concentration and the high cross-flow velocity, the microfiltration membrane underwent severe fouling due to HPAS. HPAS passed through the larger pores of the filter-press and had an electrostatic interaction with the microfiltration membrane. Increased backwashing frequency (every 600 seconds for 20 seconds) could sustain permeate flux of around 20 L·m^{-2}·h^{-1} (LMH), while reducing pH below the membrane's iso-electric point to repel cationic HPAS from the membrane surface improved performance, maintaining flux between 70 and 80 LMH. Further, a semi-continuous cascade of dark fermentation, chamber filter-press, and microfiltration was performed, and results showed that microfiltration can filter around 900 L·m$_{eff}^{-2}$ without chemical cleaning while maintaining flux in the range of 50 to 60 LMH. A volume recovery of 70 % can be achieved with microfiltration. Chemical cleaning was carried out using a basic solution (pH ≈ 12) to remove organic fouling followed by an acid solution (pH ≈ 2) to remove HPAS-based fouling which recovered at least 75 % of the permeate flux. Evaluating the particle-free permeate, around 4 g TOC$_{SCFAs}$·capita^{-1}·d^{-1} can be recovered from the sludge stream with a purity of 0.85 to 0.97 C$_{SCFAs}$·DOC^{-1}. The concept of this treatment chain is analyzed by comparing the treatment scheme of a typical municipal wastewater treatment plant in **Figure 6.1** (compare with **Figure 1.1** in **chapter 1** for the custom scheme).

A pilot-scale (100 L) rotating disk bioelectrochemical reactor (RDBER) was evaluated as a terminal treatment step to convert SCFAs obtained after microfiltration to hydrogen via microbial electrolysis. The

RDBER was inoculated with *Shewanella oneidensis* and *Geobacter sulfurreducens*, with the *G. sulfurreducens* as the primary exoelectrogens for substrate oxidation. The RDBER was operated for 200 days in batch and continuous modes to optimize pH, hydraulic retention time (HRT), conductivity, recirculation rates, rotational speed, and anode potential. The batch mode was operated in the defined dual-species incoulation in a sterilized medium, while unsterilized hydrolyzate with short-chain fatty acids was utilized for continuous feeding. In the batch mode, increasing pH in the defined dual-species start-up phase produced highest current densities of around 240 mA·m_{anode}^{-2} at 300 mV vs SHE with a Coulombic efficiency (CE) of over 70 %. During this time, the highest amount of hydrogen of 36 L H_2·$m_{reactor}^{-3}$·d^{-1} could be harvested. A sterile start-up completely prevented the development of methanogenesis, and maintained a CH_4-free gas phase with H_2-fraction reaching as high as 80 % for a 130 day-period. Among the parameters tested in the batch phase, increased recirculation rate of the medium from 1 to 3 cycles per hour increased current density by 100 %. In the continuous feeding mode with unsterile hydrolyzate, the reactor shifted towards hythane production (9 % H_2/ 86 % CH_4/ 3 % CO_2). At an HRT of 3 days (300 mV vs SHE), an average current density of 170 mA·m_{anode}^{-2} could be maintained with a Coulombic efficiency of 33 % along with the harvestation of 3 L H_2·$m_{reactor}^{-3}$·d^{-1} and 33 L CH_4·$m_{reactor}^{-3}$·d^{-1}. Image- and gravimetric based analyses revealed an inconsistent distribution and incomplete coverage of biofilm accounting for only one third of the anode's total area. Considering the effective biofilm-covered area, the highest possible current density achieved was around 510 mA·m_{anode}^{-2}. A lack of nutrients and substrate transfer due to low relative flow velocities between the anodic biofilm and the liquid bulk phase in the middle sections of the RDBER is a possible reason that could have affected biofilm growth and distribution. The rotary motion of the anode along with the potential distribution might have contributed to an annular biofilm distribution reducing the effective biofilm coverage. Based on the performance, the RDBER with further upgrades in reactor architecture bears a great potential as a promising bioelectrochemical system.
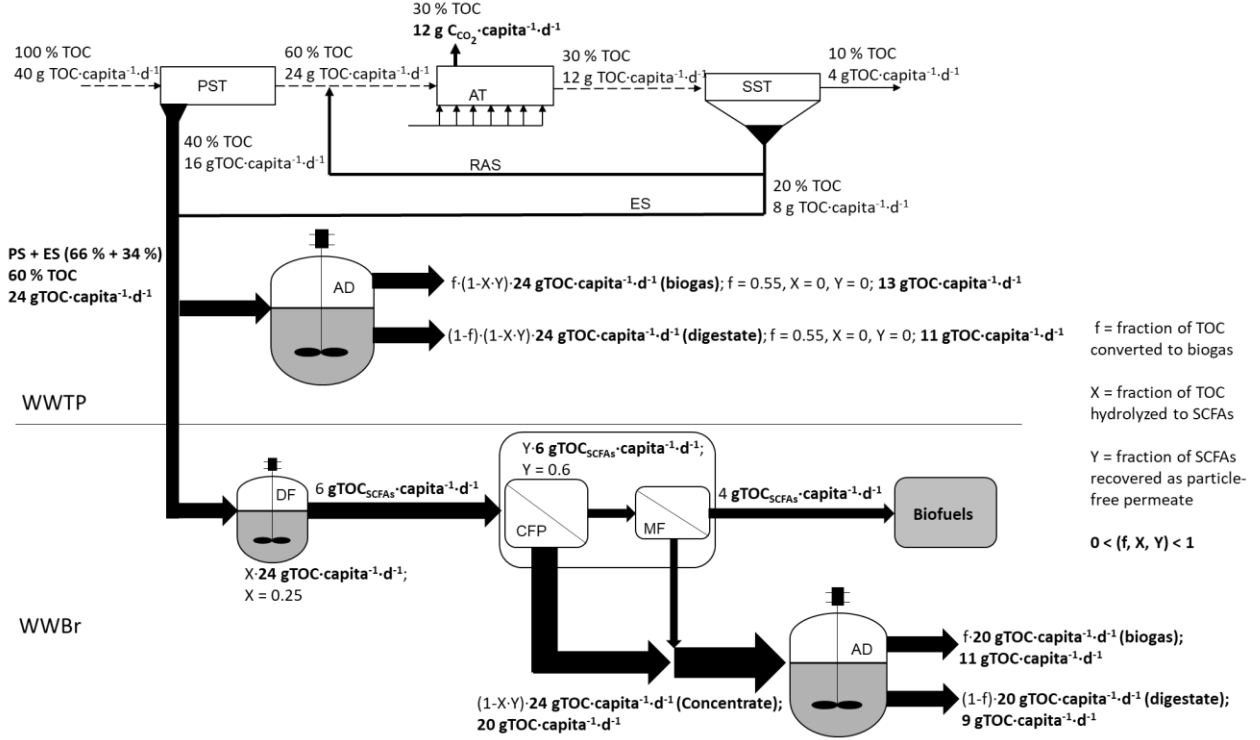
Figure 6.1: Schematic representation of the organic carbon load in a wastewater treatment plant (WWTP) and a wastewater biorefinery (WWBr). X and Y are zero for WWTP and for WWBr, the values are experimental and are obtained from this study. The values of TOC are modified based on Wan et al., 2016. (PST = Primary sedimentation tank, AT = Aeration tank, RAS = Return activated sludge, SST = Secondary sedimentation tank, ES = Excess sludge, TOC = Total organic carbon, DF = Dark fermentation, CFP = Chamber filter-press, MF = Microfiltration, AD = Anaerobic digestion).

7   References

Ali, R., Saravia, F., Hille-Reichel, A., Gescher, J., Horn, H., 2021. Propionic acid production from food waste in batch reactors: Effect of pH, types of inoculum, and thermal pre-treatment. Bioresour. Technol. 319, 124166. https://doi.org/10.1016/j.biortech.2020.124166

Al-Malack, M.H., Anderson, G.K., 1997. Use of crossflow microfiltration in wastewater treatment. Water Res. 31, 3064–3072. https://doi.org/10.1016/S0043-1354(96)00084-X

Amann, A., Weber, N., Krampe, J., Rechberger, H., Zoboli, O., Zessner, M., 2021. Operation and Performance of AustrianWastewater and Sewage Sludge Treatment as a Basis for Resource Optimization. Water 13, 1–15. https://doi.org/10.3390/w13212998

Anantharaj, S., Karthik, K., Amarnath, T.S., Chatterjee, S., Subhashini, E., Swaathini, K.C., Karthick, P.E., Kundu, S., 2019. Membrane free water electrolysis under 1.23 V with Ni3Se4/Ni anode in alkali and Pt cathode in acid. Appl. Surf. Sci. 478, 784–792. https://doi.org/10.1016/j.apsusc.2019.01.231

Andersen, L., Lamp, A., Dieckmann, C., Baetge, S., Schmidt, L.-M., Kaltschmitt, M., 2018. Biogas plants as key units of biorefinery concepts: Options and their assessment. J. Biotechnol. 283, 130–139. https://doi.org/10.1016/j.jbiotec.2018.07.041

Ashley E. Franks, Richard H. Glaven, Derek R. Lovley, 2012. Real-Time Spatial Gene Expression Analysis within Current-Producing Biofilms. ChemSusChem 5, 1092–1098. https://doi.org/DOI: 10.1002/cssc.201100714

Aspelund, M.T., 2010. Membrane-based separations for solid/liquid clarification and protein purification (Doctor of Philosophy). Iowa State University, Digital Repository, Ames. https://doi.org/10.31274/etd-180810-754

Atasoy, M., Owusu-Agyeman, I., Plaza, E., Cetecioglu, Z., 2018. Bio-based volatile fatty acid production and recovery from waste streams: Current status and future challenges. Bioresour. Technol. 268, 773–786. https://doi.org/10.1016/j.biortech.2018.07.042

Avci, A., Karagoz, I., 2009. A Novel Explicit Equation for Friction Factor in Smooth and Rough Pipes. J. Fluids Eng. 131, 061203. https://doi.org/10.1115/1.3129132

Banister, S., Pretorius, W., 1998. Optimisation of primary sludge acidogenic fermentation. Water SA 24, 35–41.

Bick, A., Yang, F., Shandalov, S., Oron, G., 2007. Immersed Membrane Bioreactor Treatment for Domestic Wastewater Reclamation: Optimal Draft Tube Selection.

Bonanni, P.S., Bradley, D.F., Schrott, G.D., Busalmen, J.P., 2013. Limitations for Current Production in *Geobacter sulfurreducens* Biofilms. ChemSusChem 6, 711–720. https://doi.org/10.1002/cssc.201200671

Boušková, A., Dohányos, M., Schmidt, J.E., Angelidaki, I., 2005. Strategies for changing temperature from mesophilic to thermophilic conditions in anaerobic CSTR reactors treating sewage sludge. Water Res. 39, 1481–1488. https://doi.org/10.1016/j.watres.2004.12.042

Bouzas, A., Gabaldón, C., Marzal, P., Penya-roja, J.M., Seco, A., 2002. Fermentation of Municipal Primary Sludge: Effect of Srt and Solids Concentration on Volatile Fatty Acid Production. Environ. Technol. 23, 863–875. https://doi.org/10.1080/09593332308618359

Caccavo, F., Lonergan, D.J., Lovley, D.R., Davis, M., Stolz, J.F., McInerney, M.J., 1994. Geobacter sulfurreducens sp. nov., a hydrogen- and acetate-oxidizing dissimilatory metal-reducing microorganism. Appl. Environ. Microbiol. 60, 3752–3759. https://doi.org/10.1128/aem.60.10.3752-3759.1994

Calise, F., Cappielo, F.L., d'Accadia, M.D., Infante, A., Vicidomini, M., 2020. Modelling of anaerobic digestion of organic wastes: Integration of heat transfer and biochemical aspects. energies 13, 1–23. https://doi.org/10.3390/en13112702

Call, D., Logan, B.E., 2008. Hydrogen Production in a Single Chamber Microbial Electrolysis Cell Lacking a Membrane. Environ. Sci. Technol. 42, 3401–3406. https://doi.org/10.1021/es8001822

Campos, J.L., Valenzuela-Heredia, D., Pedrouso, A., Río, A.V. del, Belmonte, M., A.Mosquera-Corral, 2016. Greenhouse Gases Emissions from Wastewater Treatment Plants: Minimization, Treatment, and Prevention. J. Chem. 9, 1–12. http://dx.doi.org/10.1155/2016/3796352

Chamberland, J., Lessard, M.-H., Doyen, A., Labrie, S., Pouliot, Y., 2017. Biofouling of ultrafiltration membrane by dairy fluids: Characterization of pioneer colonizer bacteria using a DNA metabarcoding approach. J. Dairy Sci. 100, 981–990. https://doi.org/10.3168/jds.2016-11829

Chen, H., Chang, S., 2017. Impact of temperatures on microbial community structures of sewage sludge biological hydrolysis. Bioresour. Technol. 245, 502–510. https://doi.org/10.1016/j.biortech.2017.08.143

Chen, M., Heijman, S.G.J., Rietveld, L.C., 2021a. State-of-the-Art Ceramic Membranes for Oily Wastewater Treatment: Modification and Application. Membranes 11, 1–23.

Chen, M., Heijman, S.G.J., Rietveld, L.C., 2021b. State-of-the-Art Ceramic Membranes for Oily Wastewater Treatment: Modification and Application. Membranes 11, 888.

Chen, Y., Jiang, S., Yuan, H., Zhou, Q., Gu, G., 2006. Hydrolysis and acidification of waste activated sludge at different pHs. Water Res. 41, 683–689. https://doi.org/10.1016/j.watres.2006.07.030

Cho, Y.H., Lee, H.D., Park, H.B., 2012. Integrated Membrane Processes for Separation and Purification of Organic Acid from a Biomass Fermentation Process. Ind. Eng. Chem. Res. 51, 10207–10219. https://doi.org/10.1021/ie301023r

Choi, H., Zhang, K., Dionysiou, D.D., Oerther, D.B., Sorial, G.A., 2005. Influence of cross-flow velocity on membrane performance during filtration of biological suspension. J. Membr. Sci. 248, 189–199. https://doi.org/10.1016/j.memsci.2004.08.027

Christensen, M.L., Jakobsen, A.H., Hansen, C.S.K., Skovbjerg, M., Andersen, R.B.M., Jensen, M.D., KimSundmark, 2022. Pilot-scale hydrolysis of primary sludge for production of easily degradable carbon to treat biological wastewater or produce biogas. Sci. Total Environ. 846. https://doi.org/10.1016/j.scitotenv.2022.157532

Coppi, M.V., Leang, C., Sandler, S.J., Lovley, D.R., 2001. Development of a Genetic System for *Geobacter sulfurreducens*. Appl. Environ. Microbiol. 67, 3180–3187. https://doi.org/10.1128/AEM.67.7.3180-3187.2001

Costa, A., Depinho, M., Elimelech, M., 2006. Mechanisms of colloidal natural organic matter fouling in ultrafiltration. J. Membr. Sci. 281, 716–725. https://doi.org/10.1016/j.memsci.2006.04.044

Cotterill, S.E., Dolfing, J., Jones, C., Curtis, T.P., Heidrich, E.S., 2017. Low Temperature Domestic Wastewater Treatment in a Microbial Electrolysis Cell with 1 m [2] Anodes: Towards System Scale-Up. Fuel Cells 17, 584–592. https://doi.org/10.1002/fuce.201700034

Crutchik, D., Frison, N., Eusebi, A.L., Fatone, F., 2018. Biorefinery of cellulosic primary sludge towards targeted Short Chain Fatty Acids, phosphorus and methane recovery. Water Res. 136, 112–119. https://doi.org/10.1016/j.watres.2018.02.047

Cumming, I.W., Holdich, R.G., Ismail, B., 1999. Prediction of deposit depth and transmembrane pressure during cross-flow microfltration. J. Membr. Sci.

Cusick, R.D., Bryan, B., Parker, D.S., Merrill, M.D., Mehanna, M., Kiely, P.D., Liu, G., Logan, B.E., 2011. Performance of a pilot-scale continuous flow microbial electrolysis cell fed winery wastewater. Appl. Microbiol. Biotechnol. 89, 2053–2063. https://doi.org/10.1007/s00253-011-3130-9

Da Ros, C., Conca, V., Eusebi, A.L., Frison, N., Fatone, F., 2020. Sieving of municipal wastewater and recovery of bio-based volatile fatty acids at pilot scale. Water Res. 174, 115633. https://doi.org/10.1016/j.watres.2020.115633

Dahiya, S., Sarkar, O., Swamy, Y.V., Mohan, S.V., 2015. Acidogenic fermentation of food waste for volatile fatty acid production with co-generation of biohydrogen. Bioresour. Technol. 182, 103–113. https://doi.org/10.1016/j.biortech.2015.01.007

Darcovich, K., Toll, F.N., Paynot, F., PÉlerin, E., 1999. Inlet plenum pressure drop calculation for a cross-flow module. Can. J. Chem. Eng. 77, 119–121. https://doi.org/10.1002/cjce.5450770119

Deutsches Institut für Normung, 1985. German standard methods for the examination of water, waste water and sludge; sludge and sediments (group S); determination of water content, of dry residue and of solids content (S 2).

DIN Deutsches Institut für Normung, 2001. Characterization of waste - Determination of total organic carbon (TOC) in waste, sludges and sediments.

Ding, A., Yang, Y., Sun, G., Wu, D., 2016. Impact of applied voltage on methane generation and microbial activities in an anaerobic microbial electrolysis cell (MEC). Chem. Eng. J. 283, 260–265. https://doi.org/10.1016/j.cej.2015.07.054

Eastman, J.A., Ferguson, J.F., 1981. Solubilzation of particulate organic carbon during the acid phase of anaerobic digestion. Water Pollut. Control Fed. 53, 352–366.

European Commission Research and Innovation - Bioeconomy., 2015.

Fan, L., Harris, J., Roddick, F., Booker, N., 2002. Fouling of microfiltration membranes by the fractional components of natural organic matter in surface water. Water Supply 2, 313–320. https://doi.org/10.2166/ws.2002.0185

Fang, W., Zhang, X., Zhang, P., Wan, J., Guo, H., Dara S.M. Ghasimi, Xavier Carol Morera, Tao Zhang1, 2020. Overview of key operation factors and strategies for improving fermentative volatile fatty acid production and product regulation from sewage sludge. J. Environ. Sci. 87, 93–111.

Feng, K., Li, H., Zheng, C., 2018. Shifting product spectrum by pH adjustment during long-term continuous anaerobic fermentation of food waste. Bioresour. Technol. 270, 180–188.

Feng, L., Wang, H., Chen, Y., Wang, Q., 2009. Effect of solids retention time and temperature on waste activated sludge hydrolysis and short-chain fatty acids accumulation under alkaline conditions in continuous-flow reactors. Bioresour. Technol. 100, 44–49. https://doi.org/10.1016/j.biortech.2008.05.028

Flemming, H.-C., 1997. Reverse osmosis membrane biofouling. Exp. Therm. Fluid Sci. 14, 382–391. https://doi.org/10.1016/S0894-1777(96)00140-9

Fornero, J.J., Rosenbaum, M., Angenent, L.T., 2010. Electric Power Generation from Municipal, Food, and Animal Wastewaters Using Microbial Fuel Cells. Electroanalysis 22, 832–843. https://doi.org/10.1002/elan.200980011

Frison, N., Katsou, E., Malamis, S., Oehmen, A., Fatone, F., 2015. Development of a Novel Process Integrating the Treatment of Sludge Reject Water and the Production of Polyhydroxyalkanoates (PHAs). Environ. Sci. Technol. 49, 10877–10885. https://doi.org/10.1021/acs.est.5b01776

Fudge, T., Bulmer, I., Bowman, K., Pathmakanthan, S., Gambier, W., Dehouche, Z., Al-Salem, S.M., Constantinou, A., 2021. Microbial Electrolysis Cells for Decentralised Wastewater Treatment: The Next Steps. Water 13, 445. https://doi.org/10.3390/w13040445

Ghimire, A., Kumar, G., Sivagurunathan, P., Shobana, S., Saratale, G.D., Kim, H.W., Luongo, V., Esposito, G., Munoz, R., 2017. Bio-hythane production from microalgae biomass: Key challenges and potential opportunities for algal bio-refineries. Bioresour. Technol. 241, 525–536. https://doi.org/10.1016/j.biortech.2017.05.156

Gholami, A., Mohkam, M., Rasoul-Amini, S., Ghasemi, Y., 2016. Industrial production of polyhydroxyalkanoates by bacteria: opportunities and challenges. MINERVA Biotecnol. 28.

Gul, A., Hruza, J., Yalcinkaya, F., 2021. Fouling and Chemical Cleaning of Microfiltration Membranes: A Mini-Review. Polymers 13, 846. https://doi.org/10.3390/polym13060846

Gunaseelan, H., Munde, A.V., Patel, R., Sathe, B.R., 2023. Metal-organic framework derived carbon-based electrocatalysis for hydrogen evolution reactions: A review. Mater. Today Sustain. 22, 100371. https://doi.org/10.1016/j.mtsust.2023.100371

Guo, W., Ngo, H.-H., Li, J., 2012. A mini-review on membrane fouling. Bioresour. Technol. 122, 27–34. https://doi.org/10.1016/j.biortech.2012.04.089

Gupta, K., Chellam, S., 2022. Revealing the mechanisms of irreversible fouling during microfiltration – The role of feedwater composition. J. Environ. Chem. Eng. 10, 107362. https://doi.org/10.1016/j.jece.2022.107362

Hackbarth, M., Gescher, J., Horn, H., Reiner, J.E., 2023. A scalable, rotating disc bioelectrochemical reactor (RDBER) suitable for the cultivation of both cathodic and anodic biofilms. Bioresour. Technol. Rep. 21, 101357. https://doi.org/10.1016/j.biteb.2023.101357

Harirchi, S., Wainaina, S., Sar, T., Nojoumi, S.A., Parchami, M., Mohsen Parchami, Sunita Varjani, Samir Kumar Khanal, Jonathan Wong, Mukesh Kumar Awasthi, Mohammad J. Taherzadeh, 2022. Microbiological insights into anaerobic digestion for biogas, hydrogen or volatile fatty acids (VFAs): a review. Bioengineered 13, 6521–6557. https://doi.org/10.1080/21655979.2022.2035986

Härrer, D., Elreedy, A., Ali, R., Hille-Reichel, A., Gescher, J., 2023. Probing the robustness of *Geobacter sulfurreducens* against fermentation hydrolysate for uses in bioelectrochemical systems. Bioresour. Technol. 369, 128363. https://doi.org/10.1016/j.biortech.2022.128363

Hazzan, O.O., Zhao, B., Xiao, Y., 2023. Strategies for Enhancing Extracellular Electron Transfer in Environmental Biotechnology: A Review. Appl. Sci. 13, 12760. https://doi.org/10.3390/app132312760

Heidrich, E.S., Dolfing, J., Scott, K., Edwards, S.R., Jones, C., Curtis, T.P., 2013. Production of hydrogen from domestic wastewater in a pilot-scale microbial electrolysis cell. Appl. Microbiol. Biotechnol. 97, 6979–6989. https://doi.org/10.1007/s00253-012-4456-7

Hermann-Josef Melcher, Jan Berg, 2013. Verfahren zur Auftrennung einer Suspension und danach hergestellte Produkte.

Hernández-García, K.M., 2020. Modeling 3D current and potential distribution in a microbial electrolysis cell with augmented anode surface and non-ideal flow pattern. Biochem. Eng. J.

Hirose, A., Kasai, T., Aoki, M., Umemura, T., Watanabe, K., Kouzuma, A., 2018. Electrochemically active bacteria sense electrode potentials for regulating catabolic pathways. Nat. Commun. 9, 1083. https://doi.org/10.1038/s41467-018-03416-4

Hofs, B., Ogier, J., Vries, D., Beerendonk, E.F., Cornelissen, E.R., 2011. Comparison of ceramic and polymeric membrane permeability and fouling using surface water. Sep. Purif. Technol. 79, 365–374. https://doi.org/10.1016/j.seppur.2011.03.025

Holman, S.R., Ohlinger, K.N., 2007. An Evaluation of Fouling Potential and Methods to Control Fouling in Microfiltration Membranes for Secondary Wastewater Effluent. Proc. Water Environ. Fed. 2007, 6417–6444. https://doi.org/10.2175/193864707787223907

Horiuchi, J.-I., Shimizu, T., Tada, K., Kanno, T., Kobayashi, M., 2002. Selective production of organic acids in anaerobic acid reactor by pH control. Bioresour. Technol. 82, 209–213. https://doi.org/10.1016/S0960-8524(01)00195-X

Hu, Y., Han, X., Shi, L., Cao, B., 2022. Electrochemically active biofilm-enabled biosensors: Current status and opportunities for biofilm engineering. Electrochimica Acta 428, 140917. https://doi.org/10.1016/j.electacta.2022.140917

Huang, H., Spinette, R., O'Melia, C.R., 2008. Direct-flow microfiltration of aquasols. J. Membr. Sci. 314, 90–100. https://doi.org/10.1016/j.memsci.2008.01.040

Huang, M., Liu, Z., Li, A., Yang, H., 2017. Dual functionality of a graft starch flocculant: Flocculation and antibacterial performance. J. Environ. Manage. 196, 63–71. https://doi.org/10.1016/j.jenvman.2017.02.078

Huang, X., Duan, C., Yu, J., Dong, W., Wang, H., 2021. Response of VFAs and microbial interspecific interaction to primary sludge fermentation temperature. J. Clean. Prod. 322. https://doi.org/10.1016/j.jclepro.2021.129081

Huang, Z., Lu, L., Jiang, D., Xing, D., Ren, Z.J., 2017. Electrochemical hythane production for renewable energy storage and biogas upgrading. Appl. Energy 187, 595–600. https://doi.org/10.1016/j.apenergy.2016.11.099

Issaoui, M., Limousy, L., 2018. Low-cost ceramic membranes: Synthesis, classifications, and applications. Comptes Rendus Chim. 22, 175–187. https://doi.org/10.1016/j.crci.2018.09.014

Janicek, A., Fan, Y., Liu, H., 2014. Design of microbial fuel cells for practical application: a review and analysis of scale-up studies. Biofuels 5, 79–92. https://doi.org/10.4155/bfs.13.69

Jiang, Y., Chen, Y., 2009. The effects of the ratio of propionate to acetate on the transformation and composition of polyhydroxyalkanoates with enriched cultures of glycogen-accumulating organisms. Environ. Technol. 30, 241–249. https://doi.org/10.1080/09593330802536347

Jones, K.L., O'Melia, C.R., 2000. Protein and humic acid adsorption onto hydrophilic membrane surfaces: effects of pH and ionic strength. J. Membr. Sci. 165, 31–46. https://doi.org/10.1016/S0376-7388(99)00218-5

Karekar, Supriya, Stefanini, Renan, Ahring, Birgitte, 2022. Homo-Acetogens: Their Metabolism and Competitive Relationship with Hydrogenotrophic Methanogens. Microorganisms 10.

Katuri, K.P., Kamireddy, S., Kavanagh, P., Muhammad, A., Conghaile, P.Ó., Kumar, A., Saikaly, P.E., Leech, D., 2020. Electroactive biofilms on surface functionalized anodes: The anode respiring behavior of a novel electroactive bacterium, *Desulfuromonas acetexigens*. Water Res. 185, 116284. https://doi.org/10.1016/j.watres.2020.116284

Kehrein, P., Loosdrecht, M. van, Osseweijer, P., Garfí, M., Dewulf, J., Posada, J., 2020. A critical review of resource recovery from municipal wastewater treatment plants – market supply potentials, technologies and bottlenecks. Environ. Sci. Water Res. Technol. 6, 877–910. https://doi.org/10.1039/c9ew00905a

Kennedy, M., Siriphannon, S., Van Hoof, S., Schippers, J., 2001. Improving the performance of dead-end ultrafiltration systems: comparing air and water flushing. Water Supply 1, 97–106. https://doi.org/10.2166/ws.2001.0104

Ketep, S.F., Bergel, A., Bertrand, M., Achouak, W., Fourest, E., 2013. Lowering the applied potential during successive scratching/re-inoculation improves the performance of microbial anodes for microbial fuel cells. Bioresour. Technol. 127, 448–455. https://doi.org/10.1016/j.biortech.2012.09.008

Kitching, M., Butler, R., Marsili, E., 2017. Microbial bioelectrosynthesis of hydrogen: Current challenges and scale-up. Enzyme Microb. Technol. 96, 1–13. https://doi.org/10.1016/j.enzmictec.2016.09.002

Kleerebezem, R., Joosse, B., Rozendal, R., Van Loosdrecht, M.C.M., 2015. Anaerobic digestion without biogas? Rev. Environ. Sci. Biotechnol. 14, 787–801. https://doi.org/10.1007/s11157-015-9374-6

Kokko, M., Epple, S., Gescher, J., Kerzenmacher, S., 2018. Effects of wastewater constituents and operational conditions on the composition and dynamics of anodic microbial communities in bioelectrochemical systems. Bioresour. Technol. 258, 376–389. https://doi.org/10.1016/j.biortech.2018.01.090

Komemoto, K., Lim, Y.G., Nagao, N., Onoue, Y., Niwa, C., Toda, T., 2009. Effect of temperature on VFA's and biogas production in anaerobic solubilization of food waste. Waste Manag. 29, 2950–2955. https://doi.org/10.1016/j.wasman.2009.07.011

Lasaki, B.A., Maurer, P., Schönberger, H., 2024. Uncovering the reasons behind high-performing primary sedimentation tanks for municipal wastewater treatment: An in-depth analysis of key factors. J. Environ. Chem. Eng. 12, 112460. https://doi.org/10.1016/j.jece.2024.112460

Li, X., Peng, Y., Ren, N., Li, B., Chai, T., Zhang, L., 2014. Effect of temperature on short chain fatty acids (SCFAs) accumulation and microbiological transformation in sludge alkaline fermentation with Ca(OH)2 adjustment. Water Res. 61. https://doi.org/10.1016/j.watres.2014.03.030

Liberato, V., Benevenuti, C., Coelho, F., Botelho, A., Amaral, P., Pereira, N., Ferreira, T., 2019. Clostridium sp. as Bio-Catalyst for Fuels and Chemicals Production in a Biorefinery Context. Catalysts 9, 962. https://doi.org/10.3390/catal9110962

Lim, A., Bai, R., 2003. Membrane fouling and cleaning in microfiltration of activated sludge wastewater. J. Membr. Sci. 216, 279–290. https://doi.org/10.1016/S0376-7388(03)00083-8

Lin, C.-Y., 1993. Mesophilic Degradation of Butyric Acid in Anaerobic Digestion. J. Chem. Technol. Biotechnol. 56, 191–194.

Lin, L., Li, R., Li, X., 2018. Recovery of organic resources from sewage sludge of Al-enhanced primary sedimentation by alkali pretreatment and acidogenic fermentation. J. Clean. Prod. 172, 3334–3341. https://doi.org/10.1016/j.jclepro.2017.11.199

Lin, W.C., Coppi, M.V., Lovley, D.R., 2004. *Geobacter sulfurreducens* Can Grow with Oxygen as a Terminal Electron Acceptor. Appl. Environ. Microbiol. 70, 2525–2528. https://doi.org/10.1128/AEM.70.4.2525-2528.2004

Liu, W., Huang, S., Zhou, A., Zhou, G., Ren, N., Wang, A., Zhuang, G., 2012. Hydrogen generation in microbial electrolysis cell feeding with fermentation liquid of waste activated sludge. Int. J. Hydrog. Energy 37. https://doi.org/10.1016/j.ijhydene.2012.04.090

Logan, B.E., 2010. Scaling up microbial fuel cells and other bioelectrochemical systems. Appl. Microbiol. Biotechnol. 85, 1665–1671. https://doi.org/10.1007/s00253-009-2378-9

Lu, L., Xing, D., Liu, B., Ren, N., 2012. Enhanced hydrogen production from waste activated sludge by cascade utilization of organic matter in microbial electrolysis cells. Water Res. 46, 1015–1026. https://doi.org/10.1016/j.watres.2011.11.073

Madigan, M.T., Bender, K.S., Buckley, D.H., Sattley, M.W., Stahl, D.A., 2020. Brock Mikrobiologie.

Matthies, C., Schink, B., 1992. Reciprocal Isomerization of Butyrate and Isobutyrate by the Strictly Anaerobic Bacterium Strain WoG13 and Methanogenic Isobutyrate Degradation by a Defined Triculture. Pplied Environ. Microbiol. 58, 1435–1439.

Merrill, M.D., Logan, B.E., 2009. Electrolyte effects on hydrogen evolution and solution resistance in microbial electrolysis cells. J. Power Sources 191, 203–208. https://doi.org/10.1016/j.jpowsour.2009.02.077

Miron, Y., Zeeman, G., Lier, J.B.V., Lettinga, G., 1999. The role of sludge retention time in the hydrolysis and acidification of lipids, carbohydrates and proteins during digestion of primary sludge in CSTR systems. Water Res. 34, 1705–1713.

Möller, B., Oßmer, R., Howard, B.H., Gottschalk, G., Hippe, H., 1984. Sporomusa, a new genus of gram-negative anaerobic bacteria including *Sporomusa sphaeroides* spec. nov. and *Sporomusa ovata* spec. nov. Arch. Microbiol. 139, 388–396. https://doi.org/10.1007/BF00408385

Moody, L.F., 1944. Friction Factors for Pipe Flow. J. Fluids Eng. 66, 671–678. https://doi.org/10.1115/1.4018140

Moretto, G., Russo, I., Bolzonella, D., Pavan, P., Majone, M., Valentino, F., 2020. An urban biorefinery for food waste and biological sludge conversion into polyhydroxyalkanoates and biogas. Water Res. 170, 115371. https://doi.org/10.1016/j.watres.2019.115371

Morgan-Sagastume, F., Hjort, M., Cirne, D., Gérardin, F., Lacroix, S., Gaval, G., Karabegovic, L., Alexandersson, T., Johansson, P., Karlsson, A., Bengtsson, S., Arcos-Hernández, M.V., Magnusson, P., Werker, A., 2015. Integrated production of polyhydroxyalkanoates (PHAs) with municipal wastewater and sludge treatment at pilot scale. Bioresour. Technol. 181, 78–89. https://doi.org/10.1016/j.biortech.2015.01.046

Mosey, F.E., 1983. Mathematical Modelling of the Anaerobic Digestion Process: Regulatory Mechanisms for the Formation of Short-Chain Volatile Acids from Glucose. Water Sci. Technol. 15, 209–232. https://doi.org/10.2166/wst.1983.0168

Nagarajan, S., Jones, R.J., Oram, L., Massanet-Nicolau, J., Guwy, A., 2022. Intensification of Acidogenic Fermentation for the Production of Biohydrogen and Volatile Fatty Acids—A Perspective. Fermentation 8, 325. https://doi.org/10.3390/fermentation8070325

Nam, J.-Y., Kim, H.-W., Lim, K.-H., Shin, H.-S., Logan, B.E., 2010. Variation of power generation at different buffer types and conductivities in single chamber microbial fuel cells. Biosens. Bioelectron. 25, 1155–1159. https://doi.org/10.1016/j.bios.2009.10.005

Ndayisenga, F., Yu, Z., Wang, B., Zhou, D., 2023. Effects of the applied voltage on electroactive microbial biofilm viability and hydrogen production in a recalcitrant organic waste-fed single-chamber membrane-free microbial electrolysis cell performance. Chem. Eng. J. 469, 144002. https://doi.org/10.1016/j.cej.2023.144002

Ntaikou, I., Valencia Peroni, C., Kourmentza, C., Ilieva, V.I., Morelli, A., Chiellini, E., Lyberatos, G., 2014. Microbial bio-based plastics from olive-mill wastewater: Generation and properties of polyhydroxyalkanoates from mixed cultures in a two-stage pilot scale system. J. Biotechnol. 188, 138–147. https://doi.org/10.1016/j.jbiotec.2014.08.015

Obotey Ezugbe, E., Rathilal, S., 2020. Membrane Technologies in Wastewater Treatment: A Review. Membranes 10, 89. https://doi.org/10.3390/membranes10050089

Ong, H.K., Greenfield, P.F., Pullammanappallil, P.C., 2002. Effect of Mixing on Biomethanation of Cattle-Manure Slurry. Environ. Technol. 23, 1081–1090. https://doi.org/10.1080/09593332308618330

Ossiansson, E., Persson, F., Bengtsson, S., Cimbritz, M., Gustavsson, D.J.I., 2023. Seasonal variations in acidogenic fermentation of filter primary sludge. Water Res. 242, 120181. https://doi.org/10.1016/j.watres.2023.120181

Pandey, A.K., Pilli, S., Bhunia, P., Tyagi, R.D., Surampalli, R.Y., Zhang, T.C., Kim, S.-H., Pandey, A., 2022. Dark fermentation: Production and utilization of volatile fatty acid from different wastes- A review. Chemosphere 288, 132444. https://doi.org/10.1016/j.chemosphere.2021.132444

Parchami, M., Wainaina, S., Mahboubi, A., I'Ons, D., Taherzadeh, M.J., 2020. MBR-Assisted VFAs Production from Excess Sewage Sludge and Food Waste Slurry for Sustainable Wastewater Treatment. Appl. Sci. 10. https://doi.org/doi:10.3390/app10082921

Patil, S.A., Harnisch, F., Koch, C., Hübschmann, T., Fetzer, I., Carmona-Martínez, A.A., Müller, S., Schröder, U., 2011. Electroactive mixed culture derived biofilms in microbial bioelectrochemical systems: The role of pH on biofilm formation, performance and composition. Bioresour. Technol. 102, 9683–9690. https://doi.org/10.1016/j.biortech.2011.07.087

Pittmann, T., Steinmetz, H., 2016. Potential for polyhydroxyalkanoate production on German or European municipal waste water treatment plants. Bioresour. Technol. 214, 9–15. https://doi.org/10.1016/j.biortech.2016.04.074

Pittmann, T., Steinmetz, H., 2013. Influence of operating conditions for volatile fatty acids enrichment as a first step for polyhydroxyalkanoate production on a municipal waste water treatment plant. Bioresour. Technol. 148, 270–276. https://doi.org/10.1016/j.biortech.2013.08.148

Ramos-Suarez, M., Zhang, Y., Outram, V., 2021. Current perspectives on acidogenic fermentation to produce volatile fatty acids from waste. Rev. Environ. Sci. Biotechnol. 20, 439–478.

Razali, M.A.A., Ariffin, A., 2015. Polymeric flocculant based on cassava starch grafted polydiallyldimethylammonium chloride: Flocculation behavior and mechanism. Appl. Surf. Sci. 351, 89–94. https://doi.org/10.1016/j.apsusc.2015.05.080

R.Canziani, Pollice, A., M.Ragazzi, 1995. Feasibility of using primary sludge mesophilic hydrolysis for biological removal of nitrogen and phosphorus from wastewater. Bioresour. Technol. 255–260.

Rice, E., Baird, R.B., Eaton, A.D., 2017. Standard methods for the examination of water and wastewater. American Public Health Association, American Water Works Association, Water Environment Federation.

Rico, C., Rico, J., Munoz, N., Gomez, B., Tejero, I., 2011. Effect of mixing on biogas production during mesophilic anaerobic digestion of screened dairy manure in a pilot plant. Wile 11, 476–481.

Rivera, I., Buitrón, G., Bakonyi, P., Nemestóthy, N., Bélafi-Bakó, K., 2015. Hydrogen production in a microbial electrolysis cell fed with a dark fermentation effluent. J. Appl. Electrochem. 45, 1223–1229. https://doi.org/10.1007/s10800-015-0864-6

Roorda, J.H., 2004. Filtration characteristics in dead-end ultrafiltration of wwtp-effluent. s.n.], [S.l.

Rousseau, R., Ketep, S.F., Etcheverry, L., Délia, M.-L., Bergel, A., 2020. Microbial electrolysis cell (MEC): A step ahead towards hydrogen-evolving cathode operated at high current density. Bioresour. Technol. Rep. 9, 100399. https://doi.org/10.1016/j.biteb.2020.100399

Rughoonundun, H., Mohee, R., Holtzapple, M.T., 2012. Influence of carbon-to-nitrogen ratio on the mixed-acid fermentation of wastewater sludge and pretreated bagasse. Bioresour. Technol. 112, 91–97.

Ruiken, C.J., Breuer, G., Klaversma, E., Santiago, T., Van Loosdrecht, M.C.M., 2013. Sieving wastewater – Cellulose recovery, economic and energy evaluation. Water Res. 47, 43–48. https://doi.org/10.1016/j.watres.2012.08.023

Rümenapf, M., 2024. Implementierung des elektroaktiven Deltaproteobakteriums *Desulfuromonas acetexigens* in mikrobiellen Elektrolysezellen. Karlsruher Institut für Technologie (KIT). DOI: 10.5445/IR/1000178701

Samanta, P., von Ungern-Sternberg Schwark, L., Horn, H., Saravia, F., 2022. Nutrient recovery and ammonia-water production by MF vacuum evaporation treament of pig manure. J. Environ. Chem. Eng. 10.

Sapireddy, V., Katuri, K.P., Muhammad, A., Saikaly, P.E., 2021. Competition of two highly specialized and efficient acetoclastic electroactive bacteria for acetate in biofilm anode of microbial electrolysis cell. Npj Biofilms Microbiomes 7, 47. https://doi.org/10.1038/s41522-021-00218-3

Sarkar, O., Katakojwalaa, R., Mohan, V., 2020. Low carbon hydrogen production from a waste-based biorefinery system and environmental sustainability assessment†. R. Soc. Chem. 23, 561–574. https://doi.org/10.1039/D0GC03063E

Sasaki, K., Morita, M., Sasaki, D., Matsumoto, N., Ohmura, N., Igarashi, Y., 2012. Single-chamber bioelectrochemical hydrogen fermentation from garbage slurry. Biochem. Eng. J. 68, 104–108. https://doi.org/10.1016/j.bej.2012.07.014

Sayegh, A., Merkert, S., Zimmermann, J., Horn, H., Saravia, F., 2022. Treatment of Hydrothermal-Liquefaction Wastewater with Crossflow UF for Oil and Particle Removal. Membranes 12, 255. https://doi.org/10.3390/membranes12030255

Sayegh, A., Shylaja Prakash, N., Pedersen, T.H., Horn, H., Saravia, F., 2021. Treatment of hydrothermal liquefaction wastewater with ultrafiltration and air stripping for oil and particle removal and ammonia recovery. J. Water Process Eng. 44, 102427. https://doi.org/10.1016/j.jwpe.2021.102427

Schneider, C.A., Rasband, W.S., Eliceiri, K.W., 2012. NIH Image to ImageJ: 25 years of image analysis. Nat. Methods 9, 671–675. https://doi.org/10.1038/nmeth.2089

Seitz, H.-J., Schink, B., Pfennig, N., Conrad, R., 1990. Energetics of syntrophic ethanol oxidation in defined chemostat cocultures 155, 89–93.

Sen Wang, Charles Liu, Qilin Li, 2011. Fouling of microfiltration membranes by organic polymer coagulants and flocculants: Controlling factors and mechanisms. Water Res. 45, 357–365.

Shylaja Prakash, N., Maurer, P., Horn, H., Hille-Reichel, A., 2024. Valorization of organic carbon in primary sludge via semi-continuous dark fermentation: First step to establish a wastewater biorefinery. Bioresour. Technol. 397, 130467. https://doi.org/10.1016/j.biortech.2024.130467

Shylaja Prakash, N., Maurer, P., Horn, H., Saravia, F., Hille-Reichel, A., 2025. Separation of Short-Chain Fatty Acids from Primary Sludge into a Particle-Free Permeate by Coupling Chamber Filter-Press and Cross-Flow Microfiltration: Optimization, Semi-Continuous Operation, and Evaluation. Membranes 15, 1–21. https://doi.org/10.3390/membranes15010022

Sikora, A., Detman, A., Chojnacka, A., Blaszczyk, M.K., 2017. Anaerobic Digestion: I. A Common Process Ensuring Energy Flow and the Circulation of Matter in Ecosystems. II. A Tool for the Production of Gaseous Biofuels, in: Jozala, A.F. (Ed.), Fermentation Processes. InTech. https://doi.org/10.5772/64645

Skalsky, D.S., Daigger, G.T., 1995. Wastewater solids fermentation for volatile acid production and enhanced biological phosphorus removal. Water Environ. Res. 67, 230–237. https://doi.org/10.2175/106143095X131402

Song, L., Elimelech, M., 1995. Theory of concentration polarization in crossflow filtration. J. Chem. Soc. Faraday Trans. 91, 3389. https://doi.org/10.1039/ft9959103389

Speers, A.M., Reguera, G., 2012. Electron Donors Supporting Growth and Electroactivity of *Geobacter sulfurreducens* Anode Biofilms. Appl. Environ. Microbiol. 78, 437–444. https://doi.org/10.1128/AEM.06782-11

Stams, A.J.M., Dijkema, C., Plugge, C.M., Lens, P., 1998. Contribution of 13C-NMR spectroscopy to the elucidation of pathways of propionate formation and degradation in methanogenic environments 9, 463–473.

Sun, D., Chen, J., Huang, H., Liu, W., Ye, Y., Cheng, S., 2016. The effect of biofilm thickness on electrochemical activity of *Geobacter sulfurreducens*. Int. J. Hydrog. Energy 41, 16523–16528. https://doi.org/10.1016/j.ijhydene.2016.04.163

Sun, H., Li, J., Yang, M., Shao, Q., 2019. Influence of Initial pH on Anodic BiofilmFormation in Single-Chambered MicrobialElectrolysis Cells. Pol. J. Environ. Stud. 28, 1377–1384. https://doi.org/10.15244/pjoes/89503

Suopajärvi, T., Sirviö, J.A., Liimatainen, H., 2017. Cationic nanocelluloses in dewatering of municipal activated sludge. J. Environ. Chem. Eng. 5, 86–92. https://doi.org/10.1016/j.jece.2016.11.021

Sutton-Sharp, E., Ravereau, J., Guennec, M., Brehant, A., Bonnard, R., 2018. Benefits of polymeric membranes in Oil and Gas produced water treatment. Water Pract. Technol. 13, 303–311. https://doi.org/10.2166/wpt.2018.019

Tamis, J., Lužkov, K., Jiang, Y., Loosdrecht, M.C.M.V., Kleerebezem, R., 2014. Enrichment of *Plasticicumulans acidivorans* at pilot-scale for PHA production on industrial wastewater. J. Biotechnol. 192, 161–169. https://doi.org/10.1016/j.jbiotec.2014.10.022

Thauer, R.K., Jungermann, K., Decker, K., 1977. Energy Conservation in Chemotrophic Anaerobic Bacteria 41.

Tuczinski, M., Saravia, F., Horn, H., 2018. Treatment of thermophilic hydrolysis reactor effluent with ceramic microfiltration membranes. Bioprocess Biosyst. Eng. 41, 1561–1571. https://doi.org/10.1007/s00449-018-1983-3.

V. Gadhave, R., Mahanwar, P.A., Gadekar, P.T., 2017. Starch-Based Adhesives for Wood/Wood Composite Bonding: Review. Open J. Polym. Chem. 07, 19–32. https://doi.org/10.4236/ojpchem.2017.72002

Valiantzas, J.D., 2008. Explicit Power Formula for the Darcy–Weisbach Pipe Flow Equation: Application in Optimal Pipeline Design. J. Irrig. Drain. Eng. 134, 454–461. https://doi.org/10.1061/(ASCE)0733-9437(2008)134:4(454)

Van De Lisdonk, C.A.C., Van Paassen, J.A.M., Schippers, J.C., 2000. Monitoring scaling in nanofiltration and reverse osmosis membrane systems. Desalination 132, 101–108. https://doi.org/10.1016/S0011-9164(00)00139-9

Venkateswaran, K., Moser, D.P., Dollhopf, M.E., Lies, D.P., Saffarini, D.A., MacGregor, B.J., Ringelberg, D.B., White, D.C., Nishijima, M., Sano, H., Burghardt, J., Stackebrandt, E., Nealson, K.H., 1999. Polyphasic taxonomy of the genus *Shewanella* and description of *Shewanella oneidensis* sp. now. Int. J. Syst. Bacteriol. 49, 705–724.

Vera, L., Villarroel-López, R., Delgado, S., Elmaleh, S., 1997. Cross-flow microfiltration of biologically treated wastewater. Desalination 114, 65–75. https://doi.org/10.1016/S0011-9164(97)00155-0

Vidal, G., Carvalho, A., Mendez, R., Lema, J.M., 2000. Influence of the content in fats and proteins on the anaerobic biodegradability of dairy wastewaters. Bioresour. Technol. 74, 231–239.

Viulu, S., Nakamura, K., Kojima, A., Yoshiyasu, Y., Saitou, S., Takamizawa, K., 2013. *Geobacter sulfurreducens* subsp. *ethanolicus*, subsp. nov., an ethanol-utilizing dissimilatory Fe(III)-reducing bacterium from a lotus field. J. Gen. Appl. Microbiol. 59, 325–334. https://doi.org/10.2323/jgam.59.325

Von Tettau, P., Thiele, P., Mauermann, P., Wick, M., Tinz, S., Pischinger, S., 2025. Per- and polyfluoroalkyl substances in proton exchange membrane fuel cells — A review. J. Power Sources 630, 236104. https://doi.org/10.1016/j.jpowsour.2024.236104

Wagner, M., Horn, H., 2017. Optical coherence tomography in biofilm research: A comprehensive review. Biotechnol. Bioeng. 114, 1386–1402. https://doi.org/10.1002/bit.26283

Wainaina, S., Lukitawesa, Mukesh Kumar Awasthi, Taherzadeh, M.J., 2019. Bioengineering of anaerobic digestion for volatile fatty acids, hydrogen or methane production: A critical review. Bioengineered 10, 437–458. https://doi.org/10.1080/21655979.2019.1673937

Wan, J., Gu, J., Zhao, Q., Liu, Y., 2016. COD capture: a feasible option towards energy self-sufficient domestic wastewater treatment. Sci. Rep. 6, 25054. https://doi.org/10.1038/srep25054

Wang, H., Du, H., Zeng, S., Pan, X., Cheng, H., Liu, L., Luo, F., 2021. Explore the difference between the single-chamber and dual-chamber microbial electrosynthesis for biogas production performance. Bioelectrochemistry 138, 107726. https://doi.org/10.1016/j.bioelechem.2020.107726

Wang, J., Liu, G., Shao, Y., Zhang, Q., Wei, Q., Fangzhou Luo, Wenzhuo Sun, Shuai Liu, Yuchen Liu, Jingbing Zhang, Lu Qi, Hongchen Wang, 2021. Regulation of anaerobic fermentation for producing short-chain fatty acids from primary sludge in WWTPs by different alkalis. Elsevier J. Environ. Manag. 299, 1–8.

Wang, S., Li, C.L., Li, Q., 2011. Fouling of microfiltration membranes by organic polymer coagulants and flocculants: Controlling factors and mechanisms. Water Res. 45, 357–65. https://doi.org/10.1016/j.watres.2010.08.009

Water analysis - Guidelines for the determination of total organic carbon (TOC) and dissolved organic carbon (DOC), 2019.

Weiler, J.R., Jürgensen, N., Cornejo Infante, M., Knoll, M.T., Gescher, J., 2024. Strain and model development for auto- and heterotrophic 2,3-butanediol production using *Cupriavidus necator H16*. Biotechnol. Biofuels Bioprod. 17, 108. https://doi.org/10.1186/s13068-024-02549-7

Wong, Y.M., Wu, T.Y., Juan, J.C., 2014. A review of sustainable hydrogen production using seed sludge via dark fermentation. Renew. Sustain. Energy Rev. 34, 471–482. https://doi.org/10.1016/j.rser.2014.03.008

Wu, H., Gao, J., Yang, D., Zhou, Q., Liu, W., 2010. Alkaline fermentation of primary sludge for short-chain fatty acids accumulation and mechanism. Chem. Eng. J. 160, 1–7. https://doi.org/10.1016/j.cej.2010.02.012

Wu, H., Yang, D., Zhou, Q., Song, Z., 2009. The effect of pH on anaerobic digestion of primary sludge at room temperature. J. Hazard. Mater. 172, 196–201. https://doi.org/10.1016/j.jhazmat.2009.06.146

Xiao, Z., Ruemenapf, M., Hackbarth, M., Horn, H., Hille-Reichel, A., Reiner, J.E., 2025. Impact of rotational speed and different counter electrode configurations on bioelectrochemical hydrogen production in a 10 L RDBER. Bioresour. Technol. Rep. Pre-Print.

Yu, H.-Q., Zheng, X.-J., Hu, Z.-H., Gu, G.-W., 2003. High-rate anaerobic hydrolysis and acidogenesis of sewage sludge in a modified upflow reactor. Water Sci. Technol. 48, 69–75.

Yuan, H., Chen, Y., Zhang, H., Jiang, S., Zhou, Q., Gu, G., 2006. Improved Bioproduction of Short-Chain Fatty Acids (SCFAs) from Excess Sludge under Alkaline Conditions. Env. Sci Technol 40, 2025–2049.

Yuan, Q., Baranowski, M., Oleszkiewicz, J.A., 2010. Effect of sludge type on the fermentation products. Chemosphere 80, 445–449. https://doi.org/10.1016/j.chemosphere.2010.04.026

Zhang, W., Luo, J., Ding, L., Jaffrin, M.Y., 2015. A Review on Flux Decline Control Strategies in Pressure-Driven Membrane Processes. Ind. Eng. Chem. Res. 54, 2843–2861. https://doi.org/10.1021/ie504848m

Zhang, X., Fan, L., Roddick, F.A., 2013. Influence of the characteristics of soluble algal organic matter released from *Microcystis aeruginosa* on the fouling of a ceramic microfiltration membrane. J. Membr. Sci. 425–426, 23–29. https://doi.org/10.1016/j.memsci.2012.09.033

Appendix

A1   Batch test with Bruchsal primary sludge

Preliminary batch experiment was carried out using 2 L-batch scale reactors with PS obtained from Bruchsal. At pH 6.5, the highest productivity could be observed for tSCFAs and individual SCFAs.
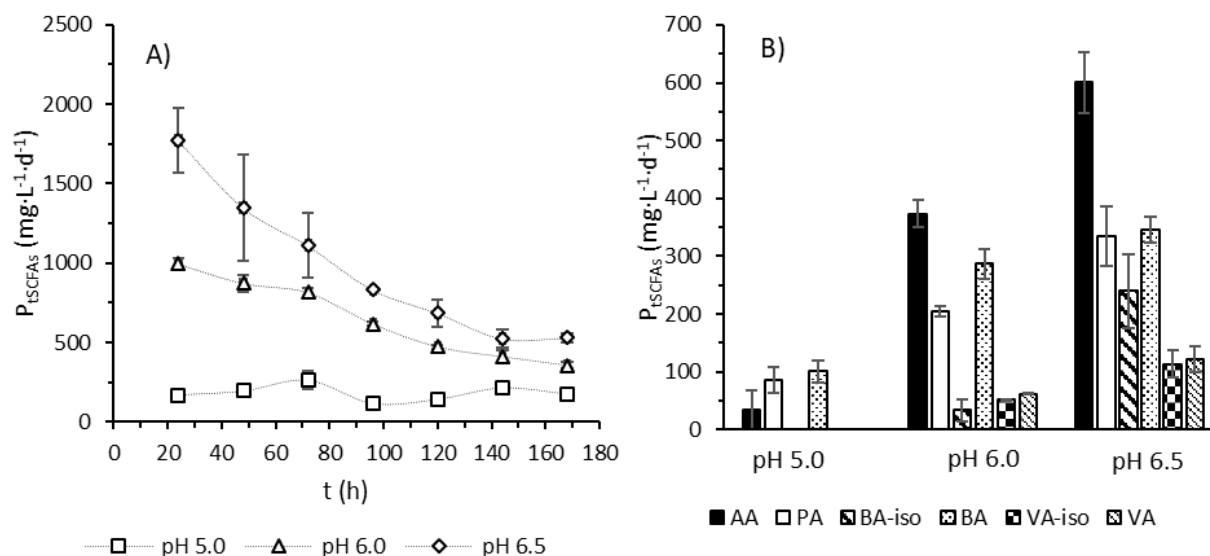
Figure A1: Daily productivities of A) tSCFAs (P_{tSCFAs}) for 168 h and, B) individual SCFAs (P_{SCFAs}) after 24 h for different pH-values 5.0, 6.0, 6.5 for PS obtained from Bruchsal.

A2   Variation of short-chain fatty acids at semi-continuous operations

Since OP-II to OP-V was performed in a semi-continuous operation, the stability of the production of SCFAs and tSCFAs was monitored using coefficient of variation (CV).

Table A1: Coefficient of variation (CV) for individual SCFAs (the highlighted SCFAs are a part of the dominant fraction) for different OPs.

OP	Dominant SCFAs	Mass fraction (%) of dominant SCFAs	CV (%)							
			FA	AA	PA	BA-iso	BA	VA-iso	VA	tSCFAs
II-A	AA:PA:BA	87.29	-	9.23	11.25	1.32	8.99	10.08	8.58	8.89
II-B	AA:PA:BA	87.47	-	11.24	10.82	0.21	8.66	12.10	4.08	9.09
II-C	AA:PA:BA	87.08	-	1.72	0.65	2.70	2.21	4.26	1.02	0.31

II-D	AA:PA:BA	85.89	-	7.38	8.79	14.01	8.66	12.05	18.06	8.27
II-E	AA:PA:BA	84.26	-	6.67	4.79	20.07	5.81	13.50	7.34	5.75
III-A	AA:PA:BA	92.25	-	16.25	32.21	141.42	22.41	73.54	71.22	4.67
III-B	AA:PA:BA	86.92	-	11.86	12.12	43.07	8.08	49.76	10.82	9.02
III-C	AA:PA:BA:BA-iso	94.34	-	1.53	1.78	11.27	7.10	3.80	1.47	3.31
III-D	AA:PA:BA:BA-iso	94.56	-	6.29	10.11	14.38	7.00	12.73	4.43	7.95
III-E	AA:PA:BA:BA-iso	95.19	-	7.08	10.74	10.35	8.31	12.54	14.78	7.59
III-F	AA:PA:BA:BA-iso	90.59	25.40	11.35	15.29	8.30	6.99	5.53	12.17	5.46
IV-A	AA:PA:BA	91.32	-	12.93	5.46	40.84	28.78	26.90	21.08	15.55
IV-B	AA:PA:BA:BA-iso	94.06	-	9.21	8.83	9.49	16.38	4.94	12.41	5.73
IV-C	AA:PA:BA:BA-iso	92.85	22.16	8.65	35.75	10.51	17.19	20.60	58.29	3.35
V-A	AA:PA:BA:BA-iso	94.90	-	10.64	9.53	7.29	3.69	4.24	8.18	5.07
V-B	AA:PA:BA:BA-iso	95.88	-	4.52	8.55	47.89	10.12	42.07	8.28	5.36

A3 Influent characteristics of primary sludge at semi-continuous operations

Table A2: Characteristics of the dissolved parameters in primary sludge at different OPs. σ denotes standard deviations determined throughout the respective operation phase.

	mg·L^{-1}																
OP	DOC	σ	NH$_4^+$	σ	AA	σ	PA	σ	BA-iso	σ	BA	σ	VA-iso	σ	VA	σ
I-A, B, C	2503	120	155	4	938	21	878	20	-	-	302	8	-	-	-	-
II-A	419	41	141	46	628	104	506	117	-	-	166	27	-	-	-	-
II-B	994	156	210	18	795	96	655	131	-	-	202	27	-	-	-	-
II-C, D, E	817	159	64	7	460	102	665	168	-	-	-	-	-	-	-	-

|																
III-A	864	48	79	3	510	54	607	83	-	-	156	17	-	-	59	9
III-B	796	23	113	21	543	90	577	100	-	-	182	20	-	-	65	7
III-C	387	29	97	3	230	24	183	23	-	-	80	1	-	-	-	-
III-D, E, F	554	57	121	30	385	54	335	48	134	7	64	11	-	-	17	12
	383	-			520	-	266	-	-	-	72	-	-	-	-	-
IV-A	535	-	66	20	607	-	380	-	-	-	87	-	-	-	-	-
	772	-			915	-	521	-	-	-	160	-	-	-	-	-
	598	-			1350	-	751	-	-	-	271	-	-	-	-	-
IV-B	1041	-	167	4	1463	-	896	-	-	-	440	-	-	-	-	-
	1101	-			1548	-	953	-	-	-	471	-	-	-	-	-
	717	-			1609	-	919	-	-	-	345	-	-	-	-	-
	1401	-			1977	-	1240	-	-	-	625	-	-	-	-	-
IV-C	2195	-	218	47	2267	-	1420	-	-	-	651	-	-	-	-	-
	2053	-			2165	-	1353	-	-	-	587	-	-	-	-	-
	1206	-			2258	-	1553	-	-	-	706	-	-	-	-	-
V-A, B	1087	136	172	35	807	47	729	128	22	14	224	51	41	23	44	11

A4   Ratio of SCFAs to DOC
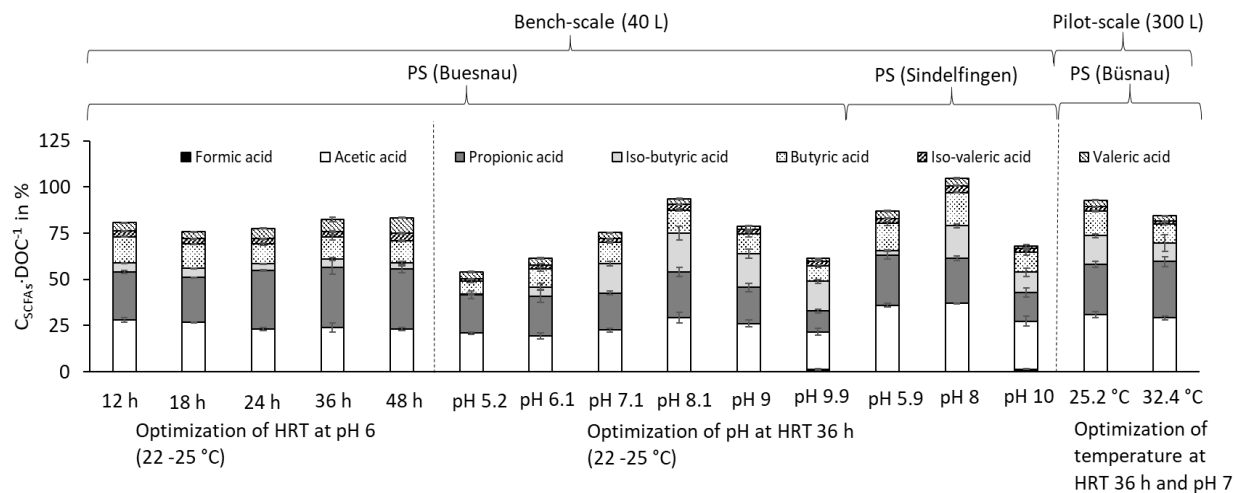
Figure A1: Mass concentrations of SCFAs as carbon equivalents and dissolved organic carbon (DOC) in the outflow for different OPs expressed as percentage.

A5   Optimization of cross-flow velocity to filtrate

This experiment was done to observe how reverting the cross-flow velocity (v_{cf}) to the highest (3.5 m·s^{-1}) after reaching the lowest v_{cf} (0.2 m·s^{-1}) would influence the shearing of the fouling layer. From the results, it is clear that a strong fouling layer is formed at low v_{cf} (0.2 m·s^{-1}).

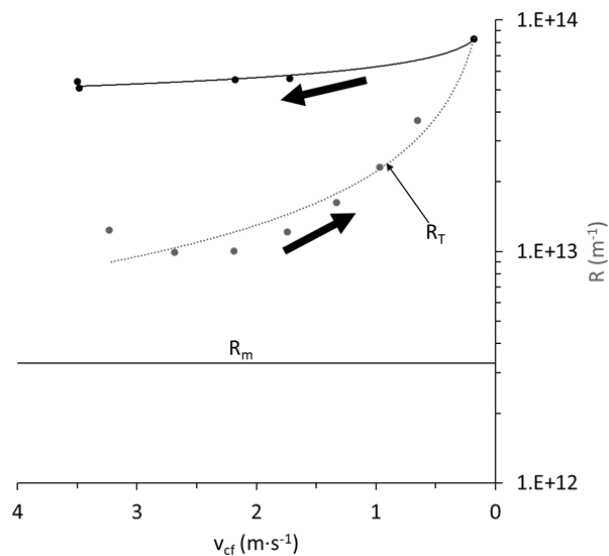**Figure A2:** Total resistance (R_T) as a function of v_{cf} for different cycles of v_{cf}. R is the sum of intrinsic membrane resistance (R_m), and fouling resistance (R_f). The black thick arrow indicates the direction of cross-flow cycle, i.e., it was started from the highest (3.5 m·s^{-1}) and changed to the lowest (0.2 m·s^{-1}), and again reverted back to the highest (3.5 m·s^{-1}).

A6   Relationship between pump efficiency and cross-flow velocity

The **Figure A4** shows the relationship between the centrifugal pump's efficiency and the cross-flow velocity.
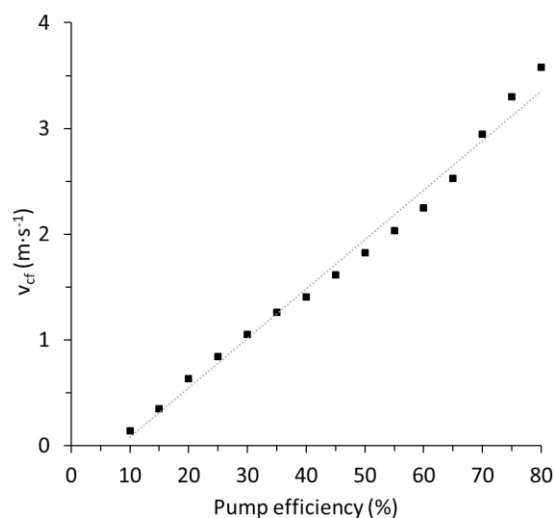

Figure A3: Relationship between the centrifugal pump's efficiency and the cross-flow velocity.

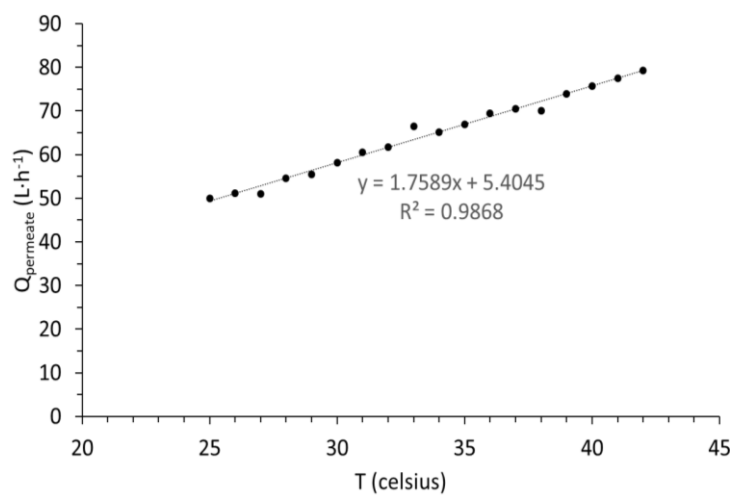## A7   Relationship between permeate flow rate and temperature

Figure A4: Relationship between permeate flow rate and temperature.

A8   Reynolds number (Re) as a function of cross-flow velocity
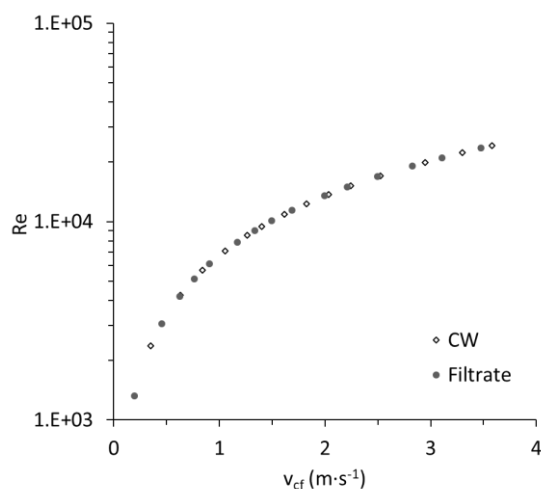
Figure A5: Relationship between Reynolds number (Re) and cross-flow velocity (v_{cf}) for clean water (CW) and filtrate (after filter-press).

A9   Retention of SCFAs by filter-press and microfiltration
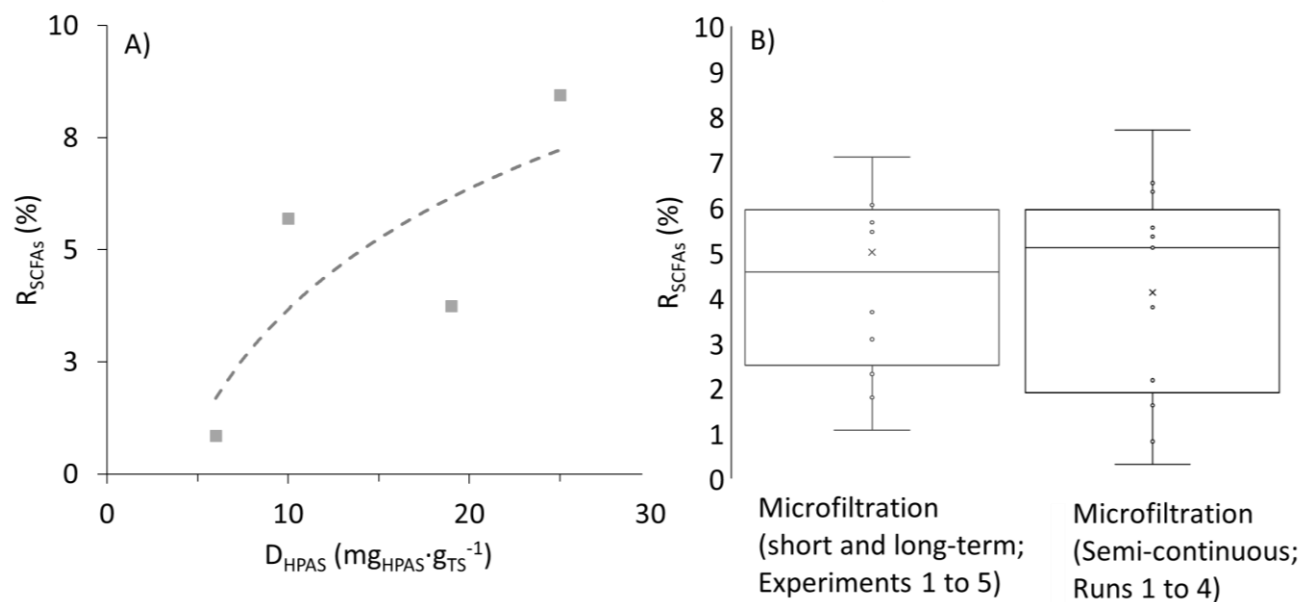
Figure A6 : A) retention of short-chain fatty acids (SCFAs) R_{SCFAs} for a pilot-scale chamber filter-press lined with a polyester membrane (pore size = 100 µm) at different dosages of hydroxypropyl trimenthyl ammonium starch (HPAS), and B) R_{SCFAs} for ceramic microfiltration membrane (pore size = 0.2 µm) during short and long-term microfiltration experiments 1 to 5 and semi-continuous microfiltration runs 1 to 4. Note: in **Figure A7B**, for experiments 1 to 5, samples were taken on a daily basis and from all the values, a histogram is generated. For runs 1 to 4, at least 2 samples for each run were combined and then a histogram was generated.

A10   Description of the BES medium

The BES medium comprised of several components, including 0.42 g·L^{-1} of KH$_2$PO$_4$, 0.22 g·L^{-1} of K$_2$HPO$_4$, 0.2 g·L^{-1} of NH$_4$Cl, 0.38 g·L^{-1} of KCl, 0.36 g·L^{-1} of NaCl, 0.21 g·L^{-1} of MgCl$_2$, and 11.92 g·L^{-1} of HEPES. After the autoclaving of the medium, some supplements were added, including 1 mL L^{-1}of a 0.4 mM CaCl$_2$ solution, 10 mL L^{-1} nutrient broth trace mineral solution (Coppi et al., 2001), and a 1.0 mL L^{-1} of a selenite-tungstate solution whose composition was 13 mM NaOH, 17 µM Na$_2$SeO$_3$, and 12 µM Na$_2$WO$_4$. Furthermore, 10 mL of Wolin´s vitamin solution (German Type Culture Collection, DSMZ, media 141)) was also incorporated. To achieve an anoxic environment, the medium was purged with nitrogen (100 vol%) for 30 minutes inside rubber-sealed bottles. For preculture, 20 mM sodium acetate was incorporated as the electron donor and 40 mM sodium fumarate was added as the electron acceptor. The pH of the medium was corrected to pH 7.4. After that, the mixed culture of *S. oneidensis* and *G. sulfurreducens* in a 9:1 ratio at initial optical density (OD$_{600}$) of 0.1 was inoculated in the reactor. Before that, the pelleted cells were washed twice with BES medium so that the growth and activity of the cells would not be hindered.

A11   Reactor sterilization

Around 90 L of 10 % v/v hydrogen peroxide (H$_2$O$_2$) (VWR, Germany) was pumped via the feed pump into the system, and was left inside for around 24 hours. Following this, the reactor was emptied and rinsed twice with around 90 L of sterilized deionized water. Approximately 90 liters of 70 % v/v ethanol (EtOH) (VWR, Germany) was introduced into the RDBER through the feed pump, and left inside for two hours. Another emptying and rinsing procedure was performed with sterile deionized water. The leftover water was pumped out of the system, and the reactor was anaerobized with 99.8 % nitrogen gas. As the least point of drainage is above the least point of the reactor, a volume of approx. 10 L of liquid (mixture of sterilized water plus EtOH) remained in the system.

A12   Microbial community analysis procedure and sampling

The process involved DNA extraction, 16S rDNA PCR on the isolated genomic DNA, indexing, and purification of the PCR product, along with qualitative assessment. Following amplicon sequencing (2 x 250 bp, with a minimum of 50,000 reads), bioinformatic analysis and phylogenetic classification were performed using the SILVA 16S database. Samples to analyze microbial community in the planktonic phase were taken between day 97 and 105, day 116 and day 200 (after termination of the experiment). Samples from the anodic and cathodic biofilms were taken in day 200 (after termination of the experiment). Samples taken between day 97 and 105, and day 116 were taken under sterile conditions, while the remaining samples (taken after termination of the experiment) were taken under unsterile conditions. Since large amounts of biofilm were scraped off during unsterile sampling, the possibility of contamination is presumably trivial. This would also be the case for samples taken for the planktonic phase (at the end of the experiment), as unsterile hydrolyzate was introduced 70 days prior to the termination of the experiment.

A13   Biomass distribution on the anodes

After the 200-day experiment, the RDBER was carefully dismantled to analyze the biofilm distribution on the anode disks. The distribution was characterized using three methods, 1) gravimetry analysis to estimate the total dry biomass on the anode surface, 2) imaging using optical coherence tomography (OCT) to evaluate biofilm thickness (L$_F$), biovolume (BV) and substratum coverage (SC), and 3) effective surface coverage (SC$_{eff}$) determination using digital photographs. In first two cases, specific disks were chosen for

analyses (see **Figure A8A**). Sides of the disks that underwent biomass or OCT-image analyses were arbitrarily chosen, at defined intervals as shown in **Figure A8A**.

1) For the gravimetric determination of the biomass, the biofilm was scraped off from the anode surface with a rubber scraper into a crucible with a known weight and dried in an oven at 105 °C for at least 48 hours. After weighing again, the empty known crucible weight was subtracted, and the final weight is referred to as the dry biomass (D_b). The results of D_b from each side of the anode disks are normalized separately to the respective area of the side, and represented as normalized biomass (m_N).

   Normalized biomass (m_N) obtained from the surface of the anode is estimated as,

   $$m_N \left[\frac{g}{m^2}\right] = \frac{D_b}{A_{anode}} \tag{A1}$$

   Visualization of the biofilm by means of OCT was carried out using GANYMEDE II spectral domain OCT system equipped with an LSM04 lens (Thorlabs GmbH, Lübeck, Germany). Reproducible adjustment of three imaging positions on the anode disks was achieved with special alignment equipment for positioning the anodes as well as the OCT lens. Single images covered an area of 10 x 10 mm^2 and image analysis of the three-dimensional data (voxel size: $8 \times 8 \times 2.06$ μm^3) was done applying ImageJ (Version 1.52n, Fiji, Schneider et al., 2012) as suggested by Wagner and Horn (2017). Quantification resulted in color-coded height maps for biofilm topography description.

2) To characterize the biofilm distribution on the anodes based on OCT images, mean biofilm thickness (L_F), mean biovolume (BV), and substratum coverage (SC) are estimated according to Hackbarth et al., 2023. Biovolume (BV) is the biofilm volume V_B (μm^3) distributed over an imaging area A_{OCT} (0.01 m × 0.01 m),

   $$BV\ (\mu m) = \frac{V_B}{A_{specific}} \tag{A2}$$

   Substratum coverage (SC) is expressed as,

   $$SC\ (\%) = \frac{A_{specific} - A_{uncovered}}{A_{specific}} \times 100 \tag{A3}$$

   Where, $A_{uncovered}$ is the area of the uncovered substratum.

3) In case of the determination of SC_{eff}, digital photographs (image resolution: 96 dpi) were utilized for all 65 disks (except for one side each of the disk numbers 63 and 65, along the direction of x (front side), as no photographs are available). The evaluation of disk number 65 was performed indirectly and the procedure can be found in the figure caption of **Figure 5.5.** Disk number 63 (along the direction of x; front side) is not evaluated due to lack of any data, but even with a complete SC_{eff} (100 %) of this particular disk side, a coefficient of variation of more than 5 % is not expected, and therefore does not significantly affect the total SC_{eff} -values. In any case, the color of the images was inverted and contrast-saturated using IMAGE ONLINE.CO (https://saturation.imageonline.co) to emphasize the biofilm-covered area (see **Figure A8C**). In almost all cases, the distribution of the biofilm on each disk is annular (see photograph in supplementary **Figure A8C**). Arbitrary x- and y-axes were established with equal grid intervals along the radial array of the anode using graphreaderV2

(http://www.graphreader.com/v2). Using the grid, Cartesian coordinates were first established on the circumference of the anode (or the circumference of the annulus) which approximates the circular shape of the anode to a multi-faceted polygon. The same number of coordinates were used on the inner circumference of the annulus (which marks the beginning of the biofilm) to generate another multi-faceted polygon. The area in the polygon on the circumference of the anode is the sum of biofilm-covered and uncovered area of the anode (i.e., total area), while the area of the polygon within the inner circumference of the annulus (or the biofilm) represents the uncovered area of the anode. In any case, the area of the respective polygons ($A_{polygon}$) was calculated using the shoelace theorem as follows,

$$A_{polygon}(-) = \frac{1}{2} \times |\sum_{i=1}^{n}\{x_i \cdot y_{i+1}\} - \sum_{i=1}^{n}\{y_i \cdot x_{i+1}\}| \qquad \text{A4}$$

Where, n is the number of vertices, and x and y are the Cartesian coordinates of the polygon.

The estimation of the effective biofilm area (BA_{eff}) is calculated as follows,

$$BA_{eff}\ (m^2) = \left[\sum_{i=1}^{N}\left\{\frac{A_{polygon,tot(x),N} - A_{polygon,uncovered(x),N}}{A_{polygon,tot(x),N}}\right\} + \right.$$
$$\left.\sum_{i=1}^{N}\left\{\frac{A_{polygon,tot(-x),N} - A_{polygon,uncovered(-x),N}}{A_{polygon,tot(-x),N}} \times\right\}\right] \times A_{anode,N} \qquad \text{A5}$$

Where, x (front side) and -x (back side) represent the respective sides of the anode disk. $A_{polygon,tot,N}$ (-) and $A_{polygon,uncovered,N}$ (-) are the total area (biofilm-covered and uncovered areas of the anode), and uncovered area of a specific anode disk N (where N ranges between 1 and 65), respectively. $A_{anode,N}$ (m^2) is the known area of a singular anode including both sides.

Effective surface coverage (SC_{eff}) is calculated via the grid-based approximation for each side of the anode disk:

$$SC_{eff}\ (\%) = \frac{A_{polygon,tot} - A_{polygon,uncovered}}{A_{polygon,tot}} \times 100 \qquad \text{A6}$$

The results of the three methods are represented as a function of reactor length along the flow direction (front side; depicted as x) and against the direction of flow (back side; depicted as -x). The results of the OCT-images are also represented as a function of the disks radii. No biomass analysis was carried out for the RDBER operated at the WWTP.
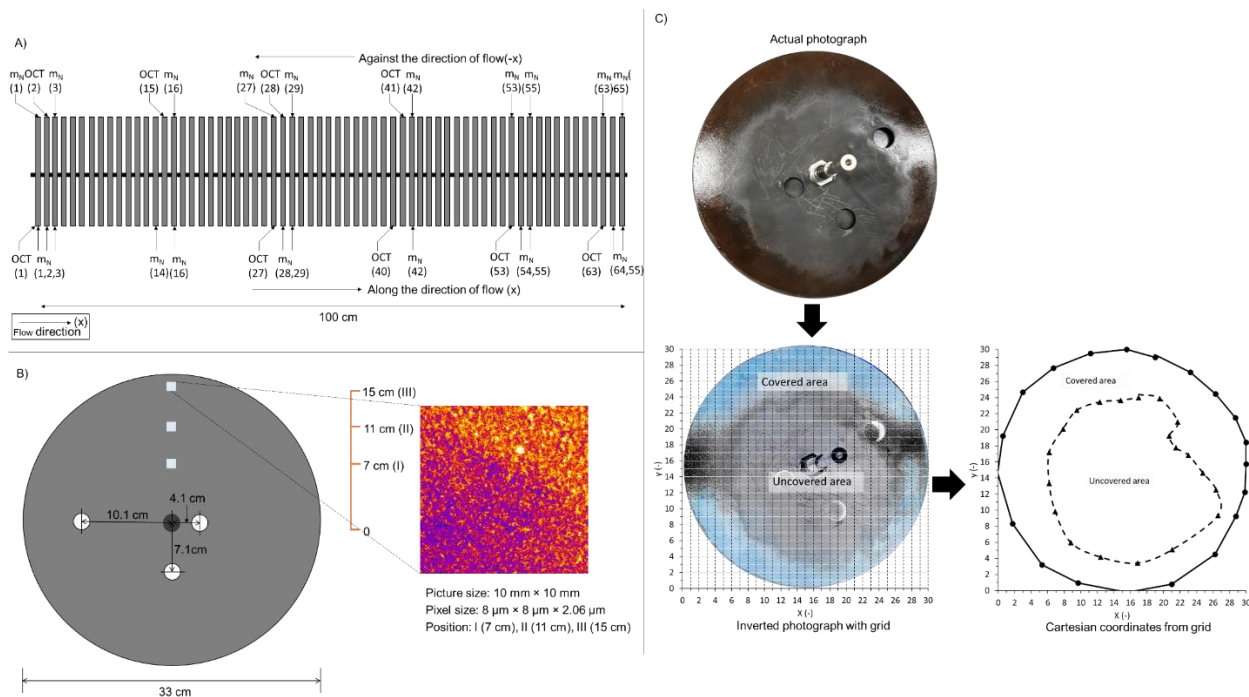
Figure A7: A) Disk numbers shown in parentheses on which normalized biomass (denoted as m_N) measurement and/or OCT imaging was carried out, B) Positions along the radius of the anode for OCT images as well as specifications of the single images, and C) grid-based estimation of effective surface coverage SC_{eff}. Note: Disk number 1 was evaluated between 7 and 15 cm radius at 1 cm intervals.

A14 Experimental conditions and overview of the RDBER's operation

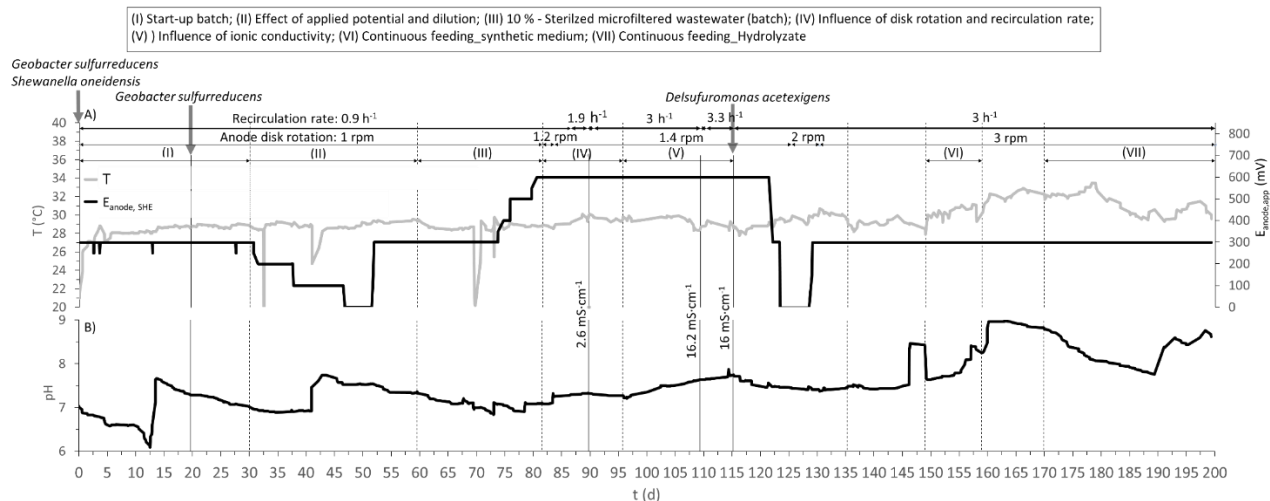**Figure A8:** Description of experimental parameters shown as phases in Roman numerals and separated by dotted vertical lines, A) temperature and applied anode potential ($E_{anode, app}$) and B) pH over the course of the experiment. Note: recirculation rate is presented as h^{-1} (i.e., recirculation rate ($L \cdot h^{-1}$)/reactor volume (L), the solid lines refer to the electrical conductivity of the reactor medium.

A15   Ethanol as a carbon source in the RDBER

Phase I was performed at an anode disk rotation of 1 rpm, pH 7 (at the start), and recirculation rate of the reactor content of 0.9 h^{-1}. As mentioned in ***section 5.2.3***, the reactor underwent two chemical sterilizations before inoculation, of which the second was performed with 70 % v/v EtOH. After drainage, approximately 10 L of diluted EtOH was leftover in the reactor, as the least point of drainage was at the point of the influent (see **Figure 5.1A**). Therefore, apart from the two carbon sources provided in the start-up medium, HAc and HLa, there was a significant concentration of EtOH in the system as another major carbon source. The resulting concentration of EtOH at the start of the experiment (based on gas chromatogram), after the 100 L-inoculated medium with HAc and HLa was introduced, was at least 6,100 mg·L^{-1} (equivalent to 133 mM or 12730 mg$_{COD}$·L^{-1}), whereas the concentrations of the acids were 25 mM HAc and 25 mM HLa. However, it is suspected that the delayed measurement of EtOH for the initial start-up samples, which was done several days later and after storing in the freezer at -20 °C, may have underestimated the actual concentration (due to evaporation as EtOH has a moderately high vapor pressure), as sCOD$_{rest}$-value (i.e., difference between sCOD and COD of SCFAs) showed that the concentration could be as high as 176 mM on day 6.5 (see **Figure A10A**). The value of sCOD was also higher on this day (19850 mg$_{sCOD}$·L^{-1}) compared to the initial days (16970 mg$_{sCOD}$·L^{-1} on day 2.5), and since it is not possible to have a higher sCOD value, the underestimation of EtOH concentration in the first sample is likely valid.

HLa was completely degraded after 6.5 d, and during this period there was a production HPr (see **Figure A10B**). In principle, *S. oneidensis* can utilize O$_2$ or the anode as terminal electron acceptors to convert lactate to acetate. However, the onset of HLa degradation was much later than O$_2$ depletion, but it is also important to mention that HLa conversion to propionate has not been described for *S. oneidensis* (Hirose et al., 2018). This means that means that the degradation of HLa might have been due to another organism. Phylogentic analysis showed that the preculture of *G. sulfurreducens* already underwent a *Clostridium* contamination (results not shown). Several species of *Clostridium* are able to produce SCFAs mixture (Liberato et al., 2019). For instance, *C. propionicum* and *C. neopropionicum* can ferment on HLa to produce HPr and HAc ($6C_3H_5O_3^- \rightarrow 4C_3H_5O_2^- + 2C_2H_3O_2^- + 2HCO_3^- + 2H^+$; ΔG^0 = -330 kJ·mol^{-1}) (Stams et al., 1998). Looking at HLa degradation and HPr production on day 4, 0.43 moles HPr were produced per mol of HLa degraded. However, the degradation of HLa should yield 0.67 moles of HPr per mol of HLa and 0.3 moles HAc per mole of HLa. In addition to HPr, there was a production of HBu, HBu-iso, HVa and HVa-iso in small concentrations at the same time HLa was degraded, with their sum reaching around 5 mM. As mentioned earlier, SCFAs fermentation is possible with several *Clostridium* species, but the exact pathway is not clear.
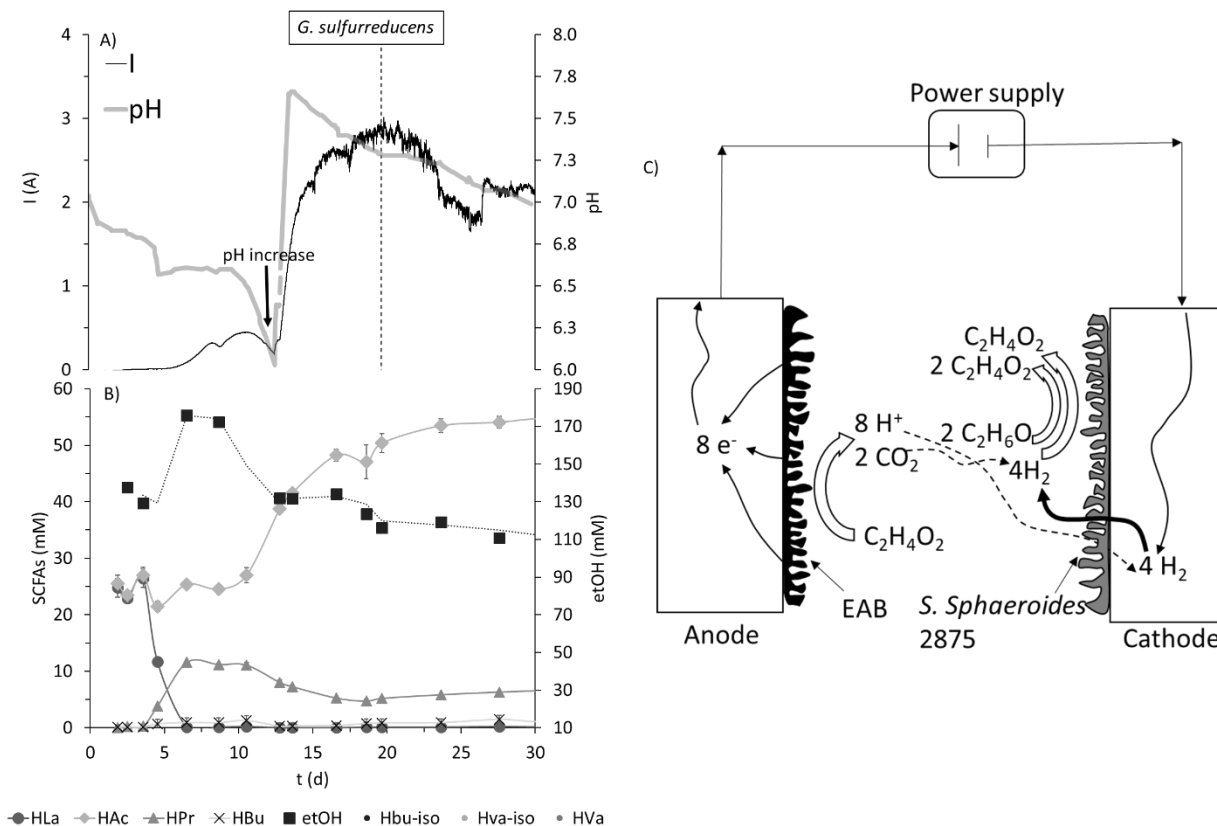
Figure A9: A) Current and pH-value, B) variation in SCFAs, HLa and EtOH concentration as a function of time, and C) hypothetical syntrophy postulated by Rümenapf, 2024 between electroactive bacteria (EAB) and Sporomusa sphaeroides DSM 2875. Conditions (between days 15 and 30, phase I): pH: 7.2 ± 0.2; T = 29.8 ± 0.2 °C; 1; recirculation rate = $0.9\ h^{-1}$; $E_{anode, app}$ = 300 mV vs SHE. Note: **Figure A10C** is a qualitative representation of the postulated syntrophy and the actual description and quantitative analysis can be found in the text below.

S. sphaeroides can use H_2 and CO_2 to produce HAc via the reductive acetyl CoA- pathway (Wood-Ljungdahl) ($4\ H_2 + 2\ HCO_3^- + H^+ \rightarrow C_2H_3O_2^- + 4\ H_2O$; ΔG^0 = -104.6 kJ·mol^{-1}) (Möller et al., 1984). However, *S. sphaeroides* can ferment short-chain alcohols like ethanol, methanol or butanol (Möller et al., 1984). The fermentation of of EtOH to HAc ($2\ C_2H_6O + 2\ H_2O \rightarrow 2\ C_2H_3O_2^- + 4\ H_2 + 2H^+$; ΔG^0 = +19.4 kJ·mol^{-1}) is thermodynamically unfavorable as H_2 production is a limiting factor (Madigan et al., 2020). However, integrating this hydrogen into the Wood-Ljungdahl pathway for CO_2 fixation could render this endergonic reaction energetically favorable and exergonic ($2\ C_2H_6O + 2\ HCO_3^- \rightarrow 3\ C_2H_3O_2^- + 2\ H_2O + H^+$; $\Delta G^{o'}$ = -85.6 kJ·mol^{-1}) (Rümenapf, 2024; Seitz et al., 1990; Thauer et al., 1977). Given that the medium was fully anaerobic, with pure nitrogen as the headspace gas, the CO_2 required for this process likely originated from acetate oxidation via *G. sulfurreducens* (global reaction combining anode and cathode: $C_2H_3O_2^- + 4\ H_2O \rightarrow 4\ H_2 + 2\ HCO_3^- + H^+$). This suggests that EtOH fermentation was mediated by interspecies metabolic interactions, presented in supplementary **Figure A10C** (Rümenapf, 2024). In addition to HAc, there was consumption of HPr, HBu-iso, HBu, HVa and HVa-iso (see supplementary **Figure A10B**; global reaction combining anode and cathode: $CH_3CH_2COOH + 4\ H_2O \rightarrow 7\ H_2 + 3\ CO_2$; $CH_3CH_2CH_2COOH + 6\ H_2O \rightarrow 10\ H_2 + 4\ CO_2$; $CH_3CH_2CH_2CH_2COOH + 8\ H_2O \rightarrow 13\ H_2 + 5\ CO_2$). To verify this, a stoichiometric

calculation was carried out between the day of the highest peak until the end of phase 1 as shown in supplementary **Table A3**. The stoichiometric calculation shows that the aforementioned syntrophy as hypothesized by Rümenapf, 2024 is plausible.

Table A3: Stoichiometric calculations based on the hypothetical syntrophy between *G.sulfurreducens* and *Sporomusa sphaeroides* in phase I.

t (d)	Values based on current (I)		Calculated											
	e- (moles)	Δe- (moles)	etOH (mM)	ΔetOH (mM)	ΔHAc (mM)	ΔHAc reactor (mM)	ΔHAc (mM)	Δe- (moles)	ΔHPr (mM))	ΔHBu (mM)	ΔHVa (mM)	Δe- (moles)	Δe- (moles)	CE (%)
9	0.5		171.7											
30	36	+36	113.3	-58.4	+87.6[a]	+30.5[b]	-57.1[c]	+41.0[1]	-4.7	-1.8	-0.1	+9.3[2]	+50.3[3]	71
	e- (moles)	Δe- (moles)	sCOD (mg·L⁻¹)	ΔsCOD (mg·L⁻¹)	ΔO₂ (moles)	Δe- (moles)								CE (%)
9	0.5		19,450											
30	36	+36	15,280	-4170	-23.5	47								77

Δ shows the change in concentration or quantity, + and – indicates production and consumption, respectively; [a]HAc produced from etOH consumption; [b]HAc production in the reactor; [c]HAc consumption (difference between [a] and [c]); [1]moles of electrons released from HAc consumption; [2]moles of electrons released from HPr, HBu and HVa consumption; [3]total electrons released from HAc, HPr, HBu and HVa consumption.

Table A4: Produced (H$_{2,\,produced}$) and harvested (H$_{2,\,harvested}$) hydrogen, average current density (J), and gas composition in phase I during a specific duration.

t (d)	Theoretical values based on current (I)			H$_{2,\,harvested}$ (L)	J (mA·m⁻²)
	Δe- (moles)	ΔH₂ released (moles)	H$_{2,\,produced}$ (L)		
9 to 30	+36	+18	403	5.5	240 ± 34

Δ shows the change in concentration or quantity

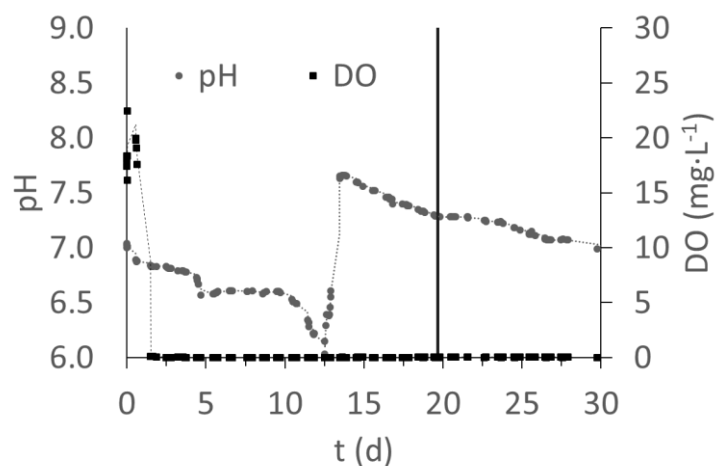## A16 pH and dissolved oxygen (DO) in phase I

Figure A10: pH and dissolved oxygen (DO) in phase I. The black line indicates the point at which reinoculation with *G. sulfurreducens* was done.

A17 Composition of hydrolyzate

The hydrolyzate used for continuous feeding in phase VI and VII was spiked with salts of SCFAs (NaHAc, NaHPr, NaHbu), and their corresponding concentration can be found in supplementary **Table A5**. In addition to SCFAs, the hydrolyzate was also spiked with 0.4 g·L^{-1} of NH$_4$Cl, 0.1 g·L^{-1} of KH$_2$PO$_4$ and 0.8 g·L^{-1} of KCl. The hydrolyzate used in phase III was not spiked. In phase III, the hydrolyzate was sterilized while sterilization was not carried out in phase VI and VII.

Table A5: Composition of hydrolyzate used in the RDBER in phases III, VI and VII.

Phases	sCOD (mg·L^{-1})	COD$_{HFa}$ (mg·L^{-1})	COD$_{HAc}$ (mg·L^{-1})	COD$_{HPr}$ (mg·L^{-1})	COD$_{HBu\text{-}iso}$ (mg·L^{-1})	COD$_{HBu}$ (mg·L^{-1})	COD$_{HVa\text{-}iso}$ (mg·L^{-1})	COD$_{HVa}$ (mg·L^{-1})	COD$_{SCFAs}$ (mg·L^{-1})	COD$_{SCFAs}$/sCOD (%)	NH$_4^+$ (mg·L^{-1})	PO$_4^{3-}$ (mg·L^{-1})
	2170	30	508	827	67	298	110	289	2129	98	173	-
III	1320	14	264	534	2	141	81	146	1184	90	135	-
	1590	16	293	630	2	165	88	175	1370	86	162	-
	688	8	95	173	2	84	30	64	457	66	121	11
VI*, VII*	4037 ± 1047	-	1905 ± 372	1524 ± 426	-	412 ± 153	-	-	3841 ± 918	96 ± 10	135	70

*Hydrolyzate was spiked with salts of SCFAs

A18   Gas bubbles trapped at the cathode
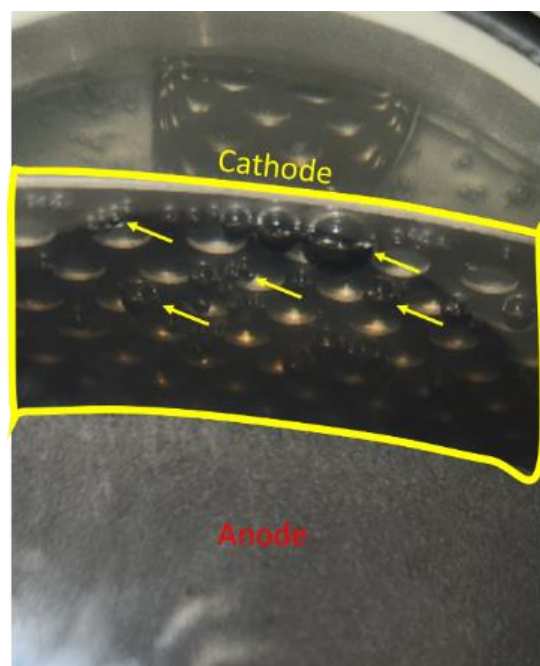
Figure A11: Small and large gas bubbles seemingly trapped at the cathode. The yellow arrows indicate a few of the bubbles that are trapped.

A19   Microbial population analysis
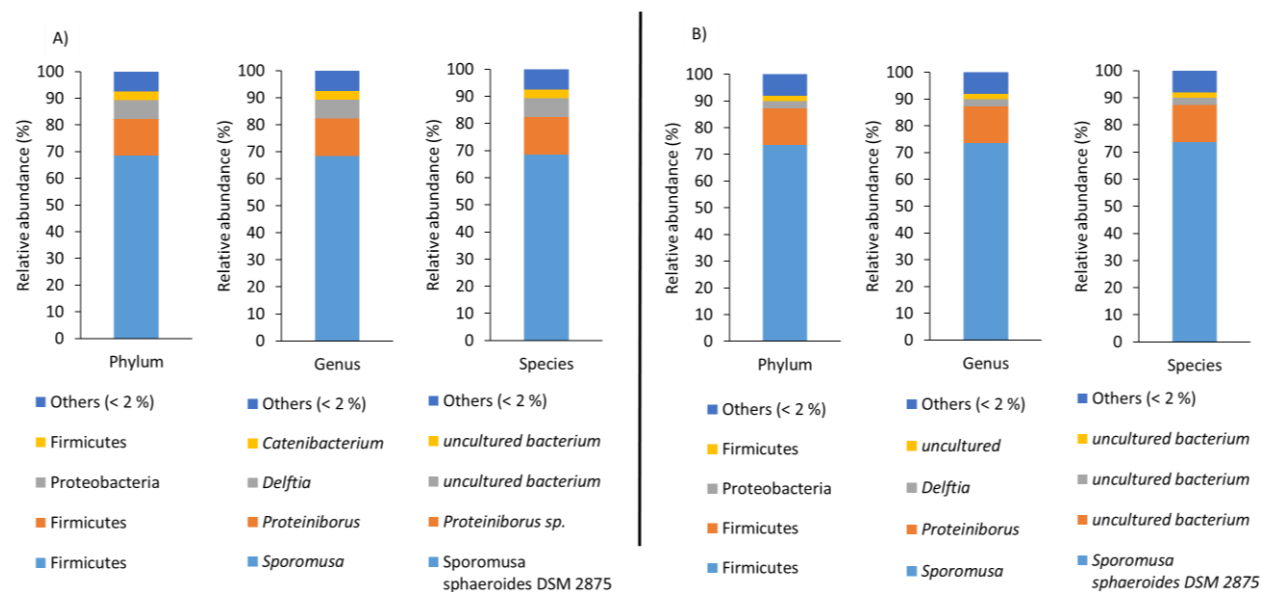
Figure A12: Microbial community in planktonic phase, A) between days 97 and 105, and B) day 116. No archaea were detected in the samples.

A20   Microbial population analysis at the end of the 200-day experiment
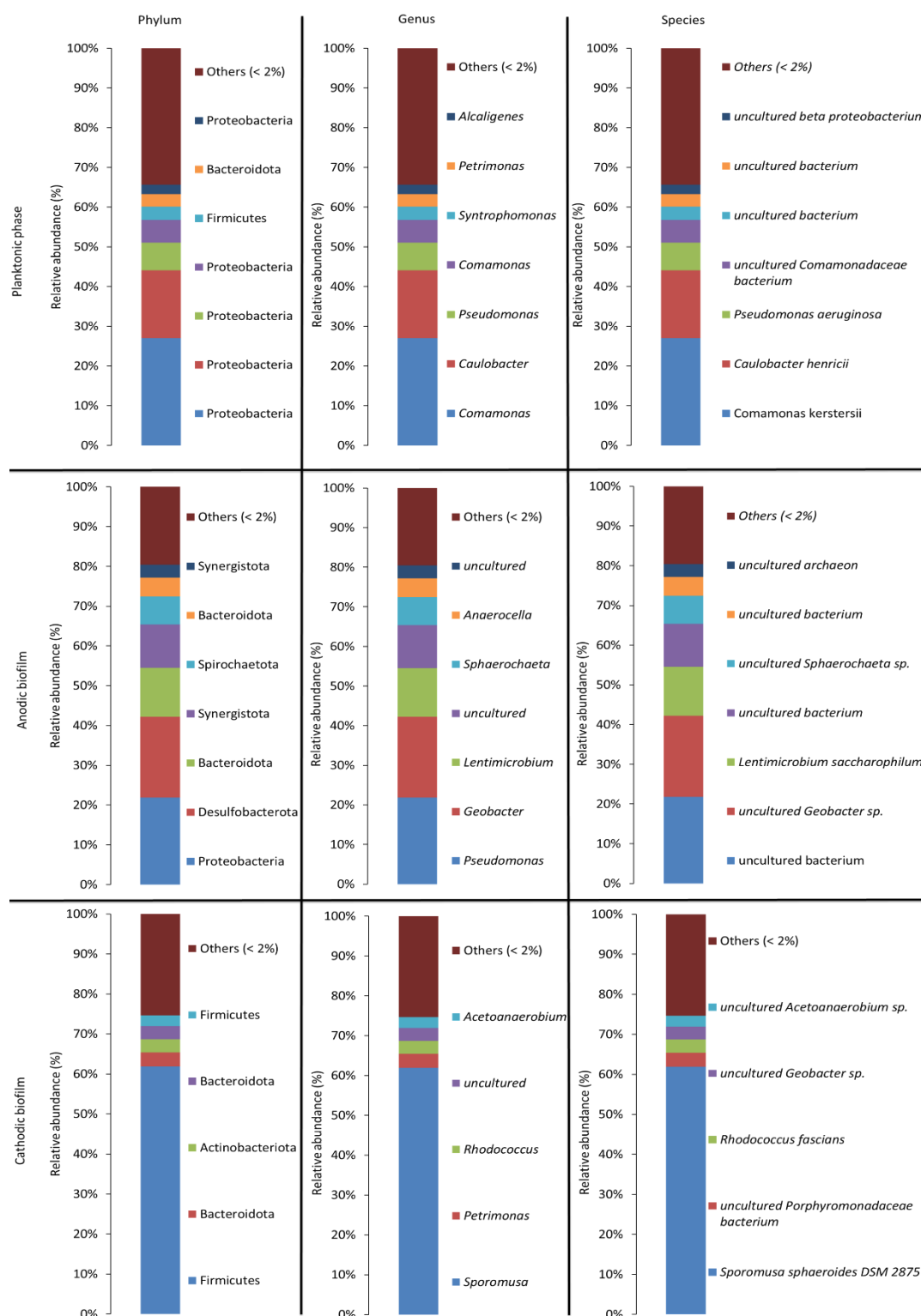
Figure A13: Bacterial community in the planktonic phase, anodic and cathodic biofilm at the end of the 200-day experiment.

A21   Archaea analysis at the end of the 200-day experiment
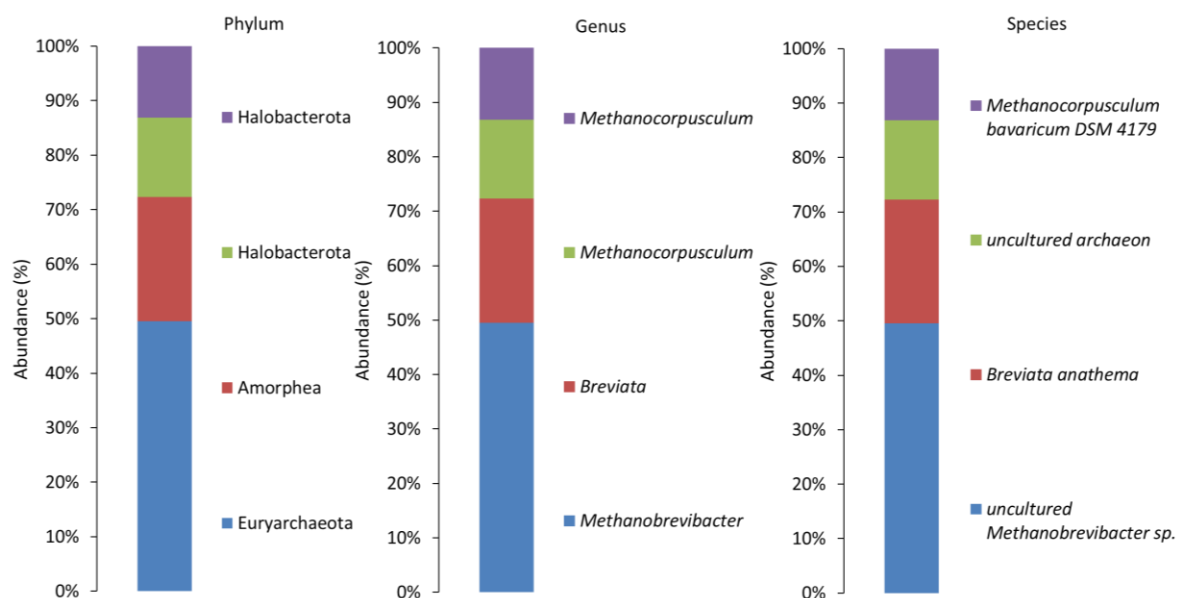
Figure A14: Archaea in the anodic biofilm at the end of the 200-day experiment. Only one strain of archaea was detected in the planktonic phase (phylum: Nanoarchaeota; genus: *uncultured euryarchaeote*) (not shown). No archaea were detected in the cathodic biofilm (not shown).

A22   Coulombic efficiency
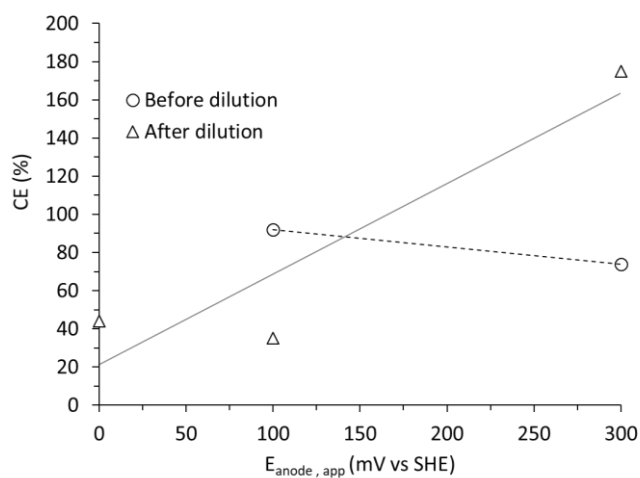
Figure A15: CE-values in phase II. Note: The CE-value at 200 mV vs SHE before dilution showed extremely high values, as there was little to no consumption of any C-source.

A23   Stoichiometric calculation

Table A6: Stoichiometric calculations for different phases in the 100L-RDBER.

Column groups: columns "e$^-$ (moles)" and the first "Δe$^-$ (moles)" are *Values based on current (I)*; the columns from "etOH (mM)" onward are *Calculated*.

| Phases	t (d)	Notes	e$^-$ (moles)	Δe$^-$ (moles)	sCOD (mg·L^{-1})	Δe$^-$ (moles)	CE (%)	etOH (mM)	ΔetOH (mM)	ΔHAc (mM)	HAc (mM)	ΔHAc (mM)	Δe$^-$ (moles)	HPr (mM)	ΔHPr (mM)	Δe$^-$ (moles)	HBu (mM)	ΔHBu (mM)	Δe$^-$ (moles)	Δe$^-$ (moles)	CE (%)
	30	200 mV vs SHE,	36																		
	37		52	+15		-															
II	37	100 mV vs SHE, before dilution	47.7		-			-	-	-	55.0			6.5			1.1				
	41		52.1	+4.4	-	-		-	-	-	49.4	-5.6	+4	6.2	-0.3	+0.3	0.9	-0.2	+0.4	+4.8	92
	41	100 mV vs SHE, after dilution	52.1		7765			59.1			24.8			3.1			0.97				
	46		56.8	+4.7	6575	+13.4	35	50.3	-8.8	-13.2	20.5	-4.3	+12.6	2.5	-0.6	+0.8	0.96	-0.02	+0.04	+13.4	35
	46	0 mV vs SHE, after dilution	56.8		6575			50.3			20.5										
	52		60.2	+3.4	5990	+7.7	44	45.0	-5.3	-8.0	20.4	-0.1	+5.8				NC			+5.8	59
	52	300 mV vs SHE, after dilution	60.2		5990			45.0			20.4										
	60		70.2	+10	5480	+5.7	175	38.0	-7.0	-10.5	19.8	-0.6	+7.9				NC			+7.9	127
III*	73	44 % dilution with hydrolyzate	86.6		3761																-
	74		87	+0.4	3725	+0.4	102														-
IV	82	Effect of rotational speed of the anode	93.0		3900																-
	89		96.8	+3.8	3655	+2.8	209						NE							-
	89		96.8		3655																-
	96		110.3	+13.5	3352	+3.4	397														-
VI	156	Continuous-unsterile synthetic medium			3686																-
	160			+2.0	3154	+6.0	33														-
VII A	179	Continuous-unsterile hydrolyzate			3897																-
	190			+0.8	3431	+5.2	16														-
VII B	191				3368																-
	200			+0.6	3123	+2.8	22														-

*done based on highest removal rate. Removal of sCOD was very low. NC = not consumed. NE= Not evaluated.
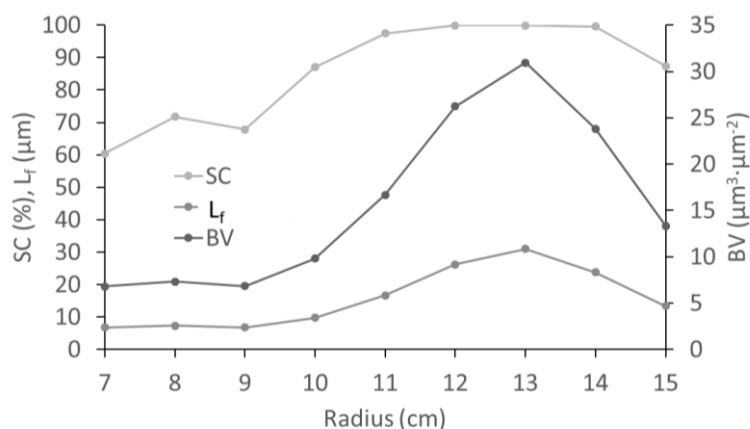
A24 Biofilm distribution along the radius of a singular anode disk

Figure A16: Substratum coverage (SC) and biovolume (BV) along the radius of the anode disk. Disk number 1, distance from inlet = 1.2 cm, flow direction = x (front side), interval = 1 cm.

A25 Stoichiometric calculations for Coulombic efficiency

Table A7: Stoichiometric calculations and yields of electrons for calculation of Coulombic efficiency

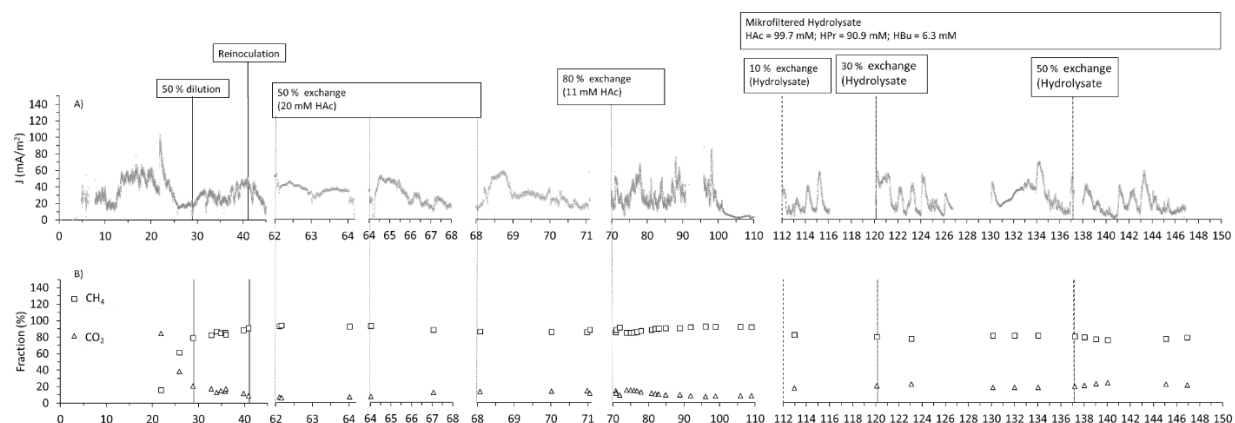| Equations	Electron yield
$1CH_3COOH + 2H_2O \rightarrow 4H_2 + 2CO_2$	8 moles per mole of HAc
$1CH_3CH_2COOH + 4H_2O \rightarrow 7H_2 + 3CO_2$	14 moles per mole of HPr
$1CH_3CH_2CH_2COOH + 6H_2O \rightarrow 10H_2 + 4CO_2$	20 moles per mole of HBu
$1CH_3CH_2CH_2CH_2COOH + 8H_2O \rightarrow 13H_2 + 5CO_2$	26 moles per mole of HVa
1 g COD $\rightarrow 1$ g $O_2 \rightarrow 0.03125$ moles O_2	0.125 moles per gram of COD

A26 100-L RDBER operated under unsterile conditions

Figure A17: A) current density (J) and B) gas fraction of 100 L-RDBER operated on-site of a wastewater treatment plant under unsterile conditions. Conditions: pH = 7.1, T = 29 ± 3 °C, $E_{anode,app}$ = 0 mV vs SHE, anode rotation = 1 rpm.

A27   Consumption of SCFAs during continuous feeding operation in phases VI and VII
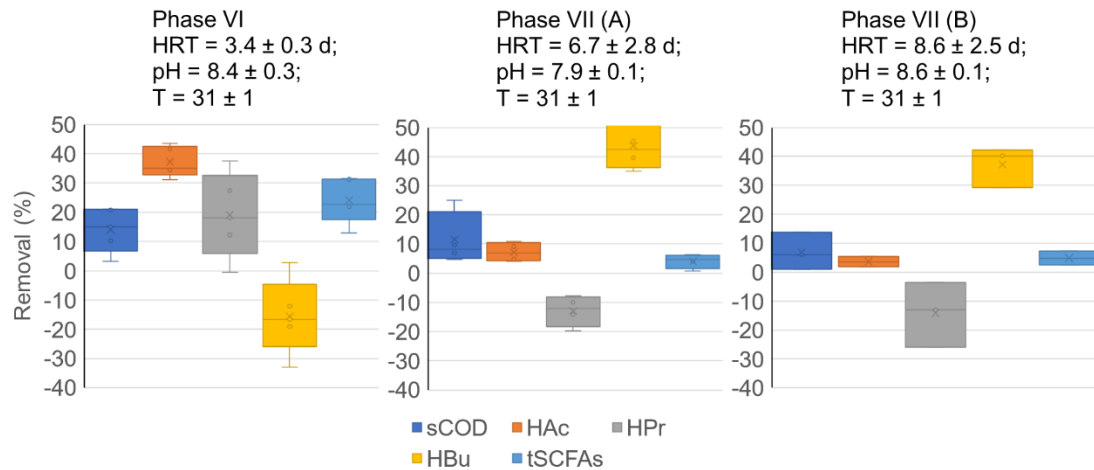

Figure A19: Removal rates of sCOD (soluble chemical oxygen demand), and short-chain fatty acids (SCFAs) in continuous phase VI, VII A and VII B.

A27   Consolidate results of biofilm paramters

Table A8: Mean values of effective surface/substratum coverage (SC$_{eff}$), normalized biomass (m$_N$), biofilm thickness, and substratum coverage (SC). **Note:** x and -x averaged indicates the average of both sides of the disks.

Parameter	Distribution	Flow direction	Length (cm)	Position (cm)	Mean	σ
Mean EC (%)	Reactor length	x	100	1 – 100	30	21
		-x			34	24
		x and -x averaged			32	22
Mean m$_N$ (g·m^{-2})	Reactor length	X	100	1 – 100	0.7	0.5
		-x			0.6	0.4
		x and -x averaged			0.6	0.5
Mean BV (µm^3·µm^{-2})	Reactor length	x	100	1 – 100	5.9	7.8
		-x			4.0	9.0
		x and -x averaged			5.0	8.5
	Radius	X	15	7	1.8	2.3
				11	3.8	5.8
				15	12.2	9.0
		-x		7	0.7	1.7

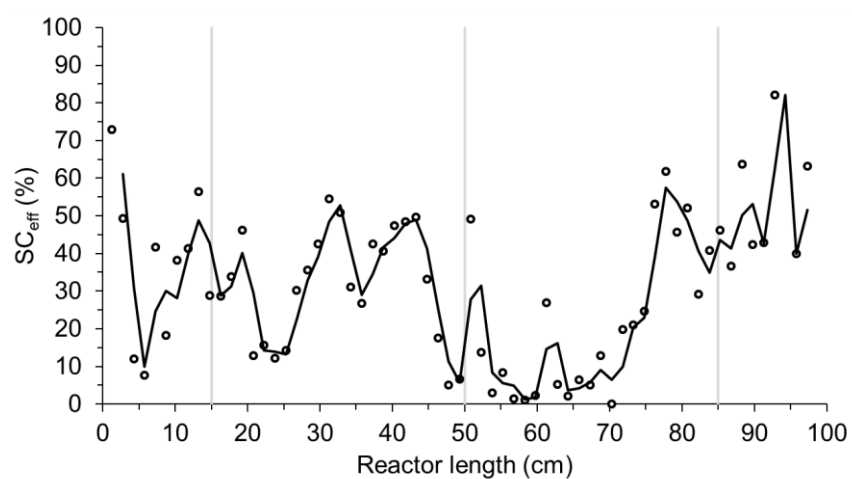|							
					11	1.7	1.9
					15	9.5	14.0
					7	1.2	1.7
		x and -x averaged			11	2.8	4.5
					15	10.9	11.8
	Reactor length	X	100	1 – 100		5.9	7.8
		-x				4.4	9.0
		x and -x averaged				5.2	8.4
					7	1.8	2.3
		x			11	3.8	5.8
					15	12.2	9.0
Mean L_F					7	1.5	1.7
	Radius	-x	15		11	1.7	1.9
					15	10.0	13.7
					7	1.6	2.0
		x and -x averaged			11	2.8	4.4
					15	11.1	11.7
		X				36	34
	Reactor length	-x	100	1 – 100		24	26
		x and -x averaged				30	31
	Radius				7	17	20
		X			11	27	32
					15	63	30
Mean SC (%)					7	8	3
		-x	15		11	18	18
					15	45	30
					7	13	15
		x and -x averaged			11	23	26
					15	54	31

Figure A20: : Effective surface coverage (SC_{eff}) calculated for both sides of the disks along reactor length. **Note:** The grey lines show the 3 outflow openings at the top of the reactor.

A28   Author verification

Title: Valorization of organic carbon in primary sludge via semi-continuous dark fermentation: First step to establish a wastewater biorefinery

Journal: Bioresource technology

Authors: Nikhil Shylaja Prakash, Peter Maurer, Harald Horn, Andrea Hille-Reichel

Position in the dissertation:

The content of this paper has been included in **Chapter 2**

Contribution of "Nikhil Shylaja Prakash"

      Conceptualization

      Methodology

      Investigation

      Data Curation

      Writing - Original Draft

Contribution of "Peter Maurer"

      Conceptualization

      Validation

Contribution of "Harald Horn"

      Writing - Review & Editing

      Supervision

      Funding Acquisition

Contribution of "Andrea Hille-Reichel"

      Conceptualization

      Validation

      Writing - Review & Editing

      Supervision

      Funding Acquisition

Signature of the authors:

Author	Signature
Nikhil Shylaja Prakash	
Peter Maurer	
Harald Horn	
Andrea Hille-Reichel	

Title: Optimizing cross-flow velocity under pressure loss conditions in pilot-scale tubular microfiltration of dewatered primary sludge

Authors: Nikhil Shylaja Prakash, Harald Horn, Florencia Saravia, Andrea Hille-Reichel

Position in the dissertation:

The content of this paper has been included in **Chapter 3**

Contribution of "Nikhil Shylaja Prakash"

Conceptualization

Methodology

Investigation

Data Curation

Writing - Original Draft

Contribution of "Harald Horn"

Writing - Review & Editing

Supervision

Funding Acquisition

Contribution of "Florencia Saravia"

Conceptualization

Validation

Writing - Review & Editing

Contribution of "Andrea Hille-Reichel"

Conceptualization

Validation

Writing - Review & Editing

Supervision

Funding Acquisition

Signature of the authors:

Author	Signature
Nikhil Shylaja Prakash	
Harald Horn	
Florencia Saravia	
Andrea Hille-Reichel	

Title: Separation of Short-Chain Fatty Acids from Primary Sludge into a Particle-Free Permeate by Coupling Chamber Filter-Press and Cross-Flow Microfiltration: Optimization, Semi-Continuous Operation, and Evaluation

Journal: Membranes

Authors: Nikhil Shylaja Prakash, Peter Maurer, Harald Horn, Florencia Saravia, Andrea Hille-Reichel

Position in the dissertation:

The content of this paper has been included in **Chapter 4**

Contribution of "Nikhil Shylaja Prakash"

 Conceptualization

 Methodology

 Investigation

 Data Curation

 Writing - Original Draft

Contribution of "Peter Maurer"

 Conceptualization

 Validation

Contribution of "Harald Horn"

 Writing - Review & Editing

 Supervision

 Funding Acquisition

Contribution of "Florencia Saravia"

 Conceptualization

 Validation

 Writing - Review & Editing

Contribution of "Andrea Hille-Reichel"

 Conceptualization

 Validation

Writing - Review & Editing

Supervision

Funding Acquisition

Signature of the authors:

Author	*Signature*
Nikhil Shylaja Prakash	
Peter Maurer	
Harald Horn	
Florencia Saravia	
Andrea Hille-Reichel	

Title: Evaluation of a novel pilot-scale rotating disk bioelectrochemical reactor for hydrogen production in a wastewater biorefinery

Journal: Chemical Engineering Journal (under review)

Authors: Nikhil Shylaja Prakash, Willow Neske, Max Rümenapf, Zhizhao Xiao, Andreas Netsch, Harald

Horn, Jonas Ulmann, Johannes Reiner, Andrea Hille-Reichel

Position in the dissertation:

The content of this paper has been included in **Chapter 5**

Contribution of "Nikhil Shylaja Prakash"

Conceptualization

Methodology

Investigation

Data Curation

Writing - Original Draft

Contribution of "Willow Neske"

Conceptualization

Methodology

Investigation

Data Curation

Writing - Review & Editing

Contribution of "Max Rümenapf"

Conceptualization

Methodology

Writing - Review & Editing

Contribution of "Zhizhao Xiao"

Conceptualization

Methodology

Writing - Review & Editing

Contribution of "Andreas Netsch"

Conceptualization

Methodology

Writing - Review & Editing

Contribution of "Johannes Reiner"

Conceptualization

Methodology

Contribution of "Jonas Ullmann"

Conceptualization

Methodology

Contribution of "Harald Horn"

Writing - Review & Editing

Supervision

Funding Acquisition

Contribution of "Andrea Hille-Reichel"

Conceptualization

Validation

Writing - Review & Editing

Supervision

Funding Acquisition

Signature of the authors:

Author	*Signature*
Nikhil Shylaja Prakash	
Willow Neske	

Max Rümenapf	
Zhizhao Xiao	
Andreas Netsch	
Johannes Reiner	
Jonas Ullmann	
Harald Horn	
Andrea Hille-Reichel	